

University of Nottingham

UK | CHINA | MALAYSIA

Design, Assembly, and Biological Evaluation of Protein Nanoparticles as Theranostic Agents and for Photodynamic Therapy

Ali Waleed Al-Ani

B.Sc. (Chemistry), M.Sc. (Biochemistry)

Thesis submitted to the University of Nottingham

for the degree of Doctor of Philosophy

22/05/2017

Declaration

The work in this thesis in chapters 3, 4, 5, 6 and 7 has been carried out by myself and no part has been submitted for any degree at the University of Nottingham or any other institutions.

Ali Waleed Numan Al-Ani

May 2017

This thesis is dedicated to the memory of my beloved father.

Abstract

Nanoparticles derived from proteins offer a smart material for the design of a new generation of anticancer therapies. In this thesis we describe a variety of novel photodynamic therapy (PDT), drug delivery, and imaging agents that have been combined to produce theranostic systems.

The initial research focus was to produce a protein nanocage of *Listeria innocua* DNA binding protein from starved cells (*Li*Dps) presenting the *Gaussia princeps* luciferase enzyme (*G*Luc) on its exterior (*G*Luc-*Li*Dps) together with the Zn (II)-Protoporphyrin IX (ZnPP) photosensitiser that has been covalently attached to the protein surface. This system operates as a PDT based on Bioluminescence Resonance Energy Transfer (BRET). The cytotoxic effect of *G*Luc-*Li*Dps-ZnPP nanoparticles in the presence of its substrate (coelenterazine) was tested against two types of breast cancer cell lines: SKBR3, MDA-MB-231, and also the MRC5 non-cancerous cell line, by means of an MTT assay. The results indicated that *G*Luc-*Li*Dps-ZnPP nanoparticles plus coelenterazine could inhibit the growth and the migration of SKBR3 cells, out of those studied. Downregulation of the Bcl-2 and Mcl-1 anti-apoptotic proteins was also observed after treatment with *G*Luc-*Li*Dps-ZnPP-mediated PDT, suggesting the SKBR3 cells may be undergoing apoptosis. Furthermore, both flow cytometry analysis and confocal microscopy images demonstrated that the *G*Luc-*Li*Dps-ZnPP appeared to be preferentially internalised in SKBR3 and MDA-MB-231 cell lines without uptake in the MRC5 cell line. Reactive Oxygen Species (ROS) levels were significantly increased in SKBR3 cells compared to MDA-MB-231 cells in the presence of this PDT agent.

Similarly, a C-terminal mini Singlet Oxygen Generator (miniSOG) photosensitiser was conjugated to *Li*Dps and human apoferritin

(HuAft). Moreover HuAft was fused with the $Z_{HER2:342}$ Affibody (Afb) targeting peptide to form Afb-HuAft. This 6.7 kDa Afb protein has a high binding affinity for the Human Epidermal Growth Factor receptor (HER2), which is overexpressed on the surface of a number of tumour cells especially breast cancers. Both miniSOG-*Li*Dps and miniSOG-HuAft fusion proteins were successfully expressed and purified and their subunits were self-assembled to form *G*Luc-*Li*Dps:miniSOG-*Li*Dps and Afb-HuAft:miniSOG-HuAft hybrid chimeric cages.

Additionally *G*Luc was directly fused with miniSOG supplemented with LTVSPWY targeting peptide to produce a novel (*G*Luc-miniSOG-LTVSPWY) for targeting of HER2 overexpressed cancer cells, potentially applicable for PDT. Further study is required in order to thoroughly characterise the *G*Luc-miniSOG-LTVSPWY and the hybrid cages as well as determine their respective cytotoxicity.

In the second objective, lead sulfide quantum dots (PbS QDs) were utilised as a drug delivery system and an imaging agent. The PbS QDs were capped with a cancer cell targeting agent (mutated Afb (Afb2C)) to form Afb2C-PbS QDs. This construct was further modified by conjugation with ZnPP to produce ZnPP-Afb2C-PbS QDs. The cytotoxic effect of Afb2C-PbS and ZnPP-Afb2C-PbS QDs were studied *in vitro* using SKBR3 (HER2 positive) and MDA-MB-231 (HER2 negative) cell lines. The results indicate that both types of PbS QDs display anti-proliferative activity against SKBR3 cells through inducement of cancer cell apoptosis and/or necrosis. This was observed from Pre-G1 phase arrest and an increase in cell population in late apoptosis and necrosis. These results may contribute to the development of cancer treatment using of nanoparticles derived from protein.

Acknowledgements

Firstly, I would like to express the most sincere thanks and appreciation to my supervisor Professor Neil R. Thomas for his support, expertise, guidance, and encouragement without which this work would not be complete. He has inspired me, and continues to do so. I am most thankful to him for guiding and supporting me, and for giving me the opportunity to work on a multidisciplinary project. This has allowed me to learn a lot of new techniques as well as meeting interesting people. I would like also to thank my country (Repoblic of Iraq) and the Ministry of Higher education and scientific research of Iraq for funding this studentship.

Especial thanks to my lab mate Dr. Lei Zhang who has taught me the alphabet of biotechnology method. I enjoyed working and discussing science with him.

Many thanks to Dr. Philip Bardelang, Dr. Luydmila Turyanska, Dr. David Harvey, and Dr. Francesco Zamberlan for their patience, enthusiasm, time, effort, and assistance in carrying out this project. I have benefited a lot of from their useful advice and discussions, and I’ve loved working with them.

I am indebted to colleagues and staff in the Centre for Biomolecular Sciences (Lab A20 and C28), School of Chemistry and the University of Nottingham. I would like to thank Dr. Tracy Bradshaw and Dr. Anchala Kuruppu for their help and training in the tissue culture lab.

Finally, my deepest thanks are for my lovely family, the real motivation behind my strength and patience. My parents, my wife, my daughters, brother, and sister who have always encouraged me and have been a huge source of support throughout my study.

Abbreviations

Å	Angstrom
Aa	Amino acids
Afb	$Z_{HER2:342}$ Affibody
Afb2C	Mutated (G82C-S84C) Affibody
AV	Annexin v-fluorescein isothiocyanate
ATP	Adenosine-5'-triphosphate
Bcl-2	B-cell lymphoma protein-2
Bp	base pairs
BRET	Bioluminescence Resonance Energy Transfer
BSA	Bovine serum albumin
CD	Circular Dichroism
CMC	Critical micelle concentration
Da	Dalton ≡ 1 atomic mass unit (a.m.u)
DLS	Dynamic Light Scattering
DNA	Deoxyribonucleic acid
dNTP	2'-deoxyribonucleotide-5'-triphosphate
Dps	DNA binding protein from starved cells
DTT	Dithiothreitol
E. coli	*Escherichia coli*
EDC	1-(3-Dimethylaminopropyl)-3-ethylcarbodiimide hydrochloride
EDTA	Ethylenediamine-N,N,N',N'-tetraacetic acid
EPR	Enhanced Permeability and Retention
FBS	Fetal bovine serum
FMN	Flavin mononucleotide
FRET	Fluorescence (or Förster) Resonance Energy Transfer
g_0	Acceleration caused by gravity
*G*Luc	*Gaussia princeps* luciferase
HCP1	Haem carrier protein-1
HER	Human epidermal growth factor receptor

HO-1	Heme oxygenase 1
HuAft	Human apoferritin
Ni-IMAC	Nickel-Immobilized Metal Ion Affinity Chromatography
IPTG	Isopropyl β-D-1 thiogalactopyranoside
LB	Luria-Bertani media
*Li*Dps	*Listeria innocua* DNA binding protein from starved cells
LOV	Light-oxygen-voltage-sensing domain
MALDI-TOF	Matrix-assisted laser desorption/ionisation time-of-flight
Mcl-1	myeloid cell leukemia-1
miniSOG	Mini Singlet Oxygen Generator
MTT	3-(4,5-Dimethylthiazol-2-yl)-2,5-diphenyltetrazolium bromide solution
MW	Molecular weight
MWCO	Molecular weight cut-off
nESI-MS	nano electrospray ionisation-mass spectroscopy
NHS	*N*-Hydroxysuccinimide
NIR	Near infrared
Nm	Nanometer
OD	Optical Density
PAGE	Polyacrylamide gel electrophoresis
PBS	Phosphate-buffered saline (KH_2PO_4 (1.8 mM) pH 7.4, Na_2HPO_4 (10 mM), KCl (2.7 mM), NaCl (137 mM))
PCR	Polymerase chain reaction
PDT	Photodynamic therapy
PI	Propidium iodide
PL	Photoluminescence
PS	Photosensitiser
QDs	Quantum dots
ROS	Reactive Oxygen Species
rpm	Revolutions per minute
SD	Standard deviation
SDS	Sodium dodecyl sulfate

SEC	Size exclusion chromatography
TBS-T	Tris (20 mM) pH7.6, NaCl (137 mM), tween (0.05% v/v)
TAE	Tris-Acetate (40 mM) pH 8.3, EDTA (1 mM)
TEM	Transmission Electron Microscopy
Tris	*tris* (Hydroxymethyl) aminomethane
v/v	Volume per volume
w/v	Weight per volume
ZnPP	Zn(II)-protoporphyrin IX

Standard amino acids abbreviations

Full name	**Three-letter code**	**One-letter code**
L-Alanine	Ala	A
L-Arginine	Arg	R
L-Asparagine	Asn	N
L-Aspartic acid	Asp	D
L-Cysteine	Cys	C
L-Glutamic acid	Glu	E
L-Glutamine	Gln	Q
L-Glycine	Gly	G
L-Histidine	His	H
L-Isoleucine	Ile	I
L-Leucine	Leu	L
L-Lysine	Lys	K
L-Methionine	Met	M
L-Phenylalanine	Phe	F
L-proline	Pro	P
L-Serine	Ser	S
L-Threonine	Thr	T
L-Tryptophan	Trp	W
L-Tyrosine	Tyr	Y
L-Valine	Val	V

Table of Contents

1. General introduction 16
1.1 Proteins and nanotechnology 16
1.2 Protein nanoparticles and cancer treatment 17
1.3 Cage-like proteins 19
1.3.1 Ferritin 20
1.3.1.1 Ferritin structure 22
1.3.1.2 Ferritin interaction with ferrous ions 25
1.3.1.3 Ferritin usage and applications 27
1.3.2 DNA binding protein from starved cells (Dps) 29
1.3.2.1 Dps protection mechanisms 30
1.3.2.2 Dps structure 32
1.3.2.3 Applications of Dps 35
1.4 Photodynamic therapy (PDT) 37
1.5 Resonance energy transfer 41
1.6 Photosensitiser 44
A photosensitiser 44
1.6.1 Zn (II)-protoporphyrin IX (ZnPP) 48
1.6.2 Mini Singlet Oxygen Species Generator (miniSOG) 50
1.7 Luciferase 52
1.7.1 *Gaussia princeps* luciferase (*G*Luc) 54
1.8 Antibody-drug conjugate 56
1.9 Quantum dots (QDs) 59
1.10 Project aim and outline 61

2. Materials and methods 68
2.1 Molecular biology techniques 68
2.1.1 Extraction and purification of DNA from cell cultures 68
2.1.2 DNA manipulation 69
2.1.2.1 Polymerase Chain Reaction (PCR) 69
2.1.2.2 Mutagenesis 70
2.1.2.3 Restriction enzyme digestion 72

2.1.2.4 Ligation 73
2.1.3 Agarose gel electrophoresis 73
2.1.4 DNA sequencing 74
2.1.5 Transformation of chemical and electro-competent *E. coli* . 74
2.1.6 Overexpression of recombinant proteins 75
2.1.7 Preparation of *E. coli* cell lysates 76
2.2 Purification techniques 77
2.2.1 Ammonium sulfate precipitation 77
2.2.2 Nickel-Immobilised metal ion affinity chromatography (Ni-IMAC) 77
2.2.3 Anion exchange chromatography 78
2.2.4 Desalting and buffer exchange 79
2.2.5 Size exclusion chromatography (SEC) 80
2.3 Determination of protein concentration 80
2.4 Polyacrylamide gel electrophoresis (PAGE) 81
2.4.1 Denaturing (SDS-PAGE) 81
2.4.1.1 Reagents and solutions 81
2.4.1.2 Procedure 82
2.4.2 Tricine-SDS-PAGE 83
2.4.2.1 Reagents and solutions 83
2.4.2.2 Procedure 83
2.4.3 Non-Denaturing (Native PAGE) 84
2.4.3.1 Reagents and solutions 84
2.4.3.2 Procedure 84
2.5 Mass spectrometry (MS) 85
2.5.1 Matrix Assisted Laser Desorption/Ionisation Time-of-Flight (MALDI-TOF MS) 85
2.5.2 Nano-Electrospray Ionization (nESI) MS 85
2.6 Dis-assembly and re-assembly of genetically modified *Li*Dps and HuAft 86
2.7 Bioluminescence activity 87
2.8 Labelling *G*Luc-*Li*Dps with ZnPP using EDC/NHS 87

2.9 Dynamic light scattering (DLS) measurements 88
2.10 Circular dichroism (CD) spectroscopy 89
2.11 Afb2C-based nanoprobes preparation 89
2.11.1 Synthesis of Afb2C-PbS QDs 89
2.11.2 Labelling of Afb2C-PbS QDs with ZnPP 90
2.12 Photoluminescence (PL) measurements 91
2.13 Transmission electron microscopy (TEM) 91
2.14 *In vitro* cell assays 91
2.14.1 Subculturing cell lines 91
2.14.2 Determination of cell viability using the MTT assay 92
2.14.3 Cellular uptake determination using flow cytometry 93
2.14.4 Reactive oxygen species (ROS) detection 94
2.14.5 Preparation of samples for confocal microscopy 95
2.14.6 Wound healing (migration) assay 95
2.14.7 Cell cycle assay 96
2.14.8 Annexin V- fluorescein isothiocyanate apoptosis detection 98
2.14.9 Western blotting 99
2.14.9.1 Reagents and solutions 99
2.14.9.2 Sample preparation 100
2.14.9.1 Procedure 101
2.15 Statistical analysis 102

3. Construction of *G*Luc-miniSOG-LTVSPWY recombinant protein as a photodynamic therapy and imaging agents 103

3.1 Introduction 103
3.2 Results 105
3.2.1 Designing of the *G*Luc-miniSOG-LTVSPWY protein 105
3.2.2 Expression and purification of the *G*Luc-miniSOG-LTVSPWY protein 110
3.2.3 Study of *G*Luc-miniSOG-LTVSPWY activity 114
3.3 Discussion 119

4. Fabrication of *G*Luc-*Li*Dps:miniSOG-*Li*Dps and Afb-HuAft:miniSOG-HuAft hybrid cages 124
4.1 Introduction 124
4.2 Results 128
4.2.1 Creation of the *G*Luc-*Li*Dps:miniSOG-*Li*Dps nanoparticles 128
4.2.1.1 Construction of a *G*Luc-*Li*Dps expression vector 128
4.2.1.2 Construction of a miniSOG-*Li*Dps expression vector 128
4.2.1.3 Expression and purification of miniSOG-*Li*Dps protein 132
4.2.1.4 Fabrication of *G*Luc-*Li*Dps:miniSOG-*Li*Dps nanoparticles 136
4.2.2 Creation of Afb-HuAft:miniSOG-HuAft nanoparticles 140
4.2.2.1 Construction of a miniSOG-HuAft expression vector 140
4.2.2.2 Expression and purification of miniSOG-HuAft protein 143
4.2.2.3 Expression and purification of Afb-HuAft 145
4.2.2.4 Fabrication of Afb-HuAft:miniSOG-HuAft nanoparticles 147
4.3 Discussion 149
4.3.1 *G*Luc-*Li*Dps:miniSOG-*Li*Dps hybrid protein 150
4.3.2 Afb-HuAft:miniSOG-HuAft hybrid protein 153

5. Preparation and chemical modification of *G*Luc-*Li*Dps-ZnPP as a photodynamic therapy and imaging agent 155
5.1 Introduction 155
5.2 Results 157
5.2.1 Creation of *G*Luc-*Li*Dps-ZnPP nanoparticles 157
5.2.1.1 Synthesis a *G*Luc-*Li*Dps recombinant protein 157
5.2.1.2 Expression, purification, and characterisation of *G*Luc-*Li*Dps 161
5.2.1.3 *G*Luc-*Li*Dps activity 163
5.2.2 ZnPP labelling of *G*Luc-*Li*Dps 166
5.2.2 1 *G*Luc-*Li*Dps-ZnPP activity 171
5.3 Discussion 172

6. Synthesis of Afb2C-PbS and ZnPP-Afb2C-PbS QDs 176
6.1 Introduction 176
6.1.1 Afb2C-PbS QDs 176

6.1.2 ZnPP-Afb2C-PbS QDs 177
6.2 Results 179
6.2.1 Afb2C preparation 179
6.2.2 Expression and purification of Afb2C 181
6.2.3 Synthesis of Afb2C-PbS QDs 183
6.2.4 Characterisation of Afb2C-PbS QDs 184
6.2.4.1 Optical activity of Afb2C-PbS QDs 184
6.2.4.2 Determination of Afb2C-PbS QDs size using TEM 185
6.2.5 Bioconjugation of Afb2C-PbS QDs with ZnPP 188
6.2.5.1 Optical activity of ZnPP-Afb2C-PbS QDs 189
6.2.5.2 Determination of ZnPP-Afb2C-PbS QDs size using TEM 190
6.3 Discussion 192
7 Protein nanoparticles for breast cancer treatment 195
7.1 Introduction 195
7.1.1 Breast cancer 195
7.1.1.1 SKBR3 cell line 198
7.1.1.2 MDA-MB-231 cell line 198
7.1.1.3 MRC5 cell line 199
7.1.2 HER family 200
7.1.3 Cell cycle 202
7.1.4 Programmed cell death pathways: apoptosis and necrosis 204
7.1.5 ROS in healthy cells and cancer cells 207
7.1.6 Enhanced permeability and retention (EPR) effect 209
7.1.7 *In vitro* effect of novel nanoparticle protein on breast cancer cell lines 210
7.2 Results 211
7.2.1 *G*Luc-*Li*Dps-ZnPP 211
7.2.1.1 Effect of *G*Luc-*Li*Dps-ZnPP plus coelenterazine on cell viability and proliferation 211
7.2.1.2 *G*Luc-*Li*Dps-ZnPP cellular uptake and localisation study 215
7.2.1.3 Intracellular ROS generated by *G*Luc-*Li*Dps-ZnPP plus coelenterazine 218

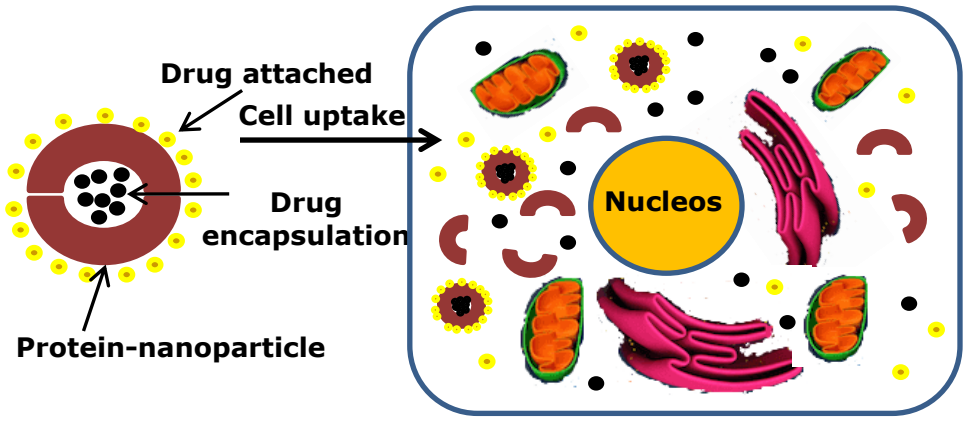
7.2.1.4 Effect of *G*Luc-*Li*Dps-ZnPP plus coelenterazine on Bcl-2 and Mcl-1 anti-apoptotic proteins 219
7.2.1.5 Effect of *G*Luc-*Li*Dps-ZnPP plus coelenterazine on cell migration 222
7.2.1.6 Confocal microscopy for monitoring the cellular localisation of *G*Luc-*Li*Dps-ZnPP 224
7.2.2 Afb2C-PbS QDs 225
7.2.2.1 Effect of Afb2C-PbS QDs on cell viability and proliferation 226
7.2.2.2 Effect of Afb2C-PbS QDs on cell cycle 229
7.2.2.3 Programmed cell death induced by Afb2C-PbS QDs .. 233
7.2.2.4 Effect of Afb2C-PbS QDs on Bcl-2 anti-apoptotic proteins 237
7.2.3 ZnPP-Afb2C-PbS QDs 238
7.2.3.1 Effect of ZnPP-Afb2C-PbS QDs on cell viability and proliferation 239
7.2.3.2 Effect of ZnPP-Afb2C-PbS QDs on cell cycle 242
7.2.3.3 Programmed cell death induced by ZnPP-Afb2C-PbS QDs..... 246
7.2.3.4 ZnPP-Afb2C-PbS QD cellular uptake and localisation study 248
7.2.3.5 Confocal microscopy study of ZnPP-Afb2C-PbS QDs .. 250
7.3 Discussion 251
7.3.1 *G*Luc-*Li*Dps-ZnPP 252
7.3.2 Afb2C-PbS QDs 255
7.3.3 ZnPP-Afb2C-PbS QDs 257
8. Conclusions and future directions 260
8.1 Cage-like proteins as PDT and imaging agents 261
8.2 HER2-targeting systems for breast cancer therapy 263
9 References 267
10 Appendix 294
10.1 Bacterial strains 294
10.2 PCR primers 294
10.3 Plasmids 295
10.4 Media 296
10.4.1 Bacteria culture media 296
10.4.2 Mammalian culture media 297

Chapter 1

1. General introduction

1.1 Proteins and nanotechnology

Recently, several different nanoparticles derived from proteins ranging in size from 10-1000 nm have been used as scaffolds for developing drug delivery systems and imaging agents [1–3]. These proteins could be utilised as drug carriers by encapsulating drug molecules within their interior spaces, or by attaching drug molecules, nucleic acids or lipids to their exterior surfaces such as the encapsulation of doxorubicin, an anticancer agent into ferritin and conjugation of fluorescein succinimidyl ester imaging agent to elastin-mimetic protein [4–7] (Scheme 1.1). Nanoparticles derived from proteins have many advantages relating to the treatment of cancer and other diseases. These include: biocompatibility, biodegradability, and enhanced stability and solubility of drug molecule cargos. Moreover, nanotechnology systems allow modulation of these proteins to allow them to specifically target tumour tissues, leading to localisation at a specific site with higher pharmaceutical effect and lower toxic side effects [8,9].



Scheme 1.1: Schematic representation the process of cellular uptake and triggering of drug from the protein cargo.

1.2 Protein nanoparticles and cancer treatment

There are over 200 different types of cancer, most of them leading cause of death worldwide without any promising therapy. In 2008, 12.7 million people were diagnosed with cancer and 7.6 million died. This figure is expected to increase by 13.1 million by 2030 [10–12]. Traditional therapies that have been used for the treatment of cancer include radiotherapy, chemotherapy, or surgical intervention. Therapies are usually combined in order to achieve more effective results. However the major drawback for these therapies are their toxic side effects, non-targeting of the tumour region, and the incomplete eradication of the cancer cells [13–15].

Protein-based nanoparticles offer a promising therapy for cancer treatment without such side effects. This is achieved through delivery

and localisation of drug molecules to the targeted area, focusing treatment on the affected region only, thus minimising the toxic side effects observed for systemic treatment. The delivery process includes neutralisation of drug toxicity within a protein carrier during transportation and release of the toxic effect at the targeting sites only [2,16,17].

The focus of this study was breast cancer which is the second most common cancer worldwide (1.7 million females diagnosed per year worldwide, 11.9% of all cancers diagnosed) [18] (Figure 1.1).

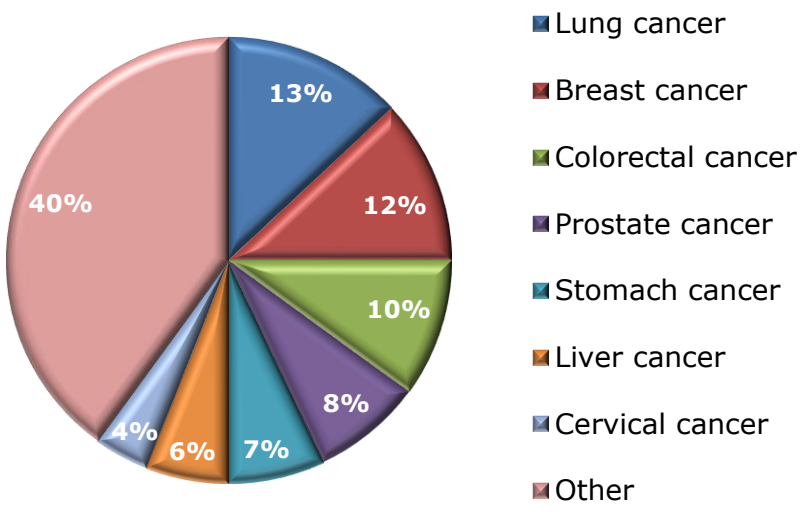
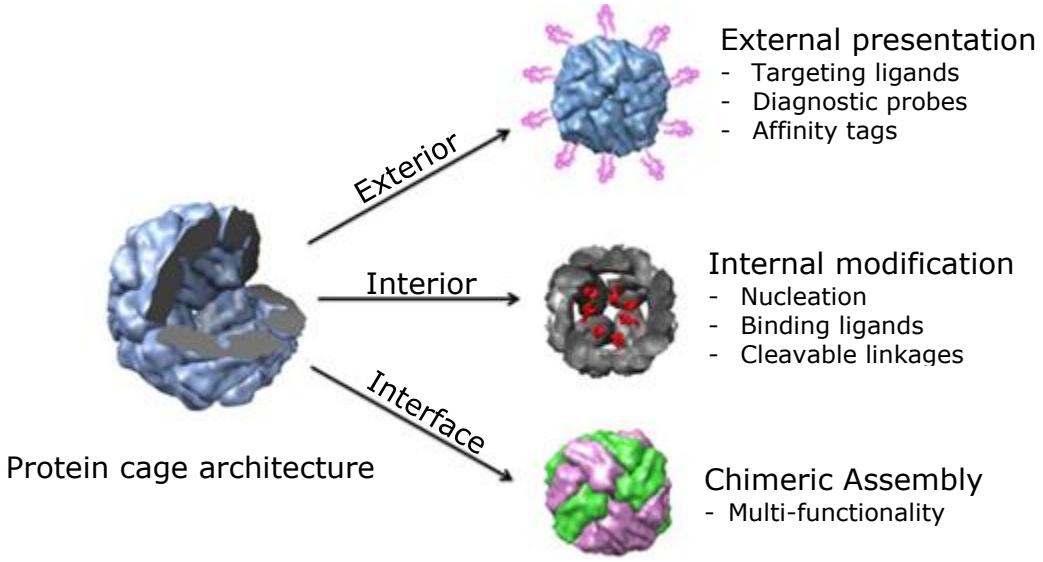


Figure 1.1: The pie is showing the percent distribution of cancer in worldwide in 2012 [19].

1.3 Cage-like proteins

Cage-like self-assembling protein complexes provide a useful platform to construct a nanoscale complex with multiple functions. This is because these proteins have three distinct architectural surfaces: interior; exterior; and the interface between subunits. These permit conjugation of functional molecules to the exterior of the cage and encapsulation of cargo within the hollow core. Consequently, these proteins have the potential to be used for theranostic, therapeutic, imaging, and drug delivery purposes [20] (Scheme 1.2).



Scheme 1.2: Schematic illustration the three surfaces of cage-like protein (adapted from M. Uchida *et al.*, The ferritin superfamily: Supramolecular templates for materials synthesis, Biochim. Biophys. Acta. 1800 (2010) 834–845) [21].

1.3.1 Ferritin

Ferritin is a ubiquitous protein and its amino acid sequence has been highly conserved for iron-binding throughout evolution in higher organisms. Ferritin a cage-like protein a member of ferritin family that plays a critical role in iron homeostasis through the control of the biosynthesis and dissolution of hydrated ferric oxides inside its cage (Figure 1.2) [22,23].

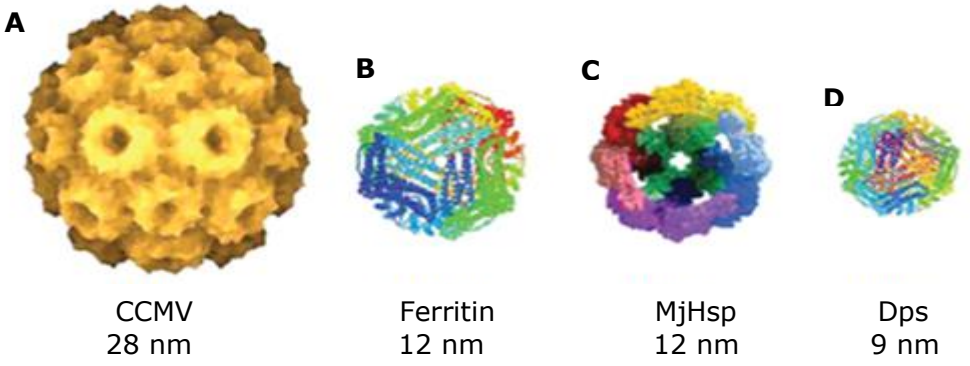


Figure 1.2: Ferritin-like family proteins. **(A)** Cowpea chlorotic mottle virus (CCMV). **(B)** Ferritin. **(C)** Small heat shock protein from *Methanococcus jannaschii* (*Mj*Hsp). **(D)** DNA binding protein from starved cells (Dps) (adapted from M.L. Flenniken *et al.*, A library of protein cage architectures as nanomaterials, Springer Berlin Heidelberg, Berlin, 2009) [24].

Iron is a fundamental mineral in biological systems, necessary for many biological processes, including electron transfer reactions, transport of oxygen, detoxification and the utilisation of oxygen in catalytic oxidation-reduction reactions in cells [25].

However, at high concentrations iron can be extremely cytotoxic. Fe^{2+} catalyses the generation of Reactive Oxygen Species (ROS) via different pathways. Perhaps the most common of these pathways is the Fenton reaction [26], in which Fe^{2+} reacts with hydrogen peroxide (H_2O_2) to produce a highly reactive hydroxyl radical ($^{\bullet}OH$) (Scheme 1.3):

$$Fe^{2+} + H_2O_2 \rightarrow Fe^{3+} + OH^- + {}^{\bullet}OH \text{ (Fenton reaction)}$$

$$Fe^{3+} + H_2O_2 \rightarrow Fe^{2+} + HOO^{\bullet} + H^+$$

Scheme 1.3: Generation of ROS through Fenton reaction [26].

ROS are strong oxidising agents which attack DNA, proteins and lipids causing irreversible damage to cells. Sustained damage often leads to organ failure and host death. Pathogenic microorganisms also require free Fe^{2+} as a nutrient for survival and replication while higher organisms usually limit the free Fe^{2+} available to suppress bacterial invasion. For these reasons, Fe^{2+} is harmful when deficient and in excess, causing living organisms to develop mechanisms for monitoring and controlling available Fe^{2+} [27,28].

Ferritin stores excess iron in many organisms in a non-toxic form, releasing it only when necessary to participate in cellular metabolism [29].

1.3.1.1 Ferritin structure

Ferritin is a roughly spherical protein (rhombic dodecahedron) and consists of a hollow protein shell with a molecular weight (MW) of approximately 450 kDa. This structure is composed of 24 subunits assembled in cubic symmetry to form the apoferritin (ferritin without the iron core) shell which has a diameter of 12 nm diameter and an aqueous cavity. This core is 8 nm in diameter and has the ability to sequester up to approximately 4500 iron atoms as ferrihydrite [30,31] (Figure 1.3). Ferritin shell subunits are of two types: the heavy (H) chains of 21 kDa and 178 amino acids (aa); and the light (L) chain of 19 kDa and 171 aa. These two types are closely related in primary sequence (~53% homology) and tertiary structure [28].

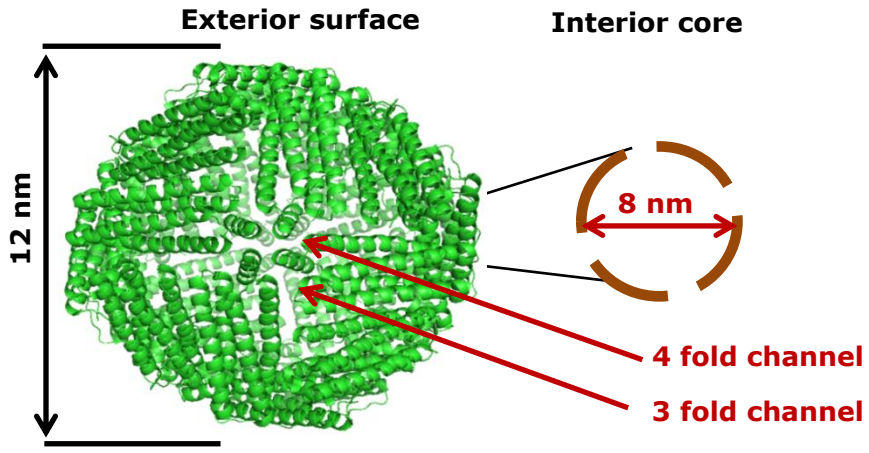


Figure 1.3: Ribbon diagram model of frog M ferritin crystal structure from the Protein Data Bank (PDB ID: 4DAS) was created by PyMol. Ribbon diagram shows the frog M ferritin with exterior surface and interior cavity [32].

However, their functions are distinct: the H-chain is essential for ferrous oxidation; it includes an enzymatic ferroxidase centre which catalyses rapid oxidation of Fe^{2+} to Fe^{3+}. Whereas the L-chain lacks this function but includes residues responsible for iron nucleation and mineralisation, promoting long-term storage of iron inside the apoferritin cavity.

Furthermore, the ratio of the two types of chain of ferritin in cells can be different according to the tissue types. For example the L-chain is the major subunit of ferritin in the iron storage organs of the liver and spleen, whereas the ferritin in organs which required greater iron detoxification, such as the heart and brain, are rich in the H-chain [31,33].

The 24 subunits which comprise the apoferritin shell are arranged in octahedral 432 symmetry, and form eight 3 Å diameter hydrophilic channels, which contain 3-fold symmetry axes and six 4 Å diameter hydrophobic channels with 4-fold symmetry axes. These channels connect the core of apoferritin with the surrounding environment. The hydrophilic channels allow entry and dissolution of divalent cations into the cavity through the apoferritin shell, while the hydrophobic channels control the transport of bimolecular oxygen inside the cavity, a process which is necessary for Fe^{2+} oxidation [34–36] (Figure 1.4).

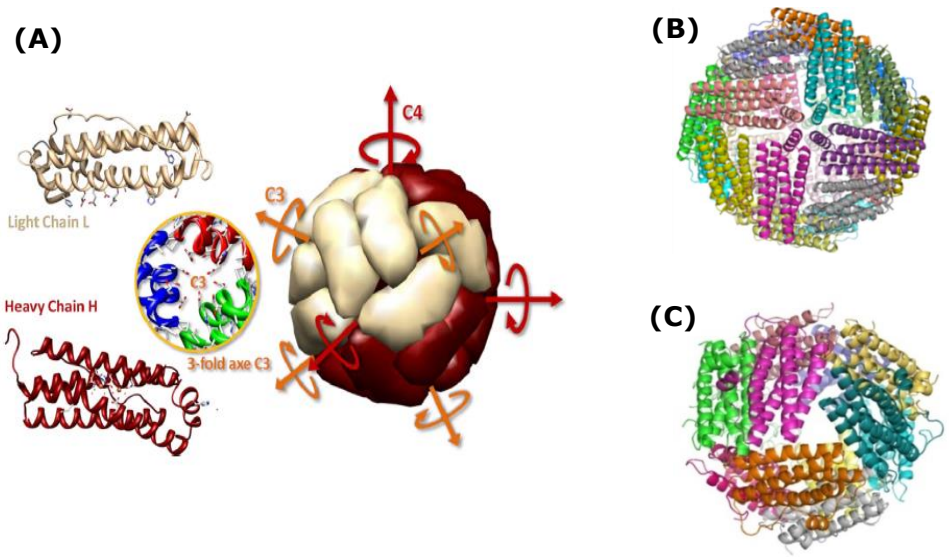


Figure 1.4: Ribbon diagram of ferritin. **(A)** The horse spleen ferritin H-chain and L-chain subunits of that form the shell of apoferritin with 3-fold and 4-fold axis (adapted from F. Carmona *et al*., Ferritin iron uptake and release in the presence of metals and metalloproteins: chemical implications in the brain, Coord. Chem. Rev. 257 (2013) 2752–2764 [28]. **(B)** Shows the ferritin subunits that form the 4-fold symmetry axis. **(C)** View ferritin subunit that form 3-fold symmetry axis (figures **B** and **C** represent ferritin crystal structure from the Protein Data Bank (PDB ID: 4DAS) were created by PyMol) [32].

The secondary structure of the ferritin subunits consists of 5 α-helices which are designated by convention A, B, C, D and E. Four parallel and anti-parallel helices A-D form a distinctive long central bundle with the small fifth helix, E attached to the C-terminal of ferritin [37] (Figure 1.5). Studies of the physical properties of ferritin demonstrate that its quaternary protein structure is stable to temperatures up to ~70 °C and over a wide range of pH values; between pH 3.0-10.0. Ferritin subunits dissociate below pH 3.0, but are reassembled into the native structure when the solution is returned to pH > 5.0 [28].

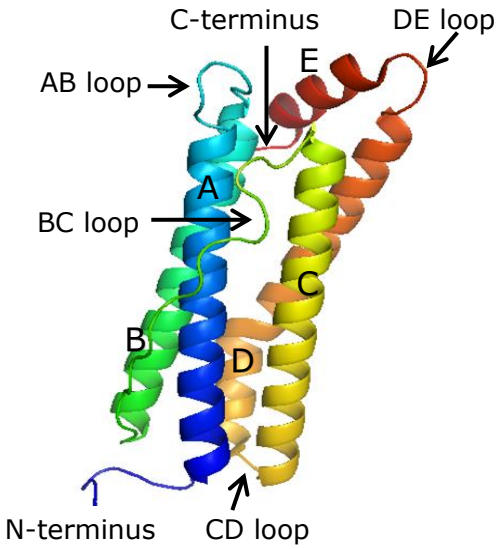


Figure 1.5: Ribbon model of human ferritin L-chain subunit crystal structure from the Protein Data Bank (PDB ID: 2FFX) created by PyMol. The ribbon diagram shows the secondary structure of ferritin subunit, the outer surface consists of A, C helices and BC loop, whereas the interior surface made from B and D helices [38].

1.3.1.2 Ferritin interaction with ferrous ions

The main function of ferritin is to detoxify excess Fe^{2+} ions by sequestering them inside its cavity in the form of Fe^{3+} ions. This is a multi-stage process, beginning with the entry of Fe^{2+} into the cavity through the hydrophilic channels of apoferritin [39]. Oxidation of Fe^{2+} ions and reduction of oxygen (ferroxidation) occurs at the ferroxidase centre of the H subunits. The catalytic reaction is described in Scheme 1.4:

$$\text{Protein}+2Fe^{2+}+O_2+3H_2O \rightarrow \text{Protein-}[Fe_2O(OH)_2]^{2+}_{(\text{Ferroxidase complex})}+H_2O_2+2H^+$$

$$\text{Protein-}[Fe_2O(OH)_2]^{2+}+H_2O \rightarrow 2FeOOH_{Core}+2H^+$$

Scheme 1.4: Oxidation of Fe^{2+} ions catalysed by the ferroxidase centre of the H-chain subunits [40].

The Fe^{3+} ions produced inside the cage preferentially accumulate at available nucleation sites on the L-chain interior surface that enhance the production of microcrystals, mostly ferrihydrite. Additional Fe^{2+} ions oxidise on the surface of the initial microcrystals and the localised microcrystals grow as shown in Figure 1.6 [28,36,39]. As well as sequestering Fe^{2+} into the centre, the other function of ferritin is to release Fe^{2+} ion in response to iron deficiency in the cell cytoplasm. Although the signal for iron deficiency remains unknown, the usual mechanism for recovery of iron from ferritin involves the disruption of ferritin in a regulated manner by lysosomal enzymes [36,39]. Therefore, the ferritin proteins are considered the main reservoir for iron homeostasis in cells.

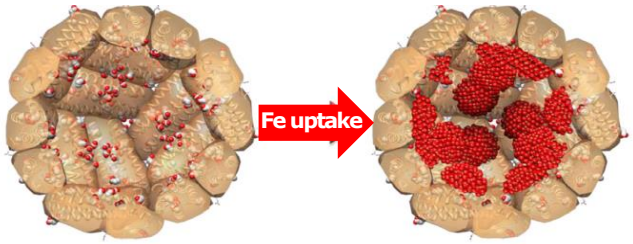


Figure 1.6: Schematic represintation iron entry and nucleation inside the ferritin cavity (adapted from F. Carmona *et al.*, Ferritin iron uptake and release in the presence of metals and metalloproteins: chemical implications in the brain, Coord. Chem. Rev. 257 (2013) 2752–2764) [28].

1.3.1.3 Ferritin usage and applications

The ferritin cage is soluble in water with a net negative charge on its internal surface at neutral pH (ferritin pI ≅ 5.3). Researchers have used ferritin in aqueous solutions as a size restriction device for nanocatalysis and the synthesis of nanomaterials and polymers [31,41]. Many studies have used ferritin nanocages solely as the template for nanoparticle synthesis. While others use ferritin not only as a template for synthesis, but also to trap different kinds of imaging agents such as fluorophores and MRI agents, anti-tumour therapies, catalysts and drugs for delivery to cells and tissues [42–44]. Furthermore, by attaching cell-specific ligands to the external surface of the cage, the delivery of therapeutic agents can be targeted to specific cells or tissue types [45,46].

Recently, Chen's group modified ferritin chemically and genetically to generate imaging agents to target specific tissues with high sensitivity and resolution. They attached the Cyanine 5.5 (Cy5.5) dye on the outer surface of ferritin for *in vivo* near-infrared (NIR) fluorescence imaging either alone or by loading its cavity with ^{64}Cu for positron emission tomography (PET). Chen's group demonstrated the proof of principle of this multimodel system for imaging of tumour xenografts in mice [47] (Figure 1.7).

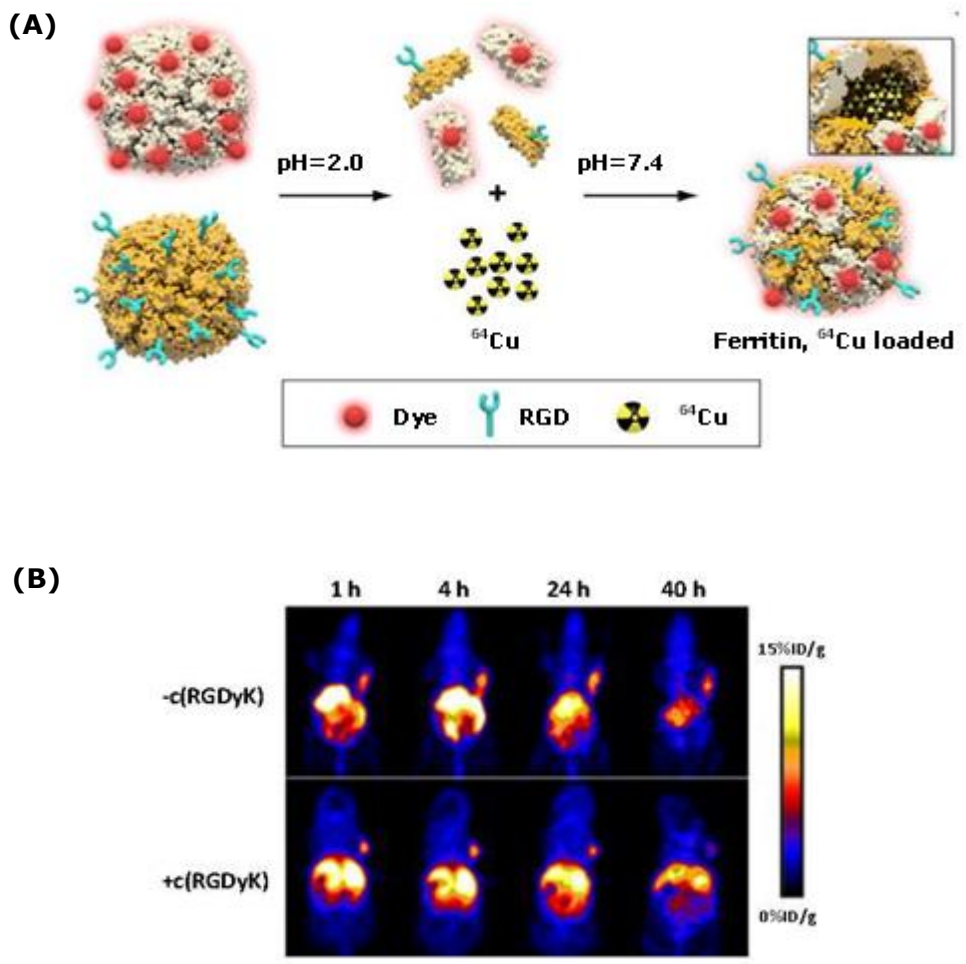


Figure 1.7: (A) schematic explains the triple loading of apoferritin with RGD4C targeting peptide, Cy5.5 and ^{64}Cu (imaging agents for PET and NIR). **(B)** *In vivo* PET image after ferritin probes administration (adapted from K. Fan *et al*., Human ferritin for tumor detection and therapy, Wiley Interdiscip. Rev. Nanomedicine Nanobiotechnology. 5 (2013) 287–298) [47].

Moreover, Crich (2015) examined the uptake of MRI contrast agents in ferritin. They loaded Gd-HPDO3A (a paramagnetic contrast agent of MRI) and curcumin (a natural molecule that exhibits anti-inflammatory and anti-neoplastic action, Figure 1.8) inside the ferritin cage. This theranostic agent was utilised to treat MCF-7 and MDA-MB-231 breast

cancer cells which overexpressed ferritin receptors. They found that the ferritin-drug construct was able to deliver 167 μg/mL of drug, resulting in significantly reduced cell proliferation [48].

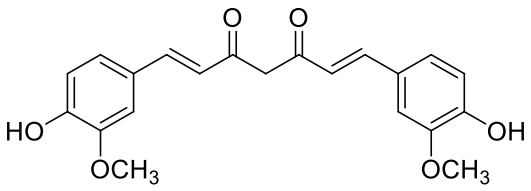


Figure 1.8: Chemical structure of curcumin in keto form.

1.3.2 DNA binding protein from starved cells (Dps)

Dps is one of a small subfamily of the ferritin-like superfamily (Figure 1.2), Dps is unique to prokaryotes and found ubiquitously in bacteria [49]. This protein was first characterised by Almiron in 1992 from *Escherichia coli* (*E. coli*) as a starvation induced protein [50,51]. Dps proteins in bacteria have three essential properties that include iron sequestration and ferroxidase activity, similar functions to ferritin, as well as DNA binding which provide significant multilateral protection during starvation and stationary phase growth as well as against environmental stresses including metal toxicity, high ultraviolet and gamma irradiation, acid/base shock, thermal and oxidative stress [50,52].

1.3.2.1 Dps protection mechanisms

Dps proteins defend bacteria from a variety of environmental factors. Firstly, Dps prevents DNA damage from excess UV irradiation or from harmful agents such as DNases, which cause DNA degradation through non-specific cleavage. At physiological pH the N-terminal region of most *E. coli* Dps protein has a net positive charge, this region is rich in lysine (Lys) residues and hence very flexible. The flexibility allows direct, non-specific interactions with DNA and the formation of a large, highly ordered but stable protein-DNA complex [53]. The resulting nucleoprotein complex provides a physical shield around the DNA, conferring a high level of protection. The stability of DNA binding to Dps is attributed to the positive charge of the N-terminus but also the C-terminal extension of Dps proteins [49,54]. However, not all Dps proteins can bind DNA if they lack a positively charged N-terminus, or possess an immobile or very short N-terminus [55,56] (Figure 1.9).

Dps provides other functions as well as DNA protection such as biomineralisation of iron and Dps ferroxidase activity. Members of the Dps subfamily share structural and functional conservation; characterised protein core structure, and a number of aa located within and around the ferroxidase centre [55].

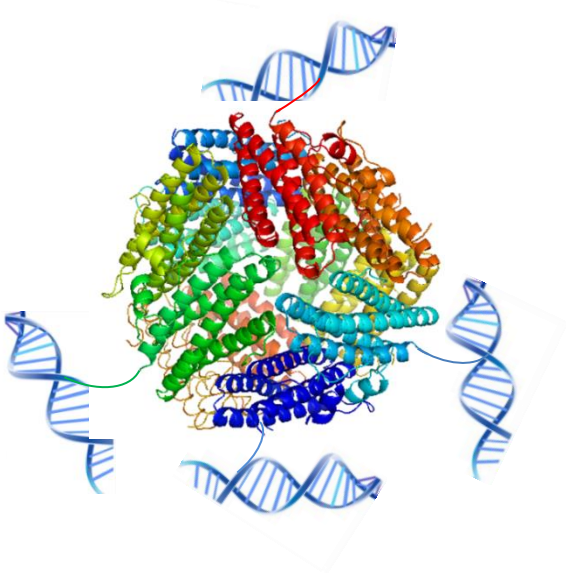
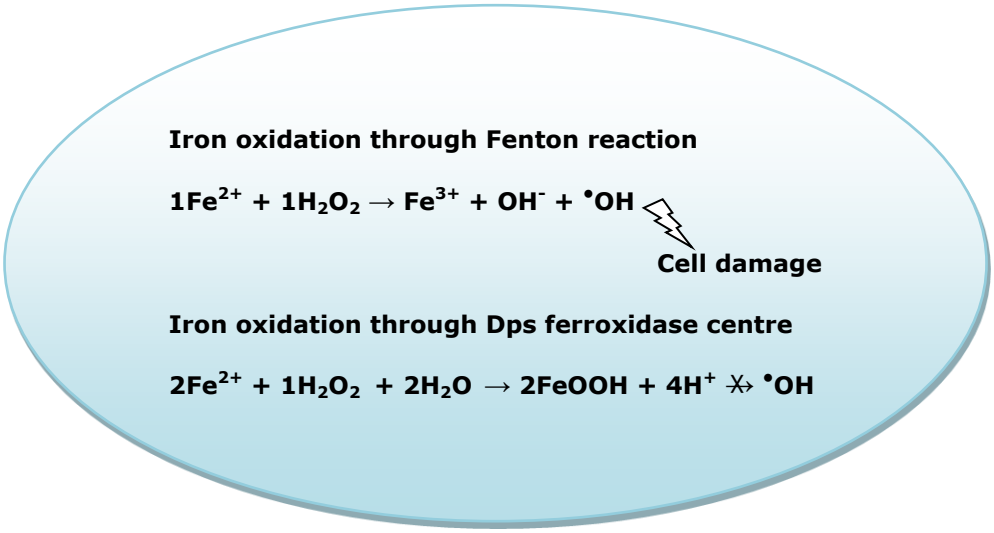


Figure 1.9: Ribbon model of Dps crystal structure from the Protein Data Bank (PDB ID: 1QGH) created by PyMol shows DNA bend into the N-terminal of Dps protein [57].

Ferroxidase sites of Dps are capable of oxidising bound Fe^{2+} ions using molecular oxygen; however, this less efficient process occurs at a much slower rate than when using H_2O_2, and is in contrast to the oxidation of ferrous ions by ferritins which preferentially utilise molecular oxygen. Therefore Dps strongly prefers to utilise H_2O_2 over O_2 as an oxidant in the process of iron storage. Many consider Dps a 'ferritin-like' protein in preference to a real ferritin that Dps proteins significantly reduce the formation of hydroxyl radicals by oxidising two Fe^{2+} ions with one molecule of H_2O_2 dramatically improving cell viability from the potentially lethal combination of ferrous ions and hydrogen peroxide [58,59] (Scheme 1.5).



Scheme 1.5: Schematic representation the Fe^{2+} ion oxidation in *E. coli*. In the first reaction Fe^{2+} is oxidised via the Fenton reaction and leads to macromolecule damage and cell death. In the second reaction Fe^{2+} is oxidised via the ferroxidase centre of Dps and the ratio of Fe^{2+} to H_2O_2 is 2:1, this reaction does not produce hydroxyl radicals and thus prevent the potential damage of cell components.

1.3.2.2 Dps structure

The Dps protein has a MW of 19 kDa and a chain length of 156 aa. It is structurally similar to the ferritin family of proteins. Like ferritin, it folds into a four helix bundle (A-D helices), but includes an additional small BC helix of a 7 aa. This BC helix is located in a loop that links the B and C helices. In contrast to ferritin, the C-terminus of Dps is located on the exterior of the Dps shell, not in the interior cavity [60]. However as in ferritin the N-terminal of Dps is positioned on the exterior surface [60–62] (Figure 1.10).

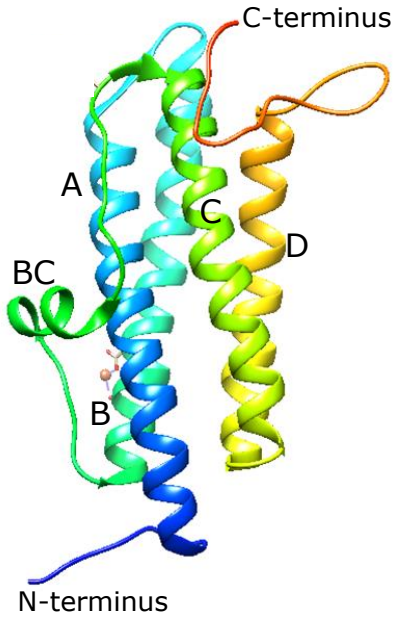


Figure 1.10: Ribbon model of *Mycobacterium smegmati*s Dps subunit crystal structure from the Protein Data Bank (PDB ID: 1VEI) created by PyMol. The four helices, labeled A-D including the small BC helix are shown in ribbon form [63].

Eukaryotic and bacterial ferritins assemble forming a rhombic dodecahedron of 24 subunits, by comparison Dps adopts a dodecamer of 12 identical subunits with a hollow cage [54]. Dps is smaller compared to ferritin, it has a 9 nm spherical shell with 4.5 nm cavity in diameter [64] (Figure 1.11).

All Dps dodecamers show tetrahedral 23 point symmetry, unlike the ferritins family, which form 432-point symmetry. The 23-point is assembled by three 2-fold and four 3-fold symmetry axes, which lead to high internal symmetry [65,66].

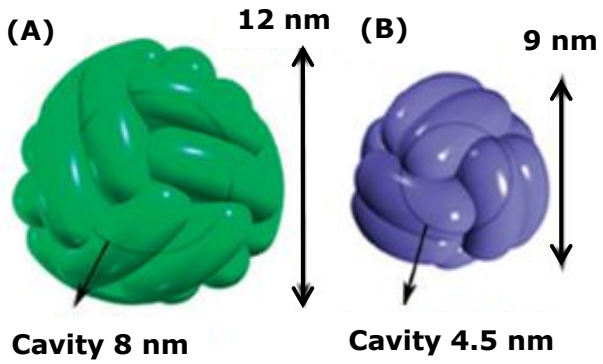


Figure 1.11: Schematic of Dps shows **(A)** apoferritin isolated from horse liver (HsAFt) and **(B)** the *Listeria innocua* Dps (*Li*Dps) (adapted from M. Okuda *et al.*, Bio-templated CdSe nanoparticle synthesis in a cage shaped protein, *Listeria*-Dps, and their two dimensional ordered array self-assembly, Chem. Commun. 46 (2009) 8797–8799) [64].

Similar to ferritin, in Dps subunits are assembled to form a shell with channels [67]. Two different kinds of pores are found at the 3-fold symmetry axes of Dps both approximately 4 Å in diameter [68]. One pore is formed by the N-terminus of subunits and is lined by negatively charged residues. This pore strongly resembles the pores that are created by the N-termini of ferritin, being hydrophilic in nature and funnel-shaped and therefore have been named as "ferritin-like". Fe^{2+} ions enter the Dps cage through the 3-fold hydrophilic channel, the protein can store up to 500 iron atoms as a ferric oxyhydroxide nanoparticle. Dps contains another pore type named "Dps-type"; this is unique to Dps and is created by the C-termini of subunits; however the function of these pores remains unknown [60]. Similarly to ferritin, Dps dissociates into individual subunits at pH 2.0 but reassociates at pH 7.0 [69].

1.3.2.3 Applications of Dps

As the smallest proteins of the ferritin superfamily, Dps proteins have been widely utilised in a variety of applications. Similar to ferritin, they have been used as biological templates for nanoparticle synthesis. Their ability to self-assemble at physiological pH, recognise and mineralise specific inorganic particles makes them highly suitable for nanoparticle synthesis. Due to the small size of the protein, Dps serves as a vessel which constrains the size of the nanocomponent synthesised, essentially acting as a nanoreactor. There are many studies which demonstrate the synthesis of semiconductor nanoparticles such as Fe_3O_4, Co_3O_4, Pt, γ-Fe_2O_3 and a CdS quantum dot, using the Dps cavity [20,64,70,71] (Figure 1.12).

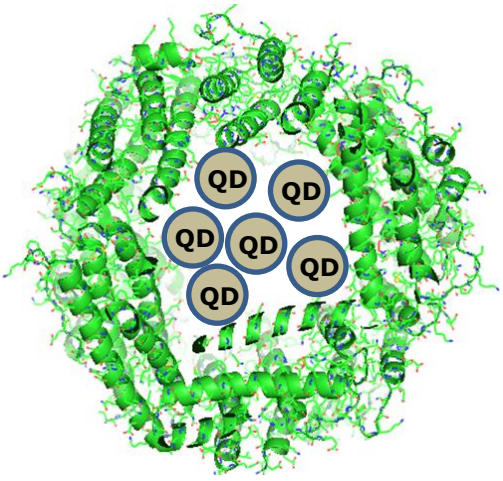


Figure 1.12: Ribbon model of Dps crystal structure from the Protein Data Bank (PDB ID: 1QGH) created by PyMol. The ribbon diagram shows the encapsulation of quantum dots within Dps [57].

Kang *et al.* modified the exterior and interior surfaces of Dps chemically and genetically to produce the platinum (Pt) binding ligand phenanthroline. Two cysteine (Cys) mutants were generated on the exterior and the interior surface of Dps. The exterior Cys mutant was conjugated with fluorescein-5-maleimide while 5-iodoacetamido-1,10-phenanthroline was conjugated to the inner Cys for metal chelation. By mass spectrometry they demonstrated that Pt^{2+} binds and Pt^{0} growth were occured as a nanocluster. Pt^{0} could be used for proton reduction and hydrogen production [21] (Scheme 1.6 & Figure 1.13):

$$2H^{+}\,(aq) + 2e^{-} \xrightarrow{Pt} H_2\,(g)$$

Scheme 1.6: Proton reduction catalysed by Pt to produce hydrogen gas.

In addition, Suci *et al.* genetically-modified Dps by attaching the tetra-peptide KLFC at the C-terminus. Biotin was then attached chemically via a poly ethylene oxide (PEO_2) spacer with the sulfhydryl group of the C-terminal Cys present in each KLFC, the resulting Dps nanoparticle could then be immobilised on a streptavidin-coated surface due to the strong biotin-streptavidin interaction. The latest complex was coupled with a biotinylated monoclonal antibody and used to target a microbial pathogen [72].

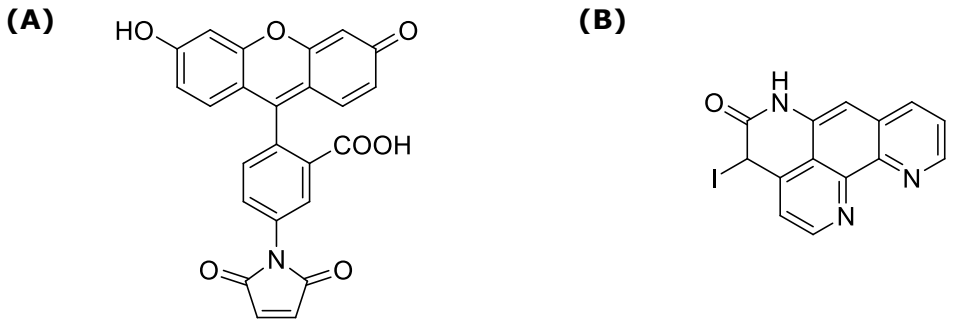
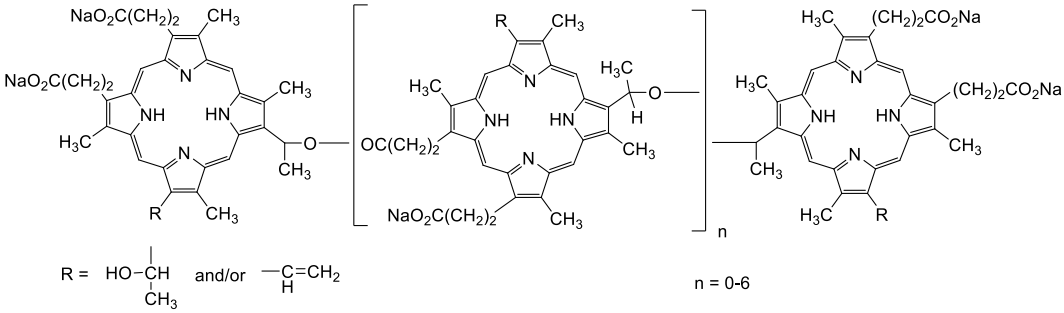


Figure 1.13: Chemical structure of **(A)** fluorescein-5-maleimide and **(B)** 5-iodoacetamido-1,10-phenanthroline.

1.4 Photodynamic therapy (PDT)

PDT is a promising treatment for cancer and other diseases such as age-related macular degeneration. It was invented in 1900 and has since been used in the clinical treatment of neoplastic conditions such as solid tumours and microvascular diseases [73–75]. PDT becomes attractive in biomedicine and clinical research due to its high safety and passivity. PDT is based on photosensitiser (PS), it can be modulated to localise to the tumour region and subsequently reduce the collateral damage to normal tissues [76,77]. Thus, PDT is preferable to use over other classical treatment methods such as radiotherapy and chemotherapy [76]. Photofrin and the pro-drug 5-aminolevulinic acid (ALA) are examples of PS that were approved by the United States Food and Drug Administration (FDA) to use as a PDT in clinic [78,79] (Figure 1.14).

(A)



(B)

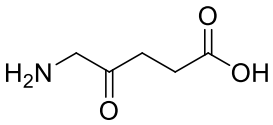


Figure 1.14: Chemical structure of **(A)** Photofrin and **(B)** ALA.

The mechanism of PDT for initiating cell death requires three essential components; a photosensitising agent or drug, molecular oxygen and a defined source of light [80,81] (Figure 1.15).

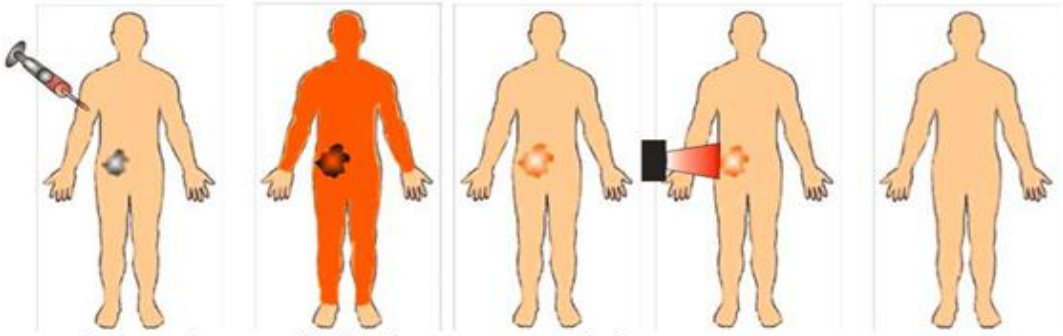


Figure 1.15: A schematic to explain how PDTs work (i.e., the interaction of the light and PS to produce ROS) (adapted from P. Mroz *et al*., Cell death pathways in photodynamic therapy of cancer, Cancers (Basel). 3 (2011) 2516–2539) [82].

This cell killing mechanism initiates when the PS is excited, by an absorbed photon, from the ground state (S_0) to a high energy singlet state (S_1), (see Scheme 1.7 (1)). PS (S_1) has a lifetime in the nanosecond range that is too short to allow interaction with adjacent molecules. However, PS (S_1) may convert to a longer-lived, high energy triplet state (T_1) via an intersystem crossing reaction (Scheme 1.7 (2)) which is able to react with available ground (triplet) state molecular oxygen in two different ways [83,84]. In the first process, an electron transfer occurs from the PS molecule in the excited state (T_1) to the acceptor oxygen molecule in the ground (triplet) state which is known as a photochemical reaction type I. Photochemical type I reactions, produces partially reduced oxygen species which include H_2O_2, superoxide anion radical ($O_2^{\bullet -}$) and $OH^{\bullet}$ (Scheme 1.7 (3)). Alternatively, photochemistry type II reactions include transfer of energy from the excited PS (T_1) to ground state molecular oxygen $^3O_2$ producing an excited oxygen singlet ($^1O_2$) [85–89] (Scheme 1.7 (4)):

$$PS\ (S_0) + h\nu \rightarrow PS^*\ (S_1) \qquad (1)$$

$$PS^*\ (S_1) \rightarrow PS^*\ (T_1) \qquad (2)$$

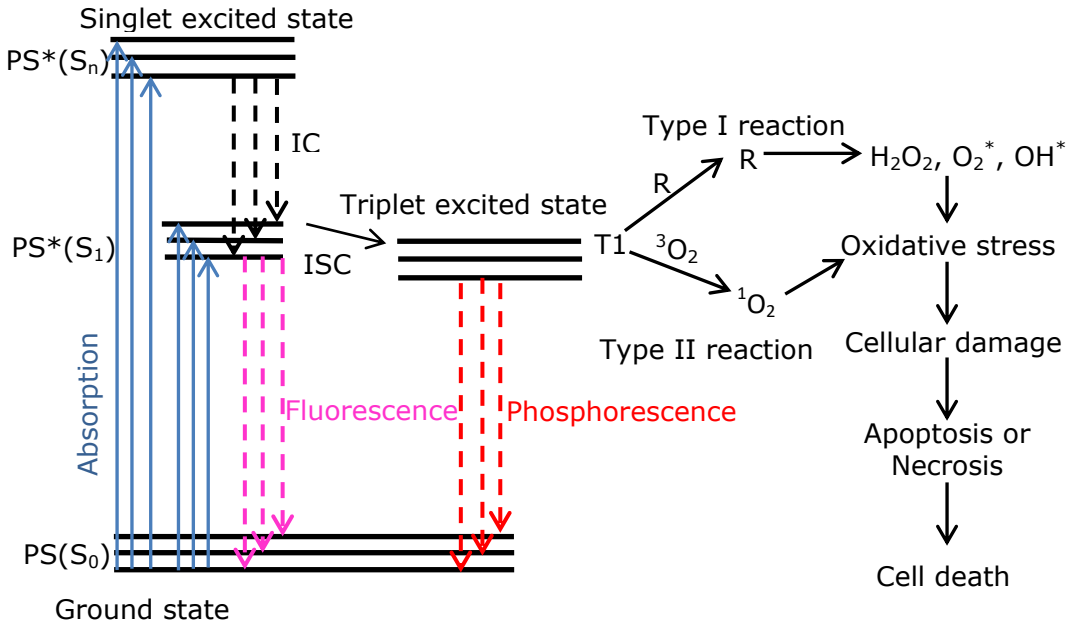
$$PS^*\ (T_1)(e^-) + {}^3O_2 \rightarrow PS\ (S_0) + ROS \qquad \text{(Type I)(3)}$$

$$PS^*\ (T_1)(h\nu) + {}^3O_2 \rightarrow PS\ (S_0) + {}^1O_2 \qquad \text{(Type II)(4)}$$

Scheme 1.7: A sequential reaction that is initiated by the excitation of PS, energy transfer, and ended by the generation of ROS.

The high reactivity both of the oxygen singlet and the oxygen radical cause acute oxidative stress and thus leads to destruction of target cells [83], (Scheme 1.8).

PDTs can be localised in a cell and induce the cellular damage through a variety of pathways such as apoptosis and necrosis [82]. In general, PDT works based on fluorescence or bioluminescence resonance energy transfer (FRET or BRET) systems where the PSs are excited using external or self-illumination light sources respectively.



Scheme 1.8: The oxidative damage for cells by oxygen radicals. The Jablonski diagram shows the energy transfer in PDT to generate Reactive Oxygen Species through type I reaction or singlet oxygen via type II reaction, where PS(S_0) refers to (Ground Singlet state photosensitiser), PS*(S_1-S_n) (Singlet excited state photosensitiser), PS*(T_1) (Triplet excited state photosensitiser), R (biological substrate), R* (oxidised biological substrate), IC (internal conversion) and ISC (intersystem crossing) (adapted from T.A. Debele *et al*., Drug Carrier for Photodynamic Cancer Therapy, Int. J. Mol. Sci. 16 (2015) 22094–22136) [90].

1.5 Resonance energy transfer

Fluorescence (or Förster) and bioluminescence resonance energy transfer involve the movement of non radiation energy from a donor to the acceptor fluorophores.

In Bioluminescence Resonance Energy Transfer (BRET), the bioluminescence light (BL) is produced by luciferase enzymes which are found in bacteria, insects, fungi, plants and marine creatures [91]. BRET occurs in similar way to fluorescence resonance energy transfer (FRET) except that FRET uses external light source initiation (Figure 1.16) [92].

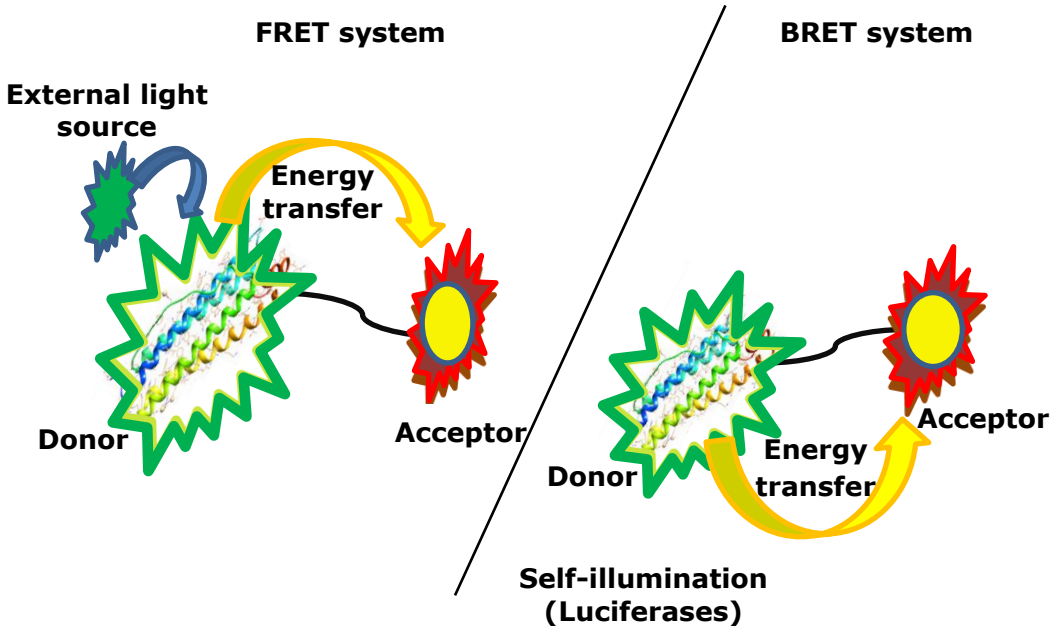


Figure 1.16: Schematic representation of the difference between BRET and FRET systems.

Consequently BRET is a more attractive approach than FRET for biomedical applications. This is because during BRET, absorption and scattering is minimal when delivering light to deep tissue; improving signal to noise ratio, this reduces background interference and the risk of photobleaching [92,93]. Several factors contribute to improve BRET and FRET efficiency including the overlap between donor emission spectrum and the excitation spectrum of the acceptor. The distance between donor and acceptor should be less than 10 nm as efficiency is related to distance between the two; efficiency is proportional inverse to the sixth power of this distance [91,94] (Equation 1.1).

$$E = 1/[1 + (r / R_0)^6]$$

Equation 1.1 Calculate FRET and BRET energy transfer efficiency where E is the efficiency of energy transfer, r is the distance between donor and acceptor, R_0 is the Förster distance of donor to acceptor at which the efficiency transfer of energy is 50%.

There are many BRET systems applied as imaging agents or PDTs such as BRET1, BRET2, and BRET3 which include the use of bioluminescent proteins, variant mutants of green fluorescent protein (GFP), and dye molecules (Table 1.1).

BRET donors			BRET acceptors			References
	Substrate	Maximum emission (nm) λ		Maximum excitation (nm) λ	Maximum emission (nm) λ	
[1] *R*Luc (protein) (BRET1)	Coelenterazine	480	[2] YFP (protein)	514	527	[95],[96]
*R*Luc (protein) (BRET2)	DeepBlueC	~ 395	[3] GFP (protein)	395/475	510	[95],[96]
Aequorin (protein)	Coelenterazine	466	GFP (protein)	395/475	510	[97],[98]
[4] FLuc (protein) (BRET3)	D-Luciferin	560-580	[5] DsRFP (protein)	558	583	[99],[100],[101],[102]
FLuc (protein) (BRET3)	D-Luciferin	560-580	[6] Cy3 (organic dye)	547	563	[103],[94]
FLuc (protein)	D-Luciferin	560-580	[7]Cy3.5 (organic dye)	591	604	[103],[94]
Aequorin (protein)	Coelenterazine	466	[8] IANBD (organic dye)	478	536	[104]
Aequorin (protein)	Coelenterazine	466	Lucifer Yellow (organic dye)	428	531	[104]
[9] Luc8 (protein)	Coelenterazine	480	[10] QD655	480	655	[105]

Table 1.1: BRET systems synthesised using donors and acceptors of various proteins and organic molecules. 1, *Renilla* luciferase; 2, Yellow fluorescent protein; 3, Green fluorescent protein; 4, Firefly luciferase; 5, Discosoma Red fluorescent protein; 6, Cyanine3; 7, Cyanine3.5; 8, *N*-((2-(iodoacetoxy)ethyl)-*N*-Methyl)amino-7-Nitrobenz-2-Oxa-1,3-Diazole; 9, *Renilla reniformis* luciferase (with eight mutants); 10, CdSe/ZnS quantum dots.

1.6 Photosensitiser

A photosensitiser (PS) is a chemical compound which upon irradiation with visible light induces different physical or chemical changes of another molecule [106]. The major biomedical use of PSs is in conjugation with PDTs for cancer diagnoses. There are many ideal properties required for use of PSs therapeutically (summarised in Table 1.2) [107,108].

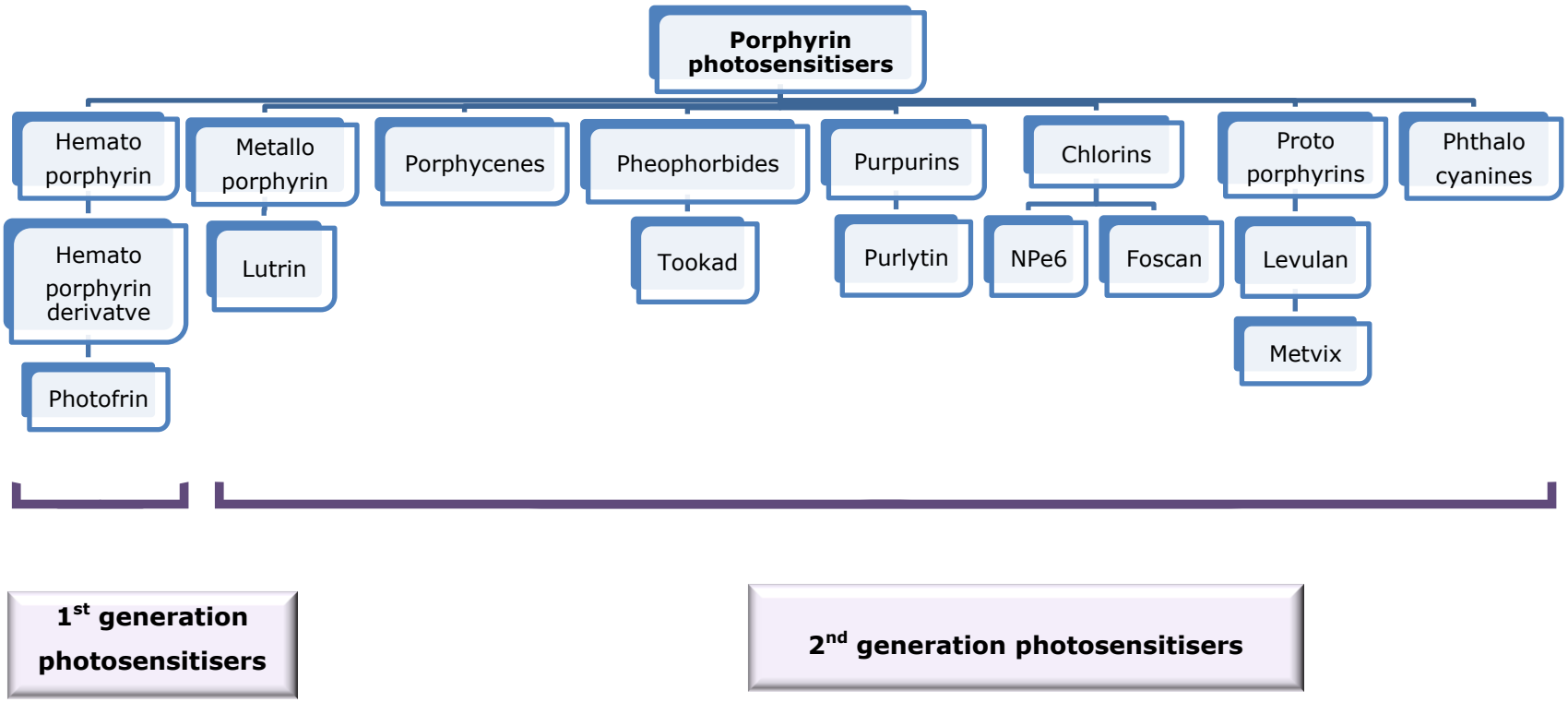
In general, PSs are divided into two groups; porphyrins and non-porphyrins (Figure 1.17). PSs based on porphyrins are mostly used in PDT systems, the group is subdivided to first, second and third generation. Hematoporphyrin and photofrin are considered to be first generation PSs, these PSs have many disadvantages for use as a treatment.

These properties have been improved in the second generation PSs where these are chemically pure and absorb the light at longer wavelengths compared to the first generation, and consequently cause substantial reduction in photosensitisation of skin. The third generation PSs are further developed than previous compounds, they are modified with various carriers such as antibodies, nanoparticles and other biological molecules [107,108].

PS Characteristics and properties	Definitions
Activation	Excited by light wavelength capable penetrating deep tissues with minimum absorption and scattering (i.e. between 700-850 nm).
Commercial availability	Available for use in cancer treatment with low-cost.
Cytotoxicity	Apoptosis and/or necrosis should be induced.
Fluorescence	The energy of light which is absorbed by the PS produces fluorescence which allows identification and diagnosis of the targeted tissues.
Mutagenicity	No mutagenic or carcinogenic side effects.
Photodynamic reaction (PDR)	The PS efficiency depends on the PDR type. Where type II (produces singlet oxygen) is more efficient than type I (produces ROS) in the presence of molecular oxygen.
Purity	High purity and temperature stability.
Quantum yield	High output of singlet oxygen or ROS when irradiated with a certain wavelength.
Safety	The PS should be inactive with minimal cytotoxicity in the absence of the required excitation wavelength light.
Selectivity	Has the ability to localise and accumulate within the targeted tissues

Table 1.2: Ideal properties for PS for use in PDT or cancer diagnosis systems [107,108].

(A)


Porphyrin photosensitisers
Hemato porphyrin
Metallo porphyrin
Porphycenes
Pheophorbides
Purpurins
Chlorins
Proto porphyrins
Phthalo cyanines
Hemato porphyrin derivatve
Lutrin
Tookad
Purlytin
NPe6
Foscan
Levulan
Metvix
Photofrin
1st generation photosensitisers
2nd generation photosensitisers

(B)

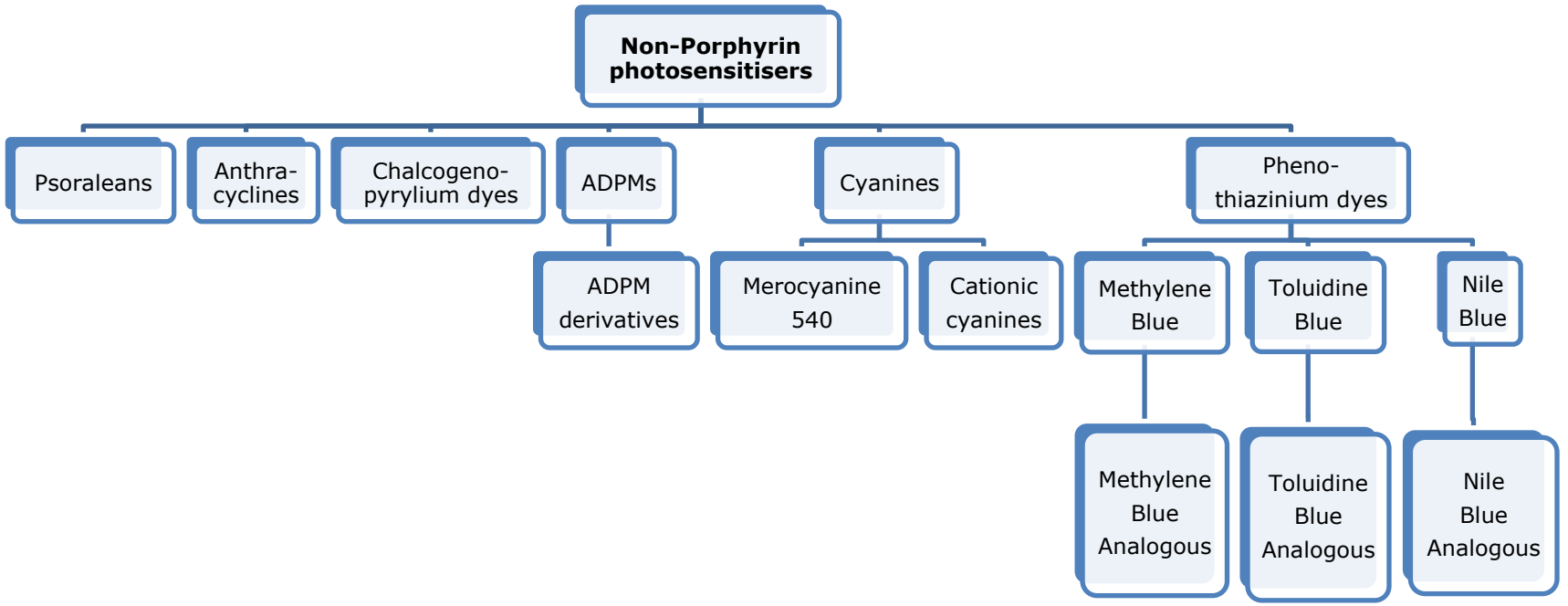


Figure 1.17: The PSs classes divided into **(A)** Porphyrin PSs and these are subdivided to first and second generation PSs, and **(B)** Non-Porphyrin PSs [107].

Porphyrin PSs are found in human blood and were first isolated and characterised in 1871. In 1948, a range of porphyrins, including hematoporphyrin, protoporphyrin, zinc hematoporphyrin and coproporphyrin, were applied to 240 transplanted tumour mice and 50 non-tumour bearing mice. Each of the porphyrins was shown to localise to the tumours rather than healthy tissues; evidenced by observation of fluorescence in the tumours. This discovery led to the modification of these prophyrin to produce a modern PDTs that have the capability to target diseased tissue and limiting light-induced damage into surrounding normal tissues [73].

Non-porphyrin based PSs also have many advantages for use in treatment. These include the capability to produce PSs exhibiting short half-lives and lower toxicities. Furthermore, these are easily modified to produce PSs that can overcome the disadvantages in treatment [107].

1.6.1 Zn (II)-protoporphyrin IX (ZnPP)

ZnPP is a member of metalloporphyrins. It was discovered in 1930 and later identified as the main non-heme porphyrin that is formed in red blood cells as a result of iron deficiency or lead poisoning (Figure 1.18) [109–113].

ZnPP has the ability to kill cancer cells either through a photosensitising mechanism, or inhibition of the heme oxygenase 1 (HO-1) enzyme [114]. The photosensitising mechanism generates singlet oxygen upon irradiation by blue light; the quantum yield of singlet oxygen efficiently formed from ZnPP is 0.91 [115–117]. Singlet oxygen causes oxidative damage to its immediate surroundings through oxidation of cell membrane amino acids (Cys, histidine (His), methionine (Met), phenylalanine (Phe), and tryptophan (Trp)), cholesterol and unsaturated fatty acids and guanine may also be oxidized [106].

The second mechanism involves the inhibition of HO-1 enzyme. This enzyme is overexpressed in cancer cells and plays an important role in heme degradation and the production of bilirubin. Bilirubin protects cells from oxidative stress by scavenging free radicals. Thus HO-1 contributes to cancer cell growth by providing the antioxidant bilirubin, which protects these cells from oxidative stress [118–120]. Therefore ZnPP shows potential to treat malignant cells, however to overcome low solubility it must be bound to a large soluble ligand such as proteins. Due to the defects in tumour tissues, the fabrications of ZnPP complexes enhance the internalisation of these macromolecules into malignant cells more than normal cells. This phenomenon is called the "enhanced permeability and retention (EPR) effect" and is based on

the increased accumulation and retention of macromolecules in tumour cells [114,121–123].

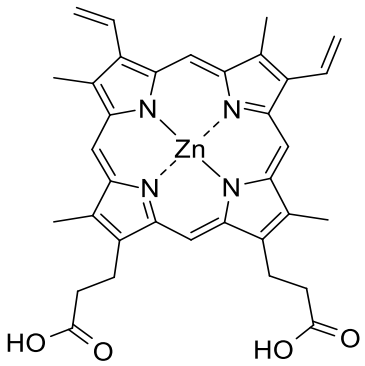


Figure 1.18: Chemical structure of Zn(II) protoporphyrin IX.

1.6.2 Mini Singlet Oxygen Species Generator (miniSOG)

MiniSOG is a small, green fluorescent flavoprotein. It is a monomeric protein of 106 aa, with a MW of 15 kDa [124,125]. MiniSOG has the ability to function as a PS and generates ROS capable of damaging cells [126–128].

A study by Shu *et al*. described miniSOG and its ability to generate singlet oxygen upon excitation by blue light (λ_{ex} = 488 nm) [126]. Recent photophysical characterisation studies of miniSOG reported that this protein photoinitiated electron-transfer reactions (photochemistry type-I reactions) and generates ROS rather than an energy-transfer (photochemistry type II reactions) mechanism with a quantum yield of $^1O_2$ at about 0.03 [129–132].

MiniSOG has become a more attractive candidate as a novel phototoxic protein over additional protein PSs, such as green fluorescent protein (26.9 kDa) and KillerRed (27 kDa) which produce ROS after irradiation with blue (λ_{ex} = 395 nm) or green light (λ_{ex} = 585 nm) respectively. This is because miniSOG is smaller in size when compared to other protein PSs and greater in photosensitisation than others. Both of these factors increase it's efficiency to employ as a photosensitiser [133–135]. However, miniSOG requires flavin mononucleotide (FMN) as a cofactor for generation of ROS [129,136,137]. FMN is ubiquitous in cells and executes essential biological functions such as fatty acid oxidation, mitochondrial electron transport and vitamin metabolism [138,139].

Shu and coworkers engineered miniSOG from the Light-oxygen-voltage-sensing (LOV2) domain of blue light photoreceptor phototropin 2 found in *Arabidopsis thaliana,* wherein the FMN excited state energy is consumed to form a covalent bond with a Cys residue [127]. They carried out a saturation mutation in the LOV2 domain of *Arabidopsis thaliana* phototropin 2 to divert this energy into ROS generation. This mutation involved the substitution of the Cys residue (C426G) positioned near to the FMN to a glycine (Gly) residue. They subsequently observed the generation of large amount of $^1O_2$ from the single site substitution compared to the wild type, alongside an increase of green emitted light with peaks at 500 nm and 530 nm, (Figure 1.19). It was hypothesised that this may be attributed to the

Gly which provides a space around the cofactor, allowing the singlet oxygen to come in close proximity with FMN for efficient energy transfer [127].

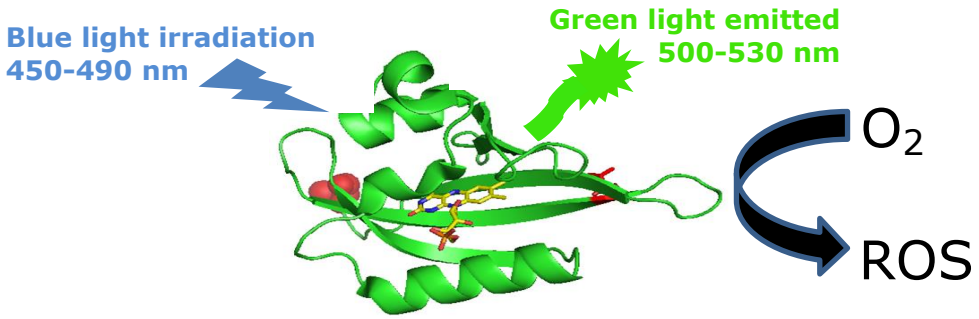
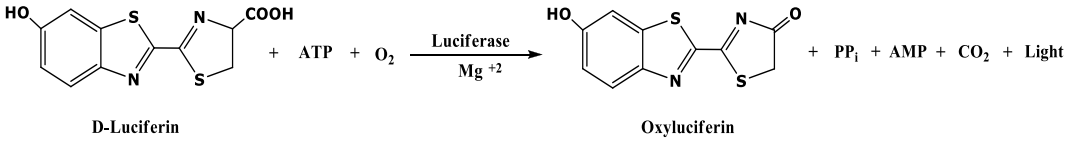


Figure 1.19: A ribbon model of miniSOG (LOV) crystal structure from the Protein Data Bank (PDB ID: 4EER) was created by PyMol [140]. This model shows protein-encased FMN (yellow) in miniSOG and its generation of ROS as well as green light emitted upon irradiation with blue light.

1.7 Luciferase

Luciferase is the generic name for the subfamily of enzymes whose reactions generate a photon of light. This monomeric enzyme has been isolated from various species. Luciferase enzymes have the ability to produce and emit bright yellow-green light (λ_{max} ≈560 nm) with a significant quantum yield, because of their function as monoxygenases [141]. Firefly luciferase (FLuc) metabolises D-luciferin, molecular oxygen and Mg^{2+}-ATP to yield an electronically excited oxyluciferin species in a chemical reaction that is called a Bioluminescence reaction [142,143] (Scheme 1.9). In this reaction, luciferase catalyses the

conversion of firefly D-luciferin to luciferyl-adenylate in the presence of ATP, which is subsequently oxidised in a multistep reaction to produce an electronically excited oxyluciferin [141,144].



D-Luciferin Oxyluciferin

Scheme 1.9: Firefly luciferase oxidation of D-Luciferin to Oxyluciferin, with emitting wavelength light in the presence of ATP and oxygen molecules.

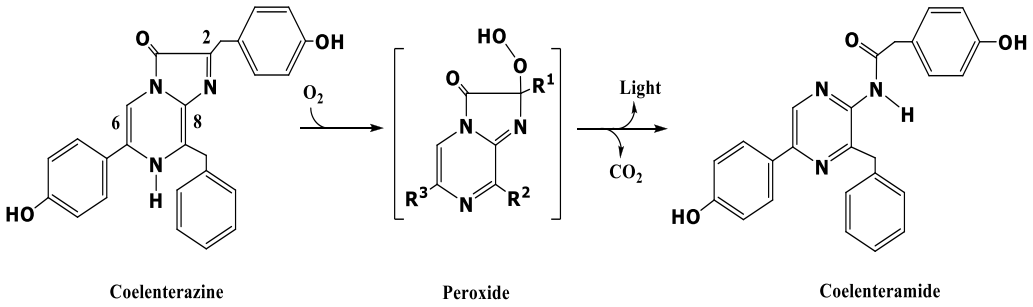
During the relaxation of excited oxyluciferin to its ground state, a photon of visible light is emitted. FLuc use bioluminescence to communicate with each other by emitting yellow-green or yellow-orange light [145].

FLuc has been widely utilised for many applications particularly in medical and biotechnological research. Examples include non-invasive imaging of tumour growth and metastasis in animal models, analysis of gene expression and as a reporter to assess the efficiency of drug delivery [144][146]. Recently, several studies have been conducted on the conjugation of a luciferase gene with other proteins as bioluminescent labelled ligands which can be used for imaging receptor targets [147–149].

However, FLuc enzymes are not suitable for protein tags, this is due to their relatively large size (MW ~62 kDa) and the requirement for ATP, Mg^{2+} and oxygen for activity. The reliance of these enzymes on ATP for activity represents an obstacle for bioluminescent tagging of proteins *in vivo*, as concentrations of ATP in serum are very low. Therefore, luciferases that use coelenterazine as a substrate are more appropriate for use as bioluminescent tags, in terms of being ATP independent and the small size of these enzymes. Examples of luciferase that utilise coelenterazine are sea pansy *Renilla reniformis* luciferase (*R*Luc) with a MW of 36 kDa and *Gaussia princeps* luciferase (*G*Luc) with MW of 19.9 kDa [150][151].

1.7.1 *Gaussia princeps* luciferase (*G*Luc)

*G*Luc is a coelenterazine-dependent luciferase. The luminescence reaction catalysed by *G*Luc, and related coelenterazine-utilising luciferases was first examined using marine copepods such as *Gaussia princeps*. The *G*Luc enzyme utilises coelenterazine and is widely distributed in luminous marine organisms. It catalyses the oxidation of coelenterazine, emitting a photon of blue light (λ_{max}~470-490 nm) during the production of coelenteramide [152–154], (Scheme 1.10). *G*Luc is a monomeric enzyme (MW 19.9 kDa) consisting of 185 aa with 10 Cys residues. This is one of the smallest luciferase enzymes currently known [155–158].



Scheme 1.10: The oxidation reaction of coelenterazine catalysed by *G*Luc enzyme.

Unlike D-luciferin type luciferases, *G*Luc utilises a single substrate (coelenterazine) and does not require energy in the form of ATP, or indeed any other cofactor for catalysis [155,157,159,160]. Furthermore *G*Luc has additional advantages over other luciferases including; preferential enzyme stability, high signal intensity, and a humanised form (h*G*Luc) has secreted the bioluminescent signal intensity > 1000 fold higher than the humanised Fluc and humanised Rulc [158]. These advantages make it far more appropriate for *in vivo* real time monitoring of biological reactions in a variety of media such as cultured cells, urine or blood in animals [152].

Similar to D-luciferases, *G*Luc has been studied in biological and medical research and utilised for sensitive, rapid and inexpensive measuring of gene expression. Furthermore, *G*Luc is inherently more efficient for following secreted proteins than other reporters such as

FLuc, GFP and RLuc which are typically folded in the cytosol [161]. Oyama *et al.* fused *G*Luc with an artificial antibody for improving immunoassay methods [155]. They fused the single chain variable fragment (scFv) monoclonal antibody gene with *G*Luc to produce a new and successful system for detection of a cortisol–albumin conjugate using a bioluminescent enzyme-linked immunosorbent assay (BL-ELISA) [155].

1.8 Antibody-drug conjugate

Most strategies for cancer treatment involve the use of drugs which affect cellular proliferation and hence survival. Healthy and cancer cells adopt the same systems for survival, consequently, there is limited selectivity for anticancer drugs to work specifically on tumour cells. Consequently, the ongoing development of novel anticancer therapies has focused on targeting treatment to malignant cells, thus minimising their toxicity on other cells. Strategies include using targeting agents ensuring that drugs are only delivered to tumour cells. A wide variety of targeting agents have been used for conjugation with drugs such as aptamers, peptides, low MW non-peptidic ligands, antibodies and small protein scaffolds to internalise into the cell via receptor-mediated endocytosis.[162]. Endocytosis is a mechanism for the active transport of molecules, including proteins and other polar molecules that are unable to penetrate the hydrophobic plasma membrane. Endocytosis is

carried out by packaging cell surface proteins, such as adhesion components and cytokine receptors, in cytoplasmic vesicles (endosomes). These lead to dissociation of the drug from the receptors in the late endosome and lysosome vesicles to release the drug inside the cells [163] (Figure 1.20).

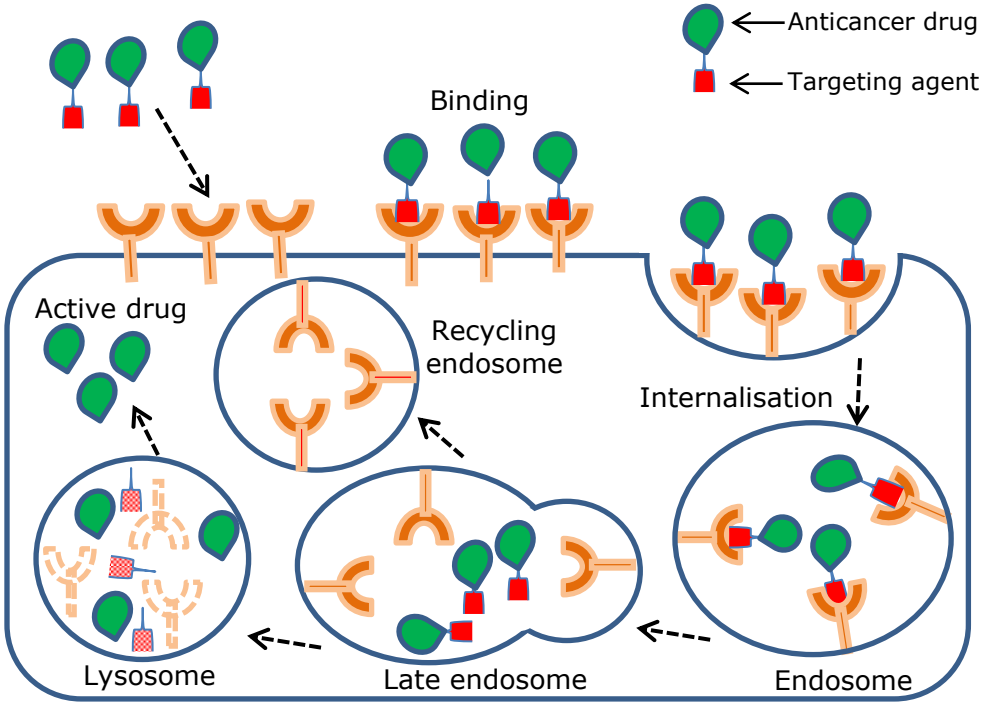


Figure 1.20: Schematic representation the mechanism of action of targeting agent. The targeting agent–drug conjugate internalises the cell though it's binding to the target receptor on the cell surface.

In this study Affibody $Z_{HER2:342}$ (Afb) and the LTVSPWY-targeting peptides were used to direct novel constructs selectively to HER2

overexpressed cancer cells. An Afb is a non-immunoglobulin highly specific binding protein, engineered from a 3-helix bundle Z from staphylococcal protein A [164,165] (Figure 1.21).

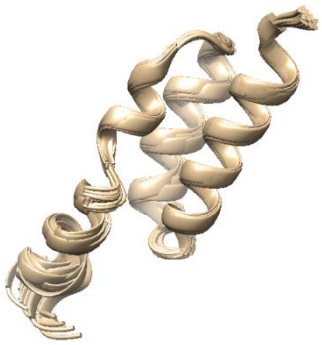


Figure 1.21: A ribbon model of Afb NMR structure from the Protein Data Bank (PDB ID: 2KZI) created by PyMol. Ribbon diagram showing the three helices of Afb. NMR was carried out at 30 °C on a sample of 1 mM uniformly ^{13}C,^{15}N-labeled ZHER2 in 160 mM NaCl and 16 mM potassium phosphate at pH 6.0 with 0.1% NaN_3 and 5% D_2O [166].

Due its small size (58 aa, ~ 6.5 kDa), an Afb has many bio-physical advantages for use as a targeting agent for drug delivery and imaging. These include; fast and reversible folding, high dissociation temperature from human epidermal growth factor receptor 2 (HER2), high solubility in aqueous solutions, an attachment surface as large as an antibody and can be easily expressed in *E.coli* [167–169]. The Afb is a known high affinity binder of the extracellular domain of HER2 (K_D = 22 pM) [168,170]. HER2 is a transmembrane protein that belongs to the human epidermal growth factor tyrosine kinase receptor family. HER2 is overexpressed in various types of cancer: 20% in breast, 9-

32% in ovarian and 15-30% in gastric cancer, this overexpression is correlated with an increased mortality rate [171]. Fortunately, HER2 is found only in small or even below detectable levels in normal adult tissues, thus making it an ideal target for Afb-mediated cancer therapies.

Similarly, the heptapeptide LTVSPWY is another targeting agent which is used in this study to target HER2 overexpressed in mammary epithelial human cancer cells. Several studies used this small peptide as a targeting agent for drug delivery *in vivo* and *in vitro*, it does not bind healthy mammary epithelial human cells nor other human cells [172–175].

1.9 Quantum dots (QDs)

Semiconductor QDs are colloidal nanostructures that have unique chemical, physical, optical and electronic properties. These include tunable sizes that enable the production of a wide range of fluorescent emission spectra, photostability, high signal brightness and excitation by many wavelengths (Figure 1.22) [176,177]. Due to their properties, QDs show potential as imaging devices over conventional fluorophores used in biological applications such as fluorescent labelling and cellular imaging [177,178]. QDs consist of either a core or a core and shell, where the shell's function is to shield the core from oxidation.

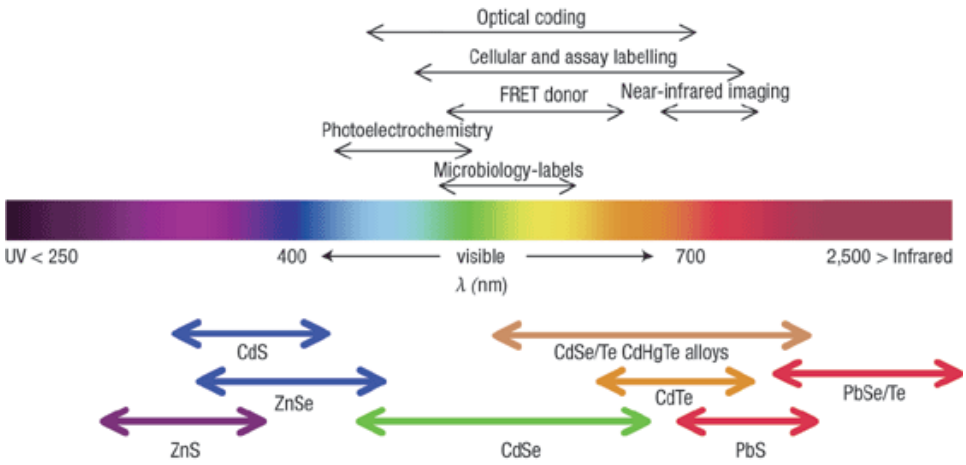


Figure 1.22: Tuning of the spectral emission of QDs based on their chemical materials [179].

This shell may be synthesised from a variety of different ligands, however QDs are usually produced with non-polar organic ligands making them inappropriate for biological applications. To overcome this drawback, the QDs' surfaces can be modified using ligand exchange where ligands have been utilised to improve the hydrophilicity of QDs surfaces such as polyethylene glycol (PEG). PEG increases QDs solubilities and diminishes non-specific binding when used for labelling of the viable cell. Also, QDs surfaces can be terminated with various groups to allow functionalisation to enable conjugation with other molecules. QDs terminated with carboxyl groups can be conjugated with molecules terminated with amine groups and *vice versa* using an amide coupling reaction. This technique is mostly used in biological applications to conjugate streptavidin/avidin QDs with biotinylated molecules [180]. More

recently, QDs have been used as imaging agents for cells in the form of QD-antibody. These conjugates dots can display various colours simultaneously upon excitation by single wavelength and with narrow and distinguishable emission peaks [181] (Figure 1.23).

Furthermore, several systems have been created including the conjugation of QDs with antibodies and peptides to endow QDs with targeting capabilities applicable in biological studies [181].



Figure 1.23: An image showing the spectrum of colours emitted by different QDs [182].

1.10 Project aim and outline

The aim of this study was to use different nano-scale proteins (*G*Luc; human apoferritin (HuAft); *Listeria innocua* DNA binding protein from starved cells (*Li*Dps); miniSOG; Afb; and Mutated G82C-S84C Affibody $Z_{HER2:342}$ (Afb2C)) to produce a new medical treatment and imaging system, see Table 1.3. The objectives of this study include:

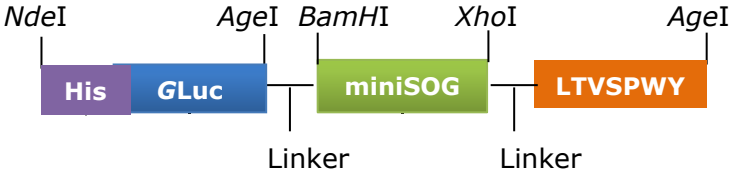
1- Fusion of *G*Luc with the miniSOG PS and LTVSPWY peptide to produce a novel *G*Luc-miniSOG-LTVSPWY PDT and imaging agent that can selectively target HER2 overexpressing cancer cells (Chapter 3).

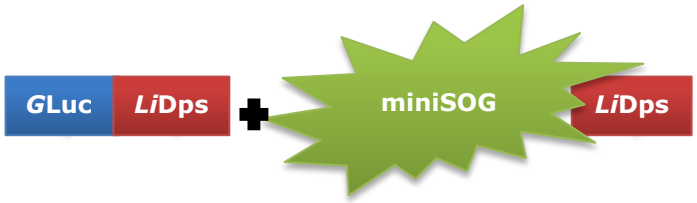
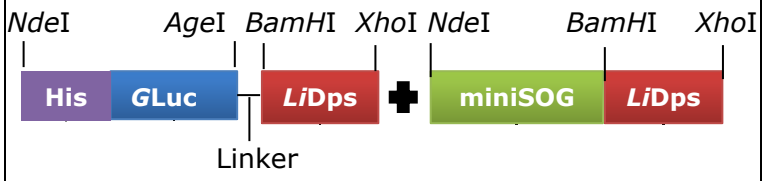
2- The production of hybrid protein cages comprised of Afb-HuAft and miniSOG-HuAft or *G*Luc-*Li*Dps with miniSOG-*Li*Dps, both capable of tumour imaging, PDT, and drug delivery (Chapter 4).

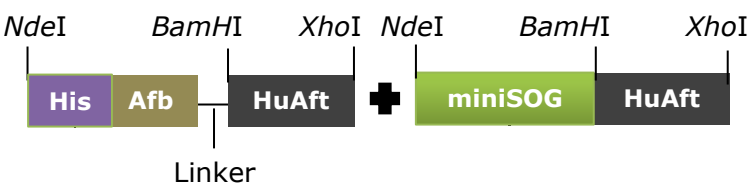
3- Fusion of *Li*Dps with *G*Luc followed by subsequent ZnPP conjugation. This construct would act as a PDT and imaging agent with the added capability to form *G*Luc-*Li*Dps-ZnPP cage, that could be loaded with therapeutic molecules (Chapter 5)

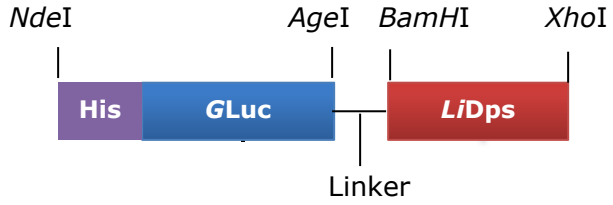
4- Synthesis of novel PbS QDs that are coated with the anti-HER2 Afb2C ligand. Further conjugation with ZnPP would produce two versions of PbS QDs (Afb2C-PbS and ZnPP-Afb2C-PbS QDs) with anticancer and tumour imaging activity (Chapter 6).

5- In order to investigate the anticancer activity and the possibility to use these systems in tumour imaging, three from the above constructs (*G*Luc-*Li*Dps-ZnPP, Afb2C-PbS QDs, and ZnPP-Afb2C-PbS QDs) have been tested *in vitro*. SKBR3 and MDA-MB-231 breast cancer cells were treated with the selected constructs and the changes in the cancer cell behaviour was monitored and analysed as described in Chapter 7.

Constructs	Type	Scheme of constructs	Description	Function
GLuc-miniSOG-LTVSPWY	Protein		PDT	Generation of ROS and imaging agent.
	Gene			

Constructs	Type	Scheme of constructs	Description	Function
***G*Luc-*Li*Dps:miniSOG-*Li*Dps**	Protein		PDT	Generation of ROS, drug delivery, and imaging agent.
	Gene			

Constructs	Type	Scheme of constructs	Description	Function
Afb-HuAft:miniSOG-HuAft	Protein		PDT	Generation of ROS, drug delivery, and imaging agent.
	Gene			

Constructs	Type	Scheme of constructs	Description	Function
***G*Luc-*Li*Dps-ZnPP**	Protein		PDT	Generation of singlet oxygen, drug delivery, and imaging agent.
	Gene			

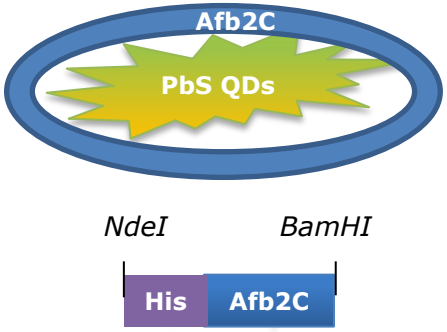
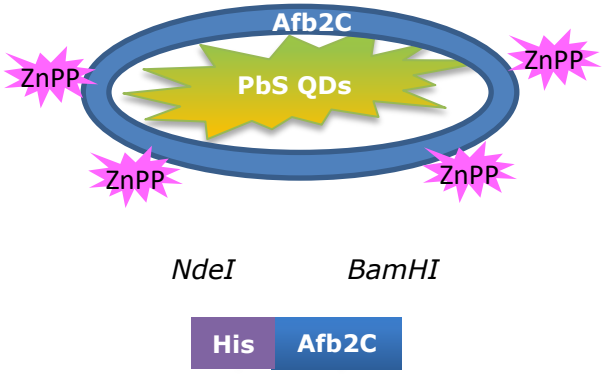
Constructs	Type	Scheme of constructs	Description	Function
Afb2C-PbS QDs	Protein		Drug delivery, PDT, and imaging agent	Targeting of HER2 overexpression cancer cells, anticancer activity, and tumour imaging tool
	Gene			
ZnPP-Afb2C-PbS QDs	Protein		Drug delivery, PDT, and imaging agent	Targeting of HER2 overexpression cancer cells, anticancer activity, and tumour imaging tool
	Gene			

Table 1.3: Schematic representations of the gene and protein maps for recombinant proteins and the novel constructs.

Chapter 2

2. Materials and methods

Bacterial strains, DNA plasmids, and DNA primers are listed in the appendix section. Solution and reagent components of polyacrylamide gel electrophoresis and the media have also included in the appendix section.

2.1 Molecular biology techniques

2.1.1 Extraction and purification of DNA from cell cultures

Plasmid DNA was extracted and purified from 10 mL cell cultures using the Wizard Plus® SV Miniprep kit (Promega) according to the manufacturer's protocol. Purified plasmid DNA was eluted with 50 µL of nuclease free water and its concentration determined spectrophotometrically by NanoDrop® A-1000 at 260 nm and the DNA was stored at -20 °C.

2.1.2 DNA manipulation

2.1.2.1 Polymerase Chain Reaction (PCR)

The target gene sequences were amplified by PCR from a vector template for cloning, generating mutations in plasmid encoded genes and screening.

Polymerase chain reactions were performed using Thermo Scientific™ 1.1 x ReddyMix™ PCR Master Mix according to manufacturer's instructions. The PCR mixture is illustrated in table 2.1.

	Volume	**Final concentration**
1.1 x ReddyMix PCR Master Mix	22.5 µL	1 x
Forward primer, 12.5 µM	1 µL	0.5 µM
Reverse primer, 12.5 µM	1 µL	0.5 µM
Template DNA	0.5 µL	0.5-125 ng
Water, nuclease-free	to 25 µL	
Total volume	25 µL	

Table 2.1: The PCR reaction mixture.

The DNA template was first denatured at 95 ºC for 2 minutes, before entering a cycle of denaturation at 95 ºC for 25 seconds, annealing at 48-63 ºC for 35 seconds (allow the PCR primer to bind with the complementary strand on the denatured DNA) and extension at 72 ºC for 65 seconds. After a total of 30 cycles the reaction entered a final

extension cycle at 72 ºC for 5 minutes. A negative control (without DNA template) was included to verify that no DNA contamination was present in reagents. The products were cooled and analysed by agarose gel electrophoresis as described in section 2.1.3.

2.1.2.2 Mutagenesis

For site directed mutagenesis (SDM), the Q5® Site-Directed Mutagenesis kit was used according to manufacturer's instructions. This method enables rapid, site-specific mutagenesis of double-stranded plasmid DNA, using the robust Q5 Hot Start High-Fidelity DNA Polymerase along with custom mutagenic primers were used to create a mutation in encoded target plasmids. Mutagenic primers were designed using NEBaseChanger™ software available online (http://www.nebasechanger.neb.com/). Mutation generation in the target gene of genomic DNA was performed in two steps:

First exponential amplification of the target gene was performed using the same procedure with normal amplification and PCR screen, but replacing with Q5 Hot Start High-Fidelity 2 x Master Mix instead of 1.1 x ReddyMix PCR Master Mix reagent. The cycling conditions are described in Table 2.2.

Step	Temperature	Time
Initial denaturation	98 ºC	30 seconds
25 cycles	98 ºC	10 seconds
	50-72 ºC	30 seconds
	72 ºC	30 seconds/kb
Final extension	72 ºC	4 min
Hold	4 ºC	

Table 2.2: Cycling conditions according to Q5 Site-Directed Mutagenesis.

The next step is the Kinase-Ligase-DpnI (KLD) reaction:

After the PCR, the amplified material is added directly to a unique KLD enzyme mix (see Table 2.3) and incubated for 5 minutes at room temperature.

	Volume	Final concentration
PCR product	1 µL	
2 x KLD reaction buffer	5 µL	1 x
10 x KLD enzyme mix	1 µL	1 x
Nuclease water	3 µL	

Table 2.3: KLD reaction mixture.

After ligation, 5 µL of product was transformed in 50 µL of DH5α calcium competent cell and grow in SOC medium, before spreading on a selective LB agar plate (Section 2.1.5 & Appendix 10.4.1).

***** All primers were purchased from Sigma.

2.1.2.3 Restriction enzyme digestion

DNA restriction digests were performed using restriction enzymes with the manufacturers' recommended buffers. The restriction reaction components are listed in Table 2.4.

Components	Amount
Restriction enzyme	10 units
DNA	1 µL
10 x NEB buffer	5 µL (1 x)
Total reaction volume	50 µL

Table 2.4: Restriction enzyme reaction mixture.

The reaction mixture was incubated at 37 °C for 20 hours and digested with different restriction enzymes, which required distinct buffers and hence were carried out sequentially. Samples of the digested DNA were subjected to agarose gel electrophoresis and visualised under UV light (ethidium bromide DNA staining) for analysis as described in section 2.1.3. DNA recovered from the digestions was purified using the Wizard® SV Gel and PCR Clean-Up kit (Promega) following the manufactures' protocols. DNA was eluted from the Clean-Up column using 23 µL of nuclease free water.

***** All restriction enzymes: BamH1, Nde1 and Xho1 were purchased from New England Biolabs™.

2.1.2.4 Ligation

Digested plasmid vector and insert DNA were ligated together using the Rapid DNA Ligation kit (Roche Life Science). The reaction components are listed in Table 2.5.

Components	Amount
T4 DNA Ligase buffer (10X)	2 µL
Vector DNA (4 kb)	50 ng
Insert DNA (1 kb)	37.5 ng
T4 DNA Ligase	1 µL
Water, nuclease-free	Up to 20 µL

Table 2.5: Ligation reaction components.

After the ligation process, the reaction product was transformed into highly competent *E. coli* DH5α or XL1-Blue cells using the procedure described in section 2.1.5.

2.1.3 Agarose gel electrophoresis

DNA was separated according to its MW using agarose gel electrophoresis. Agarose gel electrophoresis was performed according to Sambrook *et al.* [183]. Agarose 1% (w/v) was dissolved in 1× Tris-acetate-EDTA (TAE) buffer (40 mM Tris, 1 mM EDTA, pH 8.0) and cast

after the addition of 5 µL ethidium bromide to give a final concentration of 1 ng/mL. DNA samples were diluted with 6 x loading buffer (Thermo Fisher Scientific) and loaded into the gel. The gel (W x L in cm, 6 x 7) was immersed in 1× TAE buffer in a horizontal electrophoresis tank and then electrophoresed at 100 V for approximately 30 minutes [183]. DNA fragments were compared with 100 bp or 1 kb DNA marker and the images for the gels were visualised under UV light source using a Geneflow gel imaging system.

***** Agarose, ethidium bromide, Tris and EDTA were purchased from Sigma. DNA markers of 100 bp and 1 kb were purchased from New England Biolabs™.

2.1.4 DNA sequencing

Purified plasmid DNA (at 100 ng/µL) was sent to Source Bioscience of Cambridge for DNA sequencing.

2.1.5 Transformation of chemical and electro-competent *E. coli*

Transformation of *E. coli* was performed according to the method of Sambrook *et al.* [183] and Q5® Site-Directed Mutagenesis protocol (New England Biolabs™). A 50 µL aliquot of *E. coli* BL21 (DE3), Shuffle (DE3), and DH5α calcium competent cells (Appendix 10.1) were

thawed on ice and 5 µL of ~100 ng/µL plasmid DNA or ligation product was added. After incubation on ice for 30 minutes, the cells were heat shocked at 42 °C for 30-45 seconds and further incubated on ice for 5 minutes to transform the cells. Addition of 950 µL of LB or SOC medium, and 60 minutes incubation in a shaking incubator (180 rpm) at 37 °C was used to recover cells and initiate antibiotic resistance. Similarly, *E. coli* BL21 (DE3) and XL1-Blue electro-competent cells (Appendix 10.1) were thawed on ice and 5 µL of plasmid DNA added. The cells were incubated on ice for 2 minutes before electroporation transformation. Resistant *E. coli* were isolated by plating all the recovered cells on LB agar plates, including the appropriate antibiotic; either (50 µg/mL) kanamycin or (100 µg/mL) ampicillin. Plates were incubated overnight at 37 °C [183].

***** *E. coli* Shuffle (DE3) was commonly incubated in a shaking incubator (180 rpm) at 30 °C (It cannot grow at 37 °C).

***** Kanamycin and ampicillin were purchased from Sigma.

2.1.6 Overexpression of recombinant proteins

An LB starter culture (10 mL) with the appropriate antibiotic (kanamycin (50 µg/mL) or ampicillin (100 µg/mL)) added was inoculated with a single *E.coli* transformant colony and grown overnight at 37 °C with shaking at 180 rpm. This starter culture was

subcultured into 1 L of LB or M9 media (Appendix 10.4.1) containing appropriate antibiotic and grown until an OD_{600} of ~ 0.6. At this point, 1 mL of IPTG (1 M) was added to induce protein expression overnight at 30 °C for LB and 25 °C for M9 culture with shaking at 180 rpm. Cells were pelleted by centrifugation at (4000 x *g*, 4 °C) for 25 minutes, the supernatant was discarded and cell pellets were resuspended and stored in 40 mL of sonication buffer (20 mM Tris pH 8.3, 10 mM imidazole) at -80 °C.

2.1.7 Preparation of *E. coli* cell lysates

The *E.coli* biomass, acquired and stored as described in section 2.1.6, was thawed in a cold water bath. The protease inhibitor phenyl methyl sulfonyl fluoride (PMSF) (Sigma) was added to a final concentration of 0.5 mM. The cells were lysed by sonication on ice for 10 minutes (30 sec on/ 30 sec off). Subsequently, the lysate was clarified by centrifugation at 28500 x *g* for 25 minutes at 4 °C enabled isolation of soluble proteins from insoluble proteins and cell debris. The soluble fraction was applied to a purification column. Proteins in the insoluble fraction were denatured in 8 M urea, centrifuged again, and then filtered through a 0.45 µm filter and subject to purification steps.

2.2 Purification techniques

2.2.1 Ammonium sulfate precipitation

The lysate sample was firstly fractionated using ammonium sulfate before loading on the anion exchange column. Protein precipitation was achieved by gradually adding saturated ammonium sulfate solution. The protein ammonium sulfate solutions were gently mixed for 20 minutes at 4 °C and then centrifuged at 10000 x *g* for 15 minutes to pellet out protein. Pellets were dissolved in the binding buffer (20 mM Tris pH 8.3, 100 mM NaCl), analysed using SDS-PAGE and subjected to purification using chromatography.

2.2.2 Nickel-Immobilised metal ion affinity chromatography (Ni-IMAC)

Proteins designed with a Hexa-histidine-Tag (His-Tag) were purified using Ni-IMAC. An ÄKTA prime system (GE Healthcare Life Sciences, Amersham) was used for protein purification. Following GE healthcare Ni-IMAC guidelines, a pre-packed 5 mL column of HiTRAP chelating HP affinity resin (GE Healthcare Life Sciences) was used for Ni-IMAC purification. This column was charged with nickel ions (using a 50 mM solution of $NiSO_4$), before washing with 3 column volumes of water. The column was subsequently equilibrated with 30 mL of Ni-IMAC binding buffer (20 mM Tris pH 8.3, 10 mM imidazole), after which

soluble lysate was loaded into the column and the flow through collected. The absorbance of protein eluting from the column was monitored at 280 nm. The column was washed with Ni-IMAC binding buffer for soluble proteins, and binding buffer with 8 M urea for insoluble proteins until the absorbance fell to baseline. Protein bound to the column was eluted using a gradient of increasing imidazole concentration (Ni-IMAC elution buffer, 20 mM Tris pH 8.3, 1.5 M imidazole for soluble and buffer with 8 M urea for insoluble). Eluted protein was collected, kept on ice, and analysed by SDS-PAGE. The chromatography column was stripped of metal ions and recharged after each purification attempt as instructed by the column manufacturer. Fractions containing purified proteins were dialysed twice in 2 L of cold dialysis buffer for at least 4 hours, using 6-8 K MWCO dialysis tubing (Spectrum Laboratories). In the case of proteins with Cys mutations, these were dialysed overnight using 20 mM Tris pH 8.3 dialysed buffer and then swapped to dialysis buffer containing 1 mM dithiothreitol (DTT) to prevent formation of disulfide bonds between Cys residues.

2.2.3 Anion exchange chromatography

Overexpressed recombinant proteins with a net negative charge were purified using anion exchange on a HiTrap Q FF (GE healthcare) column. A 5 mL anion exchange column was prepared by washing with

3 column volumes of water before being equilibrated with 5 column volumes of anion binding buffer (20 mM Tris pH 8.3, 100 mM NaCl). The cleared lysate was applied directly to the column after ammonium sulfate precipitation (see Section 2.2.1) and the flow through collected for SDS-PAGE analysis. The column was washed with anion binding buffer until the absorbance returned to baseline. Proteins were eluted from the column by using a gradient of increasing NaCl concentration (elution buffer 20 mM Tris pH 8.3, 1.5 M NaCl). Eluted protein was collected and samples of these fractions were analysed by SDS-PAGE. The purified proteins were dialysed twice with 2 L of anion binding buffer overnight at 4 °C.

2.2.4 Desalting and buffer exchange

Purified miniSOG protein was applied to desalting columns to exchange buffer and decrease salt concentration. A 5 mL HiTrap desalting column was used where four of these columns were connected together and equilibrated with Tris buffer (20 mM Tris pH 8.3, 50 mM NaCl). Purified protein was loaded onto the desalting columns to remove the excess NaCl using Tris buffer (20 mM Tris pH 8.3, 50 mM NaCl).

2.2.5 Size exclusion chromatography (SEC)

Fractions purified previously containing the material of test were combined and subject to further purification using SEC (HiLoad 16/60, Superdex 75 prep grade, GE healthcare Life Sciences, Amersham). Fractions were collected and combined for analysis using SDS-PAGE. For mass detection of intact nanocapsule assembled proteins, the appropriate analytical gel filtration columns were used (Superdex 75 and 200 10/300 GL). Columns were equilibrated and proteins eluted using gel filtration buffer (20 mM Tris pH 8.3, 50 mM NaCl).

2.3 Determination of protein concentration

The concentration of non-fluorescent protein samples were determined directly by measuring their absorption at λ_{abs}=280 nm using NanoDrop® A-1000. Whereas the fluorescent protein concentration was detected using Bradford method. Protein sample (5 µL) was mixed with 250 µL Bradford reagent (Sigma-Aldrich) in 96 well plate and then incubated in room temperature between 5-60 minutes. The absorbance was read at λ_{abs}=595 nm using a microtiter plate reader (PerkinElmer precisely-Envision 2104 multilabel reader). The protein concentration was calculated using a standard curve that was generated using known concentrations of bovine serum albumin (BSA).

2.4 Polyacrylamide gel electrophoresis (PAGE)

2.4.1 Denaturing (SDS-PAGE)

Sodium dodecyl sulfate (SDS) PAGE separates proteins under denaturing conditions based on their MW [184].

2.4.1.1 Reagents and solutions

Gel composition		
	5% (w/v) Stacking gel	**15% (w/v) resolving gel**
H_2O	0.68 mL	1.1 mL
30% (w/v) Protogel® acrylamide	0.17 mL	2.5 mL
1.5 M Tris, pH 8.8	0.13 mL*	1.3 mL
10% (w/v) SDS	0.01 µL	50 µL
10% (w/v) ammonium persulfate	0.01 µL	50 µL
TEMED	0.001 µL	2 µL

* For stacking gel 1 M of Tris pH 6.8 was used.

Buffer composition		
	Components	**Final concentration**
Loading buffer	Tris-HCl pH 6.8 DTT SDS Glycerol Bromophenol blue	50 mM 100 mM 2% (w/v) 10% (v/v) 0.1% (w/v)
Running buffer	Tris base pH 8.8 Glycine SDS	25 mM 250 mM 0.1% (w/v)
Staining buffer	coomassie brilliant blue R-250 Glacial acetic acid Methanol	0.25% (w/v) 20% (v/v) 45% (v/v)
Destain buffer	Glacial acetic acid Methanol	10% (v/v) 25% (v/v)

2.4.1.2 Procedure

Gel electrophoresis was performed using a Bio Rad Mini-Protean3 gel system. The 15% (w/v) acrylamide resolving gel was prepared using a 1 mm gel mould, isopropanol was added to separate the gel from the air, and the gel left for 40 minutes to set. Then 6% (w/v) acrylamide of stacking gel was poured above the resolving gel after removing of isopropanol, and the 1 mm Teflon comb was inserted into the stacking gel (to provide 15 lanes for sample loading) and also left for 40 minutes. Samples were prepared by mixing 30 µL of protein and 10 µL of 4 x SDS loading buffer and applied to the gel lanes. The gel was deposited in a tank, which was filled with 1 x running buffer. The electrophoresis was performed at 180 V until the samples reached to resolving gel then the voltage was increased to 200 V until samples had travelled through the gel. The gel was shaken gently with coomassie brilliant blue buffer for 30 minutes and then placed in destaining solution for 2 hours to remove the dye. The Geneflow gel imaging system was used for visualisation of the destaining gel.

2.4.2 Tricine-SDS-PAGE

2.4.2.1 Reagents and solutions

Gel composition		
	4% (w/v) stacking gel	**16% (w/v) resolving gel**
H_2O	0.66 mL	0.4 mL
30% (w/v) Protogel® acrylamide	2.9 mL	6.4 mL
Glycerol	-	1.2 mL
3M Tris, 0.3% (w/v) SDS, pH 8.45	1.24 mL	4 mL
10% (w/v) ammonium persulfate	25 µL	50 µL
TEMED	10 µL	10 µL

Buffer composition		
	Components	**Final concentration**
Loading buffer	Tris-HCl pH 6.8 DTT SDS Glycerol Bromophenol blue	50 mM 100 mM 2% (w/v) 10% (v/v) 0.1% (w/v)
Running buffer	**Cathode buffer (inside)** Tris pH 8.25 Tricine SDS	 100 mM 100 mM 0.1% (w/v)
	Anode buffer (outside) Tris pH 8.9	 200 mM
Staining buffer	coomassie brilliant blue R-250 Glacial acetic acid Methanol	0.25% (w/v) 20% (v/v) 45% (v/v)
Destain buffer	Glacial acetic acid Methanol	10% (v/v) 25% (v/v)

2.4.2.2 Procedure

Tricine-SDS-PAGE gels were cast using a 4% (w/v) acrylamide stacking layer and 16% (w/v) acrylamide resolving layer. Samples were prepared as reported in SDS-PAGE procedure (see Section 2.4.1)

and loaded under the cathode buffer. The gels were run using cathode buffer inside the gel cassette and anode buffer around the gel cassette for 50 minutes at 150 V.

2.4.3 Non-Denaturing (Native PAGE)

2.4.3.1 Reagents and solutions

	4% (w/v) stacking gel	6% (w/v) resolving gel
H_2O	2.88 mL	6.66 mL
30% (w/v) Protogel® acrylamide	0.50 mL	2 mL
1.5 M Tris, pH 8.8	0.94 mL	3 mL
10% (w/v) ammonium persulfate	60 µL	150 µL
TEMED	6 µL	15 µL

Buffer composition		
	Components	**Final concentration**
Loading buffer	Tris-HCl pH 6.8 DTT Glycerol Bromophenol blue	50 mM 100 mM 50% (v/v) 0.1% (w/v)
Running buffer	Tris base Glycine	25 mM 200 mM
Staining buffer	coomassie brilliant blue R-250 Glacial acetic acid Methanol	0.25% (w/v) 20% (v/v) 45% (v/v)
Destain buffer	Glacial acetic acid Methanol	10% (v/v) 25% (v/v)

2.4.3.2 Procedure

The gels were prepared and run as described by Sambrook *et al*. [183]. Samples were mixed with a quarter volume of 4 x loading buffer and loaded into the gel without heating. The gels were run for 2 hours at 125 V.

2.5 Mass spectrometry (MS)

2.5.1 Matrix Assisted Laser Desorption/Ionisation Time-of-Flight (MALDI-TOF MS)

The purified protein samples were analysed on a Bruker Matrix Assisted Laser Desorption/Ionization (MALDI-TOF, Bruker Ultraflex III) MS, according to the LP-44 kDa method. Samples for MALDI-TOF MS were prepared by mixing 5 µL of protein with 10 µL of the saturated sinapic acid solution (sinapic acid was dissolved in a solvent of 1:2 acetonitrile + 0.1% (v/v) trifluoroacetic acid). Samples were loaded onto the plate and dried at room temperature. The spectrum generated was analysed using flexControl (Ultraflex) Ver 3.0 software and the MW of the protein identified.

2.5.2 Nano-Electrospray Ionization (nESI) MS

Proteins were analysed using nESI and the mass spectrum was generated by spraying protein from 80:20 MeCN:H_2O + 0.1% TFA (v/v), following C4 ZipTip desalting. Data was acquired on a Waters SYNAPT HDMS instrument.

2.6 Dis-assembly and re-assembly of genetically modified *Li*Dps and HuAft

Both miniSOG-HuAft and Afb-HuAft cages were dissociated by a gradual decrease in pH from 8.3 to 2.0. These proteins were dialysed using glycine buffer (20 mM glycine pH 2.0, 50 mM NaCl) for at least 4 hours at 4 ºC, using 6-8 K MWCO dialysis tubing (Spectrum Laboratories). Dissociated miniSOG-HuAft and Afb-HuAft subunits were mixed in 25:75, 50:50, and 75:25 molar ratio, diluted with glycine buffer (1 mg of subunits diluted to 3 mL), and shaken for 4 hours at 4 ºC. Mixed subunits were reassembled by dialysis using Tris buffer (20 mM Tris pH 8.3, 50 mM NaCl) at 4 ºC overnight. The dialysed samples were purified on a SEC column (Superdex 75 GL 10/300) as described in section 2.2.5 and eluted with Tris buffer (20 mM Tris pH 8.3, 50 mM NaCl).

By comparison, *G*Luc-*Li*Dps and miniSOG-*Li*Dps cages were dissociated using 4 M urea and reassembled by gradually removing urea through dialysis twice with Tris buffer (20 mM Tris pH 8.3, 50 mM NaCl). The products were purified using SEC column (Superdex 200 GL 10/300) and were eluted with Tris buffer (20 mM Tris pH 8.3, 50 mM NaCl).

2.7 Bioluminescence activity

The bioluminescence activity of *G*Luc was tested by monitoring the light intensity produced from *G*Luc in the presence of its substrate (coelenterazine). A 100 µL aliquot of (0.75, 1.5, 7.5, or 15 µg/mL) of *G*Luc in Tris buffer (20 mM Tris pH 8.3) was transferred to a white 96 well plate and mixed with 50 µL of (3, 6, or 12 µg/mL) of coelenterazine. The luminescent light intensity of *G*Luc was detected at 470 nm using a microplate reader (*En Vision* 2104 Multilabel Reader).

The coelenterazine solution was prepared by dissolving 1 mg of coelenterazine in 20 µL of methanol and adjusted to 1 mL with phosphate buffer (PB) (20 mM NaH_2PO_4 pH 8.3).

2.8 Labelling *G*Luc-*Li*Dps with ZnPP using EDC/NHS

The *G*Luc-*Li*Dps chimeric protein was labelled with ZnPP using a modified Thermo Scientific protocol. In all of the steps described below, the reaction was protected from light. *G*Luc-*Li*Dps in Tris buffer (20 mM Tris pH 8.3) was dialysed with PB (20 mM NaH_2PO_4 pH 8.3) to prevent interference between the amine groups in Tris and the activated carboxyl groups. To produce the activated protoporphyrin-*N*-hydroxysuccinimide ester (ZnPP-NHS), a 100 µL of ZnPP in DMSO (30 mM) was mixed with 12 µL of 500 mM of 1-(3-dimethylaminopropyl)-

3-ethylcarbodiimide hydrochloride (EDC) in MES buffer (0.1 M MES (2-[*N*-morpholino]ethane sulfonic acid) pH 6). The reaction mixture was agitated at room temperature for one minute. Following incubation, 12 µL of *N*-hydroxysuccinimide (NHS) (500 mM) in MES buffer was added. The reaction mixture was agitated for a further 15 minutes at room temperature before the solution was centrifuged at room temperature (4000 x *g*, 15 minutes) and any unwanted precipitates were discarded. The purified *G*Luc-*Li*Dps chimera was incubated with activated ZnPP-NHS ester for 24 hours at room temperature, after which dialysis with PB overnight was used to remove unreacted protoporphyrin and components.

2.9 Dynamic light scattering (DLS) measurements

A MALVERN Nano Zetasizer DLS instrument was used to determine the size of the synthesised hybrid cage proteins. Samples were filtered using a 0.22 µm syringe filter and 1 mL of each sample was loaded into a cuvette. A standard operating procedure (SOP) was applied for measuring size and used to measure each sample three times. The average size, plus or minus standard deviation and area percent were used to create the plot between the size (nm) and the intensity.

2.10 Circular dichroism (CD) spectroscopy

The Afb2C (0.5 µg/mL) was analysed in 20 mM Tris buffer at pH 7.0 and pH 11.0 using CD spectrometer (Chirascan Plus Spectroscopy). Samples were dialysed with the desired buffer at 4 ºC overnight and the pH was adjusted using 10 mM sulfuric acid.

2.11 Afb2C-based nanoprobes preparation

2.11.1 Synthesis of Afb2C-PbS QDs

The Afb modified to include two Cys at its C-terminal (Afb2C) was used as a ligand to coat the surface of PbS QDs based on the reaction between the thiol groups of the Afb2C and Pb^{2+}. This was carried out in two steps: the first step requires the generation of two specific mutants in the C-terminal of the Afb2C (G82C and S84C). The mutant Afb2C once expressed and purified was stored in Tris buffer (20 mM Tris pH 8.6 with 1 mM DTT reducing agent). In the second step the Afb2C was pelleted using 70% (v/v) ammonium sulfate and the pellet washed with Tris buffer (20 mM Tris pH 8.6) including 70% (v/v) ammonium sulfate. The Afb2C was pelleted again to remove the DTT. The pellet was immediately dissolved in 1.7 mL of 0.0167 M lead acetate trihydrate ($Pb(CH_3CO_2)_2.3H_2O$) (Sigma). The lead acetate-Afb2C mixture was diluted with the same volume (1.7 mL of Tris

buffer, 40 mM Tris pH 8.6) and the pH raised to 11.0 using 100 mM NaOH with the reaction run under a nitrogen atmosphere. The reaction mixture was stirred for 30 minutes to allow the Pb^{2+} to bind to the thiol groups of the Afb2C. After, 0.25 mL of 0.1 M of Na_2S was added to the reaction mixture which subsequently changed to a black colour, indicating the formation of Afb2C-PbS QDs. The Afb2C-PbS QDs solution was left stirring for a further 30 minutes. Finally the product was dialysed against Tris buffer (20 mM Tris pH 11.0) overnight and the solution kept in vials under a nitrogen atmosphere at 4 ºC in dark.

2.11.2 Labelling of Afb2C-PbS QDs with ZnPP

In order to label Afb2C-PbS QDs with ZnPP, Afb2C-PbS QDs in Tris buffer (20 mM Tris pH 11.0) were dialysed against PB (20 mM NaH_2PO_4 pH 11.0) overnight at 4 ºC. ZnPP was activated with EDC to allow coupling with NHS as described in section 2.8. Afb2C-PbS QDs were mixed with a 10 fold excess of the activated ZnPP-NHS ester under ambient conditions. The reaction mixture was protected from light and was gently agitated overnight at room temperature. The product was centrifuged at 5000 x *g* for 10 minutes and then dialysed with PB (20 mM NaH_2PO_4 pH 8.3) overnight at 4 ºC.

2.12 Photoluminescence (PL) measurements

The PL of PbS QDs was analysed using a Horiba Jobin Yuon Ltd.(HR800) Lab. Ram. Setup. This system uses a He-Ne laser (λ=633 nm), with a power of 2 x 10^6 W/cm^2 for sample excitation. Samples were subjected to laser light and the PL was collected through x 50 NIR objective. The PL was detected using an InGaAs array detector with detection range 900-1600 nm.

2.13 Transmission electron microscopy (TEM)

PbS QDs at a concentration of 0.1 mg/mL was deposited on a graphene-coated grid (Agar scientific) and TEM images were recorded on the JEOL2100EX microscope operating at 120 keV. Shape and size were monitored in the nm scale of view.

2.14 *In vitro* cell assays

2.14.1 Subculturing cell lines

SKBR3 and MDA-MB-231 breast cancer cell lines were subcultured when they reach approximately 70-80% confluency. They were detached from the flask surface by removing the medium and adding 1 mL of 1 x trypsin-EDTA solution (Sigma). The cells were incubated

with trypsin-EDTA at 37 ºC, 5% CO_2 for 3 minutes to enhance detachment from the culture flask surface. After incubation, 5 mL of RPMI 1640 fresh medium (Appendix 10.4.2) was added and used to resuspend the cells. A $1/5^{th}$- $1/10^{th}$ of resuspended cells were recultured. Similarly, MRC5 healthy cells (from lung tissue) were subcultured using Minimum Essential Medium (MEM) (Appendix 10.4.2). Remaining cells were counted using hemocytometer and used for other *in vitro* assays.

***** All media and their supplemented components were purchased from Sigma.

2.14.2 Determination of cell viability using the MTT assay

To quantify cell viability after exposure to anticancer agents an MTT assay was carried out on SKBR3, MDA-MB-231 and MRC5 cell lines. The cells were seeded into a 96-well plate at a density of approximately 3 x 10^3 cells in a volume of 180 µL of media per well. The plates were incubated at 37 ºC, 5% CO_2 for 24 hours. A 20 µL volume of anticancer agents with increasing concentration was added to each well along with 180 µL of fresh medium (going a final volume of 200 µL per well), and incubated at 37 ºC, 5% CO_2 for 72 hours. After 72 hours, 3-(4,5-dimethylthiazol-2-yl)-2,5-diphenyltetrazolium bromide (MTT) solution was added to each well and incubated for 3 hours at 37 ºC, 5% CO_2. Finally, the medium with MTT reagent was

removed and 150 µL of DMSO was used to dissolve the insoluble purple formazan product into a coloured solution. The absorbance of this solution was measured at 550 nm using a microplate reader (*En Vision* 2104 Multilabel Reader). A control plate was prepared without addition of anticancer agents. Cell viability was presented by plotting the optical density at 550 nm against reagent concentration, and the GI_{50} was calculated accordingly.

2.14.3 Cellular uptake determination using flow cytometry

The cellular uptake of *G*Luc-*Li*Dps-ZnPP nanoparticles was studied using flow cytometry. Cells were seeded at a density of 3.5 x 10^5 cells/well in 6 well plate in 2 mL complete growth medium and incubated at 37 ºC, 5% CO_2 for 24 hours. After incubation the cells were incubated with 2 x GI_{50} of anticancer agents for 1, 3 and 6 hours. Following this, the medium containing dead cells was removed and the adherent cells were trypsinised using trypsin-EDTA to detach them from the plate surface. The detached cells were resuspended in fresh medium to deactivate the trypsin and transferred to a labelled fluorescence activated cell sorter (FACS) tube. The cells were pelleted by centrifugation at 1200 x *g* for 5 minutes, 4 ºC, washed with PBS and pelleted again. Pelleted cells were resuspended in 500 µL PBS and then placed into an Astrios EQ flow cytometry. Cells were excited by 425 nm light, causing ZnPP to emit light (593 nm); allowing cells

containing ZnPP to be discriminated from there that did not uptake of ZnPP. Untreated cells were used as a flow cytometry control. All data were analysed using Kaluza Flow Cytometry Analysis Software (Beckman Coulter)

2.14.4 Reactive oxygen species (ROS) detection

The ROS levels were detected *in vitro* using ROS-Glo™ H_2O_2 kit (Promega) according to the manufacturer's protocols. This was achieved by seeding 0.5 x 10^5 cells/well in a white 96 well plate in 80 µL complete growth medium and incubated at 37 ºC in a 5% CO_2 for 24 hours. The cells were treated with 2 x GI_{50} for *G*Luc-*Li*Dps-ZnPP plus coelenterazine, and 20 µL of the H_2O_2 substrate was added to 80 µL of treated cell culture. This mixture was incubated for 6 hours at 37 ºC in a 5% CO_2 after which detection solution (luciferin detection reagent, D-Cys and Signal Enhancer Solution; 100 µL) was added and the cells were incubated for a further 20 minutes at room temperature. Finally, the plate was transferred to a microplate reader (En Vision 2104 Multilabel microplate reader, PerkinElmer), and luminescence detected at $\lambda_{emission}$ = 520 nm.

2.14.5 Preparation of samples for confocal microscopy

Confocal microscopy was used to study the localisation of the *G*Luc-*Li*Dps-ZnPP construct inside the cells. This was achieved by seeding 0.1 x 10^5 cells/well in 8 well µ-Slide confocal chamber (Thistle Scientific Ltd) for 24 hours before treatment with 2 x GI_{50} of anticancer agents. After this, the cells were washed twice with PBS and fixed by incubation with 4% (v/v) formaldehyde for 20 minutes. After fixation, cells were washed twice with PBS and kept at 4 ºC. The fluorescent light was visualised, after excitation at 425 nm for ZnPP, at 593 nm using a confocal microscope (LEICA DMI 4000 B), and the images were analysed using imageJ (Fiji) software.

2.14.6 Wound healing (migration) assay

The cell migration was studied to follow the physiological and pathological changes that happen after treating the cells with *G*Luc-*Li*Dps-ZnPP plus coelenterazine. Cell migration was carried out according to Rodriguez *et al.* [185]. Cells were seeded at a density of 35 x 10^3 cells/well and incubated for 24 hours in a µ-Dish (this dish containing two medium chambers separated by membrane to form a cell-free gap between the chambers that are used for cell seeding, (Thistle Scientific Ltd)), (Figure 2.1).



Figure 2.1: A 35 mm imaging dish use for cell migration. This dish contains of 2 well silicon for cell seeding with defined cell-free gap.

Subsequently, the cells were treated with 0.5 x GI_{50} of *G*Luc-*Li*Dps-ZnPP plus coelenterazine and the cell migration was monitored and the wound closure tracked every 8 hours using a Nikon ECLIPSE TS 100 microscope; the images were analysed using imageJ (Fiji) software.

2.14.7 Cell cycle assay

The DNA content of the cells was tested using the cell cycle assay to monitor the changes in the nucleus through cell divisions and study the effect of treatment in this process.

Cell cycle analysis was carried out according to Nicoletti *et al*. [186]. The cells to be analysed were seeded in a 6 well plate at a density of 75 x 10^3 cells/well in 2 mL of complete growth medium and incubated at 37 ºC, 5% CO_2 for 24 hours before treatment. The cells

were treated for 24, 48 and 72 hours and then the medium, which contained dead cells, was collected into labelled FACS tubes and kept on ice. The remaining adherent cells were trypsinised with 500 µL of 1 x trypsin-EDTA before pooling with the medium containing dead cells. The cells were centrifuged at 4 ºC (1200 rpm) for 5 minutes, the supernatant removed and the pellets washed with 1 mL chilled PBS followed by another cycle of centrifugation. The supernatant was decanted and the pellet was broken down by gently flicking the tube. The cells were resuspended in 500 µL cold hypotonic fluorochrome solution, protected from light and stored overnight at 4 ºC. Samples were vortexed and analysed on a Beckman Coulter Epics-XL MCL flow cytometer and 10,000-15,000 events were recorded for each sample (λex=535 nm, λem=617 nm). The results obtained were analysed using EXPO32 software. Flow cytometry analysis shows DNA population in G1, S, and G2/M cell cycle phases and pre-G1 phase

- Hypotonic fluorochrome solution: 50 µg/mL PI (propidium iodide) (Sigma-Aldrich), 0.1 mg/mL ribonuclease A (Sigma-Aldrich), 0.1% v/v Triton X-100 (Sigma-Aldrich), 0.1% w/v sodium citrate (Sigma-Aldrich) dissolved in PBS.

2.14.8 Annexin V- fluorescein isothiocyanate apoptosis detection

An annexin V-FITC/PI (AV/PI) (BD Pharmingen) kit was used to identify the percentage of cells that underwent apoptosis in the presence of anticancer agents, according to the V-FITC/PI manufacturer's protocols.

Cells were seeded in a 6 well plate at a density of 75 x 10^3 cells/well in 2 mL complete growth medium. Cells were allowed to attach for 24 hours. Subsequent these cells were treated with anticancer agents at 2 x GI_{50} concentrations for 24, 48, 72 hours, after each time the medium with floated cells was pooled into a labelled FACS tube and kept on ice. The attached cells were trypsinised with 500 µL of trypsin-EDTA and when detached pooled together with floating cells in a total of 1 mL complete growth medium. The cells were centrifuged at 1200 rpm for 5 minutes at 4 ºC. Subsequently, the supernatant was decanted and the pellet broken down by gently flicking the tube. The pellet was washed with 1 mL cold PBS and the cells were centrifuged as before. Thereafter, 100 µL of 1 x annexin binding buffer and 5 µL AV was added to each tube. The tube was vortexed and incubated at room temperature for 15 minutes without light. A 400 µL of 1 x annexin binding buffer and 10 µL of PI solution were added to each tube which was vortexed and incubated for 10 minutes at room temperature without light. Samples were analysed within 1hour by Beckman Coulter Epics-XL MCL flow cytometer and 10,000-20,000 events were recorded for each sample (AV λex=494 nm, λem=518 nm; PI

λex=535 nm, λem=617 nm). The results were analysed using EXPO32 software.

Flow cytometry analysis shows 4 cell populations in the quadrant plots. The lower left quadrant includes the viable cell population (J3- annexin AV-/PI-), the lower right quadrant shows the early apoptotic population (J4-annexin AV+/PI-), the upper right quadrant shows the late apoptotic population (J2- annexin AV+/PI+), and the upper left quadrant shows the necrotic population (J1- annexin AV-/PI+).

2.14.9 Western blotting

2.14.9.1 Reagents and solutions

Buffer composition		
	Components	**Quantity**
Nonidet-P40 (NP40) lysis buffer	NP40 (Fluka) NaCl (1 M) Tris pH 8.0 (1 M) Phoshatise inhibitors (Roche (PhosSTOP)) Protease inhibitors (Roche (complete ultra-tablets)) Deionised water	100 µL 1.5 mL 500 µL 1 tablet 1 tablet 7.9 mL
1 x transfer buffer	Tris Glycine SDS Methanol	25 mM 192 mM 0.038% (w/v) 20% (v/v)
1 x TBS-T	Tris pH 7.6 NaCl tween	20 mM 137 mM 0.05% (v/v)
10% (w/v) non-fat milk	non-fat dried milk	5 g in 50 mL TBS-T

2.14.9.2 Sample preparation

Proteins were extracted from the cells and prepared for Western blotting as described by Mahmood *et al* [187]. Cells were seeded in dishes (100 x 20 mm) in 10 mL of complete growth medium at a density of 10 x 10^5 cells/dish and allowed to attach for 24 hours. After this time they were exposed to 2 x GI_{50} of anticancer agent. Subsequently cells were lysed with NP40 lysis buffer and all the steps were carried out on ice. The medium was removed and cells were washed 2 x with PBS. Thereafter 300 µL of NP40 lysis buffer was added to each petri dish. A cold plastic cell scraper was used for cells scraping and the harvested cells were collected in the labelled microcentrifuge tubes. The dishes were washed with an excess 200 µL of NP40 lysis buffer to collect any remaining adherent cells and added to the labelled tubes. The microcentrifuge tubes were centrifuged at 1,500 rpm, at 4 °C for 5 minutes. The tubes were incubated on ice for 30 minutes. Subsequently, the tubes were centrifuged at 13,000 rpm for an additional 10 minutes at 4°C to pellet insoluble material. The supernatant was transferred to microcentrifuge tubes and the protein cell lysates were stored at -20 ºC. The protein contents of cell lysates was determined using Bradford colorimetric assay [188].

2.14.9.1 Procedure

Protein samples were prepared for Western blotting and detected according to Mahmood *et al*. [187]. Following separation by SDS-PAGE, the proteins were transferred from the gel matrix to a nitrocellulose membrane (Bio-Rad) by semi-dry transfer for additional analysis. The gel was equilibrated with transfer buffer for 2 minutes and the nitrocellulose membrane and chromatography paper (Whatman) were soaked in 50 mL 1 x transfer buffer for 5 minutes. The transfer apparatus (Invitrogen) was then assembled from the gel to membrane as a transfer sandwich. The trapped air bubbles were gently removed and protein transfer was migrated at 25 V for 1.5 hour. The membrane was blocked in 10% (w/v) non-fat milk to prevent nonspecific protein binding for 1 hour at room temperature with gentle shaking. Afterwards, the membrane was washed 3 x 5 minutes with fresh TBS-T. The membrane was then incubated with the appropriate primary antibody in 5% (w/v) non-fat milk with TBS-T overnight at 4 ºC with gentle shaking. Subsequently, the membrane washed again 3 x for 10 minutes in TBS-T to remove excess unbound primary antibody. The membrane was then incubated with polyclonal goat anti-rabbit HRP-conjugated secondary antibody in 5% non-fat milk with TBS-T for an additional 1 hour at room temperature with gentle shaking. Following this step the membrane was washed for 3 x

for 10 minutes in TBS-T to remove excess unbound secondary antibody.

Proteins blotted to the membrane were detected using an immunological detection system. The final washing step was followed by the incubation of the membrane with Enhanced chemiluminescence (ECL) Western blotting detection reagent (GE Healthcare Life Sciences, Amersham ECL). The membrane was scanned using LI-COR® C-DiGit™-3600 blot scanner and the images were analysed using Image Studio Lite Ver 5.2 software.

*****All primary antibodies were diluted 1:1000, whereas secondary antibodies were diluted 1:2000 for Western blotting.

*****Antibodies used in Western blotting: Bcl-2, Mcl-1, and ß-actin primary antibodies were purchased from Cell Signalling Technologies, Inc. Primary antibodies Bcl-2 and Mcl-1 were of rabbit origin, whereas ß-actin was of mouse origin. Both anti-mouse and anti-rabbit goat immunoglobulin HRP secondary antibodies were purchased from Dako.

2.15 Statistical analysis

In this study the data were analysed using one-way, two-way analyses of variance (ANOVAs), and t-test. The graphs were created using GraphPad Prism Ver 6 and the data presented as the mean ± standard deviation. The significant effect was calculated considering $P < 0.05$ as a minimal level.

Chapter 3

3. Construction of *G*Luc-miniSOG-LTVSPWY recombinant protein as a photodynamic therapy and imaging agents

3.1 Introduction

The fluorescent flavoprotein miniSOG has been widely used in biomedical applications such as PDT and as an imaging agent [189,190]. However difficulties arise when trying to excite this protein with visible light *in vivo*; due to the scattering of light by tissues. Furthermore miniSOG does not target specific cell types, causing off target effects. To address the lack of cell specificity, Shirmanova *et al*. attempted to encode miniSOG in the genome of target cells. As a result they found that miniSOG lost its ability to function as a PDT agent. The authors of the study reasoned that this might have been caused by a lack of FMN cofactor, which is essential for the activity of the protein [191].

This chapter describes the construction of a novel PDT theranostic fusion protein, *G*Luc-miniSOG-LTVSPWY (Figure 3.1).

*G*Luc was fused to miniSOG in order to address the aforementioned issues regarding the excitation of miniSOG. Here the bioluminescence of *G*Luc ($\lambda_{max(emission)}$ = 470-490 nm), catalysis by the addition of coelenterazine (a *G*Luc substrate), is used to excite miniSOG

($\lambda_{max(excitation)}$ = 450-490 nm) via a BRET mechanism. Consequently, this 'self-illuminating' system can therefore potentially used in deep tissues that are ordinarily not accessible to external optical light sources, with minimal damage to surrounding healthy tissues.

In addition the lack of cell specificity associated with miniSOG was addressed by fusing the LTVSPWY targeting peptide to the C-terminal end of *G*Luc-miniSOG. LTVSPWY was chosen as a small targeting peptide because of its ability to recognise and bind to HER2 overexpressing breast cancer cells in preference to binding normal cells [175,192–196].

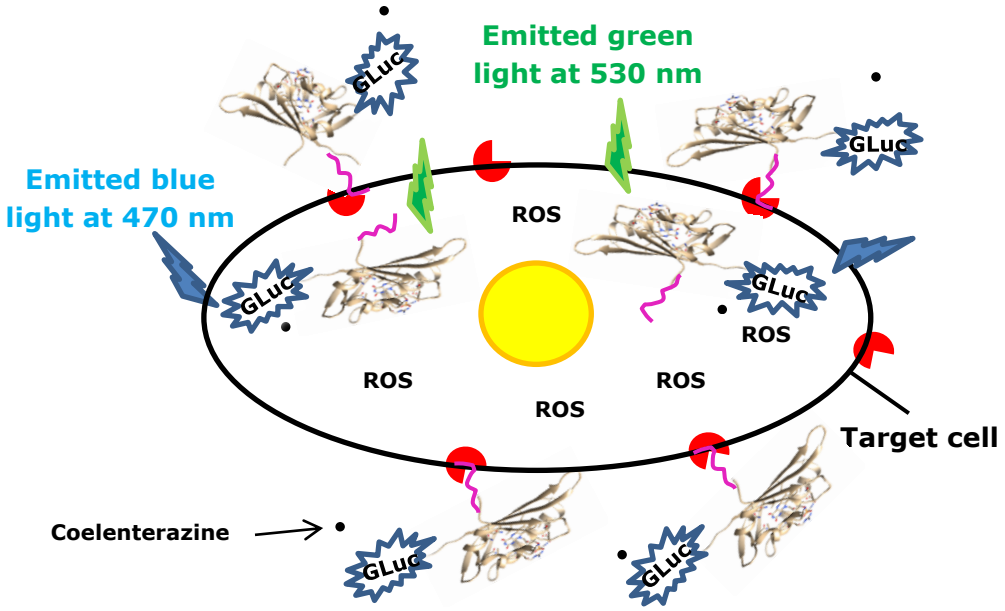
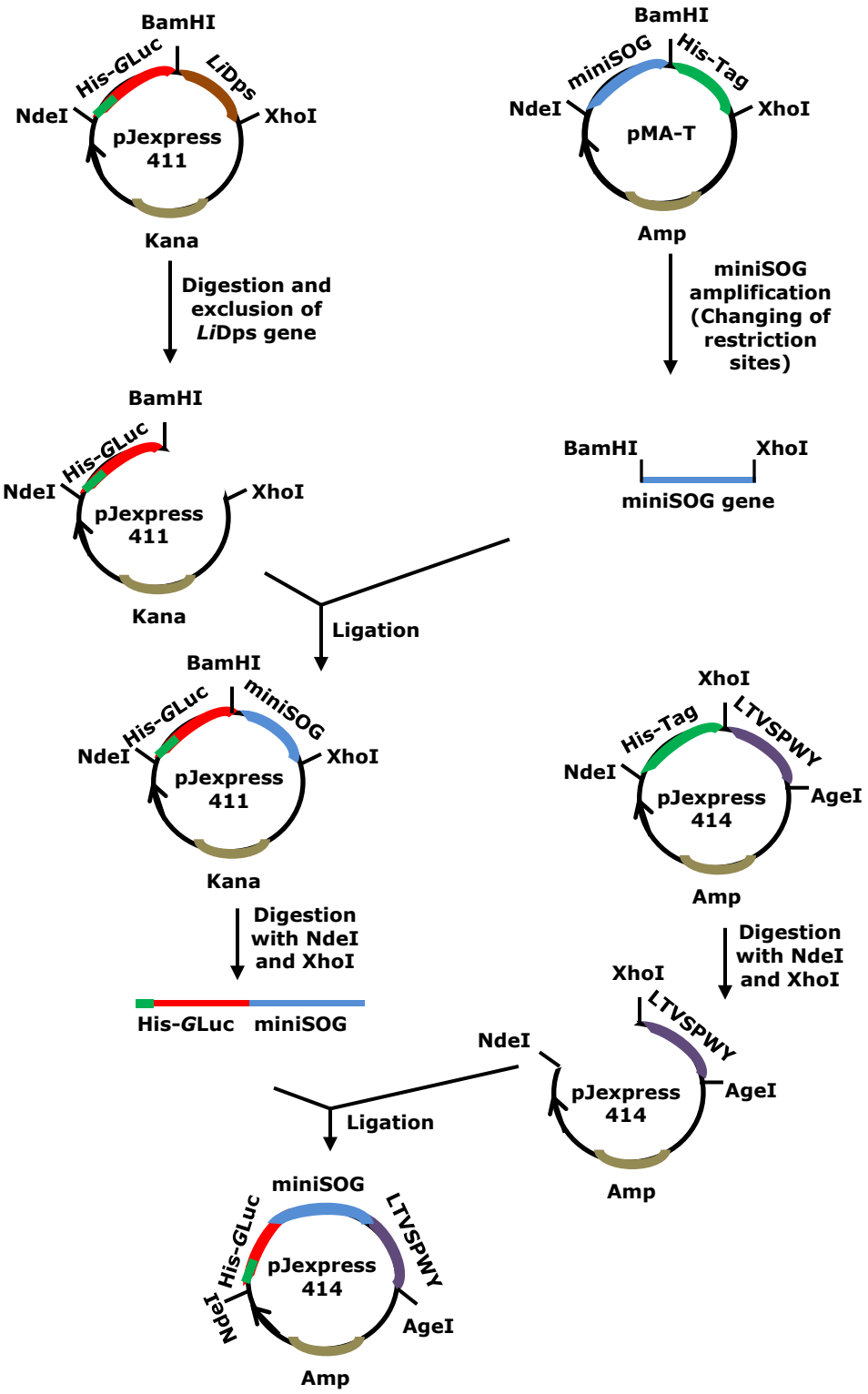


Figure 3.1: Cartoon representation of proposed uptake of the *G*Luc-miniSOG recombinant protein via the LTVSPWY peptide by HER2-overexpressing cells. *G*Luc-miniSOG-LTVSPWY acts as theranostic agent in PDT. MiniSOG generates ROS upon irradiation by *G*Luc light, and the emitted light from either *G*Luc or miniSOG is used for cell imaging. *G*Luc GLuc was fused to the N-terminus of miniSOG which was labelled with LTVSPWY peptide at the C-terminus that has the affinity to bind with HER2 receptors .

3.2 Results

3.2.1 Designing of the *G*Luc-miniSOG-LTVSPWY protein

The *G*Luc-miniSOG-LTVSPWY fusion gene was synthesised using the pJexpress411:*G*Luc-*Li*Dps plasmid (this plasmid was prepared as described in section 5.2.1.1). Furthermore, the NdeI and BamHI restriction sites upstream and downstream of the miniSOG gene were changed to BamHI and XhoI, respectively. This step, which was necessary for fusing the miniSOG gene to the C-terminus of the *G*Luc gene, was performed through PCR amplification of the miniSOG gene in the pMA-T plasmid (synthesised by DNA2.0, Appendix 10.3). This was achieved by using primers harbouring the new restriction sites (Appendix 10.2). The miniSOG gene was ligated downstream of *G*Luc after removing the *Li*Dps gene from the pJexpress411:*G*Luc-*Li*Dps plasmid. Thereafter, the *G*Luc-miniSOG gene was digested using NdeI and XhoI restriction enzymes and ligated upstream of the LTVSPWY gene in the pJexpress414:LTVSPWY plasmid (synthesised by DNA2.0, Appendix 10.3) (Scheme 3.1).



Scheme 3.1: Schematic showing the construction of pJexpress411:*G*Luc-miniSOG-LTVSPWY plasmid using pMA-T:miniSOG, pJexpress411:*G*Luc-*Li*Dps and pJexpress414:LTVSPWY plasmids.

The ligation product was transformed into DH5α *E. coli* and spread on an ampicillin LB agar selection plate. The colonies grown on LB agar plate were subjected to a PCR screen using T7 forward and reverse primers (Appendix 10.2). Here the difference in the MW between LTVSPWY (66 bp) and *G*Luc-miniSOG-LTVSPWY (927 bp) allowed for the successful discrimination between the plasmids. After 30 PCR cycles the reactions were analysed by agarose gel electrophoresis which showed that the majority of colonies contained the correct plasmid, giving a band of ~927 size (Figure 3.2).

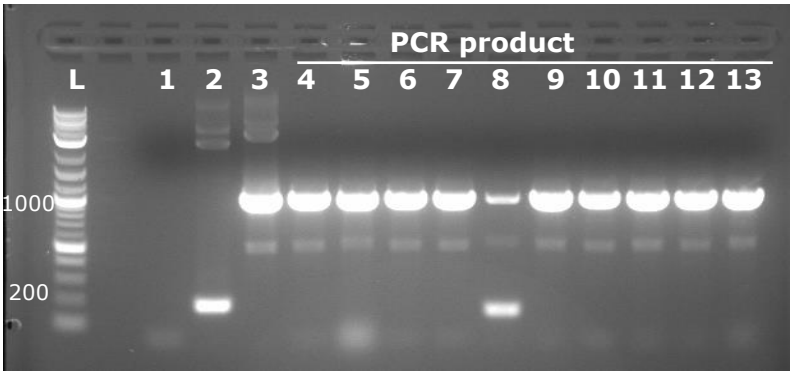
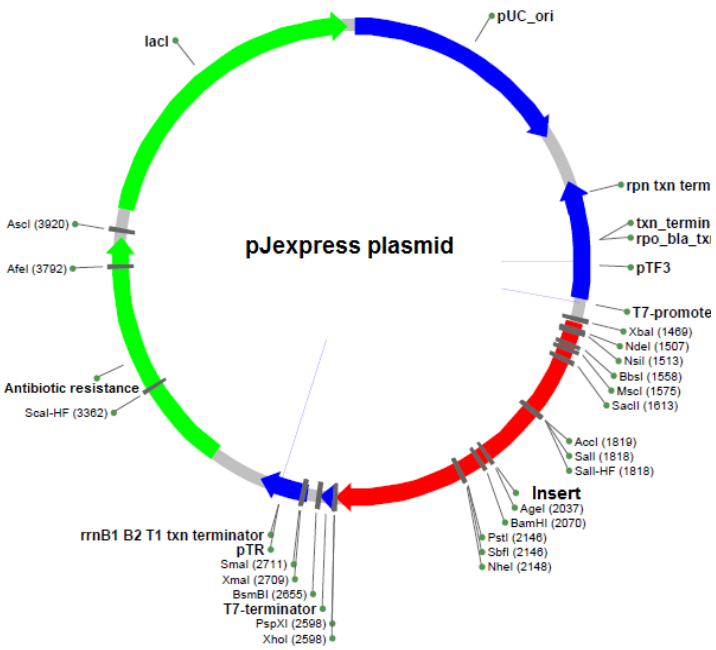


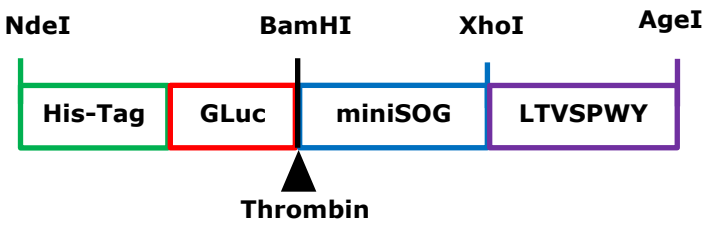
Figure 3.2: Plasmid screening on a 1% (w/v) agarose gel. DNA MW ladder (L), H_2O (negative control) (1), LTVSPWY (2), *G*Luc-miniSOG (3), and PCR colony product (4-13). T7 forward and reverse primers were used. The gel image illustrates that all DNA samples contain the ~927 bp insert expected for the *G*Luc-miniSOG-LTVSPWY gene, except sample 8, which might contain a mixture of *G*Luc-miniSOG-LTVSPWY and LTVSPWY genes.

Plasmid DNA was extracted from successful colonies using a miniprep kit and sent for sequencing to confirm the fidelity of the gene (Figure 3.3).

(A)



(B)



(C)

1 MHHHHHHAKPTENNEDFNI VAVASNFATTDLDADRGKLPGKKLPLEVLKE
51 LEANARKAGCTRGCLICLSHIKCTPK MKKFI PGRCHTYEGDKESAQGGIG
101 EAIVDIPEIP GFKDLEP LEQFIAQVDLCV DCTT GCLK GLANVQCSDLLKK
151 WLPQRCATFASKIQGQVDKIKGAGGDTGGGGGGLVPRGSAEKSFVITDPR
201 LPDNPIIFAS DGFL ELTEYSRE EILGRNGRFLQ GPET DQATV QKIRDAIR
251 DQREITVQLINYTK SGKKFW NLLHLQPMRDQKGELQYFIGVQLDLEGGGL
301 TVSPWY

Figure 3.3: (A) The pJexpress plasmid map (DNA2.0). **(B)** The *G*Luc-miniSOG-LTVSPWY gene map. **(C)** The primary amino acid sequence of the *G*Luc-miniSOG-LTVSPWY recombinant protein. The sequence comprises an N-terminal His-Tag (green), *G*Luc (red), a pentaglycine linker with the thrombin cleavage site underlined (black), miniSOG protein (blue), a tri-glycine linker (orange), and a C-terminal LTVSPWY peptide (purple).

The physical properties of the *G*Luc-miniSOG-LTVSPWY protein without FMN cofactor are described in Table 3.1.

No. of residues	MW (Da)	Theoretical pI	Molar Extinction coefficient (M/cm) at 280 nm
306	33,665	6.51	24,575

Table 3.1: The theoretical physical properties of the *G*Luc-miniSOG-LTVSPWY chimera without FMN cofactor.

3.2.2 Expression and purification of the *G*Luc-miniSOG-LTVSPWY protein

The formation of disulfide bonds between the Cys thiol groups plays a vital role in the folding and stability of many proteins. The primary sequence of *G*Luc contains a total of 10 Cys residues which are thought to contribute to the low solubility of *G*Luc-miniSOG-LTVSPWY through the incorrect formation of disulfide bridges.

To circumvent this problem and express the *G*Luc-miniSOG-LTVSPWY in soluble form, different conditions and *E. coli* expression strains were tested.

Transformed BL21 and Shuffle (DE3) *E. coli* were grown in M9 or LB media induced overnight at 20 °C. SDS-PAGE analysis of the induced cultures revealed that a relatively high amount of soluble *G*Luc-miniSOG-LTVSPWY was obtained from Shuffle *E. coli* when grown in M9 medium (Figure 3.4).

The *G*Luc-miniSOG-LTVSPWY recombinant protein with a His-Tag was purified using Ni-IMAC. The lysate fraction was applied to a nickel column after sonication and centrifugation, and the protein was eluted by gradually increasing the imidazole concentration from 0 to 1.5 M in a Tris buffer (20 mM of Tris pH 8.6). Following purification, the activity of *G*Luc-miniSOG-LTVSPWY was tested through the addition of coelenterazine, resulting in the emission of blue light.

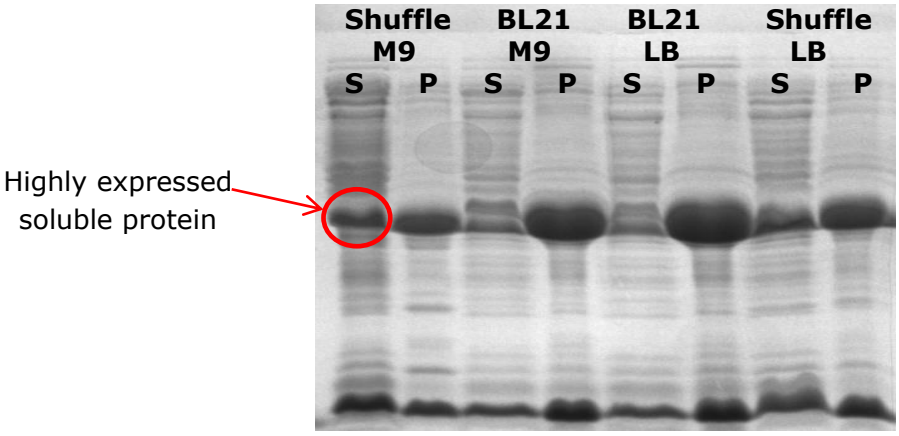


Figure 3.4: SDS-PAGE shows the increase in the expression of soluble *G*Luc-miniSOG-LTVSPWY protein when Shuffle (DE3) *E. coli* were grown in M9 medium. S = soluble fraction, P = insoluble fraction.

In addition, the protein emitted green light upon excitation with blue light indicating that *G*Luc-miniSOG-LTVSPWY was active. The purified samples were loaded on a 15% (w/v) SDS-PAGE gel to check the purity and determine the approximate MW (Figure 3.5).

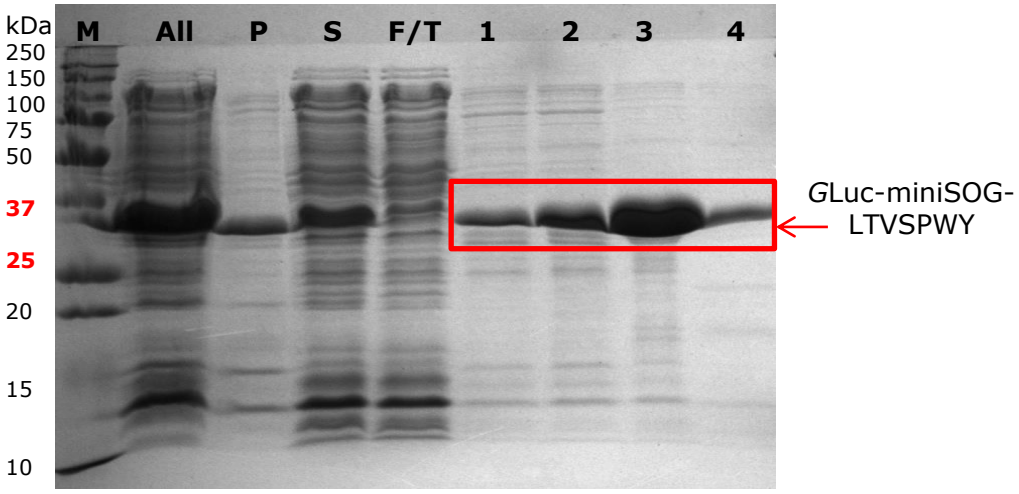


Figure 3.5: SDS-PAGE shows the crude and purified *G*Luc-miniSOG-LTVSPWY samples. M = protein marker, All = whole cell lysate, P = insoluble, S = soluble, F/T = flow through, 1 to 4 = purified fractions.

In the SDS gel, the *G*Luc-miniSOG-LTVSPWY band was located between 25 and 37 kDa. To determine the exact MW, a *G*Luc-miniSOG-LTVSPWY sample was analysed using denatured MALDI-TOF MS (Figure 3.6).

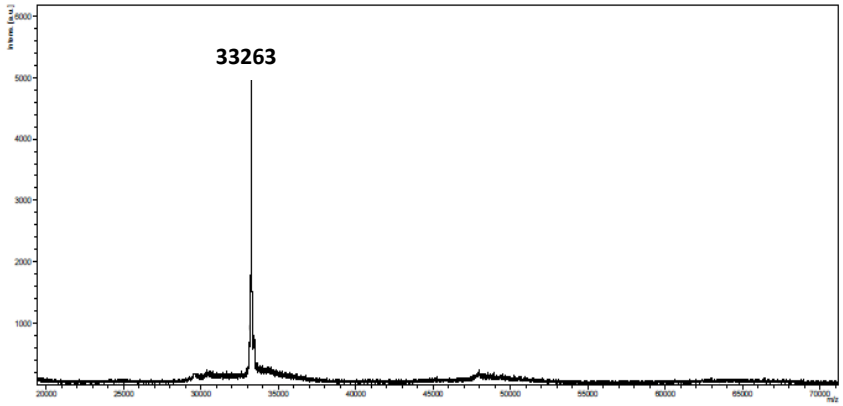


Figure 3.6: MALDI-TOF shows that the MW of *G*Luc-miniSOG-LTVSPWY without its FMN cofactor is 33,263 Da.

The MALDI-TOF MS indicated that the mass of *G*Luc-miniSOG-LTVSPWY protein without its FMN cofactor was 33,263 Da, close to the theoretical mass (calculated using software available online: http://web.expasy.org/protparam/) (Table 3.2).

	Theoretical mass (Da)	**Experimental mass (MALDI-TOF) (Da)**	**Deviation (Da)**
***G*Luc-miniSOG-LTVSPWY**	33,665	33,263	402

Table 3.2: The theoretical and measured mass of *G*Luc-miniSOG-LTVSPWY without its FMN cofactor.

Standard proteins were used to determine the variations in protein mass measurement using MALDI-TOF MS, see Table 3.3 and Figure 3.7.

	Theoretical mass	**Experimental mass (MALDI-TOF)**	**Deviation (Da)**
Cytochrome C from bovine heart	11,580	12,113	533
Lysozyme from chicken egg white	12,929	14,141	1,212
BSA	66,433	42,714; 57,057	23,719; 9,376

Table 3.3: The theoretical and measured mass of standard proteins using MALDI-TOF-MS.

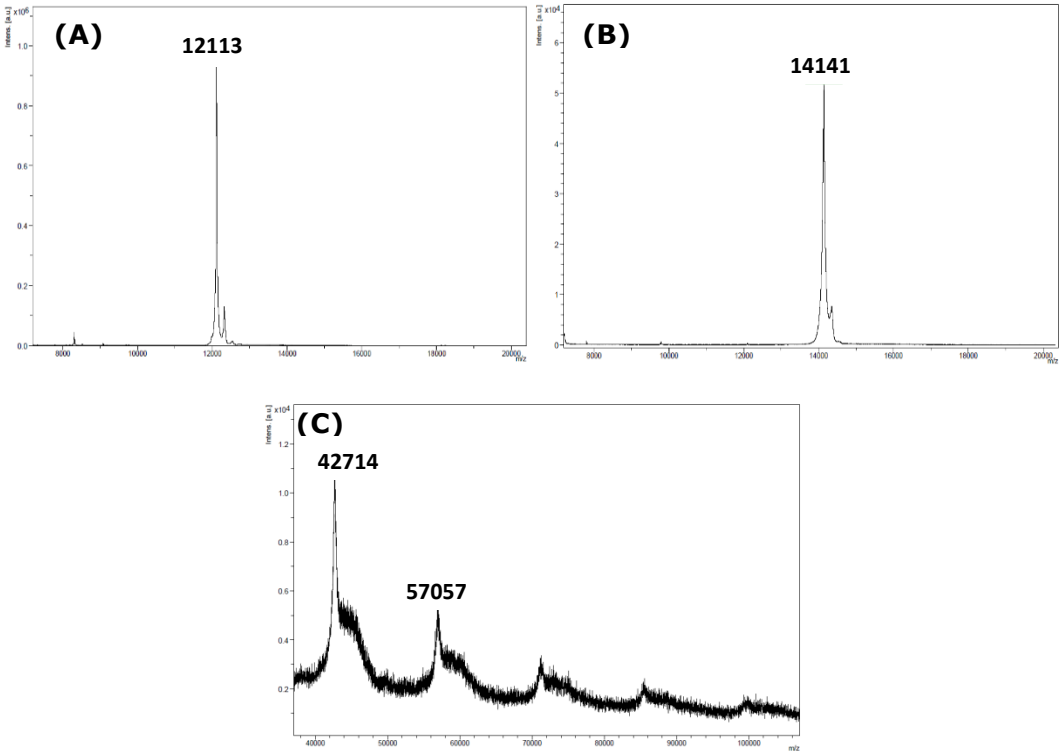


Figure 3.7: MALDI-TOF of standard proteins **(A)** Cytochrome C from bovine heart **(B)** Lysozyme from chicken egg white **(C)** BSA.

The MALDI-TOF-MS measurements show that there is a small difference in the mass (~200 Da) between the theoretical and experimental mass and this is increased with a large protein (BSA). As well the MS shows that the BSA degrades through the ionisation process.

3.2.3 Study of *G*Luc-miniSOG-LTVSPWY activity

The *G*Luc-miniSOG-LTVSPWY recombinant protein was designed for use in PDT, and the activity of this construct was assessed by monitoring changes in the bioluminescence emission of *G*Luc and the light absorption of miniSOG.

Initially, the spectra of miniSOG and its FMN cofactor were determined separately. Both absorbed at λ_{max} = 435 nm. The FMN emission spectrum λ_{max} = 545 nm shifted to λ_{max}= 495 nm with a shoulder at 530 nm when FMN was incorporated into miniSOG of *G*Luc-miniSOG-TVSPWY as a cofactor (Figure 3.8).

Furthermore, the excitation/emission spectra for *G*Luc and miniSOG within the fusion protein were measured to evaluate if BRET was possible. The measurements showed that the emission spectra of *G*Luc and the absorbance spectra of miniSOG overlapped, indicating that energy transfer (BRET) could occur between the two proteins and therefore produce ROS.

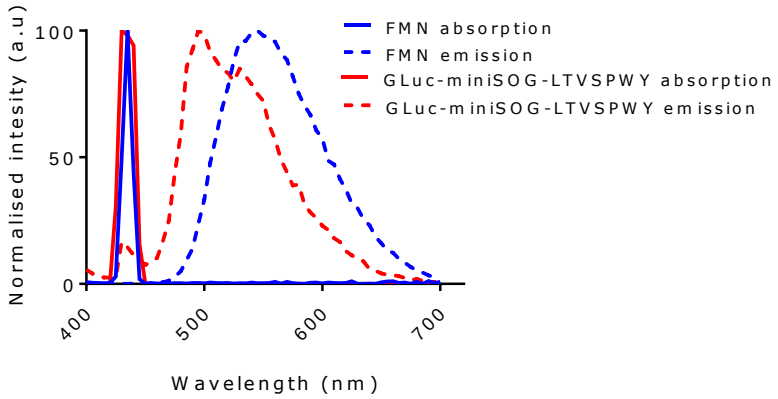


Figure 3.8: The spectra of free FMN (blue) (5 µg/mL) and *G*Luc-miniSOG-LTVSPWY-bound FMN (red) (5 µg/mL) in a Tris buffer (20 mM of Tris pH 8.6). The solid lines represent the absorption spectra, and the dashed lines represent the emission spectra (λ_{ex}=450 nm).

The *G*Luc-emitted light and the miniSOG-absorbed light were measured after fusing the proteins together. Good overlap between the emitted light spectrum of *G*Luc and the absorbed light spectrum of miniSOG was observed. This can improve energy transfer and the ROS quantum yield (Figure 3.9).

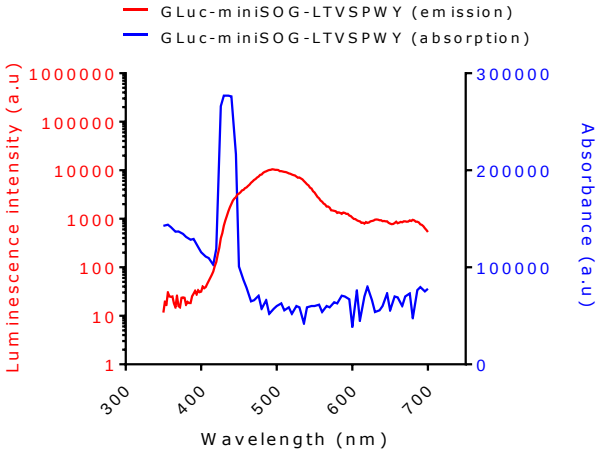


Figure 3.9: The spectral overlap between the bioluminescence spectrum of *G*Luc and the absorption spectrum of miniSOG in the *G*Luc-miniSOG-LTVSPWY construct. (5 µg/mL of *G*Luc-miniSOG-LTVSPWY was mixed with 4 µg/mL of coelenterazine in a Tris buffer (20 mM of Tris pH 8.6)).

Moreover, *G*Luc-miniSOG-LTVSPWY activity (the ability of *G*Luc to oxidise coelenterazine and emit blue light) was studied and compared with the activity of *G*Luc alone. Different concentrations of *G*Luc-miniSOG-LTVSPWY and *G*Luc were treated with coelenterazine (Figure 3.10). The results showed that at a fixed concentration of coelenterazine (4 µg/mL), the activity of *G*Luc-miniSOG-LTVSPWY almost matched the activity of *G*Luc. No significant difference in activity was observed. The main differences were observed in the period between 5 and 10 minutes (Figure 3.10 A & B).

In contrast, at a fixed concentration of *G*Luc and *G*Luc-miniSOG-LTVSPWY (5 µg/mL) and different concentrations of coelenterazine, the light intensity of *G*Luc decreased by 95% after 5 minutes, whereas the light intensity of *G*Luc-miniSOG-LTVSPWY only decreased by 70% under the same conditions (Figure 3.10 C & D). These results indicate that the fusion of *G*Luc to miniSOG alters the kinetics of the enzyme from 'flash', where substrate turnover is very fast and the photoluminescent period is very short, to 'glow', where substrate turnover is slower, prolonging photoluminescence. *G*Luc normally has a tendency for 'flash' kinetics [158].

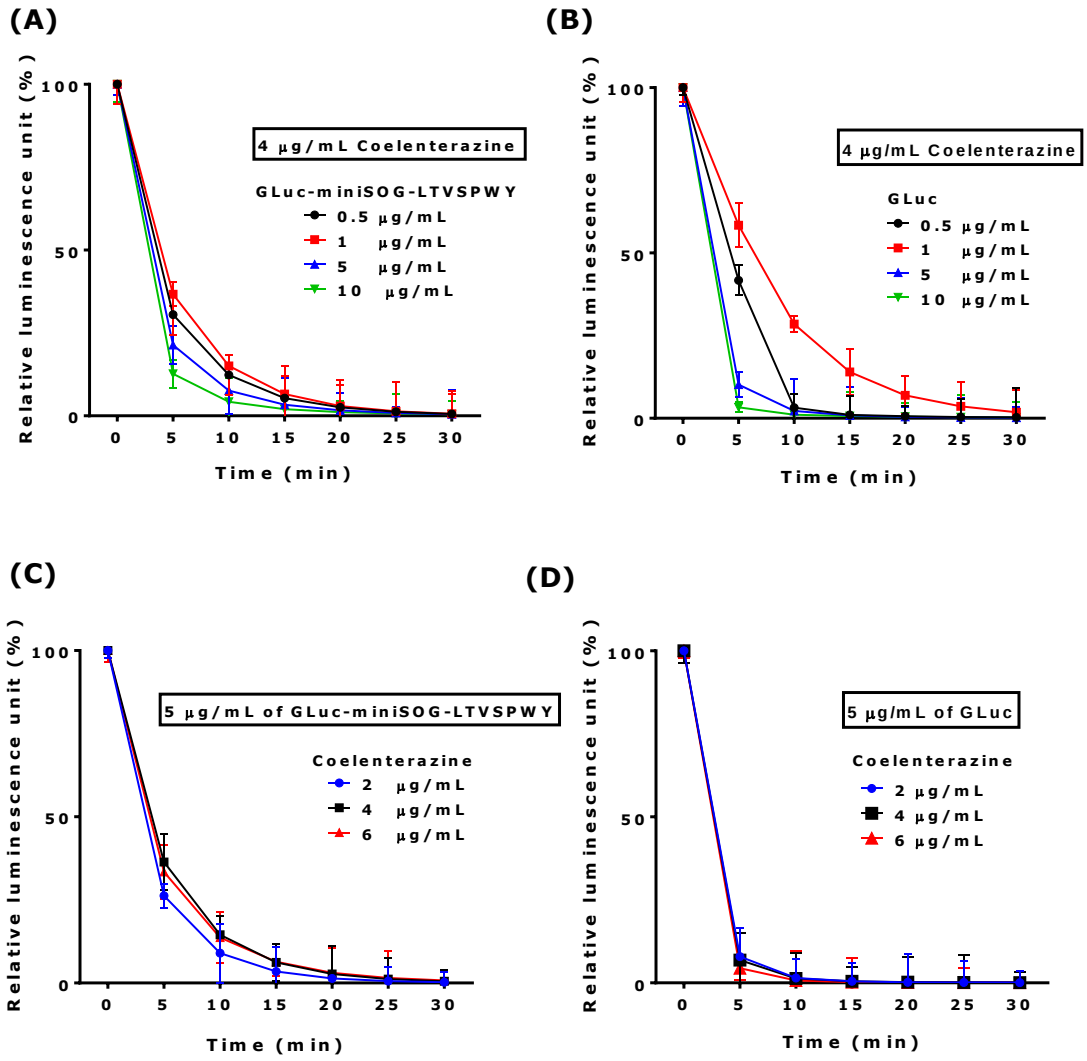


Figure 3.10: The light intensity output was monitored to study *G*Luc and *G*Luc-miniSOG-LTVSPWY activity in the presence of different concentrations of coelenterazine. The curves show the decrease in light over 30 minutes in the presence of **(A)** 0.5, 1, 5, 10 µg/mL of *G*Luc-miniSOG-LTVSPWY and 4 µg/mL of coelenterazine respectively, **(B)** 0.5, 1, 5, 10 µg/mL of *G*Luc and 4 µg/mL of coelenterazine, **(C)** 5 µg/mL of *G*Luc-miniSOG-LTVSPWY and 2, 4, 6 µg/mL of coelenterazine, and **(D)** 5 µg/mL of *G*Luc and 2, 4, 6 µg/mL of coelenterazine in a Tris buffer (20 mM of Tris pH 8.6). The emitted light was monitored every 5 minutes for 30 minutes.

Furthermore, sodium dodecyl sulfate (SDS) was used at a concentration of 0.1% (w/v), less than its critical micelle concentration (CMC) value, to examine its effect on *G*Luc-miniSOG-LTVSPWY denaturation and activity. *G*Luc-miniSOG-LTVSPWY protein exhibited high level of resistance to denaturation by SDS compared to *G*Luc alone, and the light intensity (protein activity) was approximately the same before and after treatment with SDS.

On the other hand, the light intensity of *G*Luc was slightly lower in the presence of 0.1% (w/v) SDS when compared with that of the untreated sample (Figure 3.11).

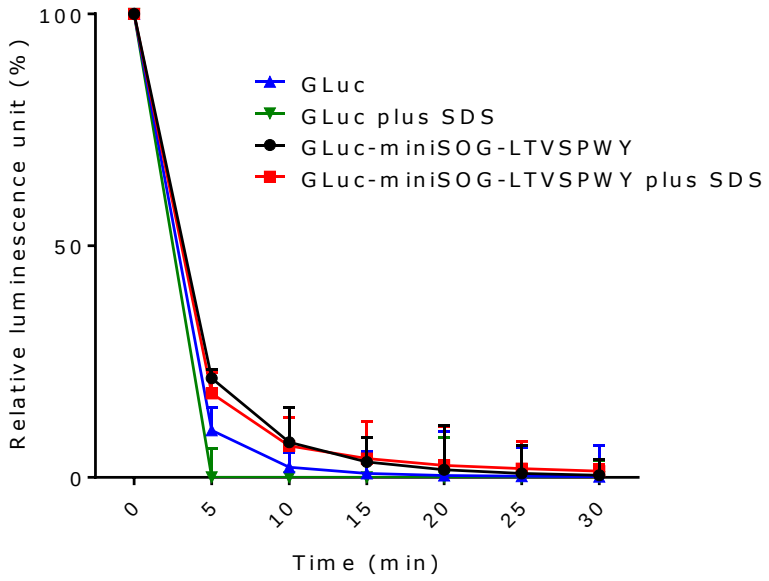


Figure 3.11: The effect of SDS on the activity of *G*Luc and *G*Luc-miniSOG-LTVSPWY. *G*Luc-miniSOG-LTVSPWY (5 µg/mL) in Tris buffer (20 mM Tris pH 8.3) was mixed with Coelenterazine (4 µg/mL) and SDS (0.1% w/v) in a white 96 well plate. The emitted light was monitored every 5 minutes for 30 minutes.

3.3 Discussion

In this study, a *G*Luc-miniSOG-LTVSPWY construct was successfully designed to act as both a PDT and an imaging agent. *G*Luc-miniSOG-LTVSPWY works as a PDT agent in a multistep process. Firstly, the targeting peptide functions to direct the construct to the intended tissues, resulting in the accumulation of *G*Luc-miniSOG-LTVSPWY in those tissues. It has been reported that the LTVSPWY peptide has the ability to recognise and specifically bind the HER2 cell surface protein that is expressed in both healthy and cancerous cells. However, in cancer cells express very high levels of HER2 cell surface protein allowing the LTVSPWY peptide to display high selectivity to target them; resulting in the internalisation of *G*Luc-miniSOG-LTVSPWY by the cancer cells [197]. Secondly, coelenterazine activates the construct by initiating the emission of blue light from *G*Luc, which in turn excites miniSOG via a BRET mechanism. Lastly, the energy emitted from miniSOG, upon returning to its ground state, excites neighbouring oxygen molecules, generating ROS.

The bioluminescent light of *G*Luc in *G*Luc-miniSOG-LTVSPWY permits targeting of deep tissues and avoids the drawbacks of using an external light source to excite miniSOG. In addition, *G*Luc has many advantages in this system including small size, good overlap between its emitted light and the absorbed light by miniSOG, and a light intensity brighter than that of other luciferases, such as Rluc and Fluc,

which might improve BRET and the generation of ROS [158] (Section 1.7.1).

As mentioned previously, *G*Luc has ten Cys residues that form five disulfide bonds when the protein folds. It is critical, in terms of protein activity, that these disulfide bonds are formed correctly i.e. the correct Cys pairings are made. However the cytoplasm of *E. coli* has a reductive environment, therefore preventing the formation of disulfide bonds in the first instance and resulting in a misfolded protein. Additionally, the disulfides that form upon oxidation (following exposure to air during purification) are incorrectly matched and only yield inactive protein. *G*Luc-miniSOG-LTVSPWY was recovered in inactive form after denaturation with 8 M urea as a result of loss of the FMN the essential cofactor for miniSOG activity. Therefore, these problems (associated with standard protein expression in *E. coli*) present a major obstacle in obtaining functional *G*Luc-miniSOG-LTVSPWY protein. To address this issue, a different expression strain of *E. coli* (Shuffle and BL21) and expression media were used. Shuffle *E. coli* carry mutations that result in a lack of glutathione reductase (*gor*) and thioredoxin reductase (*trxB*) genes, but overexpress disulfide-bond isomerase (DsbC) [198]. As a result, the cytoplasm of Shuffle is less reducing and therefore more amenable to the formation of disulfide bonds. In addition DsbC, can re-shuffle the disulfide bond pairings until the correct fold is achieved, therefore improving the

probability of achieving functional *G*Luc. In combination with Shuffle, M9 growth medium was used. This medium consists of the minimal nutritional requirements bacteria need to grow and therefore slows the growth of the culture and the expression of protein, permitting the protein to fold correctly. By using Shuffle and M9 medium functional protein was obtained. However, the majority of the protein was still expressed in the insoluble fraction (pellet).

After preparation, the *G*Luc-miniSOG-LTVSPWY mass was characterised using MALDI-TOF-MS. Because of the using denatured MALDI-TOF-MS, *G*Luc-miniSOG-LTVSPWY loss its FMN cofactor. Therefore we have compared the mass of *G*Luc-miniSOG-LTVSPWY in the unbound-FMN form. It was found that there was around a 400 Da difference between the experimental and theoretical mass. The difference in the mass might be attributed to the cleavage of methionine (131 Da) from the N-terminal of *G*Luc-miniSOG-LTVSPWY a post translation modification process that usually take place in all organisms from bacteria to eukaryotes. However methionine is utilised to initiate protein synthesis for essentially all proteins, it is consequently removed in a large percentage of cases, either by an N-terminal cleavage "signal " peptide (as part of cellular translocation mechanisms or precursor activation) or through the function of specific methionine aminopeptidases [199,200]. Furthermore selections of standard proteins were used to study the variation in the mass using

MALDI-TOF-MS. The ionisation of small protein (Cytochrome C from bovine heart and lysozyme from chicken egg white) shows that there is around a 200 Da difference in the mass and this variation significantly increased with a high protein mass (BSA). It has been also observed that the BSA gives more than one mass suggesting that degradation of large proteins through the ionisation process may be occurring. In addition, the MS shows that BSA has difficulty flying, resulting in longer flight times and lower resolution, Figure 3.7 C. For these reasons the MALDI-TOF-MS gives the approximate mass for the protein prepared in this study.

Moreover the results indicate that the *G*Luc-miniSOG-LTVSPWY folded in the active forms when fused together as one entity. This was confirmed by observing the characteristic blue light emitted from *G*Luc in the presence of coelenterazine suggesting the recovery of the correct protein fold and structure critical for *G*Luc-miniSOG-LTVSPWY activity. We note that the *G*Luc-miniSOG-LTVSPWY appeared yellow in colour and displayed a green colour upon irradiation by UV light; indicating that miniSOG was also functionally-active and had incorporated the FMN chromophore in its core.

It was noticed that the light intensity of *G*Luc-miniSOG-LTVSPWY exhibited glow kinetics, whereas *G*Luc alone exhibited flash kinetics. This might be due to steric hindrance from the miniSOG protein, which

might reduce the access of oxygen and coelenterazine molecules to the active site of *G*Luc.

SDS was also utilised as a denaturing agent to examine the protein stability. The result explains that the activity (bioluminescence emission) of *G*Luc-miniSOG-LTVSPWY was slightly affected when treated with SDS compared to the untreated sample.

In contrast, the treatment of *G*Luc alone with SDS shows a reduction in activity compared to the untreated sample. This indicates that the fusion of *G*Luc with miniSOG-LTVSPWY enhanced stability and the construct structure was not affected by SDS, as shown by the retention of activity after treatment with SDS.

From our results, we can conclude that this system has many advantages when compared to other PDT agents such as graphene QDs [201], ALA-mediated PDT [202], and meso-Acetoxymethyl BODIPY-mediated PDT [203], are as follows: *G*Luc-miniSOG-LTVSPWY is a small recombinant protein (306 aa) comprising *G*Luc and miniSOG, the smallest proteins in their families, and the hepta LTVSPWY peptide. Combining self-illumination and the photosensitiser in the same entity promoted the efficient transfer of energy between *G*Luc and miniSOG to achieve BRET and improve the quantum yields of ROS. Moreover, *G*Luc-miniSOG-LTVSPWY could be used as an imaging agent by using the fluorescent light of miniSOG after excitation or by detecting the bioluminescence light of *G*Luc.

Chapter 4

4. Fabrication of *G*Luc-*Li*Dps:miniSOG-*Li*Dps and Afb-HuAft:miniSOG-HuAft hybrid cages

4.1 Introduction

*Li*Dps and HuAft are multi subunit proteins that assemble to form spherical hollow cage structures. These proteins can be used in biotechnological applications by either exploiting the cage to encapsulate drug molecules or by functionalising the surface for drug delivery and imaging agents [20,21]. Furthermore, the subunits of these proteins dissociate at low pH 2.0 and re-associate at higher pH 7.0. This allows the potential construction of a hybrid cage protein through generating variant modifications in various subunits, mixing these subunits together and reassembling to form hybrid nanocages with novel functions [69,204–206].

This chapter focuses on the construction of hybrid cage proteins using either *Li*Dps or HuAft subunits as scaffolds to produce novel PDT and imaging agents.

Firstly, the *G*Luc and miniSOG proteins were fused to the N-terminal of the *Li*Dps subunit. Each of *G*Luc-*Li*Dps and miniSOG-*Li*Dps chimeric proteins were dissociated separately, combined in a 25:75, 50:50, and 75:25 molar ratio and reassembled to yield a *G*Luc-*Li*Dps:miniSOG-*Li*Dps hybrid cage protein. This hybrid cage protein was designed to

act as a PDT agent, where certain subunits possess *G*Luc for self-illumination and the others, carrying miniSOG, act as a photosensitiser. The activation of *G*Luc-*Li*Dps:miniSOG-*Li*Dps nanoparticles initiated by the excitation of miniSOG by the *G*Luc-emitted light to generate ROS (Figure 4.1). The utilisation of *Li*Dps as a scaffold for the binding of *G*Luc and miniSOG allowed the use of BRET as a monitoring system and consequently improved the ROS quantum yield. In addition cargo such as drug molecules can be carried inside the *Li*Dps protein cage, potentially allowing for complementary chemotherapy.

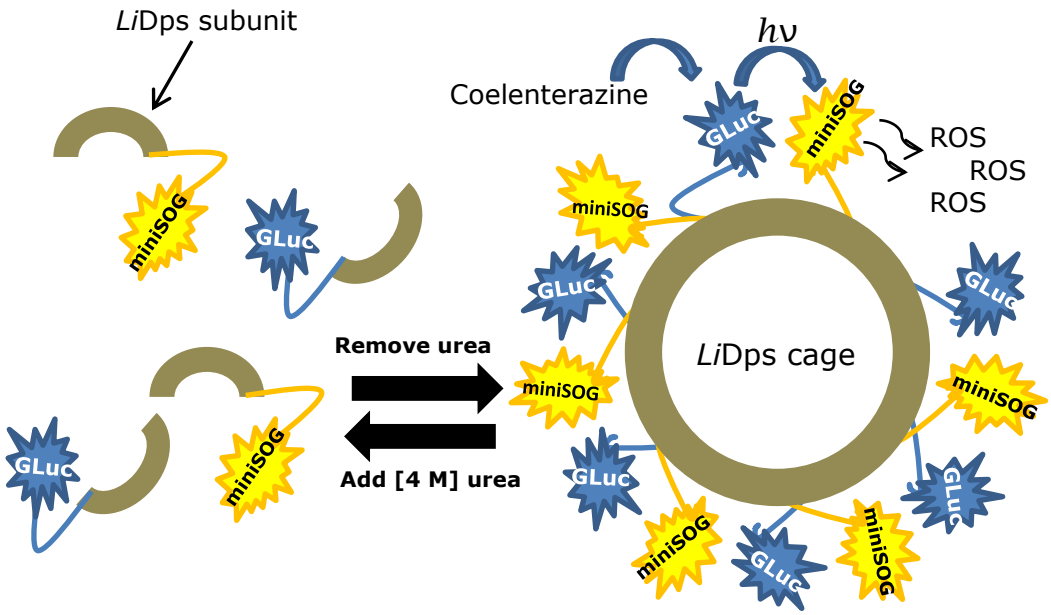


Figure 4.1: Cartoon representation of the assembly of a hybrid cage made from two different *Li*Dps fusions (miniSOG-*Li*Dps and *G*Luc-*Li*Dps) after the removal of urea. When the hybrid cage is formed, *G*Luc and miniSOG are placed in close proximity enabling BRET to take place and therefore improve its action as a PDT.

The second part of this chapter concentrates on the formation of another hybrid cage protein using HuAft subunits.

The N-termini of *Li*Dps and HuAft subunits are located on the exterior of the protein shell, whereas the C-terminal of HuAft (unlike the C-terminal of *Li*Dps) is located on the interior of protein cage. Due to the location of the C-terminus, Afb and miniSOG were fused to the N-terminal of the HuAft subunit ensuring that when cage formation occurs, Afb or miniSOG would be located on the outside of the HuAft protein cage.

Two different HuAft subunits were prepared by genetically fusing of either the miniSOG protein or the Afb to the N-terminal of HuAft. Thus Afb-HuAft:miniSOG-HuAft hybrid cage was composed of three proteins; HuAft (providing a scaffold), miniSOG fluorescent protein (acting as an imaging agent) and Afb, a protein that targets the receptor HER2 which is overexpressed on the surface of cancer cells. The Afb is a small protein that selectively binds to the HER2 transmembrane protein (Figure 4.2) [207]. This assists and enables the use of Afb for delivering drugs and imaging agents for targeting of HER2 overexpressed cancer cells [208]. Consequently, using this approach, the imaging agent or anticancer drugs would be delivered only to cancerous cells, limiting off-target side effects.

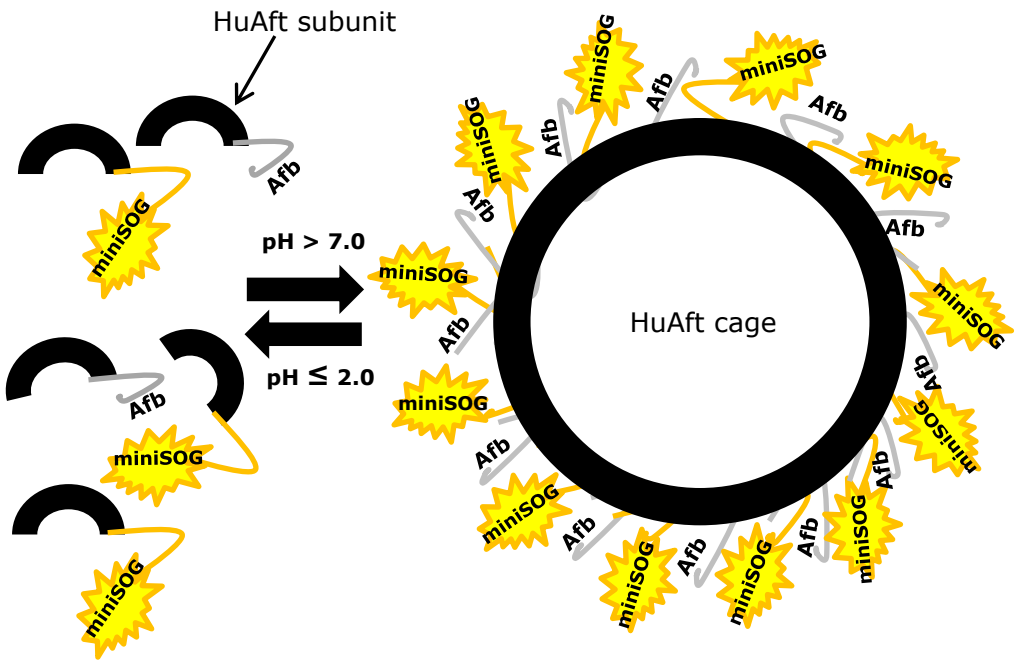


Figure 4.2: Cartoon representation of the dissociation and reassembly of miniSOG-HuAft and Afb-HuAft subunits through the changing of pH from 8.3 to 2.0 to form a hybrid cage protein.

Recently, several studies have been carried on the development of ferritin cages for drug delivery and an imaging agent such as encapsulating of PbS QDs [209], Gefitinib, a tyrosine kinase inhibitor [210] and Doxorubicin [211] for cancer treatment whereas encapsulation of Gd-HPDO3A as MRI contrast agent has been used for tumour imaging [48].

4.2 Results

4.2.1 Creation of the *G*Luc-*Li*Dps:miniSOG-*Li*Dps nanoparticles

4.2.1.1 Construction of a *G*Luc-*Li*Dps expression vector

The fabrication and characterisation of *G*Luc-*Li*Dps recombinant protein has been described in detail in Chapter 5.

4.2.1.2 Construction of a miniSOG-*Li*Dps expression vector

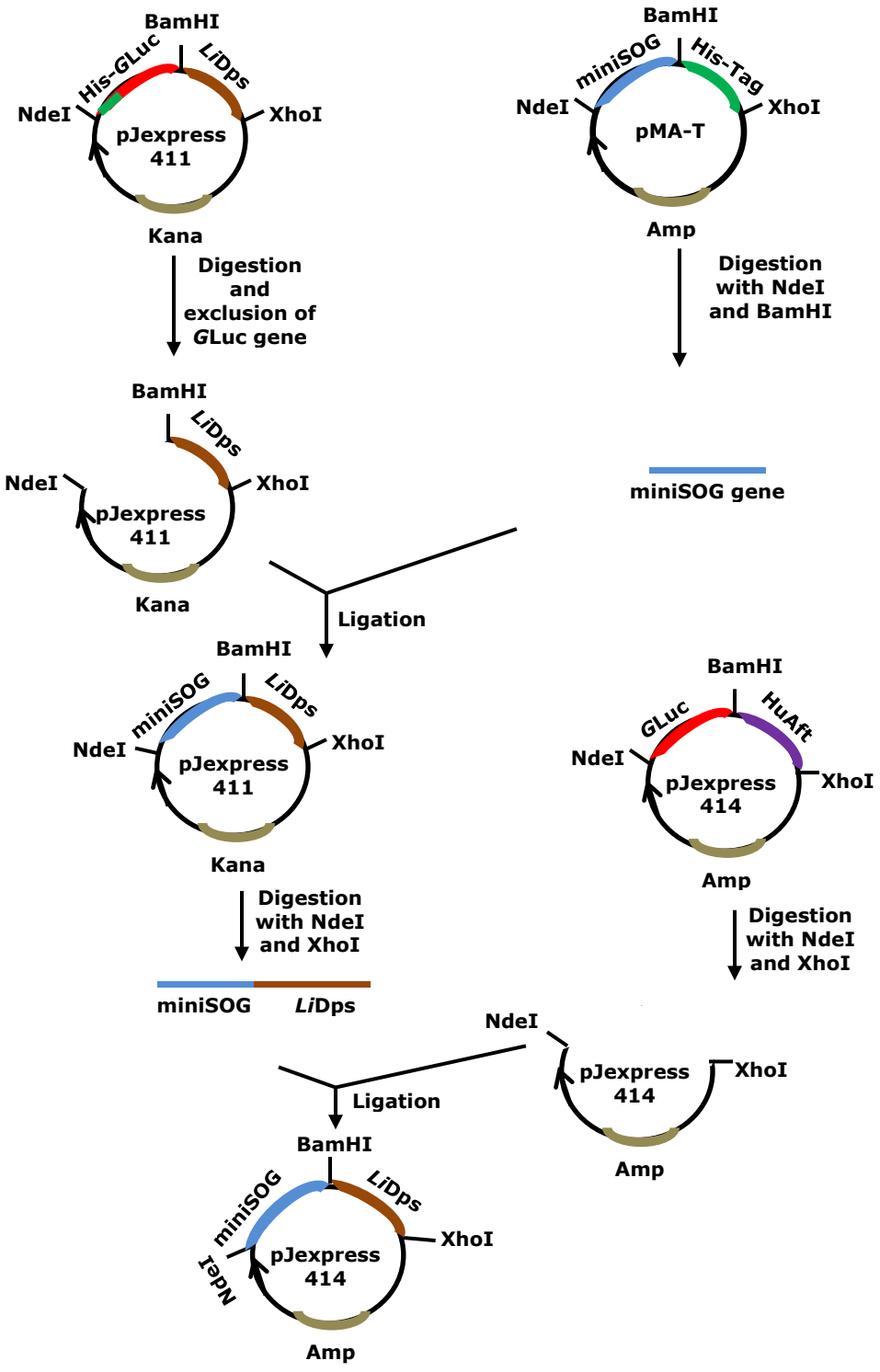
An *E. coli* vector (pJexpress411:*G*Luc-*Li*Dps) was used to express the *G*Luc-*Li*Dps chimeric protein. Along with the pMA-T:miniSOG vector it was used to construct the pJexpress411:miniSOG-*Li*Dps plasmid for the expression of the miniSOG–*Li*Dps chimeric protein.

The cloning strategy involved transferring the miniSOG gene from the pMA-T:miniSOG plasmid into the pJexpress411 plasmid by replacing *G*Luc in the *G*Luc-*Li*Dps construct. Both genes were located in frame as Nde1–BamH1 fragments in these vectors (Scheme 4.1). Excision of the miniSOG gene, using serial digestion of pMA-T:miniSOG with Nde1 and BamH1, produced a fragment that could be directly ligated into the NdeI–BamHI digested pJexpress411:*G*Luc-*Li*Dps plasmid. The miniSOG gene from the digestion of pMA-T:miniSOG and the vector backbone from pJexpress411:*G*Luc-*Li*Dps were isolated and then purified as described in section 2.1.2.3. Ligation of the purified DNA

fragments as described in section 2.1.2.4, and transformation as described in section 2.1.5, resulted in plates of antibiotic resistant *E. coli* colonies, many of which possessed the desired pJexpress411miniSOG-*Li*Dps plasmid.

Furthermore, an *E. coli* pJexpress414:miniSOG-*Li*Dps vector was prepared by transferring the miniSOG-*Li*Dps gene from pJexpress411:miniSOG-*Li*Dps to pJexpress414:39732–*G*Luc plasmids (for expression of *G*Luc-HuAft, Appendix 10.3). Digestion was performed with Nde1 and Xho1, as both genes were located in frame as Nde1–Xho1 fragments in these vectors (Scheme 4.1).

A PCR screen was performed to identify colonies with pJexpress411:miniSOG-*Li*Dps using miniSOG forward and *Li*Dps reverse primers (Appendix 10.2). Agarose gel electrophoresis showed the colonies 4 to 13 carried the miniSOG-*Li*Dps gene with a size around of 800 bp (Figure 4.3). Similarly, colonies with pJexpress414:miniSOG-*Li*Dps were tested through a PCR screen with *G*Luc-HuAft and miniSOG-*Li*Dps genes as a negative and positive control, respectively. Agarose gel electrophoresis demonstrated that colonies 5, 12 and 13 carried pJexpress414:miniSOG-*Li*Dps (Figure.4.3).



Scheme 4.1: Schematic showing the preparation of pJexpress411:miniSOG-*Li*Dps plasmid and pJexpress414:miniSOG-*Li*Dps using pMA-T:miniSOG, pJexpress411:*G*Luc-*Li*Dps and pJexpress414: 39732–*G*Luc plasmids.

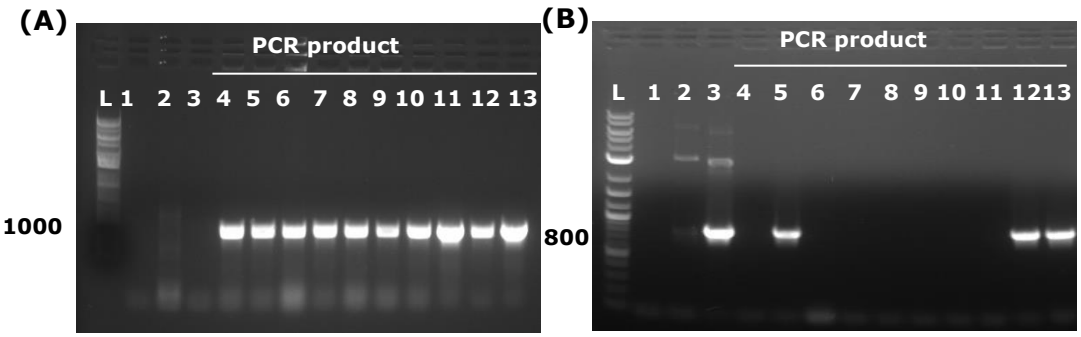
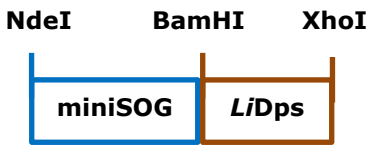


Figure 4.3: PCR screening on 1% (w/v) agarose gel. **(A)** PCR screen of the pJexpress411:miniSOG-*Li*Dps plasmid. DNA MW ladder (L), H_2O (1), miniSOG (2) & *G*Luc-*Li*Dps (3) (negative control), and PCR colony product (4-13). **(B)** pJexpress414:miniSOG-*Li*Dps plasmid. DNA MW ladder (L), H_2O (1), *G*Luc-HuAft (2) (negative control), miniSOG-*Li*Dps (3) (positive control), and PCR colony product (4-13).

The plasmids yielding positive results from the PCR screen were extracted from the colonies and sent for sequencing. The amino acid sequence and the predicted properties of miniSOG-*Li*Dps without its FMN cofactor are described in Figure 4.4 and Table 4.1, respectively.

(A)



(B)

1 MAEKSFVITDPRLPDNPIIFASDGFLELTE YSR EEIL GR NGRFLQGPETD

51 QATVQKIRDAIRDQREITVQLINYTKSGKKFWNLLHLQPMRDQKGELQYF

101 IGVQLDGSMKTINSVDTKEFLNHQVANLNVFTVKIHQIHWYMRGHNFFTL

151 HEKMDDLYSEFGE QMDEVAERLLAIGG SPFSTLKEFLENASVEEAPYTKP

201 KTMDQLMEDLVGTLELLRDEYQQGIELTDKEGDNVTNDMLIAFKASIDKH

251 IWMFKAFLGKAPLE

Figure 4.4: (A) The miniSOG-*Li*Dps gene map. **(B)** The primary amino acid sequence of the miniSOG-*Li*Dps chimera. MiniSOG (red) and C-terminal *Li*Dps protein (blue) comprises the sequence.

No. of residues	MW (Da)	Theoretical pI	Molar Extinction coefficient (M/cm) at 280 nm
264	30,516	4.97	26,930

Table 4.1: Theoretical physical properties of the miniSOG-*Li*Dps without its FMN cofactor.

4.2.1.3 Expression and purification of miniSOG-*Li*Dps protein

Initially, miniSOG-*Li*Dps was designed to include an N-terminal His-Tag, permitting Ni-IMAC purification. However, attempts to purify the protein using this approach resulted in loss of the FMN cofactor that is essential for miniSOG activity. Consequently, the His-Tag was removed, though this was to the detriment of protein solubility (Figure 4.5 A) with the overwhelming majority of the protein being expressed

within inclusion bodies. This issue was overcome by changing the growth and expression media from LB (supplemented with 0.5 M NaCl, 20% w/v glucose) to M9 minimal media at 20 °C overnight, resulting in a soluble protein (Figure 4.5 B). After induction with IPTG, the expression culture and subsequent pellets were protected from light in order to prevent miniSOG producing ROS.

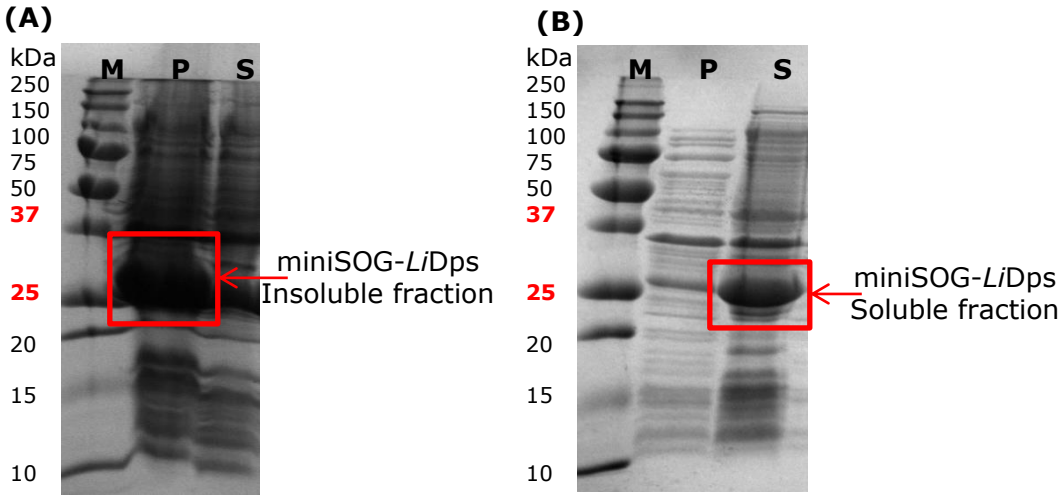


Figure 4.5: SDS-PAGE gels showing **(A)** the expression of miniSOG-*Li*Dps protein in LB medium as an inclusion body and **(B)** the expression of miniSOG-*Li*Dps protein in M9 medium in soluble form. Lane M = marker, lane S = soluble fraction, and lane P = insoluble fraction.

The protein sample was purified using ammonium sulfate precipitation and anion exchange purification as described in sections 2.2.1 and 2.2.2. It was found that miniSOG-*Li*Dps precipitated at 30% (w/v) ammonium sulfate. Fractions were applied to HiTrap desalting columns (GE healthcare/Amersham) to remove excess salt and the elution fractions identified using SDS-PAGE (Figure 4.6).

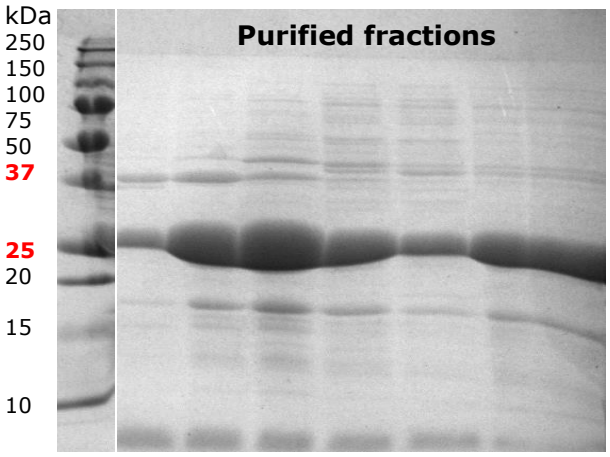


Figure 4.6: SDS-PAGE gel for miniSOG-*Li*Dps recombinant protein showing the purified fractions of miniSOG-*Li*Dps using anion exchange purification.

Fractions were pooled and further purified using a SEC column (HiLoad 16/60, Superdex 75 Prep grade), and analysed using SDS-PAGE. Purified miniSOG-*Li*Dps protein was yellow in the colour and when excited by UV light, emitted a green light (Figure 4.7).

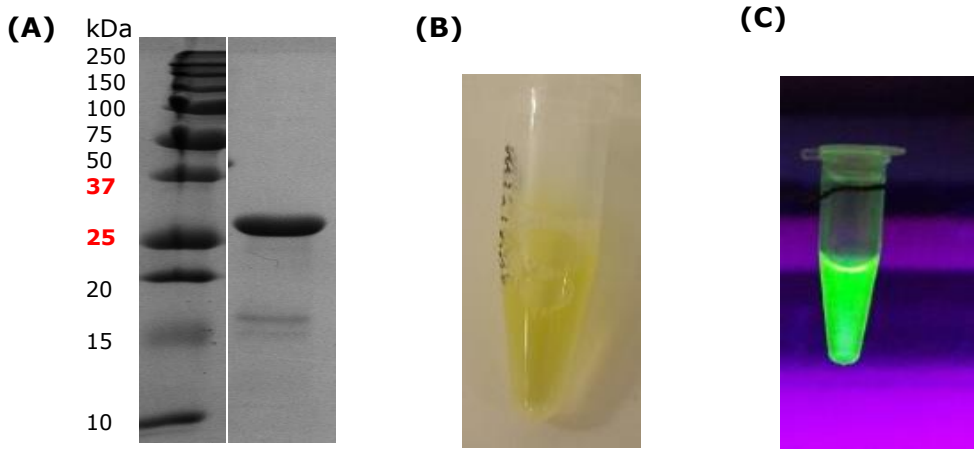


Figure 4.7: (A) SDS-PAGE gel of miniSOG-*Li*Dps purified using a size exclusion column. **(B)** MiniSOG-*Li*Dps protein displaying a yellow appearance in ambient light. **(C)** Fluorescent green light of miniSOG-*Li*Dps when excited with UV light (λ_{ex}=300-400 nm).

The protein was analysed using native PAGE electrophoresis to demonstrate its ability to form the cage structure. Before staining, the gel was placed on a UV light box for imaging and excited by UV light. The emitted light was captured and the native PAGE gel was then stained (Figure 4.8).

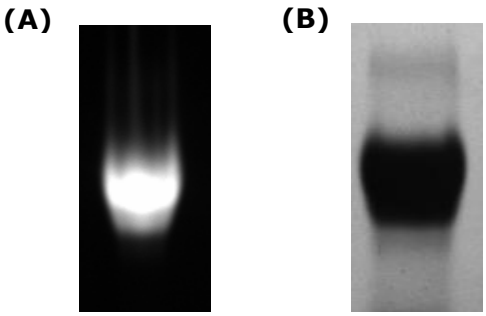


Figure 4.8: Native PAGE of miniSOG-*Li*Dps. **(A)** Before gel staining and under UV light (λ_{ex}=300-400 nm). **(B)** After gel staining with Coomassie Brilliant Blue R-250.

Furthermore, the mass of miniSOG-*Li*Dps was identified by denatured nESI-MS and compared with its theoretical MW (Figure 4.9).

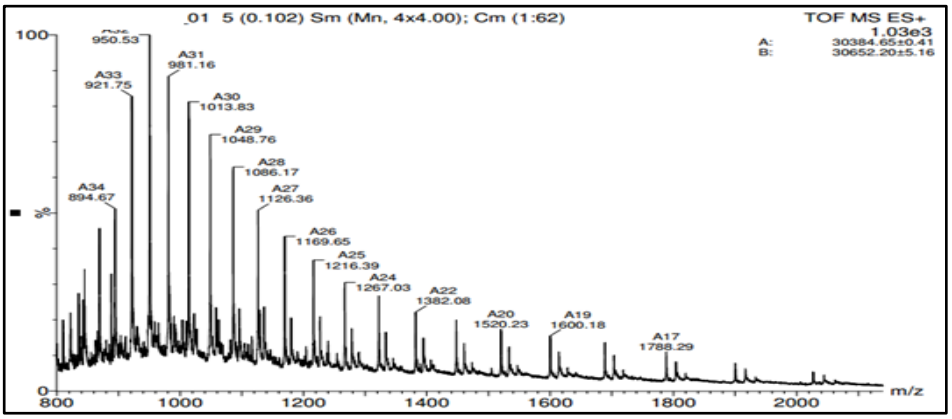


Figure 4.9: The nESI-MS showing that the MW of miniSOG-*Li*Dps subunit without its FMN cofactor is 30,385 Da.

nESI-MS indicates that the mass of miniSOG-*Li*Dps subunit without its FMN cofactor is 30,385 Da compared to its theoretical mass of 30,516 Da (calculated using software available online (http://web.expasy.org/protparam/)), suggesting that the N-terminal methionine (131 Da) was lost during expression, a well-known phenomenon in *E. coli* (Table 4.2).

	Theoretical mass (Da)	**Experimental mass (nESI) (Da)**	**Deviation (Da)**
miniSOG-*Li*Dps	30,516	30,385	131

Table 4.2: The theoretical and measured mass of miniSOG-*Li*Dps protein without its FMN cofactor.

4.2.1.4 Fabrication of *G*Luc-*Li*Dps:miniSOG-*Li*Dps nanoparticles

Two plasmids of pJexpress411:*G*Luc-*Li*Dps and pJexpress414:miniSOG-*Li*Dps were transformed into one BL21 (DE3) *E. coli* and expressed simultaneously. Despite these plasmids being incompatible (plasmids carrying the same replicon), the proteins were successfully expressed in inclusion bodies. In order to express the protein in soluble form, the IPTG concentration was reduced from 1 to 0.7 mM and the culture was incubated overnight at 20 ºC in the presence of 20% (w/v) glucose and 0.5 M NaCl. MiniSOG-*Li*Dps protein was expressed as a soluble protein, though *G*Luc-*Li*Dps remained in an insoluble form (Figure 4.10).

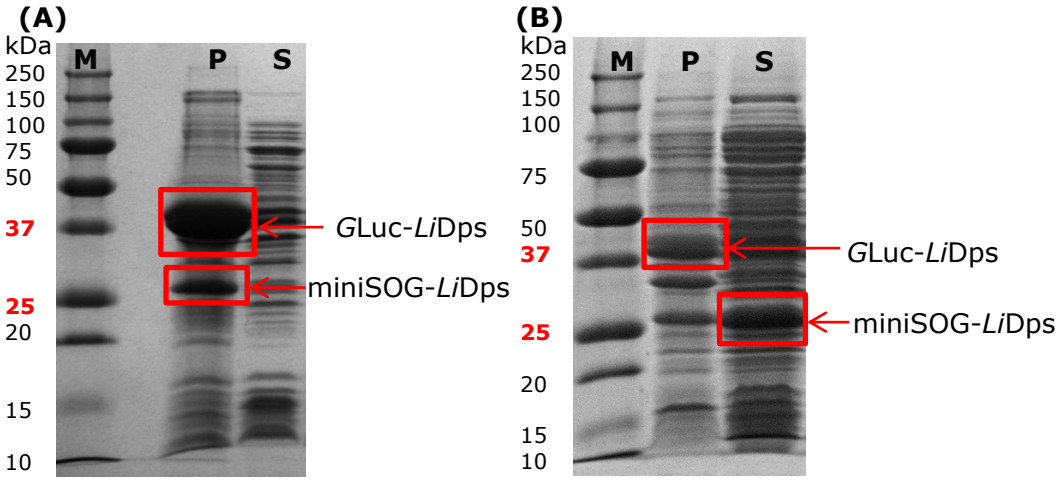


Figure 4.10: SDS-PAGE gel of *G*Luc-*Li*Dps and miniSOG-*Li*Dps, where Lane M = marker, lane S = soluble fraction, and lane P = insoluble fraction. Gel **(A)** shows that these proteins were expressed in an insoluble form. Gel **(B)** demonstrates miniSOG-*Li*Dps was expressed in soluble form while *G*Luc-*Li*Dps was still in an insoluble form.

As a consequence of the difficulties in expressing these proteins simultaneously in the same flask in soluble form, they were instead expressed separately.

To construct hybrid cages, separate preparations of both *G*Luc-*Li*Dps and miniSOG-*Li*Dps cages were firstly disassembled using 4 M urea. The dissociated subunits were mixed at molar ratio of 25:75, 50:50, and 75:25 of *G*luc-*Li*Dps:miniSOG:*Li*Dps and reassembled by slowly removing the urea using dialysis method (Section 2.6).

Different techniques were performed to study the hybrid cage formation, including native agarose gel electrophoresis, SEC, analytical ultracentrifugation (AUC), native ESI-MS and DLS.

The native agarose gel showed that the hybrid cages were smaller in size than the *G*Luc-*Li*Dps and miniSOG-*Li*Dps protein cages suggesting the incomplete formation of 12-mer cages (Figure 4.11).

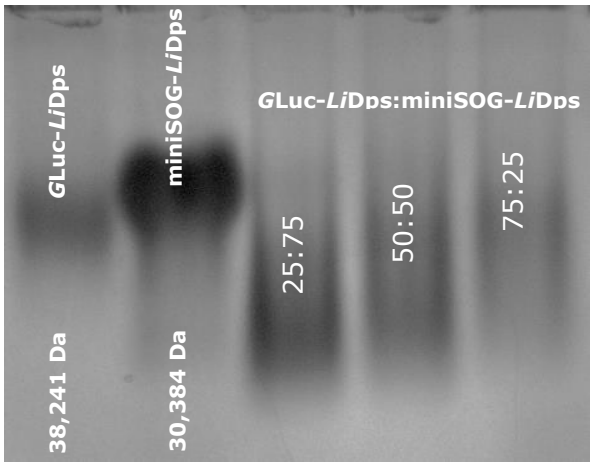


Figure 4.11: Native agarose gel. The *G*Luc-*Li*Dps and miniSOG-*Li*Dps homo cages and the 25:75, 50:50, 75:25 *G*Luc-*Li*Dps:miniSOG-*Li*Dps hybrid cages were loaded onto 0.5% (w/v) agarose gel and transferred at 100 V.

The migration of the protein through the native agarose gel depends on its size and charge. Therefore the fact that migration of the hybrid cages faster than the wild type protein might be due to the changes in both size and charge.

In contrast, the DLS results suggested that the formation of hybrid cages using 25:75, 50:50, and 75:25 *G*Luc-*Li*Dps:miniSOG-*Li*Dps was in the expected sizes (i.e. the hybrid cages vary in size between the *G*Luc-*Li*Dps and miniSOG-*Li*Dps) (Table 4.3).

Protein		DLS size (nm)	SD	MW of protein cage (kDa) experimental	MW of protein subunit (kDa) Theoretical	No. of subunit
***G*Luc-*Li*Dps**		18.88	0.81	458.9	38.2	12
miniSOG-*Li*Dps		15.00	0.36	364.6	30.3	12
25:75	***G*Luc-*Li*Dps: miniSOG-*Li*Dps**	16.26	0.34	395.2	32.3	12
50:50		16.99	0.34	412.9	34.3	12
75:25		18.39	0.85	447.0	36.2	12

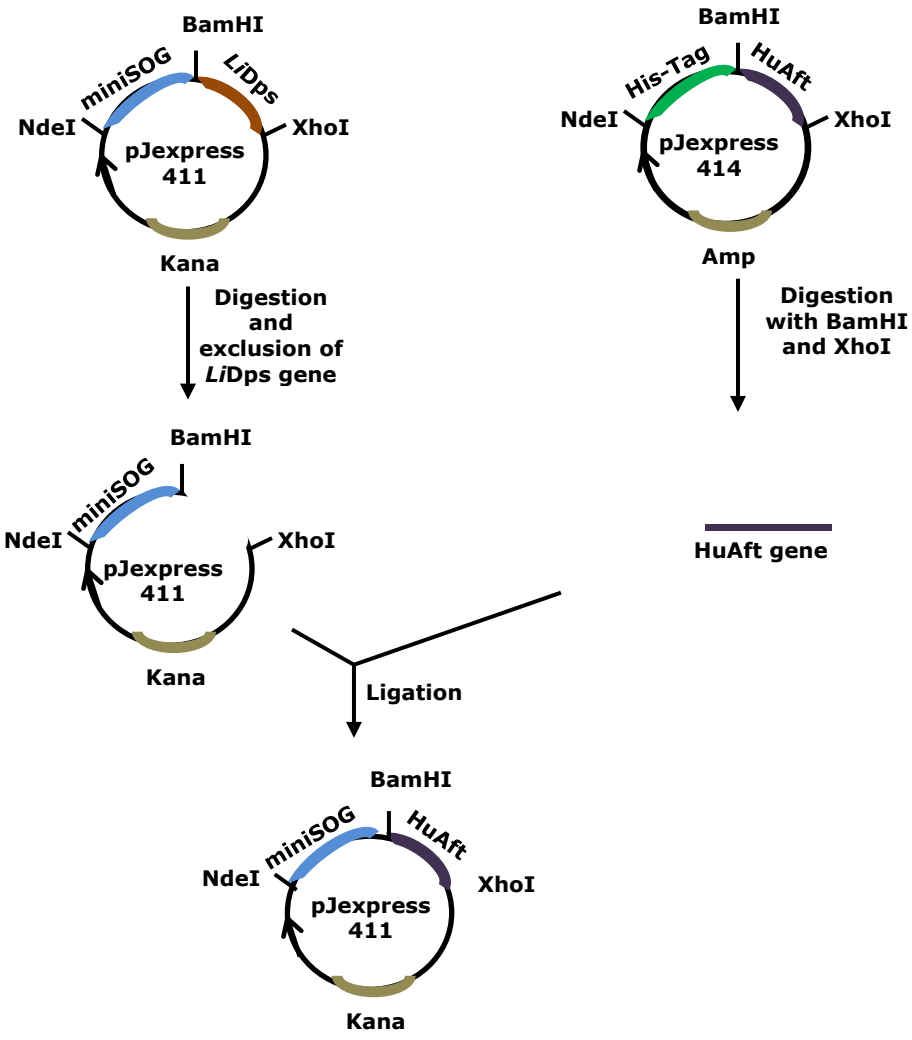
Table 4.3: The size of the *G*Luc-*Li*Dps, miniSOG-*Li*Dps, and hybrid cages determined using DLS.

The heterogeneity in the subunits of the protein cage makes it sensitive and unstable for many conditions Therefore these protein assemblies were sedimented using the AUC method, resulting in a range of masses as determined by native ESI-MS, and did not clearly separate according to their MW with the SEC method.

4.2.2 Creation of Afb-HuAft:miniSOG-HuAft nanoparticles

4.2.2.1 Construction of a miniSOG-HuAft expression vector

An *E. coli* vector for the expression of miniSOG-HuAft was constructed by serial digestion of pJexpress414:HuAft and pJexpress411:miniSOG-*Li*Dps (Appendix 10.3). BamHI and XhoI were utilised to transfer the HuAft gene from pJexpress414:HuAft into pJexpress411:miniSOG-*Li*Dps with the loss of the *Li*Dps gene (Scheme 4.2). After purification, the HuAft gene was ligated with pJexpress411 and the product was used to transform DH5α *E. coli.* The resulting colonies thought to contain pJexpress411:miniSOG-HuAft were analysed with a PCR screen.



Scheme 4.2: Schematic showing the preparation of pJexpress411:miniSOG-HuAft plasmid using pJexpress411:miniSOG-*Li*Dps and pJexpress414:HuAft plasmids.

A reverse primer specific for *Li*Dps, along with T7 forward primers was used in the PCR screen, meaning that colonies that are carrying the desired gene do not produce a band on the agarose gel. The gel shows that all PCR samples excluding 7, 8 and 11 samples are harbouring the correct gene (Figure 4.12).

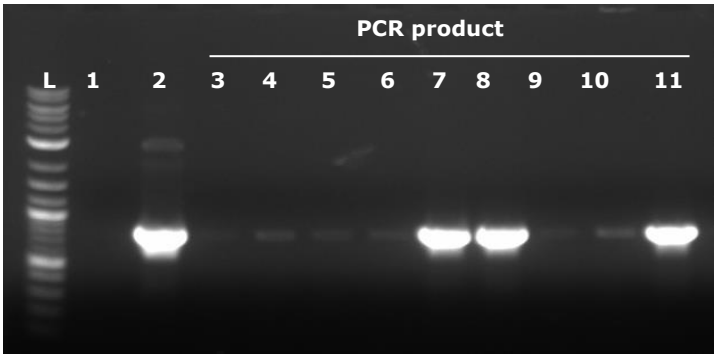
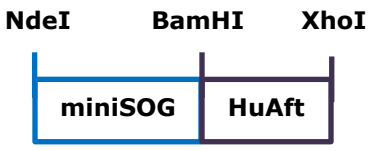


Figure 4.12: PCR screen for pJexpress411:miniSOG-HuAft vector on 1% (w/v) agarose gel using miniSOG forward and *Li*Dps reverse primers. DNA MW ladder (L), H_2O (1) (negative control), pJexpress411:miniSOG-*Li*Dps (2) and PCR products (3-11). The gel illustrates that the desired plasmid samples did not appear on the band corresponding to the positive control.

The cultures derived from miniSOG-HuAft colonies were chosen as candidates that could harbour pJexpress411: miniSOG-HuAft and were employed to prepare plasmid DNA that was sent for DNA sequencing (Figure 4.13). In addition, the physical properties of the miniSOG-HuAft protein without its FMN cofactor were calculated using software (http://web.expasy.org/protparam/) and are listed in Table 4.4.

(A)



(B)

1 MAEKSFVITDPRLPDNPIIFASDGFLELTE YSR EEIL GR NGRFLQGPETD

51 QATVQKIRDAIRDQREITVQLINYTKSGKKFWNLLHLQPMRDQKGELQYF

101 IGVQLDGSMTTASTSQVRQNYHQDSEAAINRQINL ELYASYVYLSMSYYF

151 DRDDVALKNFAKYFLHQSHEEREHAEKLMKLQNQRGGRIFLQDIKKPDCD

201 DWESGLNAMECALHLEKNVNQSLLELHKLATDKNDPHLCDFIETHYLNEQ

251 VKAIKELGDHVTNLRKMGAPESGLAEYLFDKHTLGDSDNES

Figure 4.13: (A) The miniSOG-HuAft gene map. **(B)** The primary amino acid sequence of the miniSOG-HuAft chimera. An N-terminal miniSOG (red) and C-terminal HuAft protein (blue) is present in the sequence.

No. of residues	MW (Da)	Theoretical pI	Molar Extinction coefficient (M/cm) at 280 nm
291	33,694	5.32	29,005

Table 4.4: Theoretical physical properties of the miniSOG-HuAft polypeptide without its FMN cofactor.

4.2.2.2 Expression and purification of miniSOG-HuAft protein

The miniSOG-HuAft protein was expressed in LB medium in insoluble form. Urea (4 M) was utilised to solubilise the protein which was subsequently purified under denaturing conditions using HiTrap Q HP anion exchange chromatography as described in section 2.2.3. After ammonium sulfate precipitation, the fractions were loaded onto HiTrap desalting column, and pooled to subject to SEC (HiLoad 16/60, Superdex 75 Prep grade). The purified sample was assessed using SDS-PAGE (Figure 4.14).

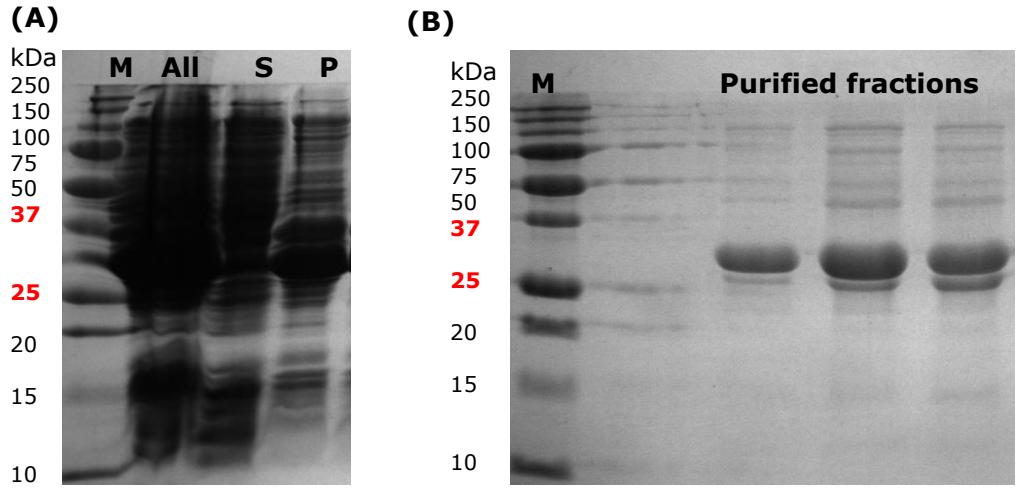


Figure 4.14: SDS-PAGE gels of miniSOG-HuAft. **(A)** The gel showing miniSOG-HuAft expressed in an insoluble form. M = marker, S = soluble, and P = insoluble fractions. **(B)** Eluted fractions of miniSOG-HuAft after SEC and anion exchange purification.

Denaturation of miniSOG-HuAft with 4 M urea led to loss the protein cofactor (FMN). To overcome this issue miniSOG-HuAft was dialysis with Tris buffer containing of 1 mM of FMN (20 mM Tris pH 8.3, 1 mM FMN), wherein the miniSOG-HuAft uptake the FMN when its refolding during removing the urea. miniSOG-HuAft was loaded onto native PAGE and compared with miniSOG-*Li*Dps protein (Figure 4.15).

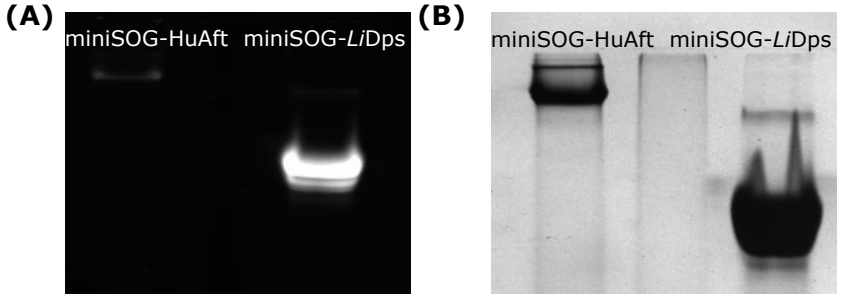


Figure 4.15: Native PAGE gels of miniSOG-HuAft and miniSOG-*Li*Dps. **(A)** Before gel staining and under UV light (λ_{ex}=300-400 nm). **(B)** After gel staining with Coomassie Brilliant Blue R-250.

4.2.2.3 Expression and purification of Afb-HuAft

E. coli BL21 cells transformed with pJexpress411:Afb-HuAft vector (created by Dr L. Zhang, University of Nottingham) were used for large-scale expression of the Afb-HuAft protein (Figure 4.16). The predicted physical properties of the expressed Afb-HuAft protein are outlined in Table 4.5.

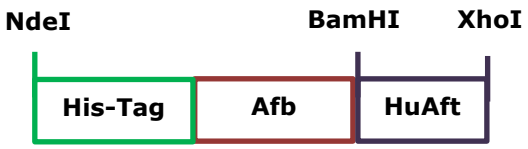


Figure 4.16: The Afb-HuAft recombinant protein gene map.

No. of residues	MW (Da)	Theoretical pI	Molar Extinction coefficient (M/cm) at 280 nm
270	30,756	6.04	27,390

Table 4.5: Theoretical physical properties of the Afb-HuAft polypeptide.

Afb-HuAft was purified under denaturing conditions using Ni-IMAC as described in section 2.2.2. Fractions were dialysed, pooled and subsequently loaded onto an SEC column (HiLoad 16/60, Superdex 75 Prep grade) (Figure 4.17).

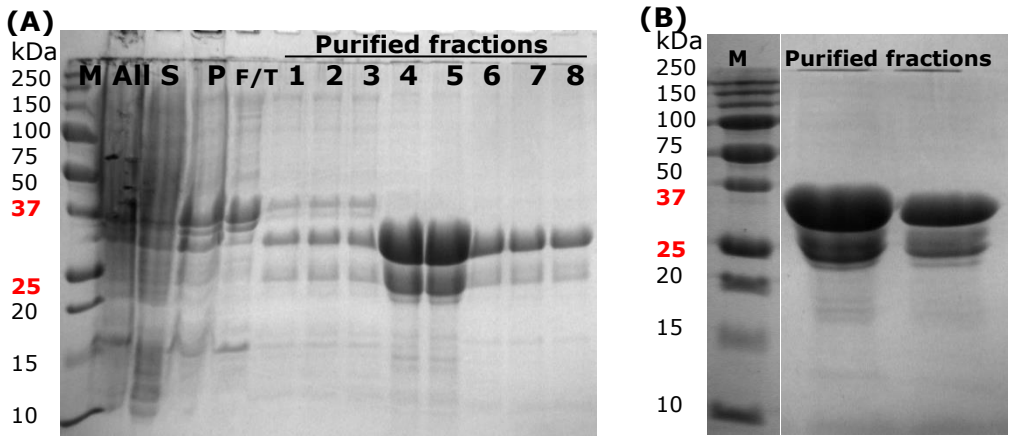


Figure 4.17: SDS-PAGE gels of Afb-HuAft. **(A)** The gel showing that the Afb-HuAft was expressed in an insoluble form; M = marker, All = the whole lysate, S = soluble, P = insoluble fractions, F/T = flow-through and 1 to 8 = fractions purified using Ni-IMAC. **(B)** Eluted fractions of Afb-HuAft with SEC.

The MW of Afb-HuAft was confirmed usin denatured MALDI-TOF MS (Figure 4.18).

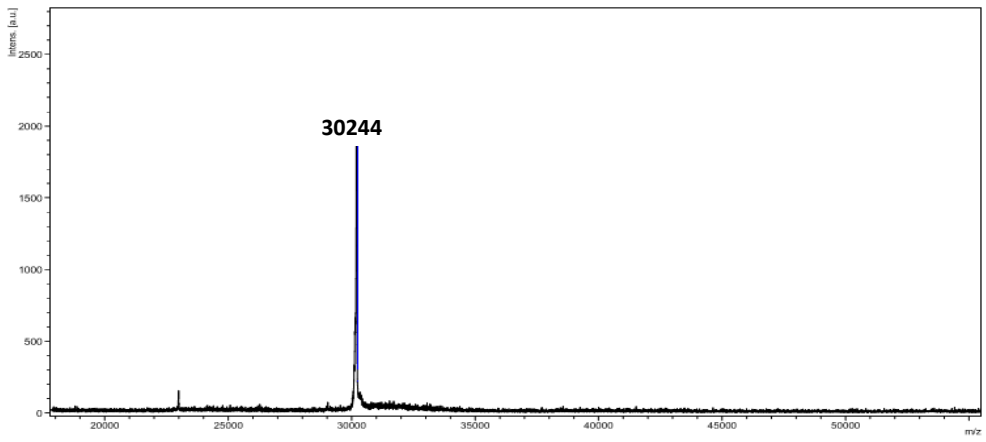


Figure 4.18: MALDI-TOF MS shows that the MW of Afb-HuAft is 30,244 Da.

The measured mass of Afb-HuAft was close to its theoretical mass (Table 4.6).

	Theoretical mass (Da)	**Experimental mass (MALDI-TOF) (Da)**	**Deviation (Da)**
Afb-HuAft	30,756	30,244	512

Table 4.6: The theoretical and measured mass of Afb-HuAft Protein.

4.2.2.4 Fabrication of Afb-HuAft:miniSOG-HuAft nanoparticles

Afb-HuAft and miniSOG-HuAft protein cages were dissociated by slowly reducing the pH of the solution to 2.0. Reassembly of protein subunits was accomplished by elevating the pH from 2.0 to 8.3 at molar ratio of 25:75, 50:50, and 75:25 of Afb-HuAft:miniSOG-HuAft (Section 2.6). The difference in the mass between the produced hybrid protein cages was examined using different techniques, including native gel electrophoresis, DLS, AUC, native ESI-MS, and SEC.

Afb-HuAft:miniSOG-HuAft, similar to *G*Luc-*Li*Dps:miniSOG-*Li*Dps, was sedimented following analysed using AUC and yielding inconclusive mass with nESI-MS and DLS. The results with the SEC column (Superdex 200 10/300 GL) and native PAGE gel indicates that only partial hybrid cages were formed, with these being only cages smaller than Afb-HuAft and miniSOG-HuAft (see Figure 4.19 and Table 4.7).

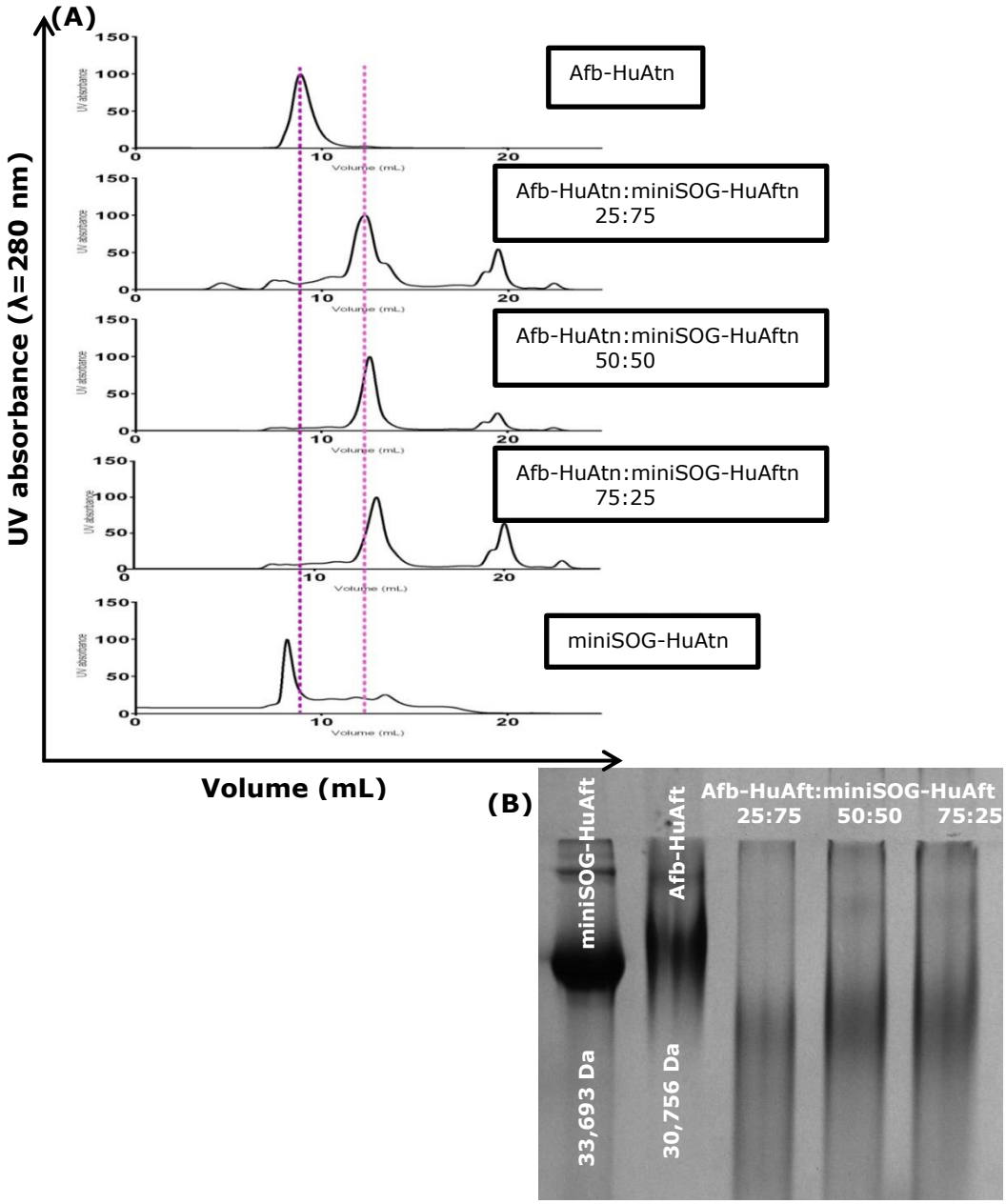


Figure 4.19: (A) Size exclusion elution profiles of hybrid protein cages at 25:75, 50:50, and 75:25 Afb-HuAft:miniSOG-HuAft ratios with the homo protein cages of Afb-HuAft and miniSOG-HuAft. Samples were loaded after reassembly into the size exclusion column. **(B)** Native PAGE of homo and hybrid protein cages.

Protein		Retention volume (mL)	MW of protein cage (kDa)	MW of protein subunit (kDa)	No. of subunits
Afb-HuAft		8.821	738.6	30.775	24
miniSOG-HuAft		8.155	808.7	33.693	24
25:75	**Afb-HuAft:miniSOG-HuAft**	12.307	492.7	32.963	15
50:50		12.583	472.4	32.324	15
75:25		12.791	457.1	31.504	15

Table 4.7: The MW of homo and hybrid protein cages calculated from the retention volume of the size exclusion column.

4.3 Discussion

The self-assembly of HuAft and *Li*Dps into hollow nanocages make them attractive candidates for use as drug or imaging agent delivery systems. In this study, the subunits of both HuAft and *Li*Dps proteins were genetically modified with other proteins to generate a novel *G*Luc-*Li*Dps:miniSOG-*Li*Dps PDT agent and an Afb-HuAft:miniSOG-HuAft imaging agent.

4.3.1 *G*Luc-*Li*Dps:miniSOG-*Li*Dps hybrid protein

*Li*Dps subunits were successfully fused with *G*Luc and miniSOG protein to produce *G*Luc-*Li*Dps and miniSOG-*Li*Dps recombinant proteins. It was noticed that the fusing of a His-Tag on the N-terminal of miniSOG-*Li*Dps led to the expression of this protein without its FMN cofactor. This might be due to the effect of the His-Tag on the binding site of miniSOG that effect on the structure and consequently interferes with the binding of FMN with miniSOG. This suggested that the His-Tag in some way interfered with or changed the conformation of the FMN binding site within miniSOG. The effect of His-Tag on the ability of protein to bind with the ligands/cofactor has been reported for a number of proteins leading to protein aggregation or changing its solubility [212]. Consequently, miniSOG-*Li*Dps was expressed without a His-Tag, permitting miniSOG to bind FMN. This gave the protein a characteristic yellow colour which could even be observed in the pelleted cells after expression. The MW of miniSOG-*Li*Dps was determined using nESI-MS and the result indicates that the N-terminal methionine (131 Da) was removed during miniSOG-*Li*Dps expression a post-translation process [199].

In order to express *G*Luc-*Li*Dps:miniSOG-*Li*Dps hybrid cages, the plasmids that are carrying of *G*Luc-*Li*Dps and miniSOG-*Li*Dps genes must be transformed in one *E. coli*. It has been reported that the incompatible plasmid, plasmids carrying the same replicon, cannot co-

exist stably in one *E. coli* unless they harbour different antibiotic resistant genes [213]. Therefore the co-transformation of pJexpress411:*G*Luc-*Li*Dps (with kanamycin resistance) and pJexpress414:miniSOG-*Li*Dps (with ampicillin resistance) plasmids in BL21 *E. coli* and the expression of both of *G*Luc-*Li*Dps and miniSOG was successfully performed. However, there is a hurdle relating to the recovery of these two proteins as a functionally-active hybrid cage because of the difficulty expressing soluble *G*Luc-*Li*Dps. The presence of five disulfide bonds in *G*Luc contributes to its insolubility, even when applying hard expression conditions that improved the solubility of miniSOG-*Li*Dps. Consequently, *G*Luc-*Li*Dps and miniSOG-*Li*Dps were expressed separately and later mixed to form hybrid cages.

Both *G*Luc-*Li*Dps and miniSOG-*Li*Dps were dissociated to their subunits using 4 M urea. The *Li*Dps quaternary structure is extremely stable and dissociation begins to take place only at pH 1.5 to produce very stable dimers that further dissociate to monomers at pH 1.0 [205]. To ensure that all the modified *Li*Dps subunits are completely dissociated and because of the protein cages resistance to variations in pH, the subunits of *G*Luc-*Li*Dps and miniSOG-*Li*Dps were treated with 4 M urea rather than decreasing pH. Here urea denatured both *G*Luc-*Li*Dps and miniSOG-*Li*Dps which were then mixed together in defined molar ratios. By gradually removing urea through dialysis, both proteins were able to refold and form the *G*Luc-*Li*Dps:miniSOG-*Li*Dps.

The DLS technique indicates that the *G*Luc-*Li*Dps:miniSOG-*Li*Dps hybrid cages were produced with twelve subunits, however native agarose gel electrophoresis showed that the hybrid cages formed partial cage in sizes smaller than *G*Luc-*Li*Dps and miniSOG-*Li*Dps. This might be because of the migration of proteins on the native agarose gel depend on both the charge and the size of the protein. The large size and the heterogeneity of the *G*Luc-*Li*Dps:miniSOG-*Li*Dps hybrid cages might make them unstable to study using different techniques. This was noticed in the precipitation and aggregation of these proteins when they were measured using AUC and the multiple peaks with high noisy resulted from ESI-MS. It has been reported that there is a challenge for the analysis of the protein assemblies (intact protein) using ESI-MS. This is because the hardness of protein assemblies to deposition successfully on a surface in the vacuum of the ESI-MS without significant distortion of their structure [214]. The small size of *Li*Dps compared to other ferritin family members permits modification of its subunits and refolding in the active form, and this was observed when *G*Luc activity was recovered directly after fusion on the N-terminal of *Li*Dps subunits while *G*Luc lost its activity when fused with HuAft, possibly a consequence of the large size of HuAft affecting protein refolding. The *G*Luc-*Li*Dps:miniSOG-*Li*Dps construct requires more studies to optimise its function as a PDT and imaging agents.

4.3.2 Afb-HuAft:miniSOG-HuAft hybrid protein

The second part of this chapter discussed the formation of the Afb-HuAft:miniSOG-HuAft hybrid cage. After expression and purification of Afb-HuAft and miniSOG-HuAft the mass of the protein was characterised using MALDI-TOF-MS. The results show that there is around 500 Da difference between the theoretical and the experimental mass of Afb-HuAft. The cleavage of N-terminal methionine, post-translation modification, and the high MW of these proteins might be contributed in the mass deviation using MALDI-TOF-MS. It was noticed that the mass of miniSOG-*Li*Dps (Figure 4.9) and *G*Luc-*Li*Dps (Figure 5.5), which were detected using nESI-MS, were more accurate than the masses of other proteins which were prepared in this study and detected using MALDI-TOF-MS. This may be because the difference in the protein ionisation between these two methods. However both of MALDI-TOF and ESI mass spectrometry use soft-ionisation of proteins, ESI is considered more convenient for determination of high protein masses. This issue was experimentally confirmed using standard proteins with different masses. It was found that there were deviations in the determined masses. BSA protein (66,500 Da) reveals a range of masses when its subjected to MALDI-TOF-MS analysis. MALDI-TOF-MS also showed noise peaks that were associated with BSA analysis. BSA analysis provides two distinct peaks with 9 and 23 kDa, see Table 3.3, Figure 3.7 and Section 3.3. Unlike *G*Luc-*Li*Dps:miniSOG-*Li*Dps, the formation of Afb-HuAft:miniSOG-

HuAft was accomplished by slowly reducing the pH to 2.0 using a glycine buffer to dissociate the subunits of Afb-HuAft and miniSOG-HuAft. These subunits reassembled to form an Afb-HuAft:miniSOG-HuAft hybrid cage by gradually increasing the pH to 8.3 by dialysing against Tris buffer.

The native PAGE and SEC results indicated that the number of subunits of the Afb-HuAft:miniSOG-HuAft hybrid cages are less than 24 as shown in the native HuAft cages (according to SEC calculation, the Afb-HuAft:miniSOG-HuAft hybrid cage possess ~15 subunits) and this might be because of the large size of these subunits preventing the reassembly/refolding into the correct form. Also, the surface charge of these subunits may contribute to repulsion between the fused proteins and lead to the formation of a smaller or partial cage. This construct requires more study to confirm the final structure of the Afb-HuAft:miniSOG-HuAft hybrid cage and the actual reasons for the formation of the cage into a smaller size than Afb-HuAft and miniSOG-HuAft. Additionally, the activity of this construct need to evaluated *in vitro* and *in vivo*

Chapter 5

5. Preparation and chemical modification of *G*Luc-*Li*Dps-ZnPP as a photodynamic therapy and imaging agent

5.1 Introduction

The mini-ferritin *Li*Dps has great potential as a scaffold for new PDT agents. *Li*Dps is a small, multi-subunit protein that can be functionalised for use in nanotechnology [69,215,216]. The usefulness of *Li*Dps arises from its nature as a highly stable protein that is amenable to dissociation, reassembly and surface modification. These advantages have been utilised for developing *Li*Dps as a drug delivery and imaging agent [20].

Chapter 4 focused on modifying *Li*Dps through genetic fusion with *G*Luc and miniSOG to produce a hybrid cage that functions as a PDT and imaging agent. Whereas this chapter describes the modification to the external surface of *Li*Dps for chemical conjugation with the ZnPP to yield a *G*Luc-*Li*Dps-ZnPP imaging and PDT agent. This has been achieved by genetic modification of *Li*Dps subunits with *G*Luc for self-illumination and chemical attachment of ZnPP on the exterior surface of the subunits to act as a photosensitiser. Similar to the construct described in chapter 4, this construct generates singlet oxygen through a BRET mechanism. Furthermore, assembly of these subunits

into a dodecamer of *G*Luc-*Li*Dps-ZnPP improves the singlet oxygen quantum yield and produces a cage that can be loaded with drugs or other molecules.

The *Li*Dps, *G*Luc and ZnPP elements used to create the *G*Luc-*Li*Dps-ZnPP construct were chosen because of their unique properties (Figure 5.1). *Li*Dps, unlike ferritin, is small enough to fuse with *G*Luc through its N-terminus while retaining *G*Luc activity, whereas fusion of *G*Luc with apoferritin leads to loss of *G*Luc activity (*G*Luc was fused with apoferritin previously in our lab by Dr. Lei Zhang-Unpublished results). Furthermore, *G*Luc is smaller than Rluc and Fluc, and the bioluminescence of h*G*Luc is greater than the bioluminescence of *R*luc and Fluc [155,158,217] (Section 1.7.1). Finally, ZnPP is a fluorescent dye that can act efficiently as a type II photosensitiser and generates singlet oxygen upon irradiation with visible light [116]. Further, ZnPP can exhibit an augmented anticancer activity through its capability to inhibit HO-1 enzyme and lead to ablation of tumours [118,218–220] (Section 1.6.1)

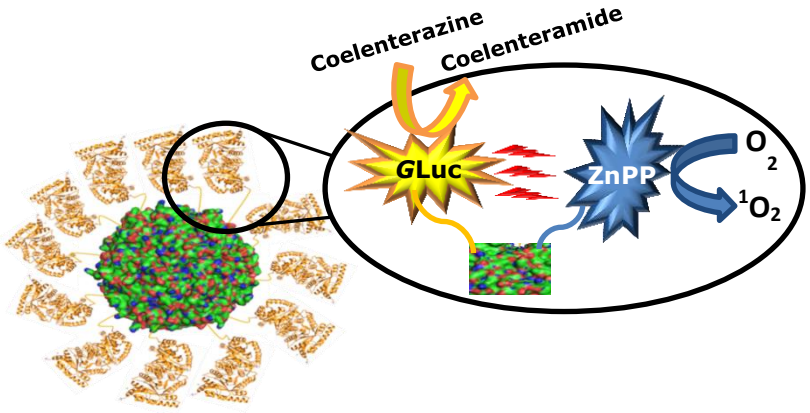


Figure 5.1: A schematic representation of the mechanism of the *G*Luc-*Li*Dps-ZnPP and coelenterazine system as a PDT agent. ZnPP is excited upon irradiation with light emitted from *G*Luc; excited ZnPP then interacts with surrounding oxygen molecules generating singlet oxygen. A *G*Luc-*Li*Dps-ZnPP model has been created in PyMol where the ZnPP molecules (blue dots) are conjugated with the Lys residues of *G*Luc-*Li*Dps protein, and the *G*Luc molecules (in orange) are fused to the N-terminus of each *Li*Dps subunit.

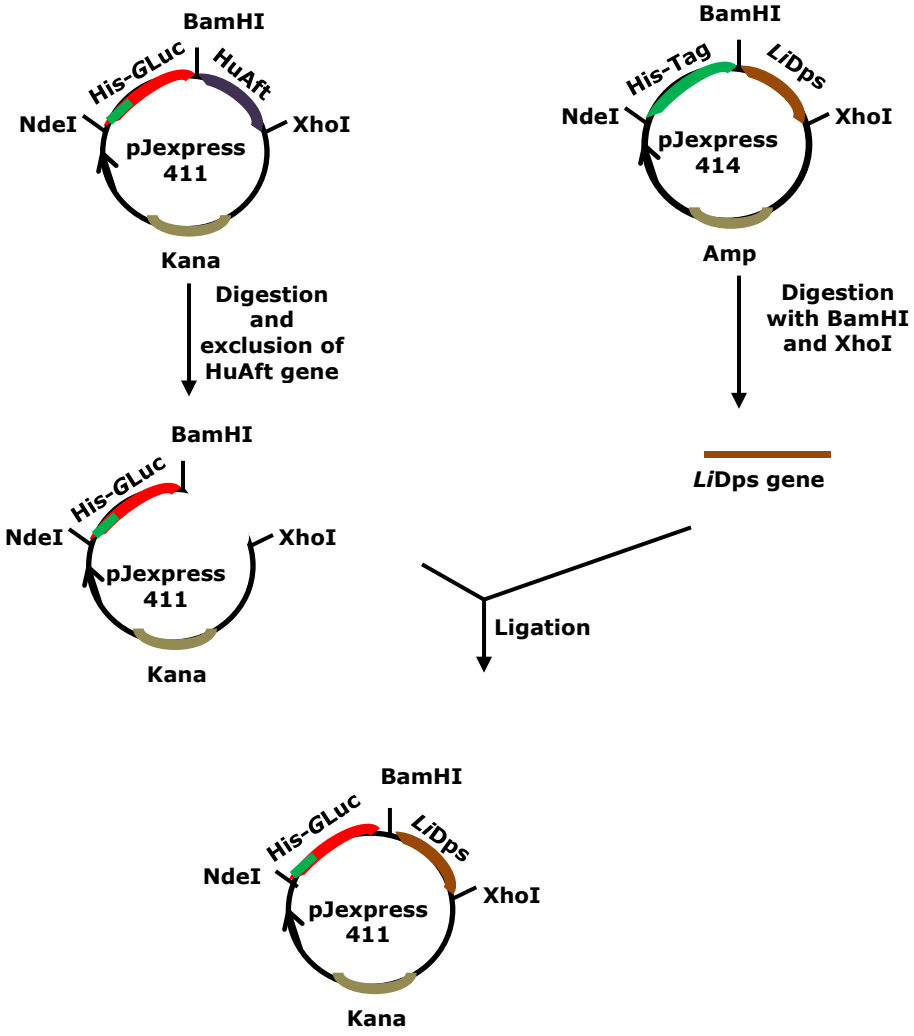
5.2 Results

5.2.1 Creation of *G*Luc-*Li*Dps-ZnPP nanoparticles

5.2.1.1 Synthesis a *G*Luc-*Li*Dps recombinant protein

To construct an *E. coli* vector for the expression of *G*Luc–*Li*Dps, the *Li*Dps gene was sub-cloned from plasmid pJexpress414:*Li*Dps into pJexpress411:*G*Luc-HuAft (Appendix 10.3), such that the ferritin gene was replaced with *Li*Dps and the remaining plasmid stayed intact, (Scheme 5.1). To identify *E. coli* colonies expressing pJexpress411:*G*Luc-*Li*Dps, 11 isolated colonies from the plates were

selected and cultured in liquid medium overnight. Samples (1 µL) were then screened by PCR. A screen using primers specific for the T7 promoter sequence present in the pJexpress411 vector and the human light chain ferritin gene of the pJexpress411:*G*Luc-HuAft vector (pJexpress411fwd and K108Crev respectively, Appendix 10.2) was employed to identify cultures in which the human light chain apoferritin gene was retained in the pJexpress411 vector.



Scheme 5.1: Schematic showing the preparation of the pJexpress411:*G*Luc-*Li*Dps plasmid using pJexpress411:*G*Luc-HuAft and pJexpress414:*Li*Dps plasmids.

Cultures that failed to yield the specific *G*Luc-HuAft amplification product were assumed to harbour plasmid pJexpress411:*G*Luc-*Li*Dps, allowing them to survive the antibiotic selection in the media. Figure 5.2 shows the agarose gel electrophoresis results for PCR products amplified in the negative selection screen. Inclusion of a positive control reaction, using pJexpress411:*G*Luc-HuAft as the PCR template, permitted the exclusion of colonies 3, 6, 9, 10, 12 and 13 because these colonies yielded a product of identical size, 1 kb, in the PCR screen. Because the PCR screen should not yield a product for pJexpress411:*G*Luc-*Li*Dps, colony 11 was also excluded.

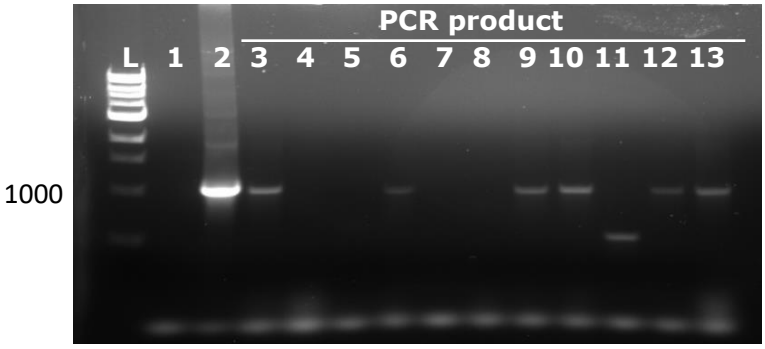
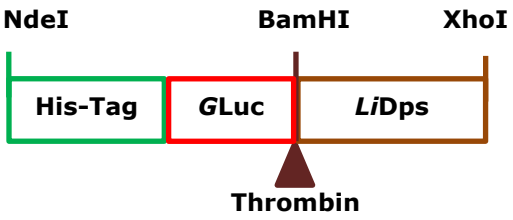


Figure 5.2: Plasmid screen on 1% (w/v) agarose gel. DNA MW ladder (L), negative control (1), positive control (2), PCR product (3-13).

The culture derived from colony 7 was chosen as a candidate for harbouring pJexpress411:*G*Luc-*Li*Dps and was used to prepare plasmid DNA for DNA sequencing (from reactions primed with primers pJexpress411 fwd and K108C rev, Appendix 10.2). The DNA

sequencing data for colony 7 confirmed that it contained a 5' *G*Luc gene in frame with a 3' *Li*Dps gene, located downstream of the T7 promoter and upstream of the strong T7 transcription terminator; it was the pJexpress411:*G*Luc-*Li*Dps design. The gene map and primary amino acid sequence of *G*Luc-*Li*Dps are shown in Figure 5.3, and the properties of the *G*Luc-*Li*Dps protein expressed by the pJexpress411:*G*Luc-*Li*Dps expression vector are listed in Table 5.1.

(A)



(B)

1 MHHHHHHAKPTENNE DFNIVAVA SNFATT DLDADRGKLPG KKLPLEVLKE
51 LEANARKAGC TRGCLICLSHIK CTPKMKKFIP GRCHT YEGD KESAQGGIG
101 EAIVDIPEIPGFKDL EPLEQ FIAQVDL CVDCT TGCLKG LANVQCS DLLKK
151 WLPQRCATFASKIQGQVDKIKGAGGDTGGGGGGLVPRGSMKTINSVDTKE
201 FLNHQVANLNVFTVKIHQIHWYMRGHNFF TLHEKMDDLYSEFGEQMDEVA
251 ERLLAIGGSPFS TLKEFL ENASVE EAPYTKP KTMD QLMEDLV GTLELLRD
301 EYQQGIELTDKEGDNVTNDMLIAFKASIDKHIWMFKAFLGKAPLE

Figure 5.3: (A) The *G*Luc-*Li*Dps gene map. **(B)** The primary amino acid sequence of the *G*Luc-*Li*Dps chimera. An N-terminal His-Tag (green), *G*Luc enzyme (red), pentaglycine linker with thrombin cleavage site underlined (black) and C-terminal *Li*Dps protein (blue) comprises the sequence.

Size in residues	MW (Da)	Theoretical pI	Molar Extinction coefficient (M/cm) at 280 nm
345	38,242	5.71	24,575

Table 5.1: Theoretical physical properties of the *G*Luc-*Li*Dps subunit.

5.2.1.2 Expression, purification, and characterisation of *G*Luc-*Li*Dps

The *G*Luc-*Li*Dps were successfully expressed and purified in BL21 (DE3) *E. coli*. Early SDS-PAGE analysis of *E. coli* biomass samples after sonication and centrifugation identified the *G*Luc-*Li*Dps chimera as present almost exclusively in the insoluble fraction (Figure 5.4 A).

Urea (4 M) was used to solubilise *G*Luc-*Li*Dps, which, after further centrifugation and sterile filtration, was subject to denaturing Ni-IMAC (Section 2.2.2). For further purification, fractions were pooled and applied to a SEC column (HiLoad 16/60, Superdex 75 prep grade). Combined fractions assumed to contain *G*Luc-*Li*Dps were analysed using SDS-PAGE (Figure 5.4 B & C).

The protein activity was checked by adding the coelenterazine substrate. Emission of blue light was observed immediately. The results demonstrate that *G*Luc-*Li*Dps refolds to its native state during dialysis after denaturation with 4 M urea.

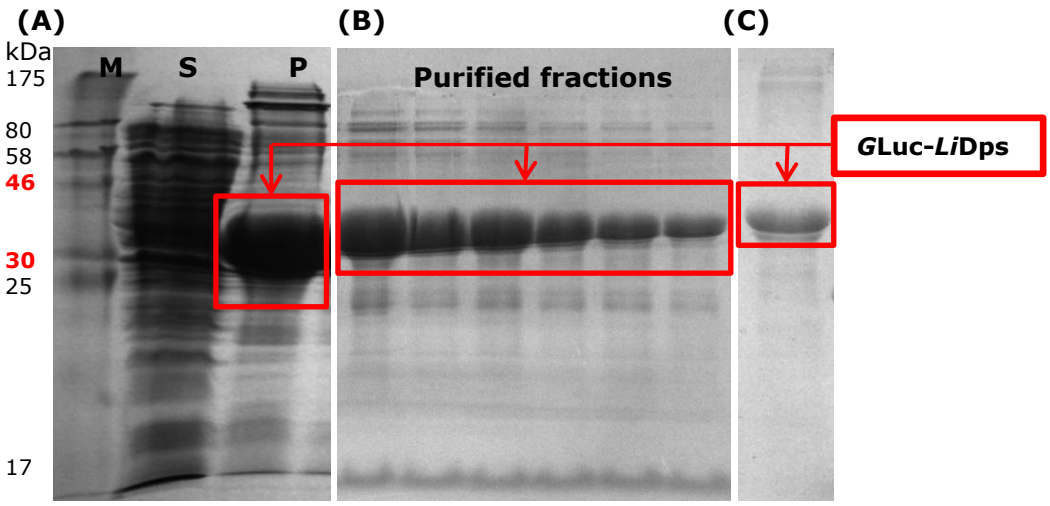


Figure 5.4: SDS-PAGE gel of **(A)** crude *G*Luc-*Li*Dps sample, **(B)** purified fractions using Ni-IMAC and **(C)** purified fractions using SEC. Lane M = marker, lane S = soluble fraction, lane P = insoluble fraction.

The MW of *G*Luc-*Li*Dps determined with nESI mass spectrometry is 38,241 Da. The data is in accordance with the expected theoretical mass (38,242 Da) of the primary amino acid sequence of *G*Luc-*Li*Dps (Figure 5.5 & Table 5.2).

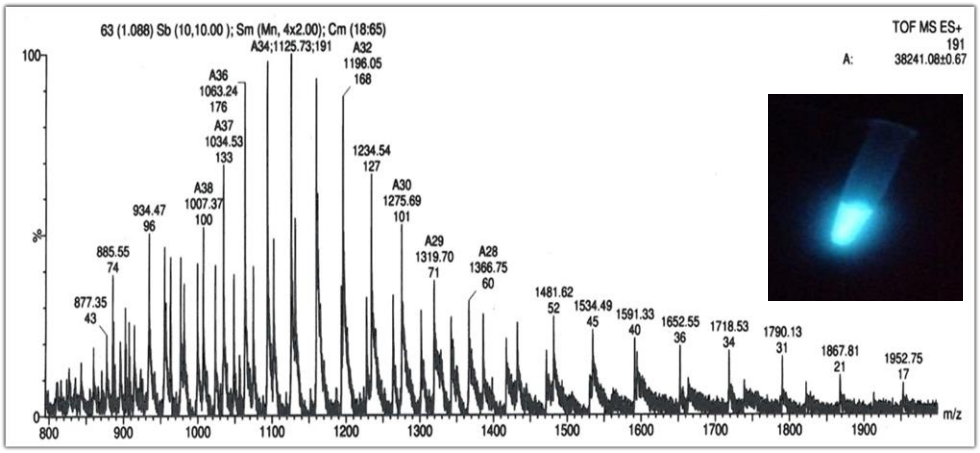


Figure 5.5: The nESI MS shows that the MW of *G*Luc-*Li*Dps is 38,241 Da, inset photograph shows the blue light emitted from *G*Luc-*Li*Dps construct following coelenterazine addition.

	Theoretical mass (Da)	Experimental mass (nESI) (Da)	Deviation (Da)
***G*Luc-*Li*Dps**	38,242	38,241	1

Table 5.2: The theoretical and measured mass of *G*Luc-*Li*Dps protein.

5.2.1.3 *G*Luc-*Li*Dps activity

To compare the activities of *G*Luc-*Li*Dps and *G*Luc, two photoluminescence assays were conducted. One assay used fixed concentrations of *G*Luc or *G*Luc-*Li*Dps and different concentrations of coelenterazine over a 30-minutes period. The other used fixed concentrations of coelenterazine and different concentrations of *G*Luc or *G*Luc-*Li*Dps over a 30-minutes period (Figure 5.6).

Over a 5-minutes period, the light intensity of *G*Luc decayed to about 75% of its initial level, while *G*Luc-*Li*Dps decayed to less than 50% (Figure 5.6 A & B), indicating that *G*Luc-*Li*Dps retains its activity better.

At a fixed concentration of *G*Luc-*Li*Dps, the light intensity gradually decreased over 30 minutes. With 2 µg/mL coelenterazine, the light intensity decreased by 50% after ~6 minutes and by 75% after ~12 minutes. The observations were very similar with 4 µg/mL and 6 µg/mL coelenterazine. In contrast, the turnover of coelenterazine was very rapid at a fixed concentration of *G*Luc (5 µg/mL); the light

intensity with 2, 4 and 6 µg/mL coelenterazine decreased to 0% after just 10 minutes (Figure 5.6 C & D).

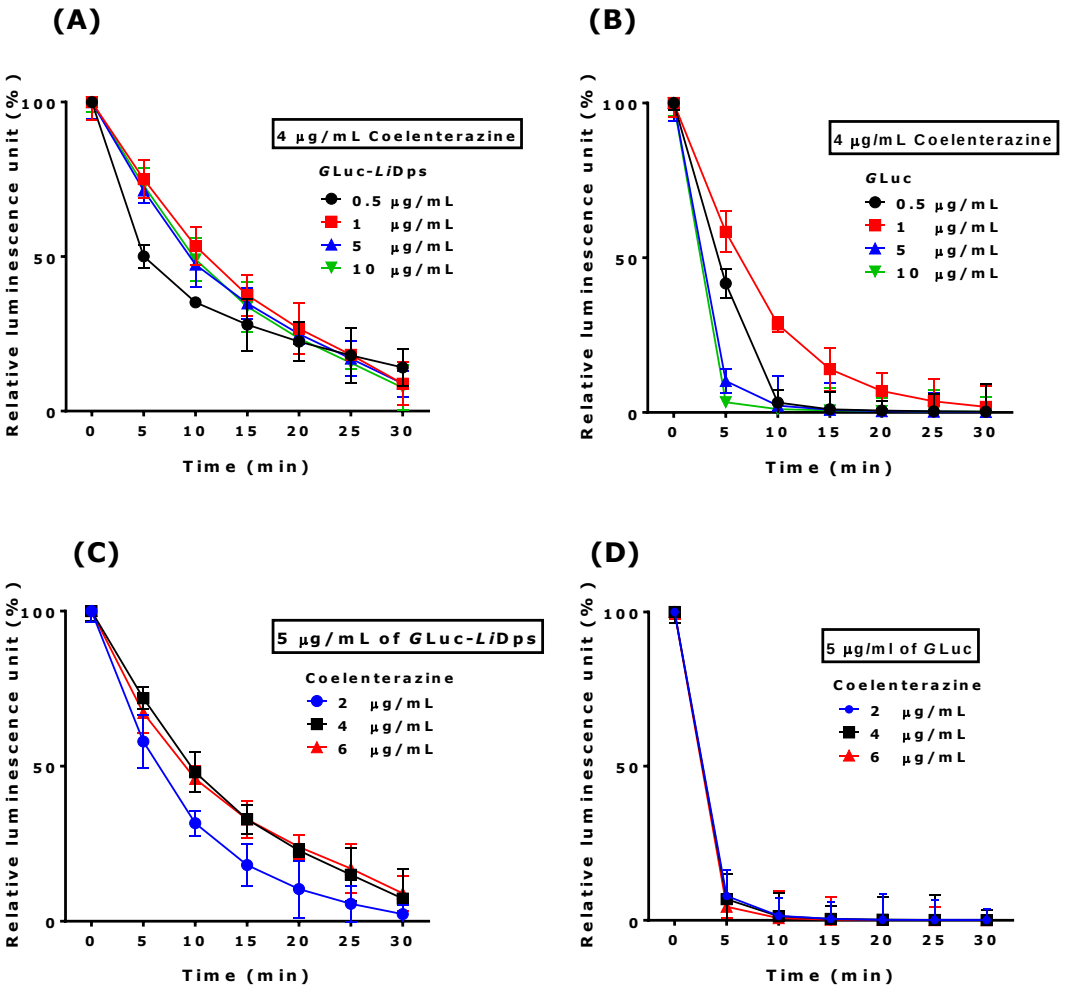


Figure 5.6: PL emission at different concentrations of **(A)** *G*Luc-*Li*Dps (0.5,1, 5, 10 µg/mL) with 4 µg/mL of coelenterazine, **(B)** *G*Luc (0.5, 1, 5, 10 µg/mL) with 4 µg/mL of coelenterazine, **(C)** coelenterazine (2, 4, 6 µg/mL) with 5 µg/mL of *G*Luc-*Li*Dps and **(D)** coelenterazine (2, 4, 6 µg/mL) with 5 µg/mL of *G*Luc in Tris buffer (20 mM Tris pH 8.3). The emitted light was monitored every 5 minutes for 30 minutes.

SDS at a concentration below its CMC value (0.1% w/v) was added to assess the effect of detergent on *G*Luc-*Li*Dps and *G*Luc activity. We also suppose that the SDS at this concentration can disrupt the dodecamer structure of *G*Luc-*Li*Dps and consequently converts it into individual subunits. When compared with the sustained PL of untreated *G*Luc-*Li*Dps, the PL period of SDS-treated *G*Luc-*Li*Dps was shorter and comparable to the activity of *G*Luc alone. This result indicates that the *G*Luc-*Li*Dps was more stable in the presence of SDS compared to *G*luc alone and the prolonged PL of *G*Luc-*Li*Dps can be attributed to a decline in the rate of coelenterazine turnover caused by steric hindrance of *Li*Dps on the active site of *G*Luc slowing down substrate binding/product. The presence of SDS, resulting in disassembly of the *G*Luc-*Li*Dps cage, removes this effect (Figure 5.7).

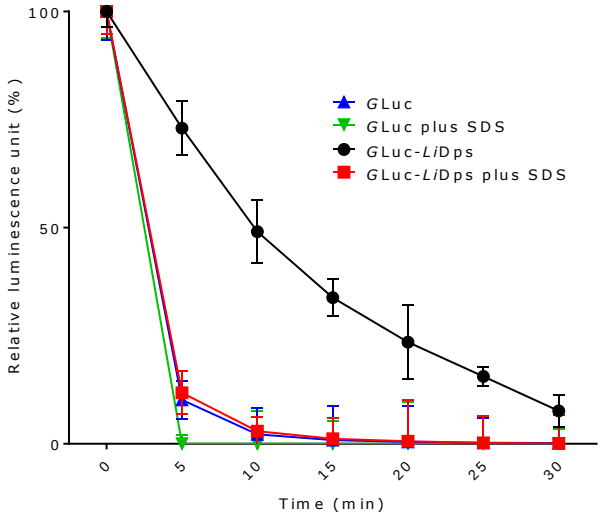


Figure 5.7: The PL decay time of *G*Luc-*Li*Dps in comparison to *G*Luc in the absence and presence of SDS at λ_{em} = 470 nm. *G*Luc-*Li*Dps (5 µg/mL) in Tris buffer (20 mM Tris pH 8.3) was mixed with Coelenterazine (4 µg/mL) and SDS (0.1% w/v) in a white 96 well plate. The emitted light was monitored every 5 minutes for 30 minutes.

5.2.2 ZnPP labelling of *G*Luc-*Li*Dps

The *Li*Dps subunit has been used as a scaffold on which to position *G*Luc and ZnPP at distances relative to each other that permit BRET and enhance the generation of singlet oxygen. Crystallographic studies of self-assembled *Li*Dps suggested that there are about 28 Lys residues positioned close to the N-terminus at distances less than that required for BRET (~100 Å). This increases the likelihood of achieving BRET between *G*Luc (fused to the *Li*Dps N-terminus) and ZnPP molecules (non-specifically bound to *G*Luc-*Li*Dps Lys residues) (Figure 5.8).

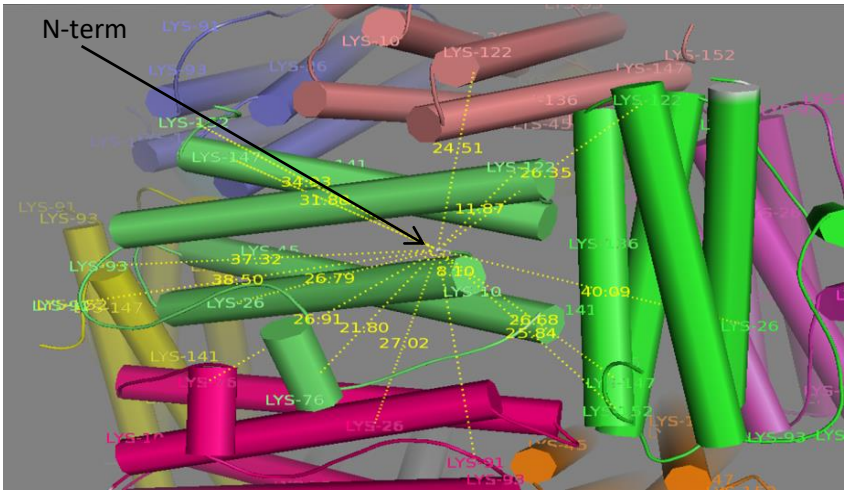
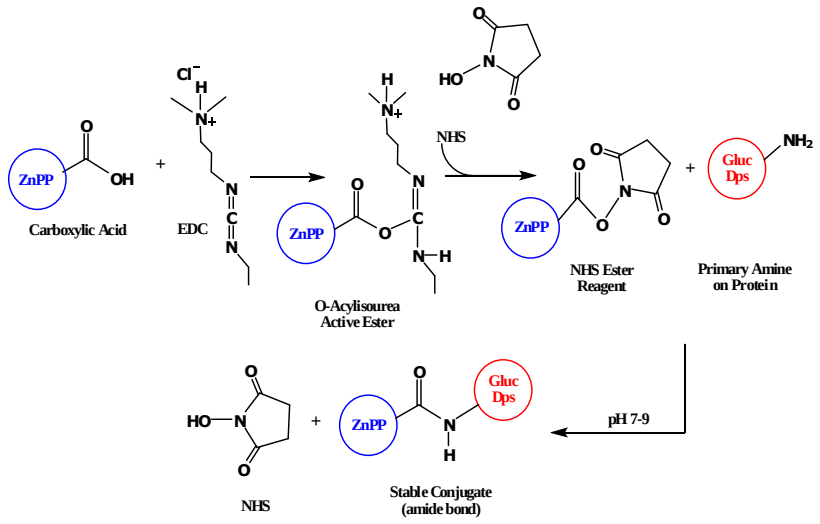


Figure 5.8: A cartoon model of the self-assembled dodecamer *Li*Dps crystal structure from the Protein Data Bank (PDB ID: 2BKC) created by PyMol. This model shows that about 28 Lys residues close to the N-terminal at a distance less than 100 Å. This distance permits transfer of the energy from *G*Luc (fused in the N-terminal of *Li*Dps) to the ZnPP molecules which are conjugated to Lys residues of *G*Luc-*Li*Dps to achieve BRET.

Accordingly, after characterisation to confirm the formation of the *G*Luc-*Li*Dps chimera, the recombinant protein was conjugated to ZnPP. Purified *G*Luc-*Li*Dps was subjected to an EDC/NHS conjugation reaction with ZnPP. This labelling process comprised two steps: initial activation of ZnPP by EDC and NHS in DMSO solvent and subsequent conjugation of the activated ZnPP carboxyl group to the free amines (Lys residues) of *G*Luc-*Li*Dps (Scheme 5.2).



Scheme 5.2: The mechanism for the conjugation of ZnPP with *G*Luc-*Li*Dps using EDC/NHS coupling agent.

Figure 5.9 shows a bright band corresponding to protein conjugated to ZnPP. Some protein precipitation occurred when performing the conjugation reaction in phosphate buffered saline (PBS) pH 7.4. Conversely, *G*Luc-*Li*Dps-ZnPP appeared more stable in PB (20 mM NaH_2PO_4 pH 8.3)

ZnPP was conjugated with *G*Luc-*Li*Dps over a range of molar ratios (*G*Luc-*Li*Dps:ZnPP=1:5, 1:10, 1:15) in order to find the optimum ZnPP concentration. The degree of conjugation at each ratio was assessed by SDS-PAGE. Before Coomassie staining, each labelling ratio yielded a fluorescent band corresponding to *G*Luc-*Li*Dps-ZnPP on SDS-PAGE when visualised under UV light (Figure 5.9). The result is highly indicative of a successful conjugation reaction.

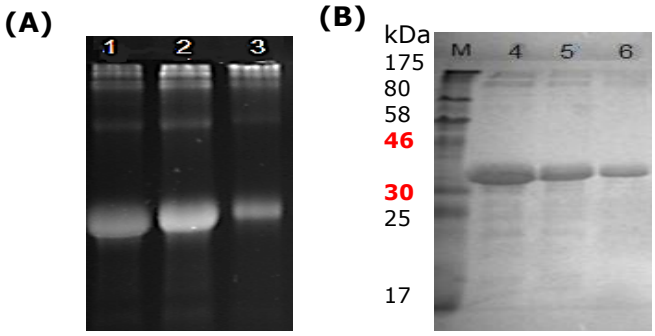


Figure 5.9: SDS-PAGE. **(A)** The gel visualised under UV light (λex=300-400 nm) before staining with Coomassie stain. **(B)** The gel after staining with Coomassie Brilliant Blue R-250. Lanes 1, 2 and 3 in **(A)** correspond to lanes 4, 5 and 6 in **(B)**, representing 1:5, 1:10 and 1:15 molar ratios of *G*Luc-*Li*Dps:ZnPP, respectively.

Further inspection of the SDS-PAGE showed less migration of the *G*luc-*Li*Dps-ZnPP through the gel when they were generated with higher concentrations of ZnPP. Precipitation was observed in the reaction with the 1:15 conjugation ratio. However, precipitation was not observed in reactions with the 1:10 and 1:5 ratios. Inspection of the fluorescent bands shown in Figure 5.9 revealed that the central band, corresponding to the 1:10 ratio, was brighter than the others. This

suggests that more ZnPP was conjugated in the 1:10 reaction than in the 1:5 reaction, and that more protein reacted without precipitation in the 1:10 reaction than in the 1:15 reaction. The nanoparticle products were dialysed against a PB (20 mM of NaH_2PO_4 buffer, pH 8.3), and the degree of conjugation was further characterised. nESI-MS was used to determine the extent of ZnPP conjugation (Figure 5.10).

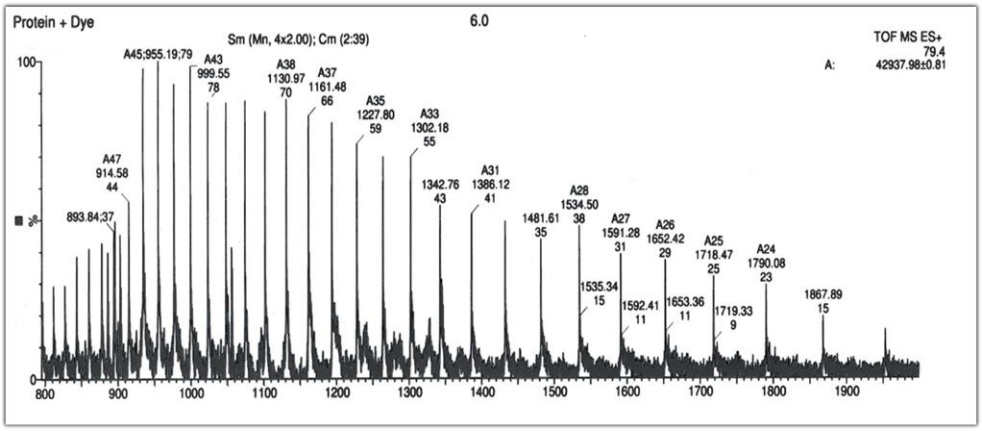


Figure 5.10: The nESI MS shows that the MW of *G*Luc-*Li*Dps-ZnPP is 42,938 Da.

The mass of *G*Luc-*Li*Dps, unlabelled and labelled with ZnPP (1:10 ratio), was first determined. Using Equation (1), the number of conjugated ZnPP molecules was then calculated. On average, 7 or 8 molecules of ZnPP were conjugated per *G*Luc-*Li*Dps subunit.

$$\frac{\textit{G}\text{Luc-}\textit{Li}\text{Dps-ZnPP mass} - \textit{G}\text{Luc-}\textit{Li}\text{Dps mass}}{\text{ZnPP mass} - H_2O} = \frac{42{,}938 - 38{,}241}{626 - 18} = 7.7 \quad (1)$$

Equation 5.1 Equation used to calculate the number of ZnPP molecules that were conjugated with *G*Luc-*Li*Dps based on the mass obtained by ESI-MS.

Furthermore, native PAGE was performed to demonstrate that *G*Luc-*Li*Dps could form the full cage structure and to investigate the effect of ZnPP conjugation on the cage structure. *G*Luc-*Li*Dps migration was compared with that of other cage proteins, previously prepared and characterised in our lab, as standard proteins to confirm cage formation (Figure 5.11). The native PAGE showed that *G*Luc-*Li*Dps (458.9 kDa) was located between Afb-HuAft (738.1 kDa) and *Li*Dps (257.3 kDa) and close to HuAft (561.5 kDa). This result suggested that the full cage had formed and the conjugation method did not affect *G*Luc-*Li*Dps cage formation, however, the migration of *G*Luc-*Li*Dps-ZnPP faster than other protein and this might be due to reduce the the net negative charge of *G*Luc-*Li*Dps after conjugation with ZnPP (Figure 5.11).

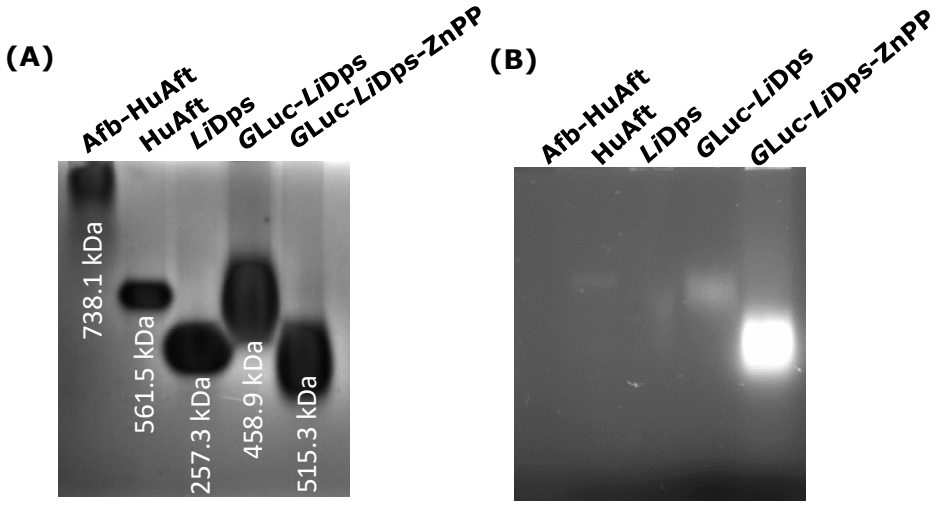


Figure 5.11: Native agarose gel with *G*Luc-*Li*Dps and *G*Luc-*Li*Dps-ZnPP. **(A)** Proteins shown after staining with Coomassie Blue R-250 stain. Afb-HuAft at 738.1 kDa, HuAft at 561.5 kDa and *Li*Dps at 257.3 kDa were used as standards. **(B)** Proteins show under UV light (λex=300-400 nm).

5.2.2 1 *G*Luc-*Li*Dps-ZnPP activity

The ability of *G*Luc-*Li*Dps-ZnPP to generate ROS through a BRET mechanism was tested using coelenterazine. The bioluminescence of *G*Luc-*Li*Dps-ZnPP (conjugated state) was lower than that emitted by *G*Luc-*Li*Dps in the presence of ZnPP (unconjugated state) under the same conditions. Moreover, the light intensity of both molecules was less than the bioluminescence intensity of *G*Luc-*Li*Dps alone (Figure 5.12). This might be because the light was quenched by ZnPP to produce singlet oxygen through BRET, and the quenching was inversely proportional to the distance between *G*Luc and ZnPP.

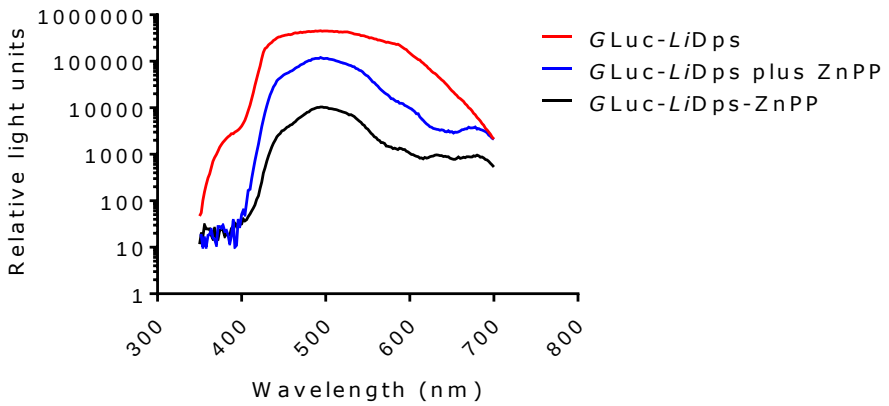


Figure 5.12: Bioluminescence spectra of *G*Luc-*Li*Dps, *G*Luc-*Li*Dps plus ZnPP (unconjugated state) and *G*Luc-*Li*Dps-ZnPP (conjugated state). A 5 µg/mL of *G*Luc-*Li*Dps in each case was mixed with 4 µg/mL of coelenterazine. The reduction in light intensity was used as an indicator of the binding of ZnPP to *G*Luc-*Li*Dps.

Further, the overlap between the light emitted by *G*Luc and the ZnPP-absorbed light was examined (this plays a vital role in achieving BRET). Good overlap between the spectra of *G*Luc and ZnPP was observed. This will improve the generation of singlet oxygen through BRET (Figure 5.13).

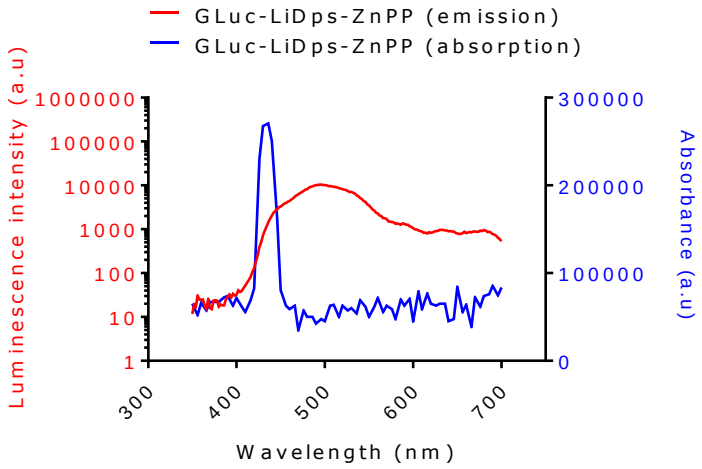


Figure 5.13: The overlap between the *G*Luc bioluminescence spectra light and the ZnPP-absorbed light.

5.3 Discussion

After the formation of *G*Luc-*Li*Dps-ZnPP, the construct was characterised and studied as a PDT agent. The construct activity initiates when *G*Luc catalyses the emission of blue light in the presence of coelenterazine. ZnPP is excited by *G*Luc bioluminescence. This leads to the generation of singlet oxygen when energy is transferred from excited ZnPP to proximal oxygen molecules. Positioning ZnPP groups

near *G*Luc improves the performance of *G*Luc-*Li*Dps-ZnPP as a PDT agent in BRET; this was achieved by binding ZnPP and *G*Luc to *Li*Dps subunits that used as a scaffold.

In a study of *G*Luc-*Li*Dps activity, the fusion of *G*Luc to *Li*Dps altered the kinetics of the *G*Luc enzyme from 'flash', in which substrate (coelenterazine) turnover is very fast and the photoluminescence period is very short, to 'glow', in which substrate turnover is slower and photoluminescence is prolonged. *G*Luc has a tendency for 'flash' kinetics [158], and the observed conversion could be due to fusion of the *Li*Dps protein close to the C-terminal domain of *G*Luc, where its active site is located [221]. The relatively large size of *Li*Dps might impede access of coelenterazine and oxygen molecules, which are necessary for *G*Luc activity. Treatment of *G*Luc-*Li*Dps with SDS significantly reduces conversion of flash kinetics to glow kinetics, possibly because dissociation of the *G*Luc-*Li*Dps subunits decreased steric hindrance close to GLuc active site. The conversion of the bioluminescence emission to glow kinetics delayed the photosensitiser excitation period and prolonged the production of singlet oxygen, thus we expect that this effect may enhance activation of the apoptosis pathway by singlet oxygen, increasing the opportunity to promote cell death.

ZnPP molecules were successfully conjugated to Lys residues on the surface of *G*Luc-*Li*Dps using the EDC/NHS linking agent. The conjugation efficiency was tested using SDS-PAGE, in which the

brightness of the protein bands and their migration were indicative of the number of ZnPP molecules bound to *G*Luc-*Li*Dps. A 1:10 molar ratio of *G*Luc-*Li*Dps:ZnPP was formed to be best for achieving high labelling efficiency with low protein precipitation. ZnPP is insoluble in aqueous solutions, and conjugation of ZnPP with protein improves its solubility. Therefore, exposure/conjugation to a high quantity of ZnPP could cause protein precipitation; this was observed when using a 1:15 ratio of *G*Luc-*Li*Dps:ZnPP.

nESI-MS and native agarose gel electrophoresis were used to analyse the mass of the *G*Luc-*Li*Dps-ZnPP subunit and to examine the effect of ZnPP conjugation on *G*Luc-*Li*Dps cage formation, respectively. *G*Luc-*Li*Dps-ZnPP is larger than *G*Luc-*Li*Dps, but *G*Luc-*Li*Dps-ZnPP moved faster than *G*Luc-*Li*Dps in the native agarose gel. This might be due to neutralisation of the positive charge of Lys when conjugated to ZnPP. Consequently, the negative charge of *G*Luc-*Li*Dps-ZnPP was higher than that of *G*Luc-*Li*Dps, increasing the migration rate of *G*Luc-*Li*Dps-ZnPP in the gel. This provides further evidence of successful ZnPP labelling. With regard to the MS calculation, given that ZnPP has two active carboxylic groups, the molecule could react with either one or two Lys residues with loss of one or two H_2O molecules. This might explain why MS analysis indicated that the number of attached ZnPP molecules is 7.7 instead of 7 or 8. The overlap between the spectra of *G*Luc and ZnPP and the quenching of *G*Luc bioluminescence by ZnPP indicate that there is a transfer of energy from *G*Luc to neighbouring

ZnPP molecules. This might be enhanced the generation of singlet oxygen through BRET.

Several PDT systems have been designed based on ZnPP as a photosensitiser and imaging agent to use in biomedical applications as it exhibits a potent anti-tumour activity. Fang *et al.* synthesised a PDT agent based on conjugation of ZnPP with *N*-(2-hydroxypropyl)methacrylamide or styrene-maleic acid polymer and they found that more than 70% of tumours disappeared in different tumour models after treatment [114,116]. Further the conjugation of ZnPP with PEG form a polymeric micelles that upon irradiation by xenon light exhibits anti-tumour activity [122]. However these PDT systems faced a hurdle in *in vivo* applications due to their requiring an external light source for initiating singlet oxygen generation. Therefore our PDT offers a promising alternative for *in vivo* tumour treatment through its providing with self-illumination (*G*Luc) for ZnPP excitation. Characterisation of *G*Luc-*Li*Dps-ZnPP suggests that the construct might perform well as a PDT and imaging agent. This was confirmed in an *in vitro* study (Section 7.2.1).

Chapter 6

6. Synthesis of Afb2C-PbS and ZnPP-Afb2C-PbS QDs

6.1 Introduction

6.1.1 Afb2C-PbS QDs

Lead sulfide (PbS) QDs have been shown to be capable of generating ROS, making them an attractive and promising tool for the treatment of cancer [209]. Furthermore PbS QDs, when excited, emit wavelengths of light in the near-infrared (NIR) region (1000-1500 nm). This wavelength of light, unlike visible light is not as easily scattered, therefore PbS QDs could potentially be used for non-invasive *in vivo* imaging [222]. QDs including PbS, silver sulfide (Ag_2S), and lead selenide (PbSe) have many advantages over traditional fluorescent probes including photostability and strong fluorescence emission [222]. Different PbS QDs have been synthesised such that their exterior was decorated with various ligands such as glutathione [223] 1-thioglycerol/dithioglycerol [209,224], oleic acid [225], dihydrolipoic acid [226], L-cysteine [227], and luciferase [228], for use in *in vitro* and *in vivo* studies. However, some coatings, such as compounds that contain thiol groups, are mostly non-biocompatible and cytotoxic [223]. Therefore this chapter describes the preparation

of new PbS QDs coated with the biocompatible Afb2C protein (Afb2C-PbS QDs) to act as a drug delivery and an imaging agent.

Afb is a small protein that binds with high affinity (K_D ~ 22 pM) to HER2 receptor, a transmembrane protein which is overexpressed in many cancer cells [229–231]. Therefore we aimed to deliver PbS QDs selectively to cancer cells overexpressing HER2, permitting the diagnosis and treatment of the targeted tissues.

6.1.2 ZnPP-Afb2C-PbS QDs

The emission of NIR light from Afb2C-PbS QDs ($\lambda_{emission}$ > 800 nm) is difficult to detect because conventional fluorescence microscopes cannot identify this wavelength of light (low sensitivity above 800 nm). Therefore, the Afb2C-PbS QDs were further modified by labelling Afb2C with ZnPP. This resulted in a construct that functioned as a treatment and imaging agent. It has previously been reported that the ZnPPs display anticancer activity through their capability to inhibit HO-1 [111,118,218,219]. These enzymes are overexpressed in cancer cells and play an important role in preventing cancer cell apoptosis [118–120,232]. In addition, the fluorescence emitted by ZnPP contributed to its use in *in vitro* and *in vivo* imaging studies [114,116,233].

In this study a novel construct of PbS QD functionalised with Afb2C and ZnPP was created (Figure 6.1) with the aim that this construct would enable tumour imaging and treatment; fulfilling the criteria for so called theranostics (therapeutic and diagnostic capabilities engineered into a single agent). Imaging could be achieved by using either the emitted light of ZnPP in the visible region after excitation ($\lambda_{max(absorption)}$ = 425 nm, $\lambda_{max(emission)}$ = 593 nm) or the emitted light of PbS QDs in the second-NIR region ($\lambda_{max(emission)}$ = 1188 nm). Treatment of the cancer could be achieved through the combination of ZnPP anticancer activity and PbS QDs which also induce ROS generation [209]. The formation of Afb2C-PbS QDs and their physical properties have been studied and characterised before and after Afb2C conjugation to ZnPP using PL, native agarose gel electrophoresis, and TEM.

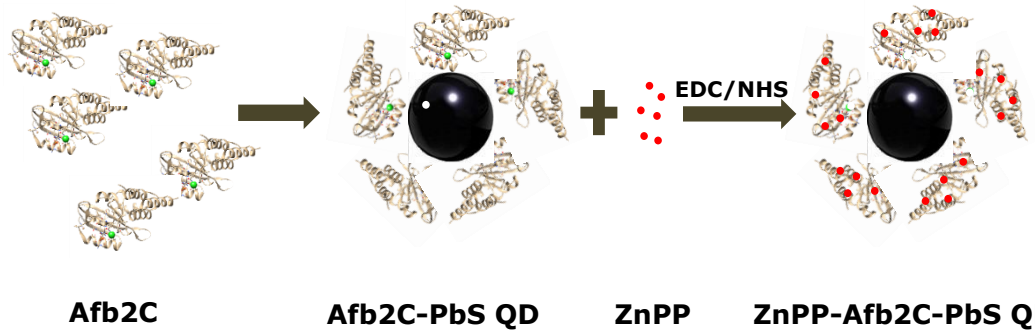


Figure 6.1: A cartoon representation the formation of ZnPP-Afb2C-PbS QDs.

6.2 Results

6.2.1 Afb2C preparation

In the pJexpress401 plasmid, the Afb2C gene was designed with an N-terminal His-Tag for Ni-IMAC protein purification and two mutations (G82C and S84C) were introduced at its C-terminal (Appendix 10.3). The mutations were generated in two steps using site-directed mutagenesis: 1) the Gly was replaced with Cys at position 82 and 2) the serine (Ser) residue at position 84 was substituted with Cys to produce Afb-G82C (AfbC) and the double mutant Afb-G82C-S84C (Afb2C).

These mutations were generated according the manufacturer's instructions of the Q5® Site-Directed Mutagenesis Kit and utilising of forward and reverse Q5SDM Afb2C primers (Appendix 10.2), which were designed using software available online (http://nebasechanger.neb.com) (Section 2.1.2.2). The strain of *E. coli*, DH5α, was successfully transformed with both mutants. Single colonies were picked and their plasmid gene sequences yielded the expected primary sequences of the mutant Afb (Figure 6.2). The properties of each Afb protein are found in Table 6.1.

AfbC **1** MAHHHHHHSSGLVPRGSLQVDNKFNKEMRNAYWEIALLPNLNNQQ
46 KRAFIRSLYDDPSQSANLLAEAKKLNDAQAPKVDGG**C**GSGGSLE

Afb2C **1** MAHHHHHHSSGLVPRGSLQVDNKFNKEMRNAYWEIALLPNLNNQQ
46 KRAFIRSLYDDPSQSANLLAEAKKLNDAQAPKVDGG**C**G**C**GGSLE

Figure 6.2: The primary amino acid sequence of the AfbC mutant, and Afb2C double mutant. An N-terminal His-Tag (green), linker with a thrombin cleavage site underlined (brown), Afb protein (red) and C-terminal cysteine mutant residues (blue) comprises the sequence.

	No. of residues	**MW (Da)**	**Theoretical pI**	**Molar Extinction coefficient (M/cm) at 280 nm (reducing form)**
AfbC	89	9,832	7.97	8480
Afb2C	89	9,848	7.87	8480

Table 6.1: Theoretical physical properties of the AfbC and Afb2C polypeptide.

The double mutant Afb2C was employed for expression and used for further applications.

6.2.2 Expression and purification of Afb2C

The mutant Afb2C protein was successfully expressed in BL21 (DE3) *E. coli*. Upon addition of the IPTG to the BL21 (DE3) culture, it was found that the culture incubation for 4 hour at 37°C with shaking at 180 rpm was optimal for expression yields. Attempts to express Afb2C for longer periods of time or overnight lead to a lack of Afb2C production.

After lysis by sonication, the soluble fraction (containing the Afb2C) was centrifuged at 40,000 x *g* for 25 minutes, 4°C to enable the separation of soluble proteins from insoluble proteins and cell debris. The soluble proteins were applied to a 5 mL nickel-purification column after its washing with a binding buffer (20 mM Tris pH 8.6, 10 mM of imidazole). The protein fraction that bound to the column was eluted by increasing the imidazole to 1.5 M in an elution buffer of 20 mM of Tris pH 8.6. Fractions containing Afb2C were pooled and purified further by SEC (HiLoad 16/60, Superdex 75 prep grade, GE healthcare/Amersham). The presence and purity of the Afb2C protein was analysed using Tricine-SDS-PAGE. The resulting PAGE gel demonstrated that Afb2C was of high purity (Figure 6.3). After purification the Afb2C protein was dialysed twice using a Tris buffer (20 mM Tris pH 8.6) containing 1 mM dithiothreitol (DTT) to prevent disulfide bond formation. After dialysis, pure Afb2C was stored at -80 °C.

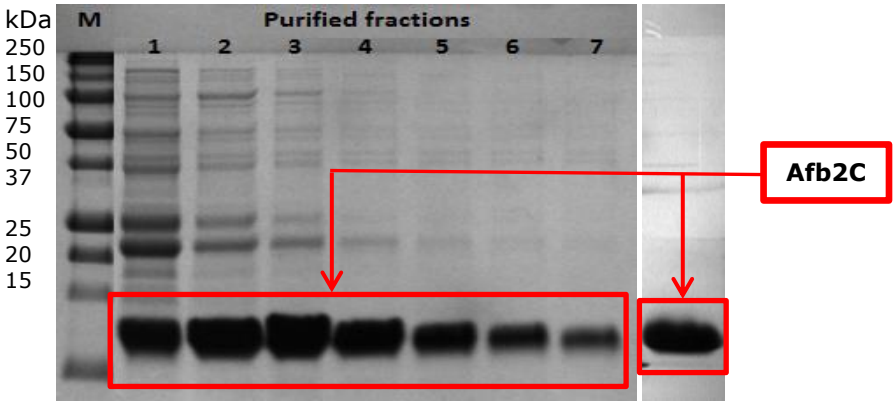


Figure 6.3: Tricine SDS-PAGE gel of mutated Afb2C purified using Ni-IMAC (the left gel) and after purification using SEC (the right gel), (M = marker).

In addition the mass of pure Afb2C was confirmed using MALDI-TOF-MS which gave a mass of 9620 Da; 228 Da less than theoretical mass (Figure 6.4 & Table 6.2).

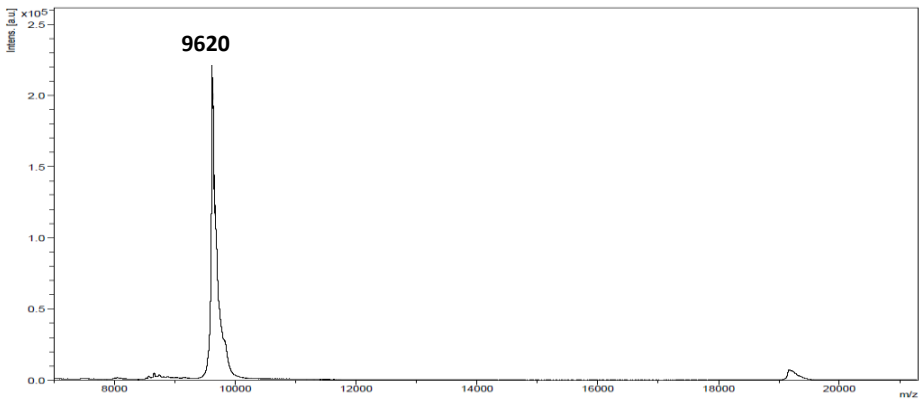


Figure 6.4: The MALDI-TOF MS shows that the MW of Afb2C is 9,620 Da.

	Theoretical mass (Da)	Experimental mass (MALDI-TOF) (Da)	Deviation (Da)
Afb2C	9,848	9,620	228

Table 6.2: The theoretical and measured mass of Afb2C protein.

6.2.3 Synthesis of Afb2C-PbS QDs

After preparation and characterisation, Afb2C was used to successfully cap the PbS QD. This resulted in soluble and stable quantum dots demonstrated by the black colloidal solution in Figure 6.5. In comparison, the control QDs which did not contain Afb2C were not stable and precipitated out of solution.



Figure 6.5: A photo showing the black colloidal solution of Afb2C-PbS QDs.

To examine the stability of the Afb2C structure in the QD reaction mixture, the secondary structure of the Afb2C protein was tested at pH 7.0 and pH 11.0 using CD spectrometry. Figure 6.6 shows that α-helical secondary structure dominate in the Afb2C. An Afb2C showed

high stability against pH changes, and its secondary structure was unaffected when the pH changed from 7.0 to 11.0 at room temperature (Figure 6.6).

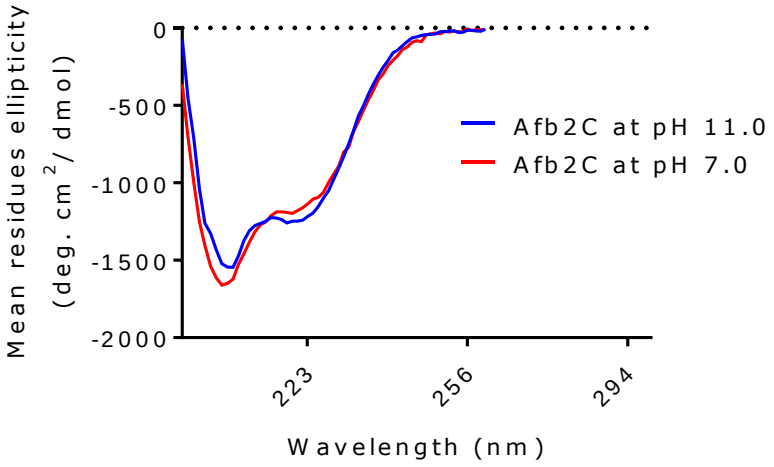


Figure 6.6: CD spectra of the Afb2C at pH 7.0 and 11.0.

6.2.4 Characterisation of Afb2C-PbS QDs

6.2.4.1 Optical activity of Afb2C-PbS QDs

Two different concentrations of Afb2C (3.4 and 4.5 mg/mL) were used to coat the PbS QDs, the resulting Afb2C-PbS QDs were characterised by monitoring their decomposition periods and by measuring their PL spectra. It was observed that increasing the concentration of the Afb2C protein improved the stability of the QDs. The QDs with lower Afb2C concentrations (3.4 mg/mL) precipitated after 3 weeks, and those with higher Afb2C concentrations (4.5 mg/mL) were stable for at

least 8 weeks in the solution. Therefore 4.5 mg/mL of Afb2C was adopted in the preparation of the Afb2C-PbS QDs for further study.

The stability of the Afb2C-PbS QDs was studied by periodically monitoring the PL spectra emitted over 5 weeks in the second-NIR window ($\lambda_{max(emission)}$ ~ 1188 nm) (Figure 6.7).

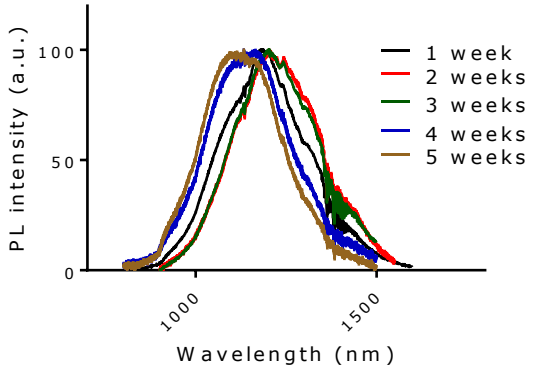


Figure 6.7: The PL intensity of Afb2C-PbS QDs measured in the second-NIR window over 5 weeks at 4 °C.

The PL study indicated that the Afb2C-PbS QDs were stable when stored in the dark at 4°C, and emitted a bright light in the second-NIR window 5 weeks after preparation.

6.2.4.2 Determination of Afb2C-PbS QDs size using TEM

The size of the Afb2C-PbS QDs was determined using TEM and the size distribution curve was generated using imageJ software (Figure 6.8).

TEM images and size distribution curve indicate that the Afb2C-PbS QDs had a size of ~5 nm and the higher magnification image (Figure 6.8 B) showed a spherical shape of Afb2C-PbS QDs.

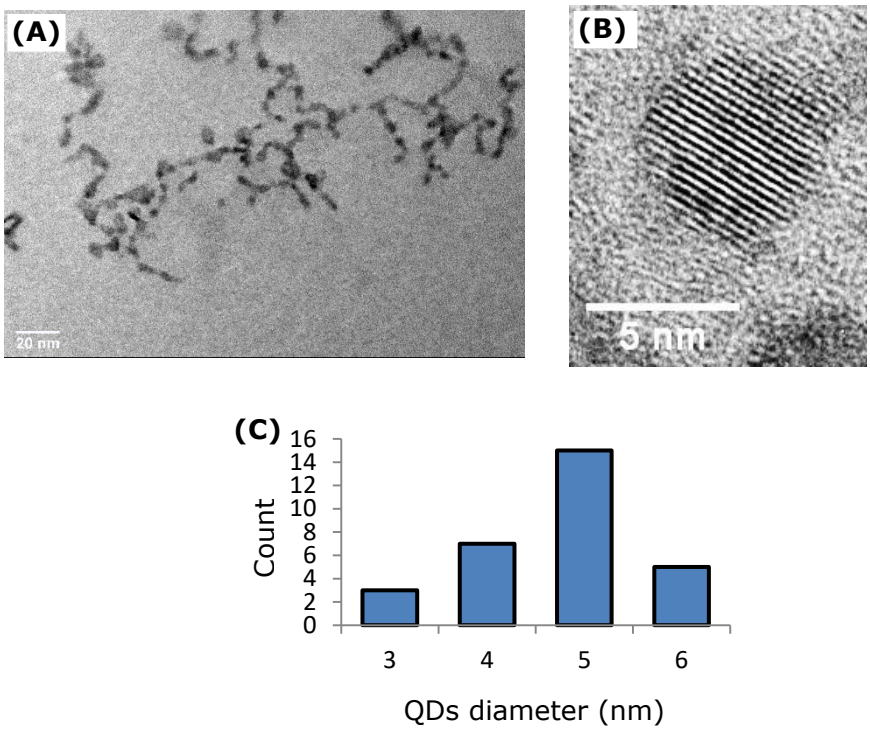


Figure 6.8: TEM images of Afb2C-PbS QDs with a focusing resolution **(A)** A 20 nm scale bar and **(B)** A 5 nm scale bar **(C)** Size distribution curve of Afb2C-PbS QDs.

The size of the PbS QDs was investigated further using PL and by determining their band gap (*E*). In general, PbS QDs have a bulk band gap of 0.41 eV and an 18 nm Bohr exciton radius. Consequently, this permits the preparation of PbS QDs with various band gaps between 0.71 and 1.28 eV (1740-970 nm) [234].

To determine the size of PbS QDs using their band gap (*E*), the photon energy that is expressed in nanometers was converted to electron volts using the Planck–Einstein equation (Equation 6.1):

$$E\ (eV) = 1239.8/\lambda\ (\text{nm})$$

Equation 6.1 The Planck–Einstein relationship was used for the conversion of QDs Band gap energy to eV.

According to Planck–Einstein equation the band gap of Afb2C-PbS QDs is 1.04 eV. Subsequently, a sizing curve (Figure 6.9) was used directly to determine the diameter of Afb2C-PbS QDs based on its band gap.

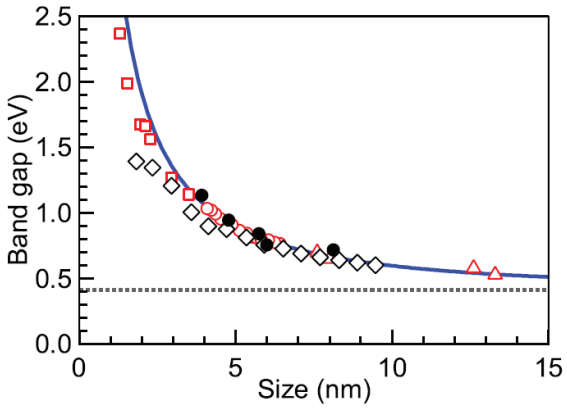


Figure 6.9: A curve showing the relationship between the band gap (*E*) of PbS QDs in (eV) and the particle size in (nm). This curve was used for the calculation of PbS QDs diameter based on its PL [234].

The band gap calculations gave the size based on the variations in the band energy of the PbS QDs regardless of the Afb2C ligand size. The size of PbS QDs calculated from the band gap is ~5 nm close to the diameter that is determined by the TEM.

6.2.5 Bioconjugation of Afb2C-PbS QDs with ZnPP

In addition the Afb2C-PbS QDs were also successfully conjugated with ZnPP, yielding ZnPP-Afb2C-PbS QDs. This was achieved by modifying the carboxyl groups on the ZnPP molecules to give a ZnPP-NHS ester (Section 2.8). The modified ZnPP was then able to react with Lys residues located within the Afb2C protein, forming a stable amide bond (Section 2.11.2). The ZnPP-Afb2C-PbS QDs were analysed using native agarose gel electrophoresis, and displayed a fluorescent band (Figure 6.10). In contrast the Afb2C-PbS QDs did not display any fluorescent bands, indicating that the fluorescence observed for ZnPP-Afb2C-PbS QDs was the result of successful ZnPP conjugation. Consequently, the conjugation of ZnPP yields QDs with dual emission properties, which could potentially provide and augmented cancer therapy.

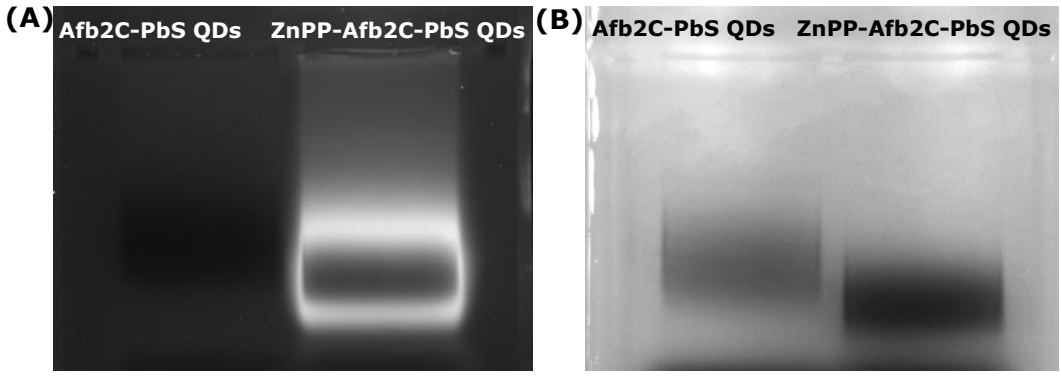


Figure 6.10: A native agarose gel electrophoresis of Afb2C-PbS and ZnPP-Afb2C-PbS QDs; **(A)** the gel under UV light (λ_{ex}=300-400 nm)and **(B)** gel under visible light. The agarose gel was prepared with a low percentage agarose (0.5% w/v), and the samples were electrophoresed at 100 V for 1 hours.

6.2.5.1 Optical activity of ZnPP-Afb2C-PbS QDs

ZnPP-Afb2C-PbS QDs were characterised using PL and TEM techniques and were compared with Afb2C-PbS QDs. Similar to Afb2C-PbS QDs, the ZnPP-Afb2C-PbS QDs emit light in the second-NIR with $\lambda_{max(emission)}$ = 1188 nm, suggesting that the binding of ZnPP with Afb2C has no effect on the PbS QDs' central core (Figure 6.11).

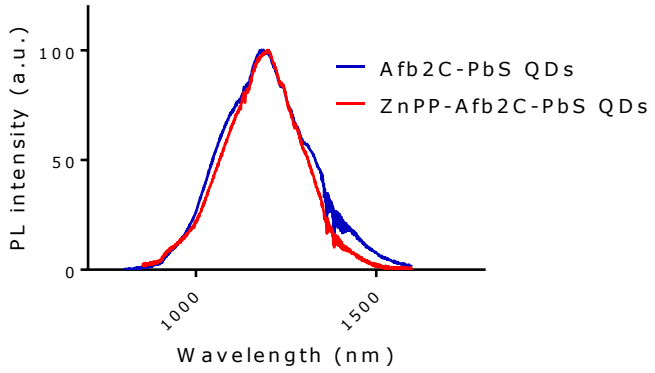


Figure 6.11: A graph of the PL intensity shows that there is a similarity in the $\lambda_{max(emission)}$ of the Afb2C-PbS QDs and the ZnPP-Afb2C-PbS QDs.

Furthermore the PL of the ZnPP-Afb2C-PbS QDs was monitored over 5 weeks in order to detect decomposition through changes in the emission spectra (Figure 6.12). It was found that the PL intensity of ZnPP-Afb2C-PbS QDs did not change during this period, indicating that these QDs were stable over 5 weeks at 4 °C.

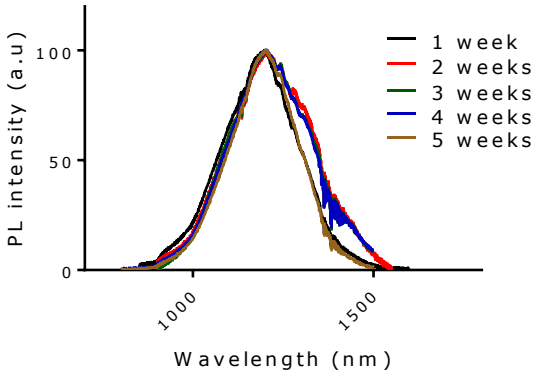


Figure 6.12: The PL intensity of ZnPP-Afb2C-PbS QDs measured in the second-NIR window over 5 weeks at 4 °C.

6.2.5.2 Determination of ZnPP-Afb2C-PbS QDs size using TEM

TEM images for the ZnPP-Afb2C-PbS QDs have been analysed to study the effect of the labelling reaction on the size of the PbS QDs' central core and the size distribution curve was generated based on these TEM images using imageJ software (Figure 6.13).

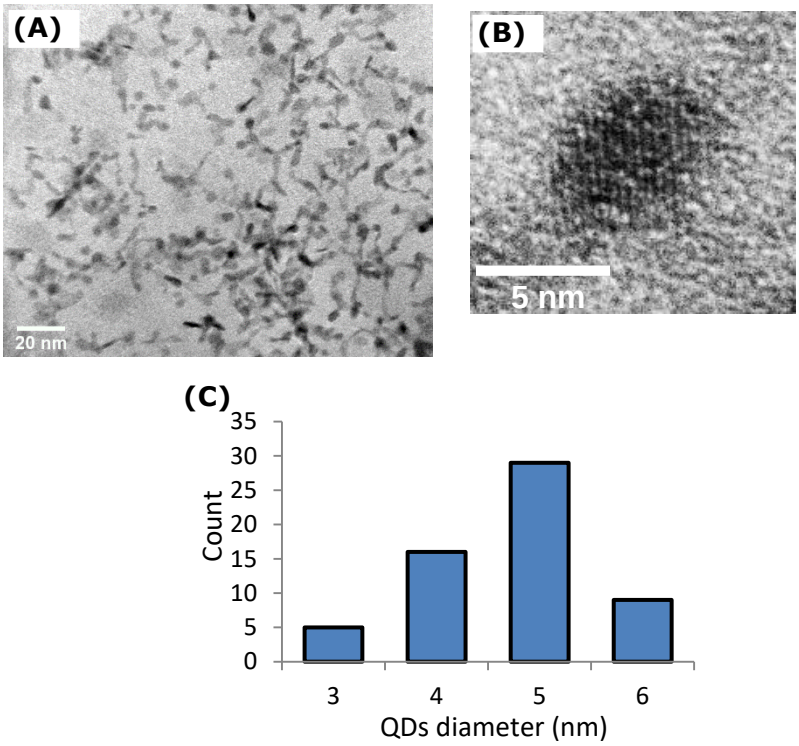


Figure 6.13: TEM images of ZnPP-Afb2C-PbS QDs with a focusing resolution of **(A)** a 20 nm scale bar and **(B)** a 5 nm scale bar. **(C)** Size distribution curve of ZnPP-Afb2C-PbS QDs.

The analysis of the TEM images and the size distribution curve indicated that the size of the ZnPP-Afb2C-PbS QDs' central core is ~5 nm. Furthermore, the PL of the ZnPP-Afb2C-PbS QDs is comparable to that of the Afb2C-PbS QDs, and this leads to the band-gap calculations for the ZnPP-Afb2C-PbS QDs being the same size as the Afb2C-PbS QDs. Thus the size calculations suggest that the binding of ZnPP molecules did not affect the PbS QDs' central core. Figure 6.13 A and B show that ZnPP-Afb2C-PbS QDs adopt an oval shape in TEM images rather than spherical shape.

6.3 Discussion

The Afb2C-PbS QDs have been designed as probes to act as a drug delivery and imaging agents with attractive properties including selective localisation and accumulation in cancer cells overexpressing HER2. Furthermore the potential work of Afb2C-PbS QDs for cancer treatment through ROS triggering in treated tumour tissues and non-invasive fluorescence imaging of the targeted deep-tissue through the Afb2C-PbS QDs' emission in the second-NIR window.

Mutated Afb2C protein was expressed using BL21 in LB medium. It was noticed that overnight induction at 30 °C did not improve yields of Afb2C. In contrast, a higher yield of Afb2C protein was obtained after a short 4 hours induction at 37 °C. There are many potential reasons for this outcome, many of which vary from protein to protein [235]. However, a high cell density can often cause many difficulties, including extreme pH reduction caused by cell metabolites, insufficient dissolved oxygen levels, and plasmid lack from *E. coli* [236]. These difficulties are frequently associated with a low or even non-detectable protein production [237]. Therefore the overnight expression approach may have resulted in a culture that suffered from these problems, resulting in reduced yield.

Due to its small size, the Afb2C's MW was determined by Tricine-SDS-PAGE where the pores of the polyacrylamide gel are quite small, thus permitting a sharp separation of the Afb2C band. Then MALDI-TOF-MS

was used to confirm the mass of the Afb2C protein, and the result showed that there was a mass deviation of about 228 Da compared to the theoretical mass. This might be due to the cleavage of the Afb2C's N-terminal methionine (131 Da). Furthermore this deviation in the mass of Afb2C protein was also noticed when use the MALDI-TOF in the determination of other standard protein masses (Section 3.2.2).

The binding of ZnPP molecules with the Afb2C ligand of Afb2C-PbS QDs was characterised using agarose gel electrophoresis. Due to their relatively large size, the Afb2C-PbS QDs and ZnPP-Afb2C-PbS QDs migrate on low-density 0.5% (w/v) agarose gel and separated at 100 V for 1 hour to protect them from degradation by heating effect. The agarose gel confirmed the successful binding of ZnPP molecules with Afb2C through two different interpretations. First, the fluorescence of the band of ZnPP-Afb2C-PbS QDs under UV light was not observed on the Afb2C-PbS QDs band. Second, the migration of the ZnPP-Afb2C-PbS QDs on the gel was faster than that of the Afb2C-PbS QDs, however, Afb2C-PbS QDs are smaller in size than ZnPP-Afb2C-PbS QDs. We expect that the binding of ZnPP molecules with Lys residues on the Afb2C leads to a reduction of the positive charge and an increase in the net negative charge of the Afb2C. This was also observed when ZnPP molecules were conjugated with *G*Luc-*Li*Dps (Section 5.2.2) suggesting that the binding of ZnPP with Afb2C was achieved using the EDC/NHS linking agent.

The size of Afb2C-PbS QDs and ZnPP-Afb2C-PbS QDs has been scrutinised under TEM. TEM provides the size of the PbS core without the ligand. This is because TEM gives the images based on the contrast that arises from the interaction of the electron beam with the samples. The main components of protein (carbon, hydrogen, nitrogen, and oxygen) have very low electron absorption compared to the electron beam's intensity [238]. Therefore TEM for Afb2C-PbS QDs and ZnPP-Afb2C-PbS QDs provided images of the PbS QDs, since the Afb2C ligand give a relatively low contrast sensitivity. TEM images show that the PbS diameter is the same in these QDs and the binding of ZnPP molecules did not affect the Afb2C-PbS QDs' central core. This was also observed from the PL measurements. Hence it can be stated that the result of TEM corroborates with the results of the PL assay by demonstrating that the size of Afb2C-PbS QDs and ZnPP-Afb2C-PbS QDs' central core is ~5 nm. However ZnPP-Afb2C-PbS QDs were oval-shaped (Figure 6.13 A & B) compared to the spherical shape of Afb2C-PbS QDs (Figure 6.8 A & B) in the TEM images. We assume that the conjugation of ZnPP might be effected on the shape of ZnPP-Afb2C-PbS QDs when they were loaded on graphene-coated grid for TEM imaging

Within this thesis Afb2C-PbS QDs and ZnPP-Afb2C-PbS QDs were assayed for *in vitro* activity against breast cancer cell lines. In addition, their imaging capabilities were also assessed.

Chapter 7

7 Protein nanoparticles for breast cancer treatment

7.1 Introduction

7.1.1 Breast cancer

Breast cancer is the second leading cause of cancer deaths among women, [239,240] (Section 1.2). Although improvements in breast cancer treatment have helped reduce mortality, breast cancer is still a main cause of cancer deaths in women [240]. Breast cancer is mainly treated by chemotherapy, radiotherapy, and surgery [241,242]. Most patients with breast cancer are usually subject to more than one of the treatment options to control this disease. However these treatments often produce side effects, and much current effort is centred on the development of targeted therapies that reduce the side-effects of the chemotherapy on the normal cells and are selective of cancer cells [242]. Targeted cancer therapies are drugs modified to interfere with specific molecules required for tumour growth and metastasis and which also differentiate between normal cells and cancer cells. In this study we have designed novel targeted cancer therapies for use as theranostic agents for the diagnosis and treatment of breast cancer. Theranostic agents have advantages including cost-effective medication strategies, highly efficient and specific treatment protocols,

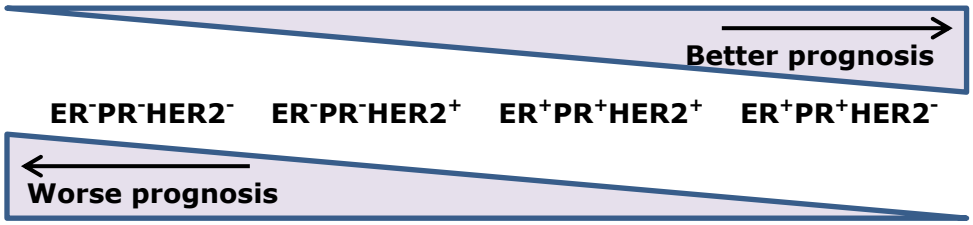
providing a guidance in preclinical therapy development or clinical trial suitability to gain positive results [243].

At the molecular level, breast cancer is a group of heterogeneous diseases that comes with variant clinical and histological features [244,245]. Immunohistochemistry of oestrogen receptor (ER), progesterone receptor (PR), and HER2 markers along with clinicopathological features such as tumour grade, size, histologic type, surgical margins, and nodal involvement have been used to divide breast cancer cell lines into 5 distinct subtypes [246,247] (Table 7.1).

Types	**Immunoprofile**	**Other specifications**	**Model cell lines**
Basal	PR^-, ER^-, $HER2^-$	Often chemotherapy responsive	MDA-MB-468, SUM190
Claudin-low	PR^-, ER^-, $HER2^-$	Intermediate chemotherapy responsive	BT549, Hs578T, MDA-MB-231, SUM1315
Luminal A	$PR^{+/-}$, ER^+, $HER2^-$	Often chemotherapy responsive	MCF-7, SUM185, T47D
Luminal B	$PR^{+/-}$, ER^+, $HER2^+$	Variable response to chemotherapy. $HER2^+$ are trastusumab responsive	BT474, ZR-75
HER2	PR^-, ER^-, $HER2^+$	Trastusumab responsive, high response to chemotherapy	MDA-MB-453, SKBR3

Table 7.1: Breast cancer cell classification and specifications [246].

ER, PR and HER2 receptors are an essential factor for disease prognosis and cellular recognition of therapy [244,245,248]. Breast cancer cells that lack the aforementioned receptors are associated with poor prognosis and resistance to hormonal therapies (Scheme 7.1). However, in the current study MDA-MB-231 and SKBR3 cell lines were chosen which lose ER and PR receptors. These cell lines have a varied response to chemotherapy, from intermediate in MDA-MB-231 to high in SKBR3 cell line.



Scheme 7.1: explains the patient's prognosis based on ER, PR and HER2 markers.

Herein, the SKBR3 ($ER^-PR^-HER2^+$) and MDA-MB-231 ($ER^-PR^-HER2^-$) cell lines, which differ in their responses to therapy, were treated with three novel protein systems, *G*Luc-*Li*Dps-ZnPP plus coelenterazine, Afb2C-PbS QDs, and ZnPP-Afb2C-PbS QDs, and their behaviour was assessed. In addition, MRC5, a non-cancerous cell line from lung tissue, was used as a control for cells treated with *G*Luc-*Li*Dps-ZnPP plus coelenterazine.

7.1.1.1 SKBR3 cell line

SKBR3 is a human breast cancer cell line isolated from a pleural effusion in a 43-year-old female with breast adenocarcinoma [249]. These cells exhibit epithelial morphology and form poorly cohesive grape-like structures in tissue culture [246] (Figure 7.1). SKBR3 cells express between 1,000,000 and 2,000,000 HER2 receptors per cell, whereas non-cancerous cells express about 20,000 HER2 receptors per cell. Consequently, the SKBR3 cell line is used as a positive control in HER2 assays. In addition, SKBR3 cancer cells are a suitable preclinical model for screening therapies that target HER2 [250].

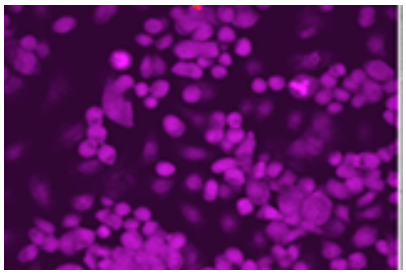


Figure 7.1: Confocal image shows the grape-like structure of SKBR3 breast cancer cells.

7.1.1.2 MDA-MB-231 cell line

The MDA-MB-231 breast cancer cells were obtained from a pleural effusion in a 51-year-old female with metastatic breast adenocarcinoma [249]. The cells display epithelial morphology with a spindle-shaped structure [246] (Figure 7.2). MDA-MB-231 cells lack

ER, PR, and HER2 receptor and are thus characterised as triple negative. Consequently, the cells are associated with poor prognosis, and they exhibit highly invasive characteristics [251].

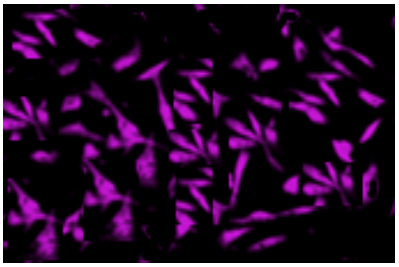


Figure 7.2: Confocal image shows a spindle-shaped structure of MDA-MB-231 breast cancer cells.

7.1.1.3 MRC5 cell line

MRC5 human lung cells were derived from the tissue of a 14-week-old male foetus aborted from a physically healthy 27-year-old woman [252]. The cells have a fibroblast morphology with a typically small spindle shape (Figure 7.3). MRC5 cells have been widely used in preclinical studies as a non-cancerous control [253].

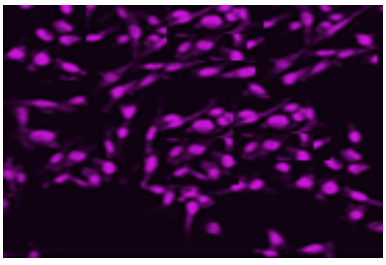


Figure 7.3: Confocal image shows a spindle-shaped structure of MRC5 human lung cells.

7.1.2 HER family

The Human Epidermal Growth Factor receptor (HER) is a large family of receptors that plays a vital role in the pathogenesis of numerous human cancers. HER receptors control cell proliferation, survival, and differentiation through several signal transduction pathways and contribute to cellular growth and differentiation. The family is structurally related to tyrosine kinase proteins and it comprises four members: HER1, HER2, HER3, and HER4 also known as ErbB1, ErbB2, ErbB3, ErbB4 respectively. All HER receptor members contain an extracellular ligand binding site: a transmembrane lipophilic domain, as well as an intracellular protein tyrosine kinase domain [254,255].

HER receptors are found as a monomer on the cell surface. There are 11 ligands that bind to HER receptors, some of these bind to HER1 and the others bind to HER3 and/or HER4 receptors [242,256]. Once the ligand binds to the extracellular domains, the intracellular segments of HER receptors undergo homo- or hetero-dimerisation and transphosphorylation. These processes lead to HER receptor activation. HER2 has no known ligand for binding and may be activated upon heterodimerisation with other HER members such as HER1 and HER3. Upon homo or heterodimerisation, the tyrosine residues within the cytoplasmic segment of the receptors undergo autophosphorylation and this initiates a range of signalling pathways [242]. Breast cancer cells have been shown to need activated HER receptors to proliferate, invade, and metastasize in trial models.

Overexpression of HER2 receptors has been recognised in breast cancer and this is normally associated with a poor prognosis in patients with breast cancer. HER2 overexpression has also been observed in many types of cancers such as ovarian, stomach, uterine serous, endometrial carcinoma, colon, lung, bladder, head and neck, esophagus and uterine cervix [254].

Recently, therapeutic approaches include the use of monoclonal antibodies, i.e. trastuzumab (Herceptin®) for blockade of specific receptors and inhibition of tyrosine kinase activity. Consequently, various biological therapies focused against growth factor receptor pathways are currently in clinical trials such as lapatinib, and pertuzumab [257,258]. Trastuzumab, a humanised monoclonal antibody is the first therapy approved by FDA for HER2-positive breast cancer treatment. However it was reported that most cancers develop resistance to trastuzumab, demanding the requirement for alternate HER2-directed therapeutic strategies [258]. Anther HER2-targeted therapy is Kadcyla® that comprises of the trastuzumab conjugate with emtansine drug which inhibits tubulin polymerisation. This drug has been approved by FDA and the European Medicine Agency (EMA) to use for treatment of HER2-overexpressed cancer cells [259,260]. One such molecule is the Afb that is known to bind with high affinity to HER2 receptors, competes with neither pertuzumab [230] nor trastuzumab [231], and there are no detectable biological effects

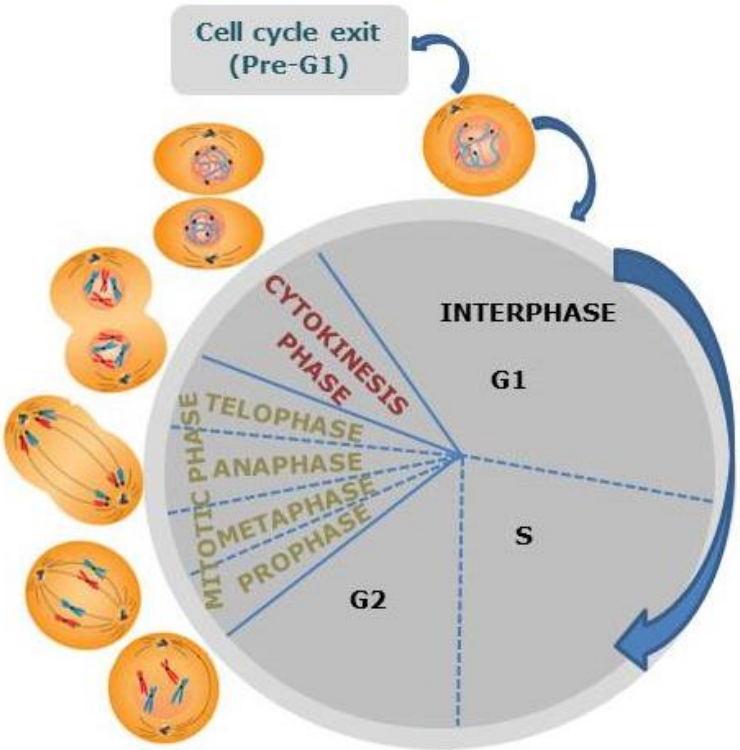
appears upon using of the Afb molecules [261]. These advantages make it more suitable to use as a drug delivery in biological studies [166].

7.1.3 Cell cycle

The cell cycle is a multi-step process involving DNA division and duplication and leads to the production of two separated cells [262]. **Pre-G1 phase** (quiescence) is a resting phase in which cell division has stopped and the cell has exited the cell cycle. Some cells, including non-proliferative/non-dividing cells, enter pre-G1 phase from G1 phase and remain quiescent for a long time, perhaps forever. Cellular death (senescence) caused by DNA damage or degradation (non-viable) also promotes entry into pre-G1 phase. In contrast, cells that divide continuously do not enter pre-G1 phase but remain in the cell cycle.

The cell cycle is divided into three phases. **Interphase** (intermitosis) is the first step of the cell cycle. In this phase, a cell prepares to divide through a series of changes that take place in the cell and its nucleus before division. Interphase is subdivided into three phases: G1, S, and G2 phases. In ***G1 phase*** (growth), the cell synthesis proteins and increases in size. The number of organelles (such as ribosomes and mitochondria) also increases. The G1 checkpoint ensures the cell is ready for DNA synthesis. ***S phase*** (DNA replication) starts with DNA

replication to double the number of chromosomes and produce two sister chromatids. ***G2 phase*** (growth) involves protein production and cell growth. The G2 checkpoint ensures the cell is ready to enter the second phase of the cell cycle, mitosis. In the **mitotic phase** (chromosome separation), the cell nucleus separates into two nuclei with identical numbers and types of chromosomes as the parent cell. This phase proceeds in four sequential steps: prophase, metaphase, anaphase, and telophase. During these steps, chromosomes condense, and sister chromatids attach to fibers that separate the sister chromatids and draw them to opposite sides of the cell. Finally, in the last phase of the cell cycle, known as **cytokinesis,** the cell cytoplasm and other organelles divide into identical daughter cells [263,264] (Scheme 7.2). Anti-proliferative signals play important roles in the cell cycle by inhibiting cell proliferation, forcing a cell to exit to pre-G1 phase, and promoting terminal differentiation. These signals include growth inhibitors in the extracellular matrix and on the surfaces of neighbouring cells. However, mutations allow cancer cells to escape these signals [265]. The DNA of cancer cells that are active in the cell cycle can be targeted by cancer therapies because it is relatively exposed during cell division and consequently sensitive to degradation by anticancer therapies [266].



Scheme 7.2: Schematic showing the mammalian cell cycle. The cell either enters the cell cycle starting from interphase, passing through the mitotic phase to produce two identical sister cells in the cytokinesis phase. Or the cell exits from cell cycle to Pre-G1 phase as a result of DNA damage or cell division arrest.

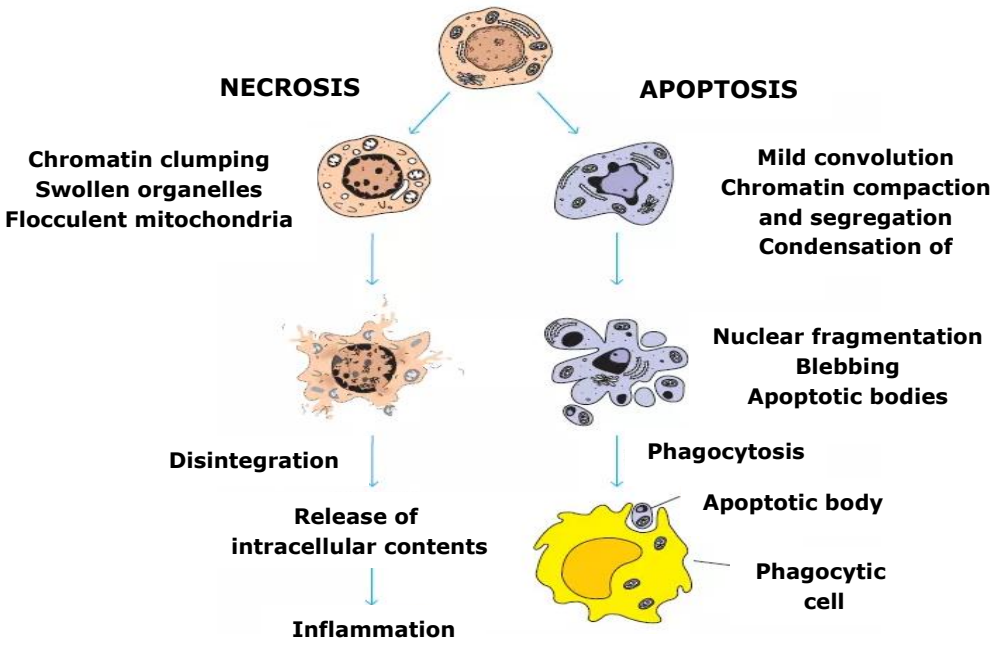
7.1.4 Programmed cell death pathways: apoptosis and necrosis

Programmed cell death is an essential process for balancing cell death and normal cell survival. There are many pathways for programmed cell death, including apoptosis and necrosis [267,268]. Apoptosis, the

main pathway, usually occurs during cell progression and ageing as part of the metastatic process in tissues. In addition, apoptosis can occur as a result of defence mechanisms, such as in immune reactions or responses to cell damage by disease or other agents [267]. Apoptosis involves biochemical and morphological changes, including nuclear condensation and fragmentation, cell shrinkage, loss of adhesion to neighbouring cells or the extracellular matrix, and dynamic membrane blebbing [268]. Apoptosis is stimulated in response to various physiological and pathological factors. Further, cancer therapies that target and damage DNA in cancer cells may induce apoptosis in certain cells. Anti-apoptotic proteins such as those in the Bcl-2 (B-cell lymphoma protein-2) family protect the cell from apoptosis and promote cell survival under conditions that stimulate cell death through apoptosis. In cancer cells, overexpression of Bcl-2 together with other family members such as Mcl-1 (myeloid cell leukemia-1) allows cancer cells to avoid apoptosis. Reducing Bcl-2 expression might promote apoptosis induced by anticancer therapies [269,270].

Necrosis is a specific type of programmed cell death. It occurs through an unsystematic and uncontrolled process after energetic failure and/or physical damage. Furthermore cells may be undergo necrosis under normal physiological and regulated (programmed) event [271]. Cells in necrosis undergo several morphological changes, including

organelle swelling, an increase in cell volume, and plasma membrane damage, followed by the release of intracellular contents [268]. Necrosis, similar to apoptosis, might lead to programmed cell death, although the consequences of apoptotic and necrotic cell death are very different for the whole organism. In necrosis, the integrity of the cell membrane is disturbed, and intracellular materials are released into the intercellular space, leading to inflammatory responses by immune cells; this might stimulate tumour growth. In contrast, during apoptosis intracellular materials are securely isolated inside macrophages [267]. Programmed cell death pathways have been widely exploited in new strategies for cancer treatment that trigger the signal that initiates apoptosis or necrosis (Scheme 7.3).



Scheme 7.3: Difference in morphology of cells undergoing apoptosis and necrosis [272].

7.1.5 ROS in healthy cells and cancer cells

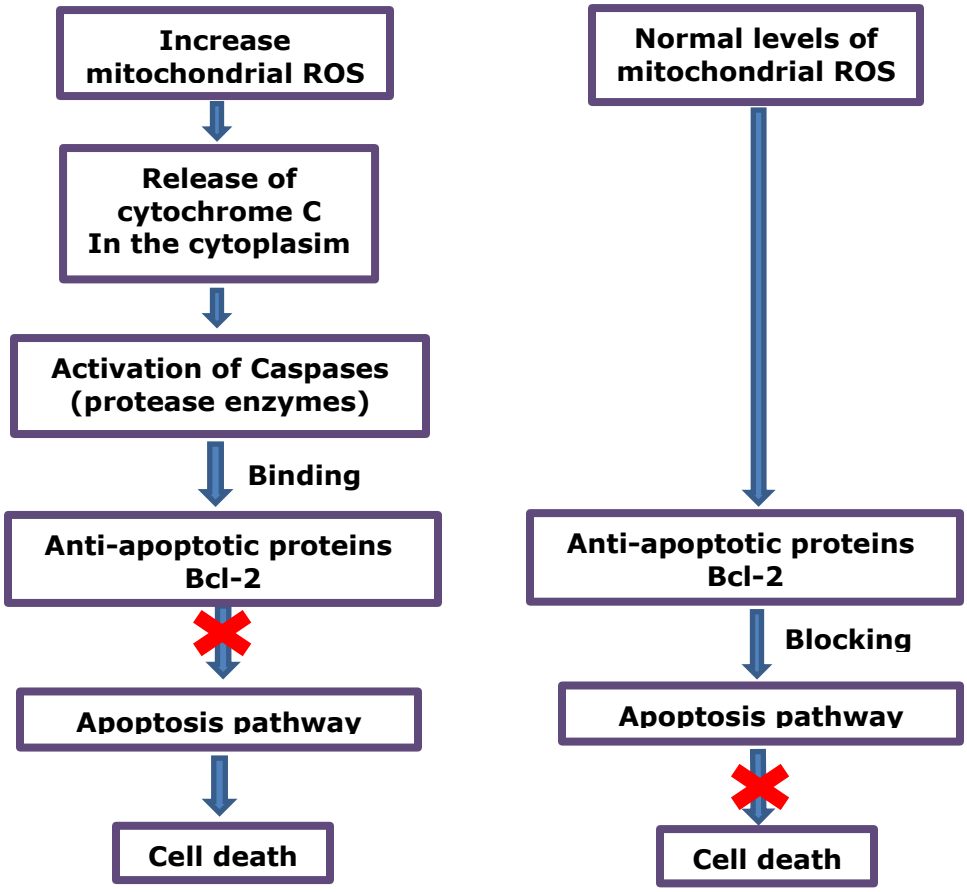
ROS are molecules, ions, or radicals with an unpaired single electron in their outer electron shell and are therefore highly reactive. They can be classified into two types: free oxygen radical ROS (such as superoxide ($O2^{\bullet -}$), hydroxyl radical ($^{\bullet}OH$), and peroxyl radicals ($ROO^{\bullet}$)) and non-radical ROS (such as singlet oxygen ($^1O_2$) and hydrogen peroxide (H_2O_2)) [273]. ROS are normally produced in all aerobic cells in equilibrium with antioxidant molecules or enzymes such as catalase, ascorbic acid, and superoxide dismutase. In the case of an acute excess of ROS, the balance with antioxidants is disrupted, and oxidative stress occurs [274]. ROS are highly toxic molecules that produce cell damage by reacting with nucleotides in DNA, sulfhydryl groups in proteins, and lipids in cellular membranes and by cross-linking/fragmenting ribonucleoproteins [274].

Increased production of ROS is a hallmark of several cancer cell lines and other tumours. In cancer cells, ROS production increases for many reasons, such as mitochondrial dysfunction, increased metabolic activity, peroxisome activity, increased signalling of cellular receptors, and increased activity of oxidases, lipoxygenases, and cyclooxygenases [273].

Mitochondrial ROS, which function as signalling molecules for cellular physiological modifications, are believed to promote genomic

instability that is capable of initiating tumour growth (tumourigenic). The increase in ROS levels in cancer cells can induce tumorigenesis by activating signalling pathways that regulate cellular proliferation, metabolic alterations, and angiogenesis [275].

Alternatively release of ROS from Mitochondria at high levels can causes cellular damage and promote cell cycle arrest and apoptosis in cancer cells. In this process, an increase of mitochondrial oxidative stress leads to the release of cytochrome C, which induces the activation of specific proteases known as caspases, and a lack of asymmetry in membrane phospholipids, resulting in phosphatidylserine externalisation. This mechanism has been exploited by anticancer therapies that induce the generation of free radicals in the cancer cell [273,276] (Scheme 7.4).



Scheme 7.4: Roles of ROS in triggering of cancer cell apoptosis.

7.1.6 Enhanced permeability and retention (EPR) effect

The EPR effect is a phenomenon in which tumour tissues accumulate and retain macromolecules such as polymers and proteins of a certain molecular weight (> 40–50 kDa) for periods of time longer than observed in healthy tissues. This effect has been widely exploited to design anticancer therapies in which macromolecules are targeted to malignant tissues where they accumulate to concentrations 10–200

times higher than in normal tissues [277]. The EPR effect is due to leaky vessels and poor lymphatic drainage in solid tumours. Because the macromolecules are not small enough to be excreted by the kidney and not large enough to be rapidly distinguished and trapped by the reticuloendothelial system (RES), they tend to circulate for long times. This leads to preferential leakage of these molecules across the permeable tumour vasculature and into solid tumours, where they are retained.[278].

7.1.7 *In vitro* effect of novel nanoparticle protein on breast cancer cell lines

This study focused on the design and synthesis of novel theranostic agents that can act as imaging agents, PDTs, and/or drug delivery systems for cancer treatment. This chapter describes in detail the *in vitro* study of three of these potential therapies, *G*Luc-*Li*Dps-ZnPP plus coelenterazine, Afb2C-PbS-QDs, and ZnPP-Afb2C-PbS QDs.

7.2 Results

7.2.1 *G*Luc-*Li*Dps-ZnPP

7.2.1.1 Effect of *G*Luc-*Li*Dps-ZnPP plus coelenterazine on cell viability and proliferation

To assess the inducible cytotoxicity of *G*Luc-*Li*Dps-ZnPP plus coelenterazine, the MTT assay was performed using SKBR3 and MDA-MB-231 human breast cancer cell lines and the MRC5 non-cancerous cell line.

Initially, the cytotoxic effect of coelenterazine (*G*Luc's substrate) was examined at concentrations between 4 to 10 µg/mL to determine a safe dose to use in subsequent *in vitro* assays. Exposure to coelenterazine at a concentration of 5 µg/mL for 72 hours did not affect the proliferation of SKBR3, MDA-MB-231, or MRC5 cells. Consequently, this concentration was used in further studies (Figure 7.4).

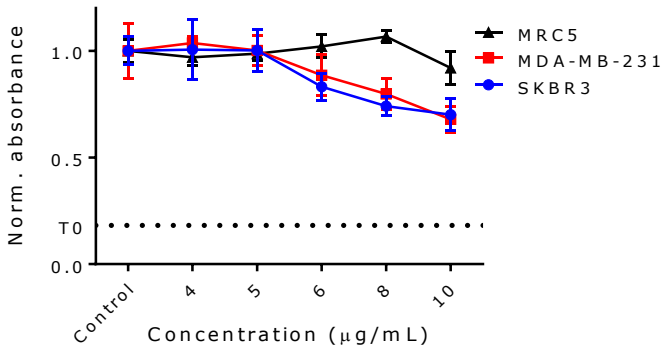


Figure 7.4: Cell proliferation study using the MTT assay. The growth inhibitory effect of coelenterazine on SKBR3, MDA-MB-231, and MRC5 cell lines. Cells were seeded at a density of 3×10^3 cells/well in 96-well plates incubated for 24 hours, and treated with coelenterazine for 72 hours.

The inhibitory effect of *G*Luc-*Li*Dps-ZnPP plus coelenterazine on SKBR3 cell growth was highly significant ($P < 0.0001$) when compared to the effect on MDA-MB-231 and MRC5 cell lines (Figure 7.5).

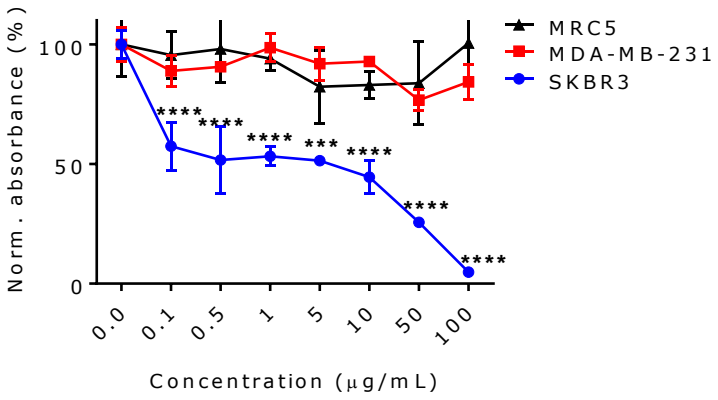


Figure 7.5: Cell proliferation study using the MTT assay. The growth inhibitory effect of *G*Luc-*Li*Dps-ZnPP plus coelenterazine on SKBR3, MDA-MB-231, and MRC5 cell lines. Cells were seeded at a density of 3×10^3 cells/well in 96-well plates, incubated for 24 hours, and treated with *G*Luc-*Li*Dps-ZnPP plus coelenterazine for 72 hours.* indicates significant difference when compared to MRC5 cells. ***P < 0.001, ****P < 0.0001.

The *G*Luc-*Li*Dps-ZnPP plus coelenterazine concentration that reduced growth 50% (GI_{50}) in SKBR3 cells was 14.8 µg/mL (standard error of the mean 0.28). These results indicate that *G*Luc-*Li*Dps-ZnPP plus coelenterazine has a selective and potent growth inhibitory effect on SKBR3 cells. This was not observed in the MDA-MB-231 and MRC5 cell lines. The growth inhibitory activity of each component was separately examined by exposing SKBR3 cells to *G*Luc-*Li*Dps-ZnPP, *G*Luc-*Li*Dps, *G*Luc-*Li*Dps plus coelenterazine, and ZnPP. Anticancer activity of ZnPP

was reported in different cell lines and tumours [118,219,220]. However our results show that ZnPP and other *G*Luc-*Li*Dps-ZnPP components had a small effect on SKBR3 when compared to the effect of *G*Luc-*Li*Dps-ZnPP plus coelenterazine, indicating that the growth inhibitory effect is mainly due to the generation of singlet oxygen by *G*Luc-*Li*Dps-ZnPP plus coelenterazine (Figure 7.6).

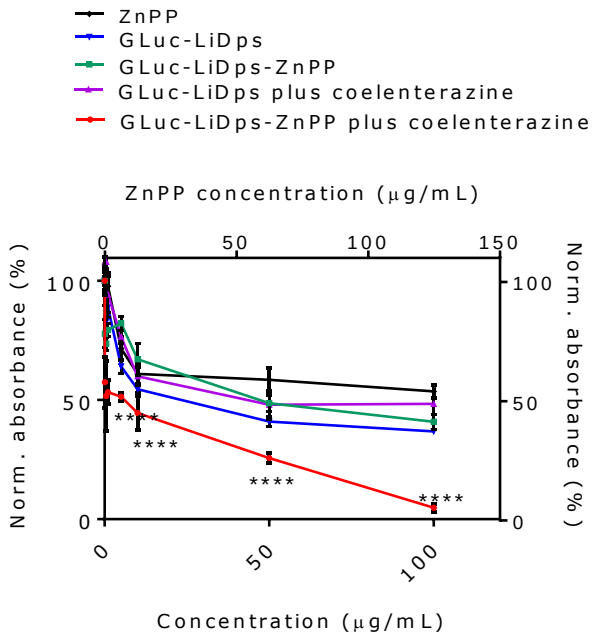
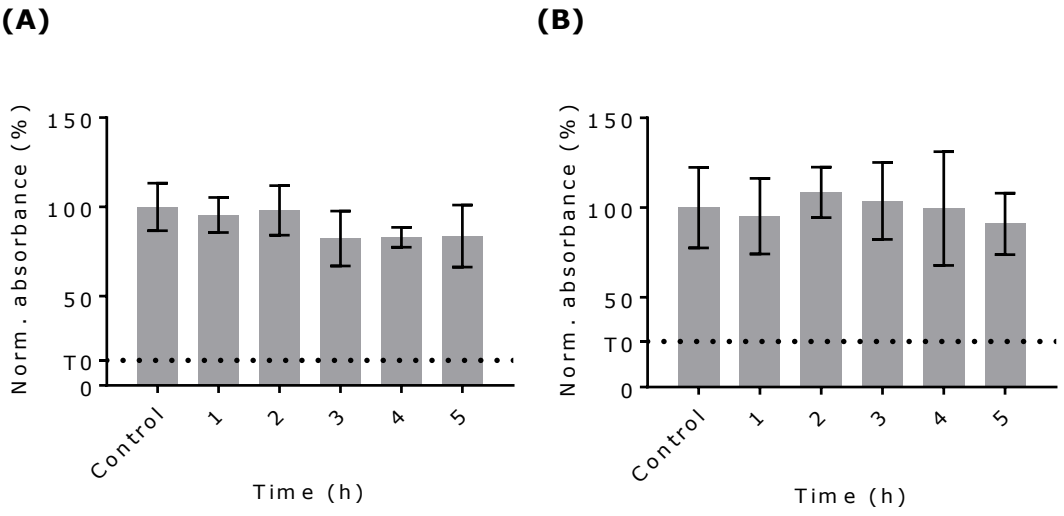


Figure 7.6: Growth inhibitory effect of *G*Luc-*Li*Dps-ZnPP plus coelenterazine, *G*Luc-*Li*Dps-ZnPP, *G*Luc-*Li*Dps plus coelenterazine, *G*Luc-*Li*Dps, and ZnPP on the SKBR3 cell line. Cells were seeded at a density of 3×10^3 cells/well in 96-well plates, incubated for 24 hours, and treated with each component for 72 hours. * indicates significant difference compared to control ****(P<0.0001).

Furthermore, a time course was used to determine the intracellular effect of *G*Luc-*Li*Dps-ZnPP plus coelenterazine and the optimum time

for the addition of coelenterazine. SKBR3, MDA-MB-231, and MRC5 cell lines were treated with *G*Luc-*Li*Dps-ZnPP for different times. The medium was removed. Cells were then washed with phosphate buffered saline (PBS) and incubated for 72 hours in fresh medium containing 5 µg/mL coelenterazine. A clear time-dependent response was observed for SKBR3 cells, while MDA-MB-231 and MRC5 cells showed no response to *G*Luc-*Li*Dps-ZnPP-mediated PDT (Figure 7.7).

The results indicated that maximum inhibition ($P < 0.0001$) was achieved when coelenterazine was added after 5 hours of SKBR3 cell treatment with *G*Luc-*Li*Dps-ZnPP. An effect was not observed in MRC5 or MDA-MB-231 cells.



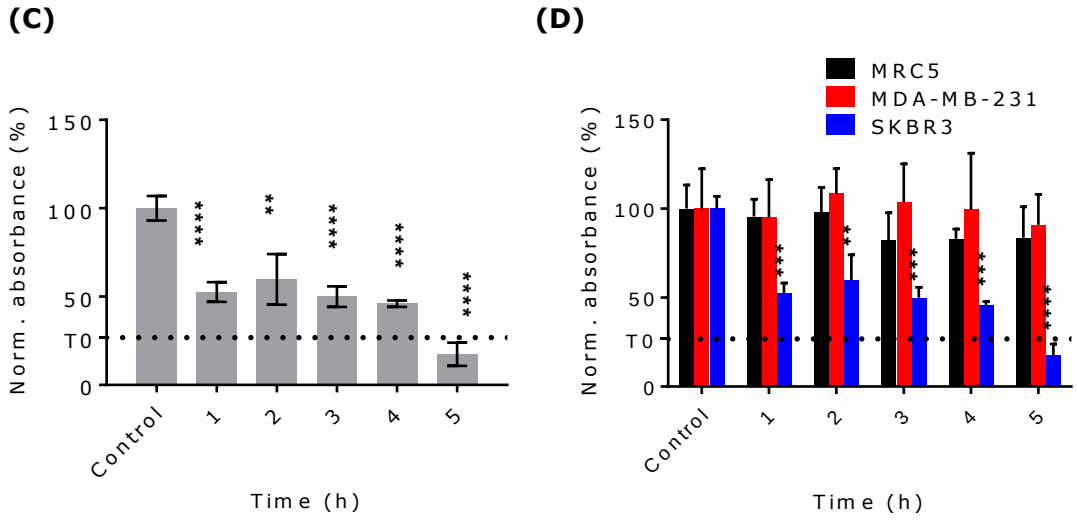
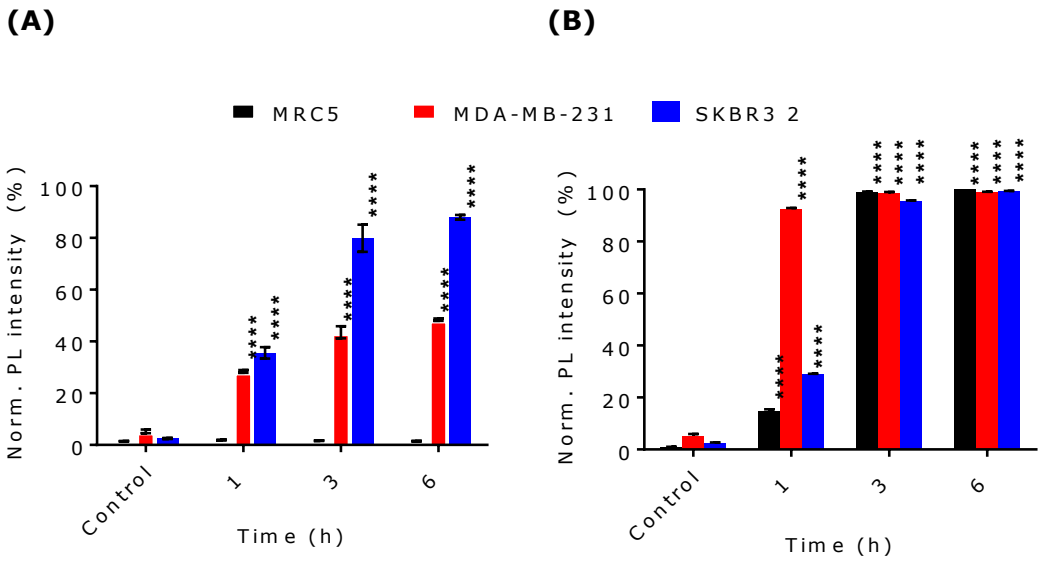


Figure 7.7: Time-dependent course of *G*Luc-*Li*Dps-ZnPP plus coelenterazine treatment. The growth inhibitory effect of *G*Luc-*Li*Dps-ZnPP plus coelenterazine on **(A)** MRC5, **(B)** MDA-MB-231, and **(C)** SKBR3 cell lines. **(D)** The comparison of *G*Luc-*Li*Dps-ZnPP plus coelenterazine effect on the above cell lines. Cells were seeded at a density of 3×10^3 cells/well in 96-well plates. * indicates significant difference compared to control **(P<0.01), ***(P<0.001), and ****(P<0.0001).

7.2.1.2 *G*Luc-*Li*Dps-ZnPP cellular uptake and localisation study

To explain the variation in the growth inhibitory effects, cellular uptake in MRC5, MDA-MB-231, and SKBR3 cells was studied in the presence of *G*Luc-*Li*Dps-ZnPP and compared with ZnPP uptake using flow cytometry. The cell lines were treated with a *G*Luc-*Li*Dps-ZnPP concentration of 2× GI_{50}, and fluorescence was detected over 6 hours. The fluorescence intensity detected by flow cytometry represents the cellular uptake efficiency. Interestingly, SKBR3 cells revealed fluorescent light twice higher than that detected in MDA-MB-231 (P <

0.0001), while fluorescence in MRC5 cells was at trace level or non-detectible after 6 hours of incubation. *G*Luc-*Li*Dps-ZnPP was mostly taken up by the cells after 3 hours; the amount increased by ~8% after 6 hours of treatment (Figure 7.8 A). These results are consistent with the cytotoxic effect of *G*Luc-*Li*Dps-ZnPP plus coelenterazine on these cell lines (Section 7.2.1.1), and they suggest that *G*Luc-*Li*Dps-ZnPP elicited dose-dependent growth inhibition through its ability to recognise and target breast cancer cells. In addition, ZnPP alone, non-selectively penetrated all the cells at levels greater than *G*Luc-*Li*Dps-ZnPP ($P < 0.0001$) (Figure 7.8 B).



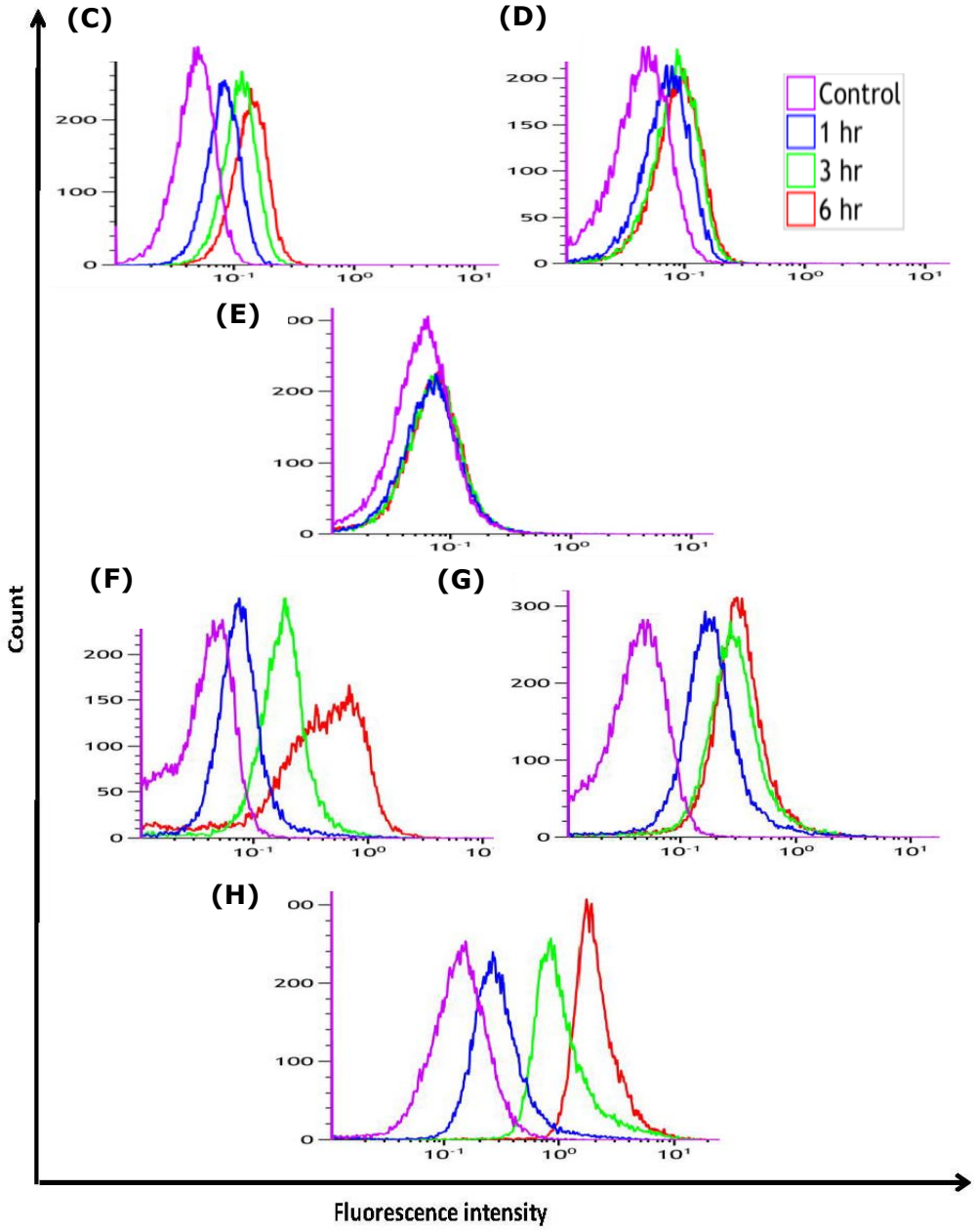


Figure 7.8: Cellular uptake efficiency of **(A)** *G*Luc-*Li*Dps-ZnPP and **(B)** ZnPP by MRC5, MDA-MB-231, and SKBR3 cells. Flow cytometry analysis graph in **(C)**, **(D)**, and **(E)** depict SKBR3, MDA-MB-231, and MRC5 uptake of *G*Luc-*Li*Dps-ZnPP, respectively, while those in **(F)**, **(G)**, and **(H)** depict SKBR3, MDA-MB-231, and MRC5 uptake of ZnPP, respectively. Cells were seeded at a density of 3.5 × 10^5 cells/well in 6-well plates and treated with a *G*Luc-*Li*Dps-ZnPP concentration of 2× GI_{50}. * indicates significant difference compared to control ****(P<0.0001).

7.2.1.3 Intracellular ROS generated by *G*Luc-*Li*Dps-ZnPP plus coelenterazine

*G*Luc-*Li*Dps-ZnPP plus coelenterazine was designed to act as a PDT and kill cancer cells through the generation of singlet oxygen. In this study, the H_2O_2 level was determined *in vitro* to investigate the balance between singlet oxygen and other ROS generated or triggered by *G*Luc-*Li*Dps-ZnPP plus coelenterazine and the H_2O_2 that is scavenged by *Li*Dps protein.

To assess the increase in intracellular ROS generated by *G*Luc-*Li*Dps-ZnPP plus coelenterazine, ROS levels in resting (untreated) cells were first measured. Previous experiments indicated that MRC5 cells do not internalise *G*Luc-*Li*Dps-ZnPP. Consequently, ROS levels were studied in MDA-MB-231 and SKBR3 cells. Under normal conditions, ROS levels in SKBR3 cells were higher than in MDA-MB-231 cells. The levels increased in both SKBR3 and MDA-MB-231 cells in the presence of *G*Luc-*Li*Dps-ZnPP plus coelenterazine, but this increase was significantly higher when SKBR3 cells were exposed compared to MDA-MB-231 cells ($P < 0.0001$).

The ROS levels which were induced by *G*Luc-*Li*Dps-ZnPP plus coelenterazine was significantly higher than the increase that induced by other components (Figure 7.9). Therefore, we concluded that the increase in ROS levels and the growth inhibitory effect is mainly attributable to *G*Luc-*Li*Dps-ZnPP-mediated PDT. These observations are supported by the MTT assay results (Section 7.2.1.1).

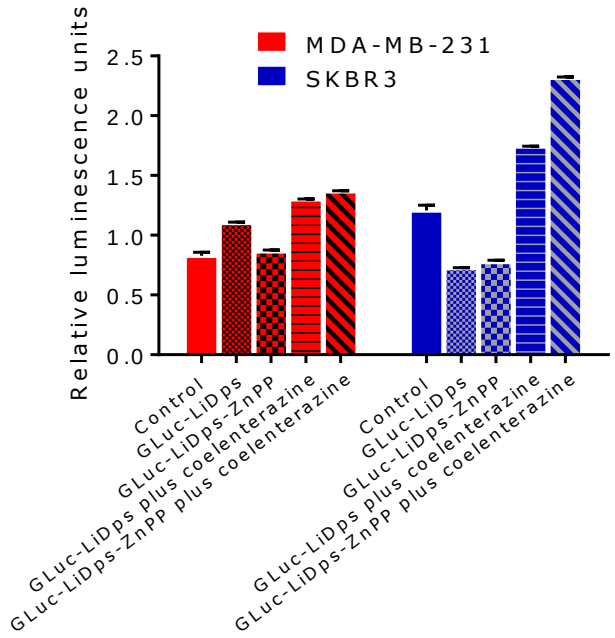


Figure 7.9: Intracellular ROS levels in SKBR3 and MDA-MB-231 cells treated with *G*Luc-*Li*Dps-ZnPP plus coelenterazine, *G*Luc-*Li*Dps-ZnPP, *G*Luc-*Li*Dps plus coelenterazine, or *G*Luc-*Li*Dps compared with levels in untreated cells (control). Cells were seeded at a density of 0.5 × 10^5 cells/well in white 96-well plates and treated with *G*Luc-*Li*Dps-ZnPP plus coelenterazine at a concentration of 2× GI_{50} and the corresponding concentration of each component.

7.2.1.4 Effect of *G*Luc-*Li*Dps-ZnPP plus coelenterazine on Bcl-2 and Mcl-1 anti-apoptotic proteins

Bcl-2 and Mcl-1 which belong to the Bcl-2 anti-apoptotic protein family are commonly upregulated/overexpressed in cancer cells. Their downregulation reduces cancer cell proliferation [279,280]. The proteins play a key role in protecting cells from apoptosis through

various mechanisms. Consequently, Bcl-2 family members have been targeted in anticancer therapies [270].

PDT is thought to enhance photo-damage to Bcl-2 and other related anti-apoptotic proteins and activate the apoptotic pathway. Alteration in the expression of Bcl-2 family proteins following exposure to PDT has been characterised in many tumours and cell lines [82]. Therefore, using Western blots, Bcl-2 and Mcl-1 proteins were investigated in SKBR3 cells after treatment with *G*Luc-*Li*Dps-ZnPP plus coelenterazine for 1, 3, and 6 hours. SKBR3 cells wrere showed downregulation in the expression of Bcl-2 and Mcl-1, and the proteins were undetectable in the presence of *G*Luc-*Li*Dps-ZnPP plus coelenterazine after 6 hours of treatment (Figure 7.10). Both Bcl-2 and Mcl-1 were undetectable after 1 hour of treatment with *G*Luc-*Li*Dps-ZnPP-mediated PDT. Bcl-2 levels partially recovered after 3 hours, but then fell again to undetectable levels after 6 hours of exposure of SKBR3 cells to *G*Luc-*Li*Dps-ZnPP plus coelenterazine. We speculate that Bcl-2 might recover as part of an antioxidant defence mechanism to neutralise *G*Luc-*Li*Dps-ZnPP-mediated PDT activity. This is consistent with a previous study performed by Xue *et al* [281]. They found that Bcl-2 partially recovered in 5A100-Bcl2 cells after 2 hours of treatment with phthalocyanine Pc4 PDT. They also demonstrated that PDT caused a unique type of Bcl-2 damage that was not observed with other apoptosis-inducing agents such as staurosporine and β-lapachone

[281]. Furthermore, the study showed that the rapid disappearance of Bcl-2 was mainly due to a photochemical damage mechanism that led to the loss of Bcl-2 protein from the mitochondrial membrane; the effect extended to the Bcl-2 epitope [281]. It has also been reported that exposure to methylene blue PDT reduces the expression of Mcl-1 protein in A549 cells, in agreement with our results [282].

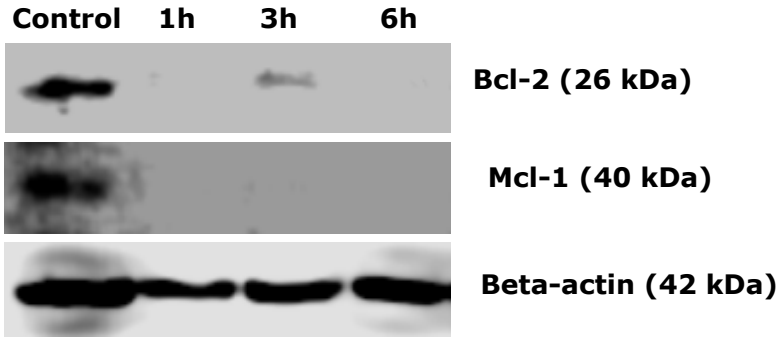


Figure 7.10: Protein expression in SKBR3 lysates following 1, 3, or 6 hours exposure of cells to *G*Luc-*Li*Dps-ZnPP plus coelenterazine. Lysates containing 50 µg proteins were loaded into each well and separated by SDS-PAGE. Western blots were performed using antibodies to detect Mcl-1 and Bcl-2 and the housekeeping gene beta-actin. SKBR3 cells were seeded at a density of 10×10^5 cells/dish in Petri dishes and treated with a *G*Luc-*Li*Dps-ZnPP plus coelenterazine concentration of $2\times$ GI_{50}.

The results strongly suggest that damage to Bcl-2 and Mcl-1, indicative of destruction of the mitochondrial membrane and release of cytochrome C, induces the apoptosis pathway in SKBR3 cells as a result of *G*Luc-*Li*Dps-ZnPP plus coelenterazine activity. Cytochrome C is an essential element of the complex that activates the death

protease caspase-3 [283]. Caspases are protease enzymes expressed in cells in inactive form; they are activated only in response to cytochrome C release (intrinsic apoptotic pathway) or extracellular ligand via death receptors on the cell surface (extrinsic apoptotic pathway). A chain reaction results from caspase initiator activation; this leads to the activation of many other executioner caspases. Over 600 cellular components are degraded by executioner caspases to induce the morphological changes for apoptosis [284,285].

7.2.1.5 Effect of *G*Luc-*Li*Dps-ZnPP plus coelenterazine on cell migration

Cell migration is often studied as an indicator of changes in physiological and pathological processes, including cancer metastasis, wound healing, embryonic development, and immune defence [286]. In the case of tumours, cell migration is prerequisite for cancer metastasis and progression [287]. In this study, the effect of *G*Luc-*Li*Dps-ZnPP plus coelenterazine on SKBR3 cell migration was investigated to understand the relationship between the observed *in vitro* changes and cell migration under apoptosis. SKBR3 cells were treated with *G*Luc-*Li*Dps-ZnPP plus coelenterazine, and wound closure was tracked every 8 hours. The migration rate was compared to that in untreated SKBR3 cells, used as a control. The results demonstrated that *G*Luc-*Li*Dps-ZnPP plus coelenterazine suppressed SKBR3 cell

migration relative to migration in control cells after 40 hours of treatment (Figure 7.11). Accordingly, *G*Luc-*Li*Dps-ZnPP plus coelenterazine seems to be a promising PDT with which to treat malignant tumours, not only because of its growth inhibitory effects, but also because of its ability to inhibit the metastasis and invasiveness of incompletely treated cancer cells.

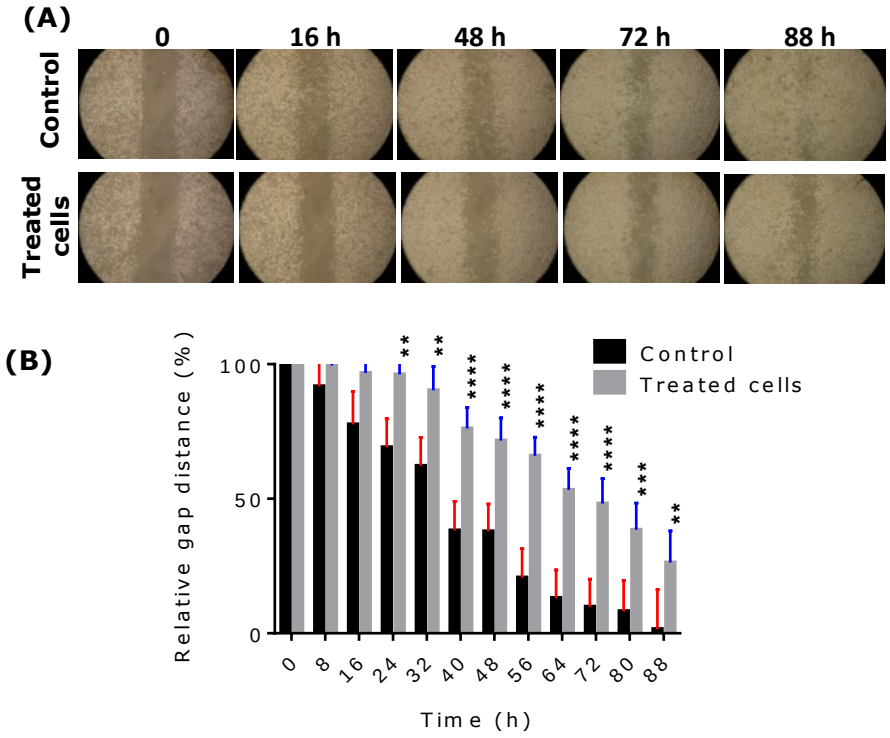


Figure 7.11: A wound healing assay was performed to assess SKBR3 cell migration after treatment with *G*Luc-*Li*Dps-ZnPP plus coelenterazine relative to migration in control (untreated) cells. **(A)** Cell migration images captured immediately after treatment (T = 0) and every 8 hours thereafter. **(B)** The cell migration rate was calculated for treated and untreated SKBR3 cells. The graph show that SKBR3 migration was significantly inhibited after 24 hours of treatment. The effect was more apparent after 40 hours. Cells were seeded at a density of 35 × 10^3 cells/well and treated with a *G*Luc-*Li*Dps-ZnPP plus coelenterazine concentration of 0.5× GI_{50}. * indicates significant difference compared to control **(P<0.01), ***(P<0.001), and ****(P<0.0001).

7.2.1.6 Confocal microscopy for monitoring the cellular localisation of *G*Luc-*Li*Dps-ZnPP

Confocal microscopy was used to investigate the ability of *G*Luc-*Li*Dps-ZnPP to act as a targeted tumour imaging agent. The cells were treated with *G*Luc-*Li*Dps-ZnPP for 1, 3, and 6 hours, and the cells were fixed using 4% (v/v) formaldehyde. *G*Luc-*Li*Dps-ZnPP localisation was monitored under a confocal microscope (Figure 7.12). *G*Luc-*Li*Dps-ZnPP nanoparticles were observed to be localised in the cytoplasm of the cell evidenced by blue fluorescences. Confocal images showed brighter fluorescence in SKBR3 cells than in MDA-MB-231 cells, and fluorescence was not observed in MRC5 cells. In addition, the fluorescent light intensity was a time-dependent response to the cell incubation periods with *G*Luc-*Li*Dps-ZnPP. These results are consistent with our findings obtained using flow cytometry (Section 7.2.1.2). These results suggest that *G*Luc-*Li*Dps-ZnPP offers a promising non-invasive method for optical imaging in the diagnosis and treatment of tumour tissues.

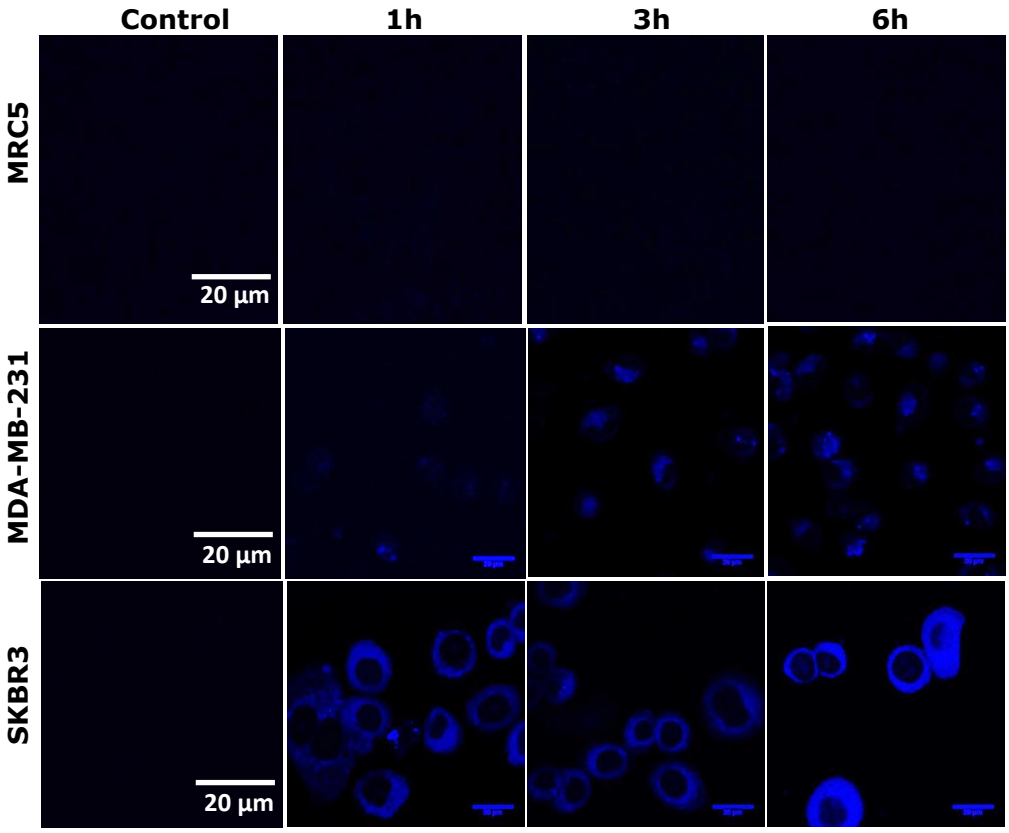


Figure 7.12: Confocal images show the fluorescent light emitted from SKBR3 and MDA-MB-231 cells after exposure to *G*Luc-*Li*Dps-ZnPP for 1, 3, and 6 hours. Fluorescence was not observed in MRC5 non-cancerous cells treated with *G*Luc-*Li*Dps-ZnPP under the same conditions. A control for each cell line was prepared for comparison. Cells were seeded at a density of 0.1×10^5 cells/well in 8-well plates and treated with a *G*Luc-*Li*Dps-ZnPP concentration of $2\times$ GI_{50}.

7.2.2 Afb2C-PbS QDs

PbS QDs are promising anticancer therapy agents that trigger ROS generation and induce cancer cell apoptosis [209]. Accordingly, PbS QDs have been designed to target HER2-overexpressing cancer cells

by coating PbS QDs with Afb2C, a protein with a high affinity for the HER2 transmembrane protein.

In addition to the advantages previously mentioned (Section 1.8), Afb binds to a HER2 conformational epitope that is distant from the binding sites recognised by the therapeutic antibodies pertuzumab and trastuzumab. This property has been exploited when using Afb for diagnosis and/or drug delivery in HER2-overexpressing tumour cells when pertuzumab and trastuzumab antibodies have already been administered [166]. It was reported that patients have revealed resistance after treating with pertuzumab and trastuzumab anti-HER2 therapies suggesting the requirement of novel therapy for breast cancer [242].

In this study, SKBR3 and MDA-MB-231 breast cancer cells were used to assess the ability of Afb2C to recognise and deliver PbS QDs to HER2-overexpressing SKBR3 cells without affecting MDA-MB-231 cells, which lack the HER2 receptor.

7.2.2.1 Effect of Afb2C-PbS QDs on cell viability and proliferation

The MTT assay was used to study the growth inhibitory effect of Afb2C-PbS QDs on SKBR3 and MDA-MB-231 cell lines. Following exposure for 72 hours, dose-dependent growth inhibition was observed in SKBR3 cells in the presence of Afb2C-PbS QDs. The GI_{50} was 26 µg/mL (standard error of the mean 0.13). MDA-MB-231 cells did not exhibit any effect when they were treated with Afb2C-PbS QDs

(Figure 7.13). These results suggest that the Afb2C coating successfully and selectively delivered QDs to HER2-overexpressing SKBR3 cells. The MTT results are consistent with a previous study, and they demonstrate that PbS QDs can inhibit the growth of targeted cancer cells [209].

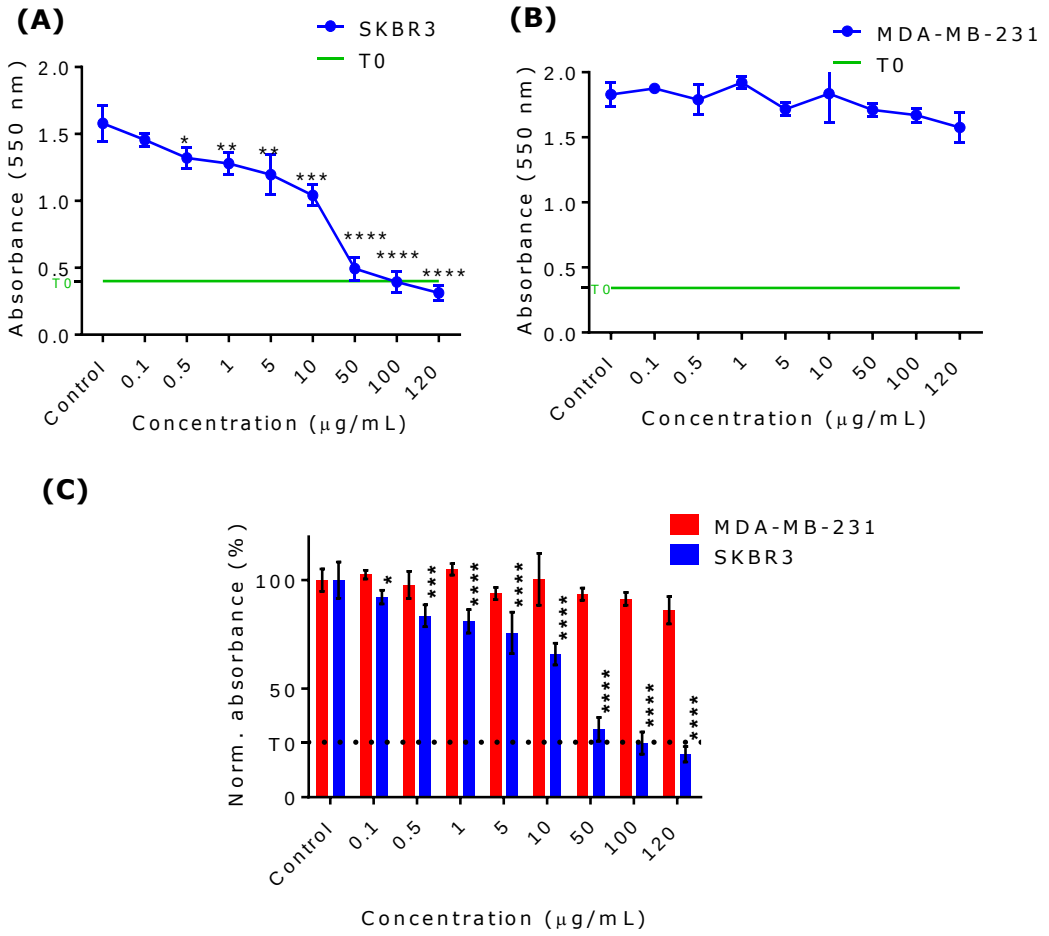


Figure 7.13: Growth inhibitory effect of Afb2C-PbS QDs on **(A)** SKBR3 and **(B)** MDA-MB-231 breast cancer cells. **(C)** Comparison of growth inhibition in the two cell lines. Cells were seeded at a density of 3×10^3 cells/well in 96-well plates and incubated for 24 hours before treatment with Afb2C-PbS QDs for 72 hours. * Significant difference compared to control in (A) and for the proliferation of SKBR3 cells compared to that of MDA-MB-231 cells in **(C)**. *(P < 0.5)., **(P<0.01), ***(P<0.001), and.****(P<0.0001).

We also studied the growth inhibitory effect of Afb2C alone to determine whether this effect interferes with the Afb2C-PbS QDs in SKBR3 and MDA-MB-231 cell lines. The MTT assay was used, and treatment with Afb2C was performed under the same conditions used with Afb2C-PbS QDs. A small growth inhibitory effect of Afb2C was detected in SKBR3 cells, and to a lesser extent in MDA-MB-231 cells. The effect was apparent at 50 µg/mL Afb2C (Figure 7.14).

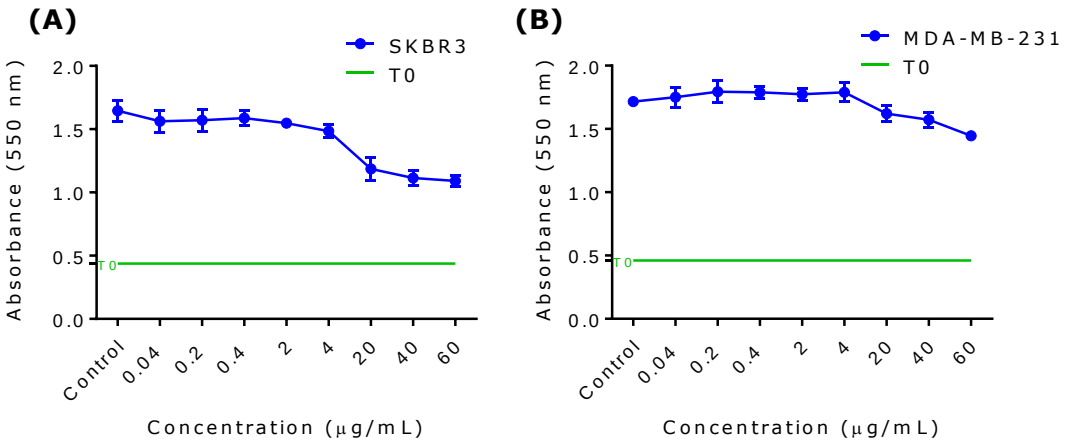


Figure 7.14: Growth inhibitory effect of Afb2C on **(A)** SKBR3 and **(B)** MDA-MB-231 breast cancer cells. Cells were seeded at density of 3×10^3 cells/well in 96-well plates and incubated for 24 hours before treatment with Afb2C for 72 hours.

However, the Afb2C growth inhibitory effect on SKBR3 and MDA-MB-231 cell lines was negligible when compared to the effect of Afb2C-PbS QDs (Figure 7.15). Therefore, we can conclude that the growth inhibitory effect was mainly attributable the PbS QDs and that the

Afb2C coating led to their accumulation in SKBR3 cells, without recognition of MDA-MB-231 cells.

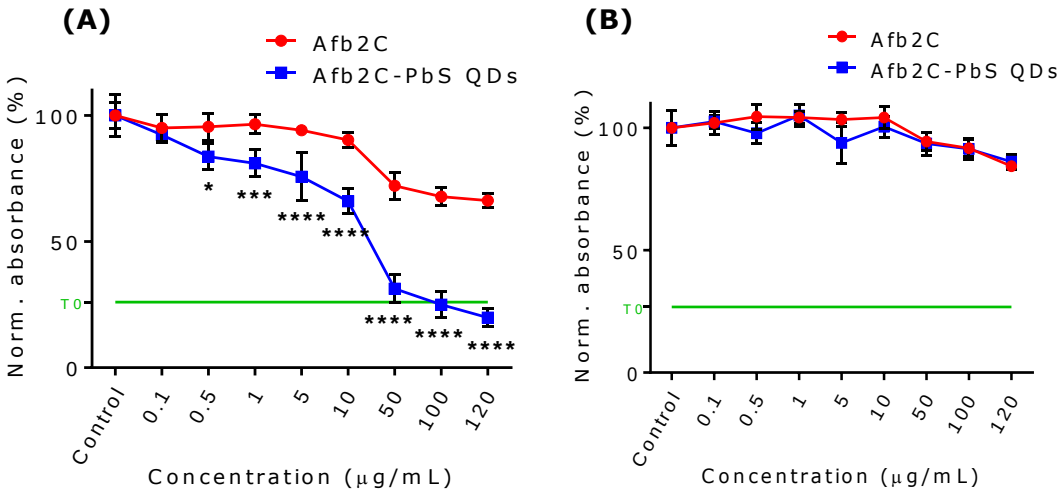


Figure 7.15: Comparison of the growth inhibitory effects of Afb2C and Afb2C-PbS QDs in **(A)** SKBR3 and **(B)** MDA-MB-231 breast cancer cells. Cells were seeded at a density of 3 × 10^3 cells/well in 96-well plates and incubated for 24 hours before treatment with Afb2C or Afb2C-PbS QDs for 72 hours. * indicates significant difference between Afb2C and Afb2C-PbS QDs. *(P<0.5), ***(P<0.001), and ****(P<0.0001).

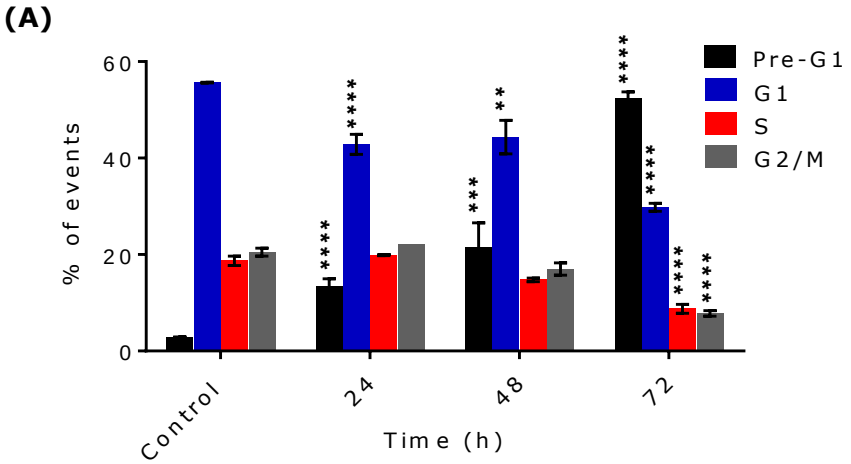
7.2.2.2 Effect of Afb2C-PbS QDs on cell cycle

As previously mentioned, the cell cycle includes all changes that take place in the cell nucleus as prerequisites for cell division. DNA is more sensitive to damage or mutation during this process.

Because MDA-MB-231 cells did not exhibit any response to treatment with Afb2C-PbS QDs, only SKBR3 cells were used to investigate whether Afb2C-PbS QDs inhibit cell growth by affecting DNA during cell division. SKBR3 cells were exposed to Afb2C-PbS QDs at a concentration 2× GI_{50} for 24 hours, 48 hours, and 72 hours, and the cell cycle was followed using flow cytometry (Figure 7.16). From the cell cycle analysis, we observed that cells began to leave the cell cycle and accumulate in pre-G1 phase after 24 hours of exposure to Afb2C-PbS QDs. Treatment with Afb2C-PbS QDs elicited a significant increase in the pre-G1 peak (13.3%; $P < 0.0001$). This was followed by a significant reduction in the G1 peak (42.9%; $P < 0.0001$), but no significant change in the S (19.9%) and G2/M (22%) peaks when compared to peaks in control cells (pre-G1 phase 2.9%, G1 phase 55.7%, S phase 18.7%, and G2/M 20.5%).

The number of pre-G1 phase cells increased significantly after 48 hours of treatment (21.5% vs. 2.9% in control cells; $P < 0.001$). This corresponded with a decrease in S (14.8%) and G2/M (17%) phase cells. However, these changes were not statistically significant when compared to the control (S phase 18.7% and G2/M phase 20.5%). In contrast, the number of cells in G1 phase did not change significantly after 48 hours of treatment compared to treatment for 24 hours. These results show that SKBR3 cell cycle progression was altered towards pre-G1 phase in response to the effects of Afb2C-PbS QDs. This suggests that the cells lost their ability to divide or even survive.

A long exposure period of 72 hours forced more cells to exit the cell cycle. Cell accumulation in pre-G1 phase increased from 13.3% after 24 hours to 52.3% ($P < 0.0001$) after 72 hours of exposure to Afb2C-PbS QDs. Additionally, the percentage of G1 cells decreased dramatically (29.8%; $P < 0.0001$ compared to control). Exposure to Afb2C-PbS QDs for 72 hours evoked significant pre-G1 cell cycle arrest. The percentage of cells in S and G2/M phases dropped significantly to 8.8% ($P < 0.0001$) and 7.8% ($P < 0.0001$), respectively. This led to cell cycle blockage, and cells accumulated in pre-G1 phase. Perturbation of the SKBR3 cell cycle as a result of Afb2C-PbS QDs activity was evident from the dramatic changes in the cell cycle profiles of treated cells relative to those of control (untreated) cells. Furthermore, the induction of pre-G1 cell cycle arrest by Afb2C-PbS QDs strongly indicated DNA degradation and cell apoptosis (Figure 7.16).



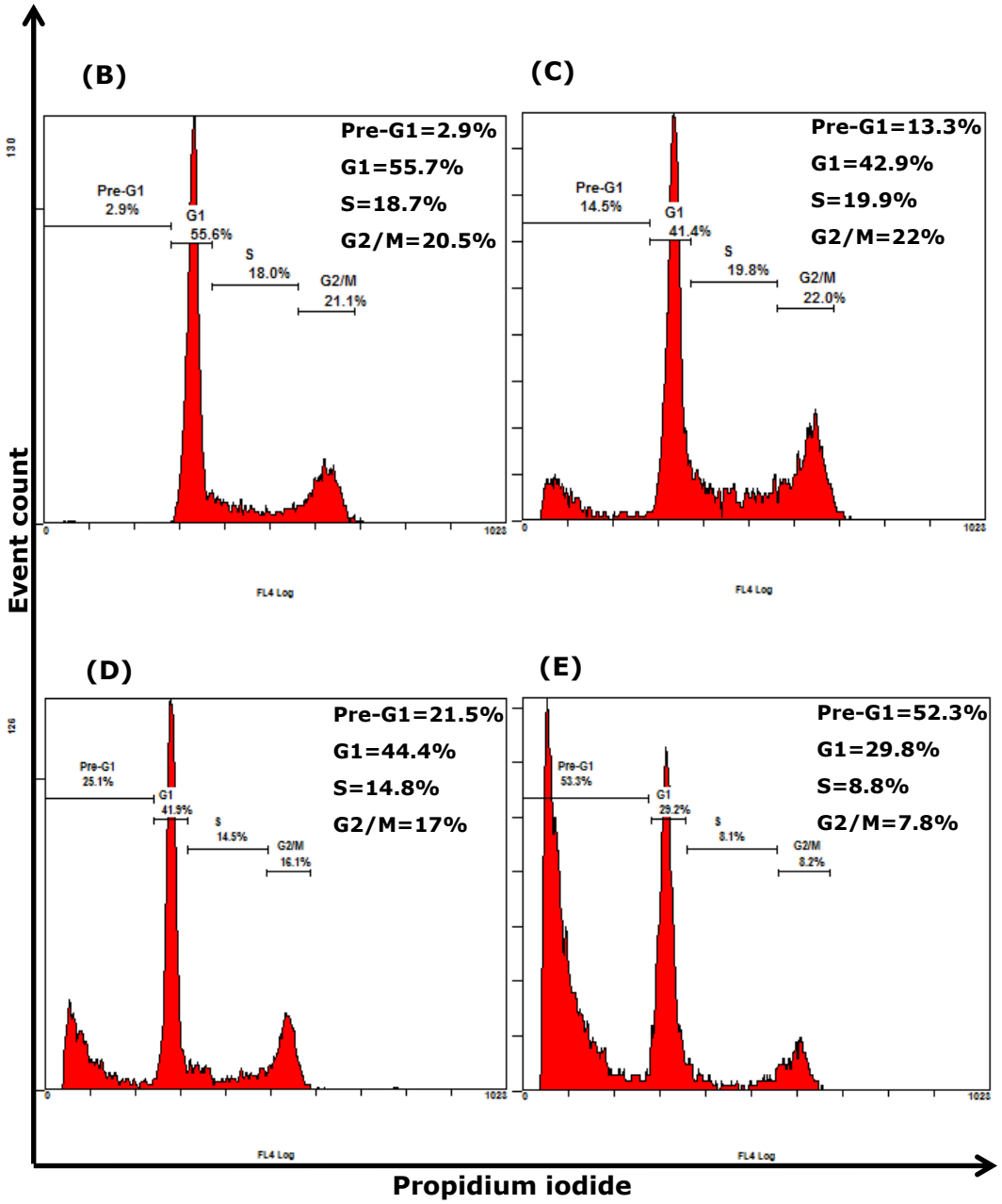


Figure 7.16: (A) Cell cycle analysis. SKBR3 cells were seeded at a density of 1×10^5 cells/well in 6-well plates and incubated for 24 hours before treatment with Afb2C-PbS QDs at 2x GI_{50} for 24 hours, 48 hours, and 72 hours. Histograms show the time-dependent response of **(B)** control (untreated) cells and **(C)** 24 hours, **(D)** 48 hours, and **(E)** 72 hours exposure to Afb2C-PbS QDs. * indicates significant difference compared to control ****(P<0.0001).

7.2.2.3 Programmed cell death induced by Afb2C-PbS QDs

The previous cell cycle results indicate that exposing SKBR3 cells to Afb2C-PbS QDs perturbs the cell cycle, as demonstrated by the exit of cells from the cell cycle and arrest in pre-G1 phase. Pre-G1 is indicative of apoptosis-associated DNA fragmentation [288].

Cell apoptosis was studied to understand whether the changes in the cell cycle that resulted from DNA fragmentation induced programmed cell death. Cell resistance to apoptosis is a major hallmark of human cancer, and it considered the main cause of tumourigenesis and resistance to treatment. Therefore, inducing apoptosis in cancer cells is a major goal for anticancer therapies [209]. Apoptosis, characterised by DNA fragmentation and changes in cell morphology, was assessed using annexin V-FITC (AV) and propidium iodide (PI) dyes. Annexin V is a member of the annexin family of intracellular that binds specifically to phosphatidylserine. It has conjugated to green-fluorescent FITC dye to assess the externalisation of phosphatidylserine in apoptotic cells. Plasma membrane phosphatidylserine is a marker of apoptosis: in early apoptosis, phosphatidylserine flips from the inside to the outside surface, allowing AV to bind phosphatidylserine. PI is used more commonly than other nuclear stains because it is stable and economical, as well as a good indicator of cell viability: living cells are able to exclude the dye. The ability of PI to penetrate a cell is dependent on membrane permeability. The presence of an intact plasma membrane prevents PI from staining viable cells and early

apoptotic cells. In late apoptosis and in necrosis, the integrity of the nuclear and plasma membranes decreases, allowing PI to enter through the membranes, bind with nucleic acids, and emit red fluorescence [289] (Figure 7.17).

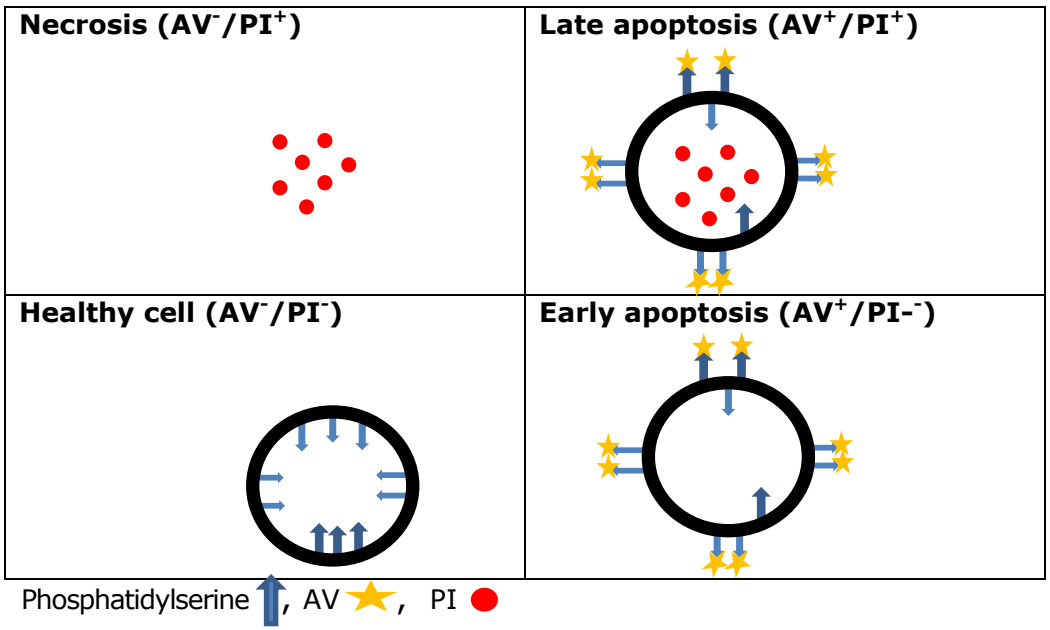
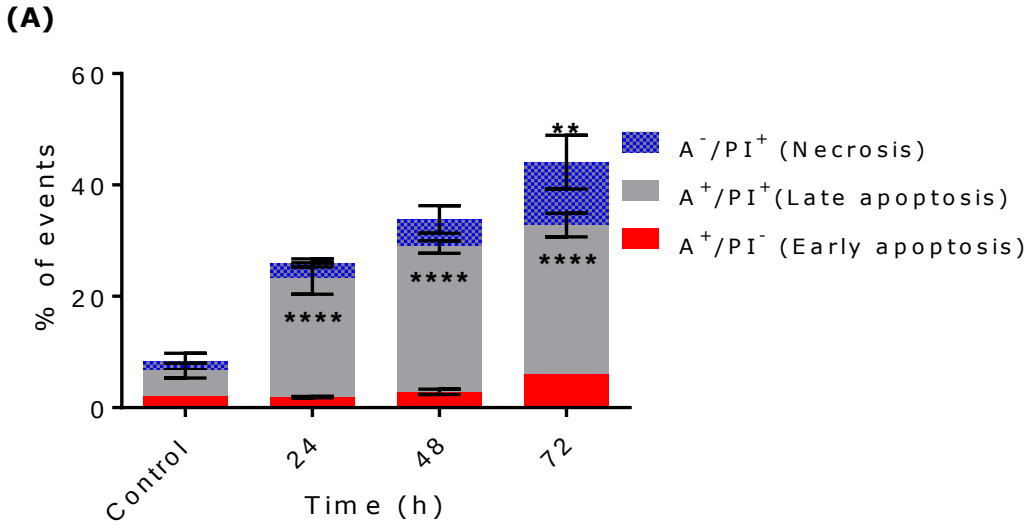


Figure 7.17: Programmed cell death monitoring using AV and PI stains. In control cells, there is no signal for either AV or PI (A^-/P^-). In early apoptosis, only signal for AV (A^+/P^-) is detected. In late apoptosis, cells display signals for AV and PI (A^+/P^+). In necrosis, only the signal for PI (A^-/P^+) is detected.

After exposing SKBR3 cells to Afb2C-PbS QDs at 2× GI_{50} for 24 hours, 48 hours, and 72 hours, programmed cell death was analysed using flow cytometry. There was no significant change in the cell populations in early apoptosis and necrosis after 24 hours of treatment when comparing treated and control cells. However, the population of SKBR3 cells in late apoptosis increased significantly after 24 hours of exposure to Afb2C-PbS QDs (19.5% vs. 4.7% in control; $P < 0.0001$).

We also observed a significant increase in late apoptosis (25%; $P < 0.0001$) after 48 hours of treatment. This was combined with a statistically insignificant increase in early apoptosis and necrosis.

After 72 hours treatment with Afb2C-PbS QDs, the late apoptosis population increased dramatically to 28% ($P < 0.0001$ compared to control). This was an increase of ~30% ($P < 0.01$), from 19.5% after 24 hours to 28% after 72 hours. Interestingly Afb2C-PbS QDs induced significant SKBR3 cell necrosis (11.3% vs. 1.7% in control; $P < 0.01$). Additionally, the early apoptosis population increased when SKBR3 cells were exposed to Afb2C-PbS QDs for 72 hours, though the difference between treated cells and control cells was not significant (Figure 7.18).



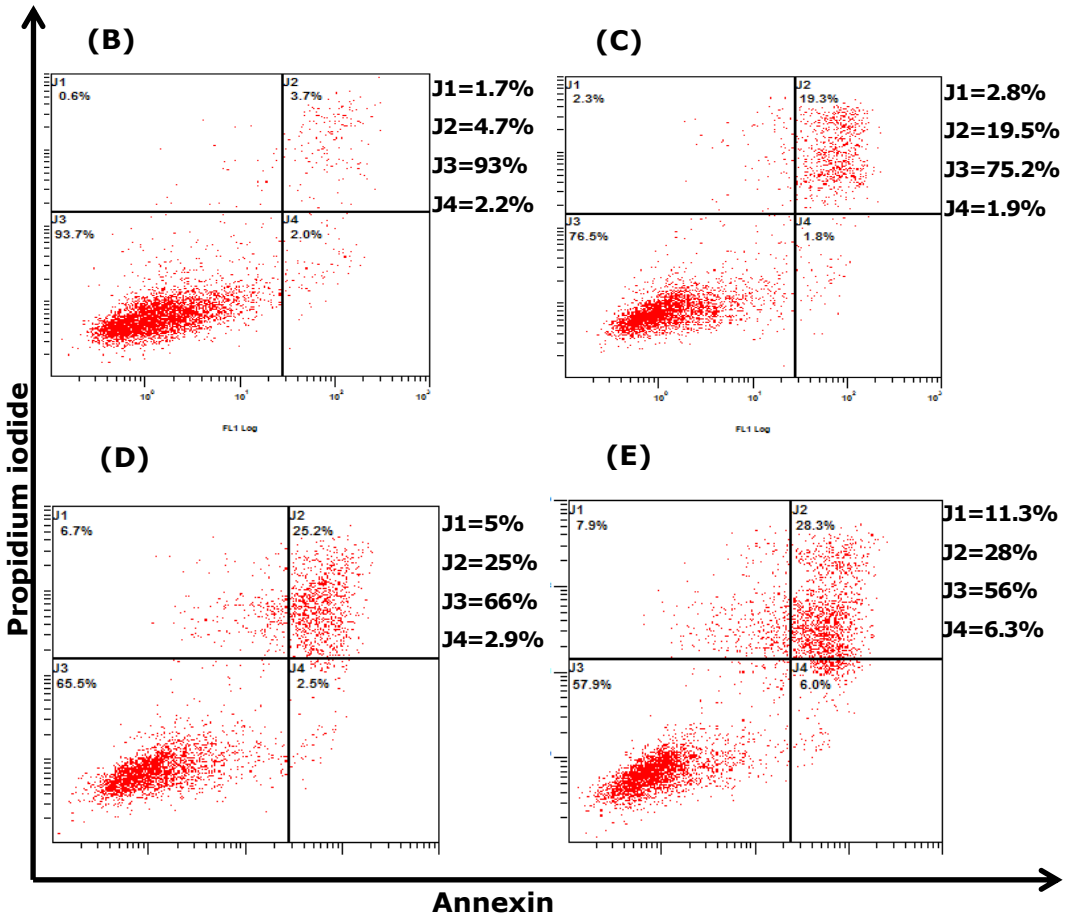


Figure 7.18: (A) Programmed cell death analysis of SKBR3 cells following exposure to Afb2C-PbS QDs. Cells were seeded at a density of 1 × 10^5 cells/well in 6-well plates and treated with an Afb2C-PbS QDs concentration of 2× GI_{50} for 24 hours, 48 hours, and 72 hours. Figures **(B)**, **(C)**, **(D)**, and **(E)** show apoptotic quadrant plots of SKBR3 control (untreated) cells and SKBR3 cells after 24 hours, 48 hours, and 72 hours of exposure to Afb2C-PbS QDs, respectively.

The aforementioned results showed that Afb2C-PbS QDs induced late apoptosis in SKBR3 cells after 24 hours of treatment and that their effect increased by 30% after 72 hours. In addition, SKBR3 cell necrosis was detected after 72 hours of treatment, but at lower levels than late apoptosis.

Accordingly, we propose that the cytotoxic effect observed in the MTT assay could be due to Afb2C-PbS QD-induced SKBR3 cell apoptosis and necrosis, the main cell death pathways. These results are consistent with the cell cycle results.

7.2.2.4 Effect of Afb2C-PbS QDs on Bcl-2 anti-apoptotic proteins

Our hypothesis attributes the potent anti-proliferative effects of Afb2C-PbS QDs to the induction of cancer cell apoptosis through the production of ROS triggered by Afb2C-PbS QDs. To substantiate this idea, the levels of the Bcl-2 protein was assessed using Western blot. As previously mentioned, Bcl-2 plays a vital role as an anti-apoptotic protein in cancer cell proliferation and survival. The cytoprotective effects of Bcl-2 regulate the antioxidant pathway, protect cells from H_2O_2, and completely suppress lipid peroxidation. Further, localisation of Bcl-2 to intracellular sites of oxygen free radical generation, such as the endoplasmic reticula, mitochondria, and nuclear membranes, inhibits most types of apoptosis by maintaining free radical balance [279,290].

In this study, SKBR3 cells were treated with Afb2C-PbS QDs at 2× GI_{50} for 24 hours, 48 hours, and 72 hours, and the protein expression of Bcl-2 was evaluated. Afb2C-PbS QDs enhanced total Bcl-2 protein expression at 24 hours. However, Afb2C-PbS QDs downregulated Bcl-2 levels after 48 hours. Complete inhibition of Bcl-2 expression was observed after 72 hours (Figure 7.19).

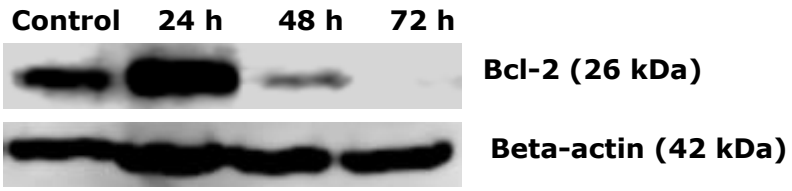


Figure 7.19: Western blot analysis of Bcl-2 following exposure of SKBR3 cells to Afb2C-PbS QDs. SKBR3 cells were seeded at a density of 10×10^5 cells/well in Petri dishes and incubated for 24 hours before treatment with Afb2C-PbS QDs at 2× GI_{50} for 24 hours, 48 hours, and 72 hours.

The results revealed upregulation of Bcl-2 after exposure to Afb2C-PbS QDs for 24 hours. This might be an early cell response against oxidative stress. As expected, Bcl-2 expression was inhibited after 48 hours and suppressed after 72 hours in response to Afb2C-PbS QDs treatment. Bcl-2 downregulation suggests that Afb2C-PbS QDs promote cellular apoptosis. Taken together, the aforementioned results strongly indicate that SKBR3 cells undergo apoptosis in response to Afb2C-PbS QDs activity.

7.2.3 ZnPP-Afb2C-PbS QDs

In the current study, Afb2C-PbS QDs exhibited high selectivity for HER2-overexpressing SKBR3 cells and potent anti-proliferative activity. This encouraged further development of the QDs to improve their activity. To this end, we conjugated a ZnPP fluorescent dye to the Afb2C, thus permitting identification of ZnPP-Afb2C-PbS QDs *in vivo* using a microscope with a detector in the visible region. In addition, ZnPP molecules act as anticancer agents by inhibiting the HO-1

enzyme and consequently suppressing the synthesis of bilirubin, an antioxidant. Therefore, we expected that conjugation of ZnPP molecules to amino-Afb2C-PbS QDs would serve a dual function, providing an imaging method for NIR of PbS QDs and ZnPP visible light and an additional cytotoxic element.

7.2.3.1 Effect of ZnPP-Afb2C-PbS QDs on cell viability and proliferation

MTT assays were performed to study the anti-proliferative effect of ZnPP-Afb2C-PbS QDs on SKBR3 and MDA-MB-231 breast cancer cell lines. The growth inhibitory effect of ZnPP-Afb2C-PbS QDs was investigated and compared to that of Afb2C-PbS QDs. After 72 hours of treatment, ZnPP-Afb2C-PbS QDs significantly inhibited the growth of SKBR3 cells (GI_{50} = 25 μg/mL; standard error of the mean = 0.23). Surprisingly, an effect was also observed in MDA-MB-231 cells (GI_{50} = 62 μg/mL; standard error of the mean = 0.33) (Figure 7.20). However, the growth inhibitory effect of ZnPP-Afb2C-PbS QDs on MDA-MB-231 cells was not as significant as the effect on SKBR3 cells.

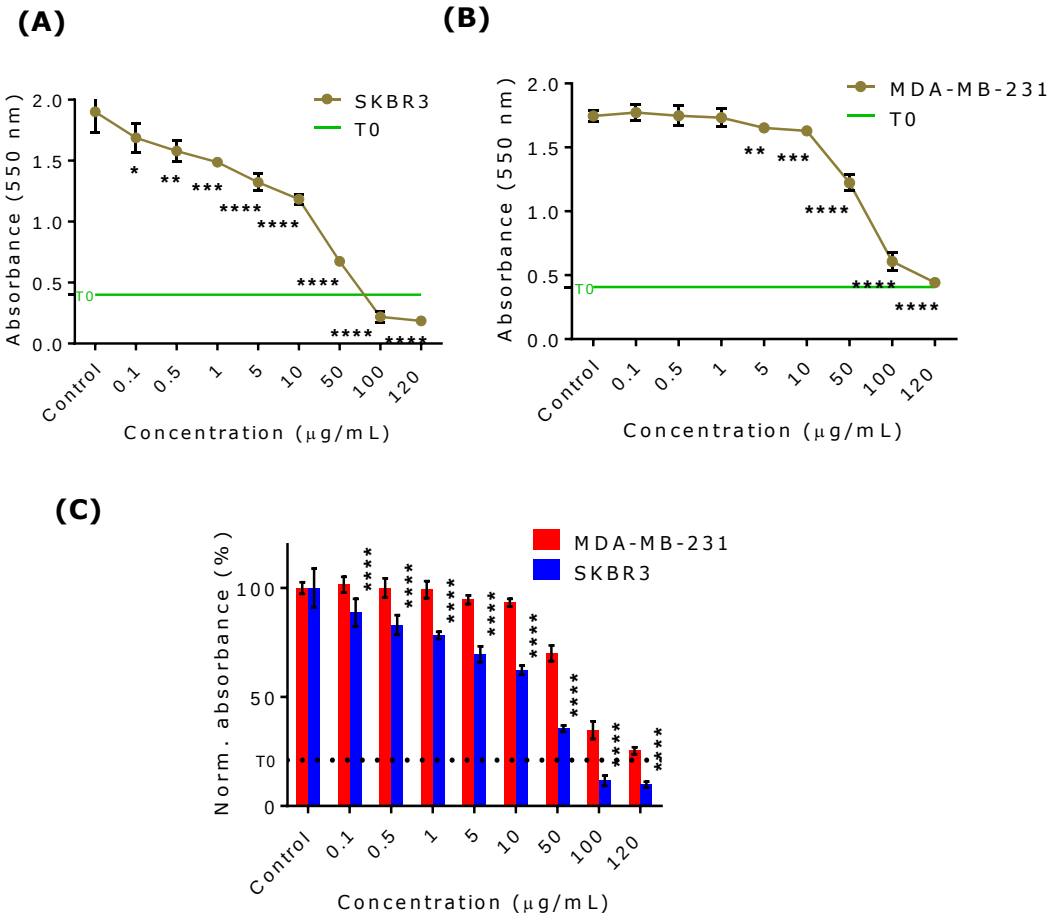


Figure 7.20: Growth inhibitory effect of ZnPP-Afb2C-PbS QDs on **(A)** SKBR3 and **(B)** MDA-MB-231 breast cancer cells. **(C)** Growth inhibition comparison of the two cell lines. Cells were seeded at a density of 3 × 10^3 cells/well in 96-well plates and incubated for 24 hours before treatment with ZnPP-Afb2C-PbS QDs for 72 hours. * indicates significant difference compared to control in **(A)** and **(B)** and the proliferation of SKBR3 cell compared to MDA-MB-231 cell in **(C)**. ****(P<0.0001).

The results indicated that conjugation of ZnPP to Afb2C-PbS QDs decreases Afb2C selectivity for the HER2 receptor. This can be clearly observed by comparing the inhibitory effects of ZnPP-Afb2C-PbS QDs and Afb2C on cell growth (Figure 7.21).

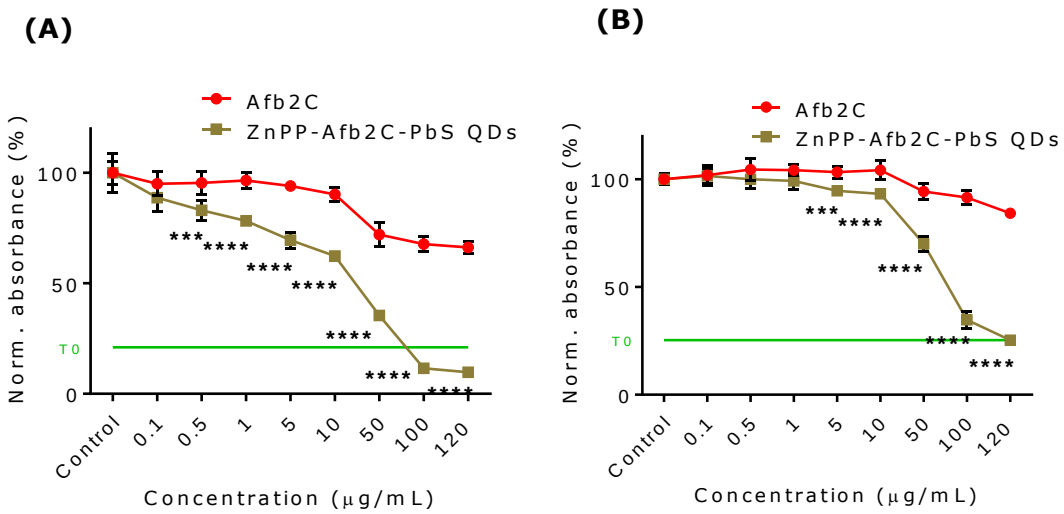


Figure 7.21: Comparison of the growth inhibitory effects of Afb2C and ZnPP-Afb2C-PbS QDs on (A) SKBR3 and (B) MDA-MB-231 breast cancer cells. Cells were seeded at a density of 3×10^3 cells/well in 96-well plates and incubated for 24 hours before treatment with Afb2C or ZnPP-Afb2C-PbS QDs for 72 hours. * indicates significant difference between Afb2C and ZnPP-Afb2C-PbS QDs. ***(P<0.001) and ****(P<0.0001).

Furthermore, the anti-proliferative effect of ZnPP-Afb2C-PbS QDs was compared to that of Afb2C-PbS QDs. The results indicate that ZnPP-Afb2C-PbS and Afb2C-PbS QDs have a similar effect on SKBR3 cells. However, the effect increased significantly at higher concentrations of ZnPP-Afb2C-PbS QDs. In MDA-MB-231 cells, ZnPP-Afb2C-PbS and Afb2C-PbS QDs displayed similar behaviour, and they did not affect the growth of these cells up to concentrations of 10 µg/mL. ZnPP-Afb2C-PbS QDs had a stronger inhibitory effect than Afb2C-PbS QDs on MDA-MB-231 cell growth at concentrations above 10 µg/mL.

However, the effect in MDA-MB-231 cells was lower than that in SKBR3 cells (Figure 7.22). Because of the potent anti-proliferative effect of ZnPP-Afb2C-PbS QDs on SKBR3 cells and the significantly lower GI_{50} value compared to that observed in MDA-MB-231 cells, SKBR3 cells were chosen for further study of ZnPP-Afb2C-PbS QDs.

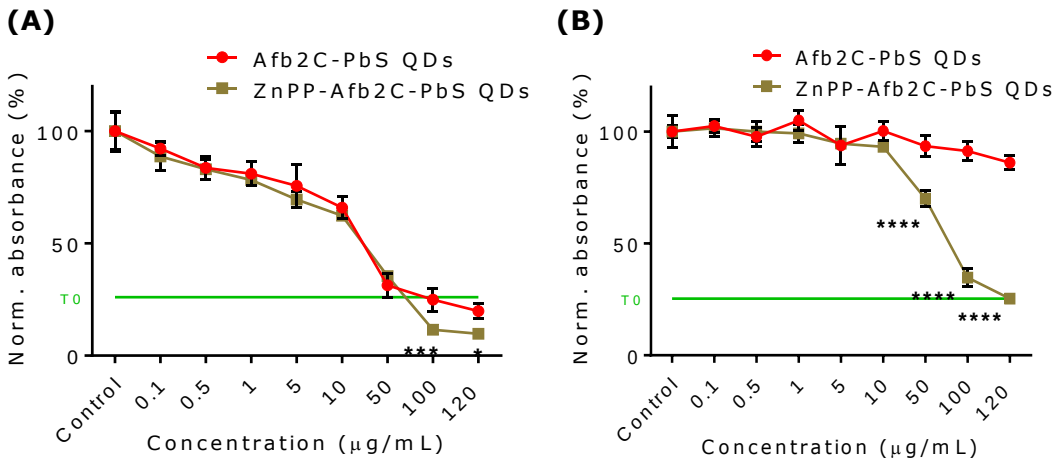


Figure 7.22: Comparison of the growth inhibitory effects of Afb2C-PbS and ZnPP-Afb2C-PbS QDs on **(A)** SKBR3 and **(B)** MDA-MB-231 breast cancer cells. Cells were seeded at a density of 3×10^3 cells/well in 96-well plates and incubated for 24 hours before treatment with Afb2C or ZnPP-Afb2C-PbS QDs for 72 hours. * indicates significant difference between Afb2C-PbS and ZnPP-Afb2C-PbS QDs. *(P<0.5), ***(P<0.001) and ****(P<0.0001).

7.2.3.2 Effect of ZnPP-Afb2C-PbS QDs on cell cycle

Flow cytometry was used to investigate the relationship between the growth inhibitory effect of ZnPP-Afb2C-PbS QDs and the cell cycle in SKBR3 cells. SKBR3 cells were exposed to ZnPP-Afb2C-PbS QDs at 2×

GI_{50} of for 24 hours, 48 hours, and 72 hours. Figure 7.23 shows that SKBR3 cells escaped the cell cycle to pre-G1 phase; the effect was significant after 24 hours of treatment (18.9% vs. 2.1% in control; $P < 0.0001$). A corresponding decrease in G1 phase cells was observed after 24 hours (40.3% vs. 56% in control; $P < 0.0001$); this was associated with insignificant changes in S (16.3% vs. 18.3%) and G2/M (22.6% vs. 20%) phases. From these results, we conclude that treatment with ZnPP-Afb2C-PbS QDs for 24 hours decelerates the SKBR3 cell cycle.

We observed that ZnPP-Afb2C-PbS QDs induced G1 cell cycle arrest and that the effect was extremely significant after 48 hours of treatment (55%; $P < 0.0001$) when compared to the effect after 24 hours of treatment (40.3%). The effect was associated with a significant decrease in G2/M (13%; $P < 0.0001$) relative to the levels after 24 hours of treatment (20%). Pre-G1 (16%) and S (14%) phases did not exhibit significant changes compared to levels at 24 hours. However, pre-G1 in treated cells was significantly higher than in control.

Furthermore, the cell population had more pre-G1 cells after 72 hours of treatment with ZnPP-Afb2C-PbS QDs (52.8%; $P < 0.0001$) than after 24 hours treatment or with control. The decrease in G1 phase cells was highly significant (27.4%; $P < 0.0001$ relative to control). In addition, perturbation of the SKBR3 cell cycle after exposure to ZnPP-Afb2C-PbS QDs for 72 hours can be significantly observed from the

reducing in S phase cells (9.3%; $P < 0.0001$ relative to control). Similarly, G2/M phase cells decreased significantly (8.7%; $P < 0.0001$ relative to control). The results suggest that ZnPP-Afb2C-PbS QDs have a time-dependent effect on the cell cycle and the ability to block the SKBR3 cell cycle after 72h of treatment. This is evident from the reversal of usual cell cycle progression. Cell arrest in pre-G1 phase corresponded to decreases in the G1, S, and G2/M cell populations. In addition, G1 arrest after 48 hours suggests that DNA synthesis was inhibited in S phase and that this led to cell accumulation in G1 phase. These results suggest that SKBR3 cells undergo apoptosis induced by DNA degradation.

We expected that ZnPP-Afb2C-PbS QDs would exhibit augmented anti-proliferative effects as a result of conjugation with ZnPP. However, Afb2C-PbS QDs and ZnPP-Afb2C-PbS QDs had similar effects on the SKBR3 cell cycle. Our results suggest that conjugation of ZnPP with Afb2C-PbS QDs decreases the affinity of Afb2C for HER2 receptors and consequently reduces the effects of ZnPP-Afb2C-PbS QDs on HER2-overexpressing SKBR3 cells. Therefore, we attribute the similarity in the growth inhibitory effects of ZnPP-Afb2C-PbS QDs and Afb2C-PbS QDs to the reduction in the dose of ZnPP-Afb2C-PbS QDs targeted to HER2-overexpressing cancer cells.

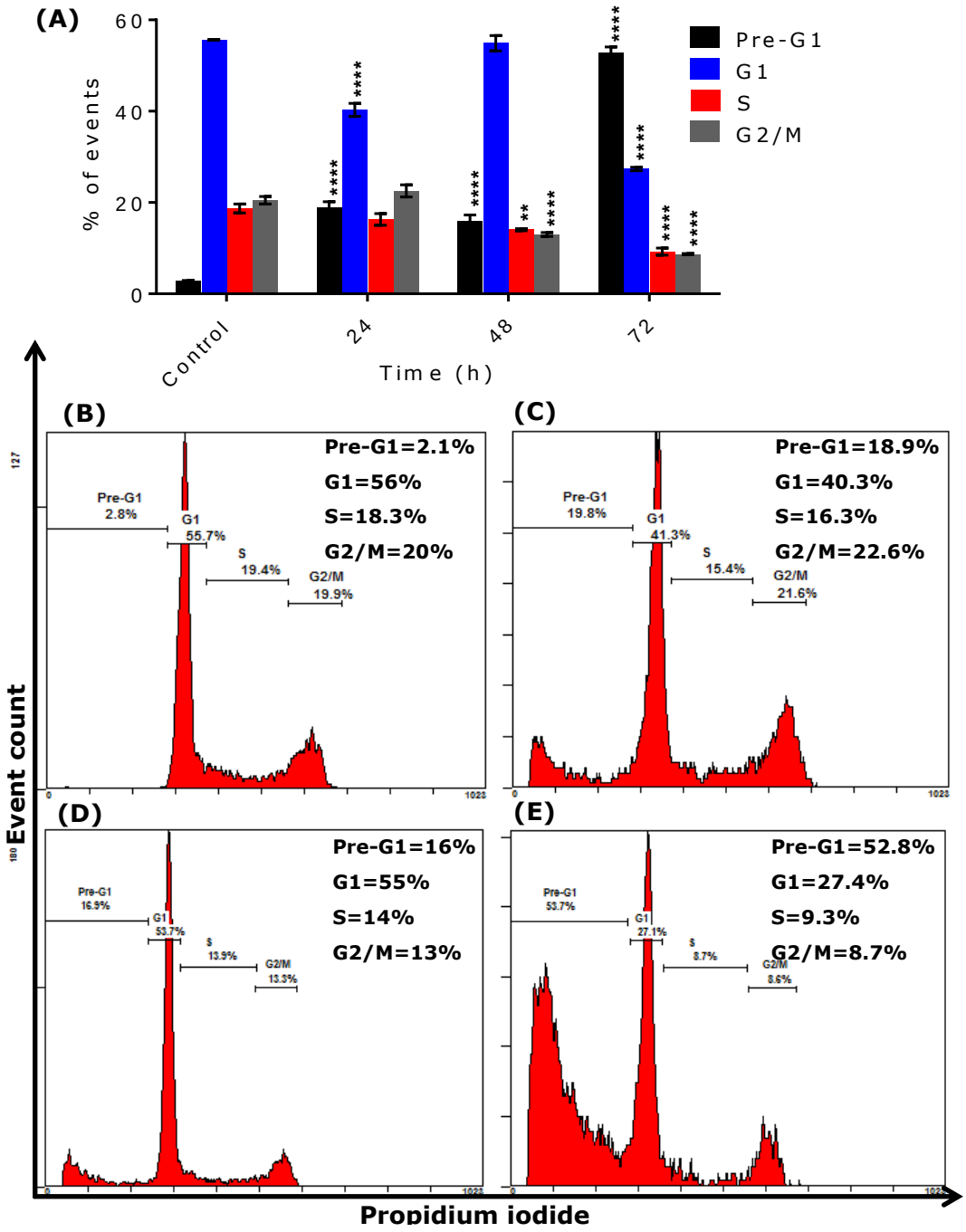


Figure 7.23: (A) Cell cycle analysis. SKBR3 cells were seeded at a density of 1 × 10^5 cells/well in 6-well plates and incubated for 24 hours before treatment with ZnPP-Afb2C-PbS QDs at 2× GI_{50} of for 24 hours, 48 hours, and 72 hours. Histograms show the time-dependent response of **(B)** control (untreated) and **(C)** 24 hours, **(D)** 48 hours, and **(E)** 72 hours exposure to ZnPP-Afb2C-PbS QDs. * indicates significant difference compared to control ****(P<0.0001).

7.2.3.3 Programmed cell death induced by ZnPP-Afb2C-PbS QDs

To investigate the mechanism by which ZnPP-Afb2C-PbS QDs induce programmed SKBR3 cell death, an AV/PI assay was performed. SKBR3 cells were exposed to ZnPP-Afb2C-PbS QDs at 2× GI_{50} for 24 hours, 48 hours, and 72 hours. Thereafter, the cell population was analysed with flow cytometry (Figure 7.24).

The SKBR3 cells underwent necrosis after 24 hours of exposure to ZnPP-Afb2C-PbS QDs. The effect was highly significant (10.4%; $P < 0.001$ relative to control, 1.7%). However, no significant changes in the early and late apoptosis quadrant plots were observed.

SKBR3 cell necrosis continued to increase significantly after 48 hours of treatment (16.5%; $P < 0.0001$ relative to control). The increase in cell necrosis corresponded to a decrease in early and late apoptosis; however, the effect was not significant. Thus, even cells that underwent apoptosis after 24 hours progressed to necrosis after 48 hours of treatment.

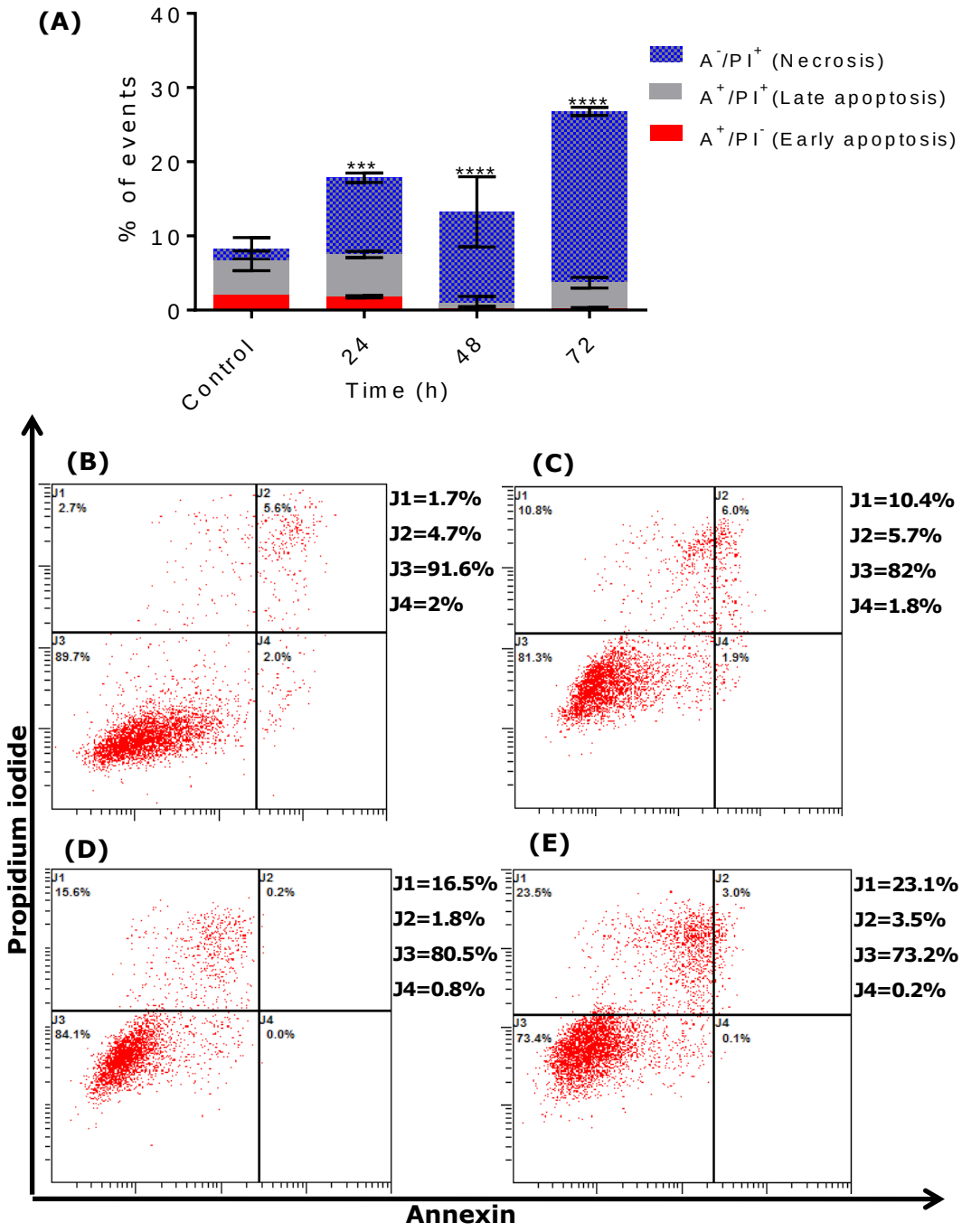


Figure 7.24: (A) Programmed cell death analysis of SKBR3 cells following exposure to ZnPP-Afb2C-PbS QDs. Cells were seeded at a density of 1 × 10^5 cells/well in 6-well plates and treated with ZnPP-Afb2C-PbS QDs at 2× GI_{50} for 24 hours, 48 hours, and 72 hours. *(P<0.5), ****(P<0.0001). Figures **(B)**, **(C)**, **(D)**, and **(E)** represent apoptotic quadrant plots of SKBR3 cells control (untreated) and after 24 hours, 48 hours, and 72 hours of exposing to ZnPP-Afb2C-PbS QDs respectively.

Interestingly, cell necrosis doubled between 24 hours and 72 hours of treatment (23.1%; $P < 0.0001$ relative to 24 hours and control). Some SKBR3 cells underwent late apoptosis, and no early apoptosis was observed after 72 hours of exposure to ZnPP-Afb2C-PbS QDs. These results indicate that ZnPP-Afb2C-PbS QDs have a potent anti-proliferative effect on SKBR3 cells and that they force most cells to undergo necrosis. Therefore, we conclude that conjugation of ZnPP with Afb2C-PbS QDs switches SKBR3 cell fate from apoptosis to necrosis.

7.2.3.4 ZnPP-Afb2C-PbS QD cellular uptake and localisation study

The ability of ZnPP-Afb2C-PbS QDs to enter and localise in SKBR3 and MDA-MB-231 cells was monitored using flow cytometry. Cells were incubated with ZnPP-Afb2C-PbS QDs at 2× GI_{50} for 3 hours (Figure 7.25). The uptake of ZnPP-Afb2C-PbS QDs in MDA-MB-231 and SKBR3 cell lines was significantly higher ($P < 0.0001$) after 3 hours compared to control (untreated cells). Furthermore the uptake of ZnPP-Afb2C-PbS QDs was higher in SKBR3 cells than in MDA-B-231 cells; the difference in cellular uptake was significant ($P < 0.0001$) after 3 hours. The results indicate that ZnPP-Afb2C-PbS QDs retain their affinity for HER2 receptors even though the affinity is reduced by ZnPP conjugation with Afb2C-PbS QDs.

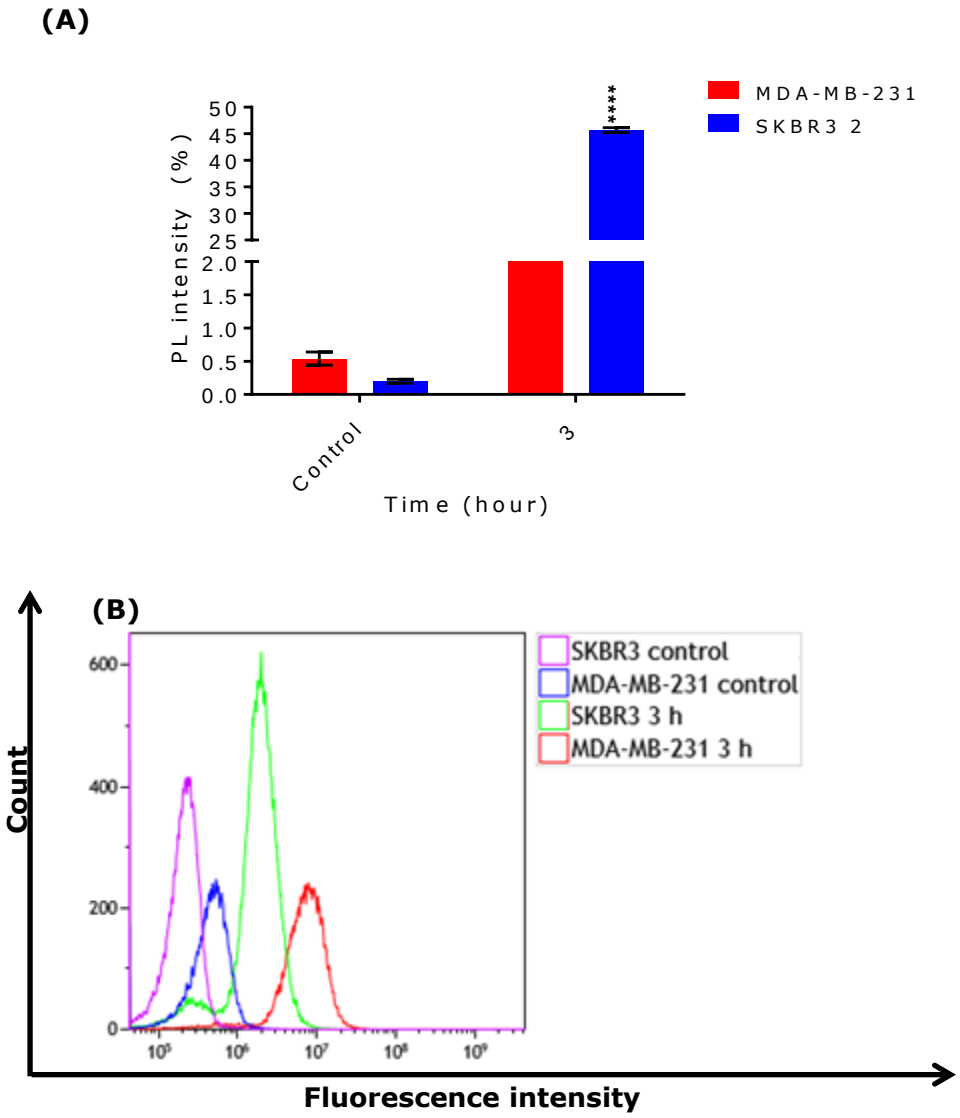


Figure 7.25: (A) Cellular uptake efficiency of ZnPP-Afb2C-PbS QDs by SKBR3 and MDA-MB-231 cells. **(B)** Flow cytometry histogram shows the SKBR3 and MDA-MB-231 cells uptake of ZnPP-Afb2C-PbS QDs. Cells were seeded at a density of 3.5 × 10^5 cells/well in 6-well plates and treated with ZnPP-Afb2C-PbS QDs at 2× GI_{50} for 3 hours. * indicates significant difference compared to control ****(P<0.0001).

7.2.3.5 Confocal microscopy study of ZnPP-Afb2C-PbS QDs

The localisation of ZnPP-Afb2C-PbS QDs and their utility as an imaging agent were studied using confocal microscopy. SKBR3 and MDA-MB-231 cells were exposed to ZnPP-Afb2C-PbS QDs at 2× GI_{50} for, 3 hours. The intracellular fluorescence emitted from ZnPP-Afb2C-PbS QDs was detected at λ_{em}= 593 nm after excitation of ZnPP at 425 nm. ZnPP-Afb2C-PbS QDs penetrated and localised in the SKBR3 cells. The fluorescent light is clearly apparent when images of treated SKBR3 cells are compared to those of untreated SKBR3 cells, which do not display any detectable fluorescent light (Figure 7.26 A-E). In contrast, no signal was detected in MDA-MB-231 cells after treatment with ZnPP-Afb2C-PbS QDs (Figure 7.26 F-I).

Confocal images also showed that treatment with ZnPP-Afb2C-PbS QDs resulted in dramatic changes in SKBR3 cell morphology resembling those of apoptosis. These changes were apparent when comparing treated SKBR3 cells to untreated SKBR3 cells (control) and treated and untreated MDA-MB-231 cells. The confocal images and the demonstrated anti-proliferative effect provide good evidence that ZnPP-Afb2C-PbS QDs have a potent cytotoxic effect.

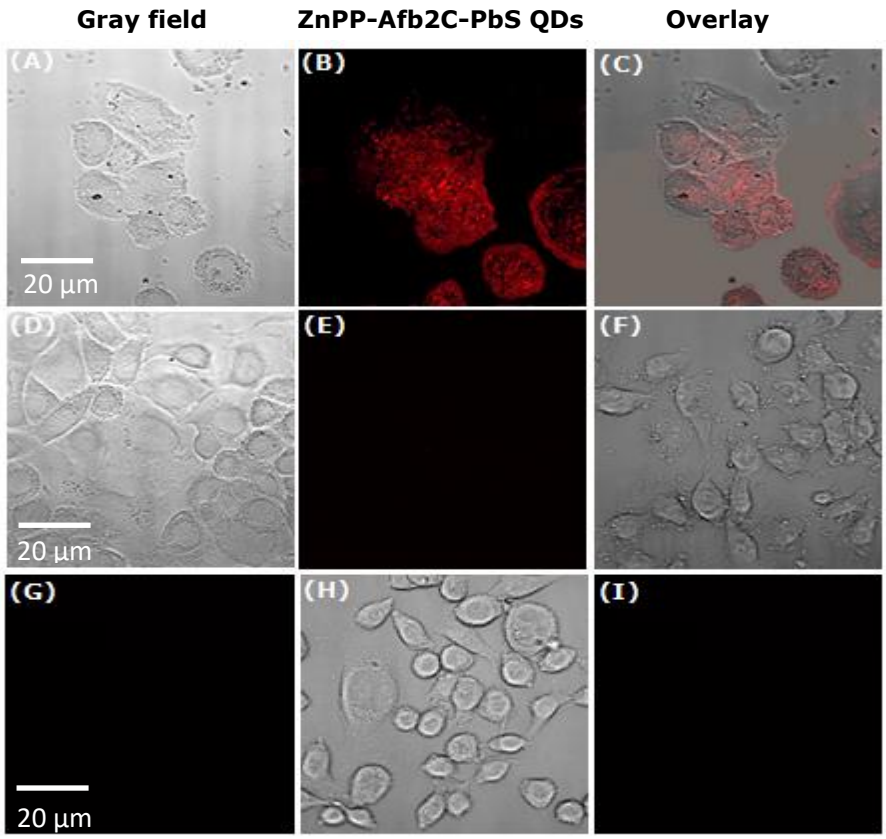


Figure 7.26: Confocal images show the fluorescence emitted from SKBR3 cells after exposure to ZnPP-Afb2C-PbS QDs for 3 hours (**A**–**C**) and from control cells (**D** & **E**). Fluorescence was not observed in treated (**F** & **G**) or untreated (**H** & **I**) MDA-MB-231 cells. Cells were seeded at a density of 10 × 10^3 cells/well in 8-well plate and treated with ZnPP-Afb2C-PbS QDs at 2× GI_{50}.

7.3 Discussion

This chapter described the use of *G*Luc-*Li*Dps-ZnPP plus coelenterazine, Afb2C-PbS QDs, and ZnPP-Afb2C-PbS QDs as theranostic agents for cancer treatment and tumour cell imaging.

7.3.1 *G*Luc-*Li*Dps-ZnPP

The *G*Luc-*Li*Dps-ZnPP construct was designed to act as both a PDT and an imaging agent. *G*Luc-*Li*Dps-ZnPP-mediated PDT has anti-proliferative activity against SKBR3 breast cancer cells. This effect was not observed in MDA-MB-231 breast cancer cells or MRC5 non-cancerous cells. Although ZnPP also displayed anti-proliferative activity, the activity of *G*Luc-*Li*Dps-ZnPP plus coelenterazine was much more significant than that of ZnPP alone. The results provide strong evidence for the ability of this construct to inhibit the growth and migration of SKBR3 cells.

For several reasons, we attribute the differences in cell line response to *G*Luc-*Li*Dps-ZnPP: First, flow cytometry analysis and confocal images showed that *G*Luc-*Li*Dps-ZnPP uptake in SKBR3 cells was twice that in MDA-MB-231 cells and that uptake was not observable in MRC5 cells. Interestingly, these results give an indication about the ability of *G*Luc-*Li*Dps-ZnPP to target SKBR3 and MDA-MB-231 breast cancer cells without affecting MRC5 non-cancerous cells. This might be due to the difference in rates of the internalisation-mediated endocytosis between healthy and cancer cells. Moreover, SKBR3 cells overexpress the HER2 surface receptor protein and lack expression of hormonal receptors (oestrogen and progesterone), whereas MDA-MB-231 cells express neither HER2 nor hormonal receptors. Therefore, the curvature and tension of the cell membrane may possibly lead to dissimilar accumulation and endocytosis because of differences in

membrane stiffness between the SKBR3 and MDA-MB-231 cell lines. Consequently, the MDA-MB-231 triple-negative cell line is considered the most difficult to treat because anti-HER2 and hormonal treatments are ineffective in this cancer cell line [291][292].

Second, the ROS determination results illustrate that ROS levels in SKBR3 cells were greater than in MDA-MB-231 cells. In addition, treatment with *G*Luc-*Li*Dps-ZnPP-mediated PDT led to greater increases in intracellular ROS levels in SKBR3 cells than in MDA-MB-231 cells and other controls. These variations in ROS levels might result from differences in *G*Luc-*Li*Dps-ZnPP cellular uptake by SKBR3 and MDA-MB-231 cells. Thus, MDA-MB-231 cells are less sensitive to increased ROS levels than SKBR3 cells. We speculate that elevated ROS levels push the SKBR3 cell line to the brink of its toxic threshold, causing high sensitivity to ROS-generating agents. Furthermore, because of the relatively low level of intracellular ROS, MDA-MB-231 cells can resist singlet oxygen generated by *G*Luc-*Li*Dps-ZnPP-mediated PDT. On the other hand, we assume that this effect is negligible in MRC5 cells because they do not internalise *G*Luc-*Li*Dps-ZnPP.

Furthermore, we observed that treatment with *G*Luc-*Li*Dps-ZnPP plus coelenterazine suppressed the expression of anti-apoptotic Bcl-2 and Mcl-1 proteins. Consequently, we expect that *G*Luc-*Li*Dps-ZnPP-mediated PDT promotes SKBR3 cell apoptosis by inducing Bcl-2 and Mcl-1 photo-damage. However, alterations in the expression of Bcl-2

family members after treatment with PDT has been reported in different cell lines and tumours [82]. Several PDTs, such as phthalocyanine Pc 4 [293], 5-aminolevulinic (5-ALA) [82], Methylene blue (MB) [282], induce cell apoptosis associated with the suppression of Bcl-2 and/or Mcl-1 expression.Taken together, these results provide evidence for the ability of *G*Luc-*Li*Dps-ZnPP plus coelenterazine to act as a PDT agent through its anti-proliferative activity and ability to enhance SKBR3 cell apoptosis.

Confocal images showed localisation of *G*Luc-*Li*Dps-ZnPP preferentially in the cytoplasm of SKBR3 and MDA-MB-231 cell lines. This was clearly observed from the fluorescent signal detected after irradiation of ZnPP in *G*Luc-*Li*Dps-ZnPP with visible light (λ_{ex}= 425 nm). Interestingly, no fluorescent signal was detected in the MRC5 cell line, consistent with flow cytometry results. The ability of *G*Luc-*Li*Dps-ZnPP to localise in SKBR3 and MDA-MB-231 breast cancer cells without targeting MRC5 non-cancerous cells and to provide a high-resolution confocal image indicates that it is a promising tool for tumour imaging.

We expect that *G*Luc-*Li*Dps-ZnPP nanoparticles, given their relatively large size, can be delivered more selectively to tumour tissues because of the EPR effect. However this needs to be confirmed through *in vivo* studies (Section.7.1.6).

Aside from the development of an effective PDT agent, another significant issue for *in vivo* anticancer and imaging applications of *G*Luc-*Li*Dps-ZnPP derives from its immunogenicity, which might arise from using the *Li*Dps bacterial protein as a scaffold for the *G*Luc-*Li*Dps-ZnPP construct. However, the present results encourage the use of *G*Luc-*Li*Dps-ZnPP-mediated PDT in further studies to investigate the possible immunogenic response which could be addressed by conjugation of *G*Luc-*Li*Dps-ZnPP with PEG [294,295], hence assessing the potential of the developed nanoconstruct as PDT agent.

7.3.2 Afb2C-PbS QDs

Novel PbS QDs were synthesised by coating with the anti-HER2 Afb2C protein. There are many advantages in using Afb2C protein to coat PbS QDs in terms of biomedical applications. These include its ability to target HER2 receptors that are overexpressed in several types of cancer cells [229]. In addition, Afb2C binds to HER2 far from the epitopes recognised by the therapeutic antibodies pertuzumab and trastuzumab. Therefore, it can be used for diagnosis and drug delivery in HER2-overexpressing tumour tissues in conjunction with pertuzumab and trastuzumab treatment [166]. Moreover, Afb2C is a non-toxic protein, and our MTT results showed only small effects on SKBR3 cells after exposure to a high Afb2C concentration. These

results agree with the findings of Altai *et al.* who reported that Afb is neither toxic nor immunogenic in humans [296].

It was previously reported that the PbS QDs have an anti-proliferative effect on colorectal carcinoma by triggering ROS production [209]. Our MTT results showed that Afb2C-PbS QDs inhibited the growth of SKBR3 cells without affecting the growth of MDA-MB-231 cells. This could be attributed to the Afb2C-PbS QDs internalisation in SKBR3 cells by receptor-mediated endocytosis pathway. This provides evidence that PbS QDs successfully target and penetrate HER2-overexpressing SKBR3 cells without recognising MDA-MB-231 cells, which lack the HER2 receptor. The growth inhibitory effect of Afb2C-PbS QDs on SKBR3 cells was associated with perturbation of the cell cycle. Flow cytometry analysis showed blockage of cell cycle progression when SKBR3 cells were treated with Afb2C-PbS QDs; most cells exited the cell cycle and arrested in pre-G1 phase. This indicated that apoptosis is mediated by DNA fragmentation. This hypothesis was confirmed using AV/PI analysis. The results showed that most SKBR3 cells underwent late apoptosis when treated with Afb2C-PbS QDs. Similar effects of PbS QDs on colorectal carcinoma have been previously reported by Bradshaw *et al.* [209]. In addition, Western blotting showed that the Afb2C-PbS QDs downregulated Bcl-2 anti-apoptotic protein and thus sensitised SKBR3 cells to apoptosis.

With regard to using PbS QDs as an imaging agent, previous studies have described variants of PbS QDs successfully employed for obtaining high-resolution images of cancer cells [297,298]. Future studies are required to confirm the suitability of Afb2C-PbS QDs for use in cancer cell imaging.

In general, the results demonstrate the selectivity and potent anticancer activity of Afb2C-PbS QDs against HER2-overexpressing cancer cells and introduce an attractive tool for use as a potential chemotherapeutic agent.

7.3.3 ZnPP-Afb2C-PbS QDs

Given the encouraging results, Afb2C-PbS QDs were further developed by conjugating them to ZnPP molecules to produce novel ZnPP-Afb2C-PbS QDs. ZnPP molecules were used as a complement to Afb2C-PbS QD therapy because of their ability to act as anticancer and imaging agents (Section 1.6.1). In our MTT results, ZnPP-Afb2C-PbS QDs and Afb2C-PbS QDs had the same anti-proliferative effect on SKBR3 cells. However, above 50 μg/mL of agent, the effect of ZnPP-Afb2C-PbS QDs was slightly stronger than that of Afb2C-PbS QDs. The enhancement in the anti-proliferative activity of ZnPP-Afb2C-PbS QDs was coupled with a negative effect on its selectivity. This can be observed from the inhibitory effect of ZnPP-Afb2C-PbS QDs on MDA-MB-231 cell growth

above 10 μg/mL. Nevertheless, the SKBR3 cell line was more sensitive than the MDA-MB-231 cell line to the growth inhibitory effect of ZnPP-Afb2C-PbS QDs (GI_{50} = 25 μg/mL vs. GI_{50} = 62 μg/mL, respectively). The MTT results showed no significant difference in the GI_{50} of ZnPP-Afb2C-PbS and Afb2C-PbS QDs when applied to the SKBR3 cell line, suggesting that the affinity of Afb2C for HER2 was unchanged by ZnPP conjugation. However, we speculate that conjugation of ZnPP with Afb2C did affect its affinity for HER2 receptors: ZnPP was expected to enhance the growth inhibitory effect of Afb2C-PbS QDs, but ZnPP-Afb2C-PbS QDs and Afb2C-PbS QDs had similar growth inhibitory effects. Therefore, we hypothesise that ZnPP conjugation increased Afb2C-PbS QD cytotoxicity but reduced its affinity and selectivity for HER2 over-expressing SKBR3 cells.

Cell cycle analysis was also performed on SKBR3 cells after treatment with ZnPP-Afb2C-PbS QDs. ZnPP-Afb2C-PbS QDs similar to Afb2C-PbS QDs, blocked the cell cycle: SKBR3 cells arrested in pre-G1 and exited the cell cycle after 72 hours of treatment. Interestingly, SKBR3 cells became unable to synthesise DNA and prepare for cell division through their accumulation in G1 phase and failed to progress to G2/M phase after 48 hours. DNA degradation followed after 72 hours of treatment. In contrast, treatment with Afb2C-PbS QDs led to direct DNA fragmentation in SKBR3 cells.

The difference in the effect on cell cycle led us to investigate the type of programmed cell death occurring in SKBR3 cells treated with ZnPP-

Afb2C-PbS QDs. Flow cytometry analysis demonstrated that SKBR3 cells progressed to necrosis in the presence of ZnPP-Afb2C-PbS QDs, rather than to apoptosis as observed after treatment with Afb2C-PbS QDs. These results suggest the cytotoxicity of ZnPP-Afb2C-PbS QDs is more potent than that of Afb2C-PbS QDs.

Flow cytometry was also used to investigate the cellular uptake of ZnPP-Afb2C-PbS QDs. The results indicate that ZnPP-Afb2C-PbS QDs localised to both SKBR3 and MDA-MB-231 cell lines. In addition, ZnPP-Afb2C-PbS QDs internalised in SKBR3 cells in quantities greater than detected in MDA-MB-231 cells. This result explains the difference in the responses of these two cell lines to treatment with ZnPP-Afb2C-PbS QDs.

Confocal microscopy provided high-resolution images of SKBR3 cells after exposure to ZnPP-Afb2C-PbS QDs. Fluorescent ZnPP-Afb2C-PbS QDs were not observed in MDA-MB-231 cells, but flow cytometry analysis showed localisation of ZnPP-Afb2C-PbS QDs to these cells. Thus, the quantity of ZnPP-Afb2C-PbS QDs might have been too low for detection by confocal microscopy.

We conclude that ZnPP-Afb2C-PbS QDs are a promising candidate for anticancer and imaging agents. In the future, more detailed studies are required to complete the characterisation the effect of ZnPP-Afb2C-PbS QDs on MDA-MB-231 cell line and for use in *in vivo* applications.

Chapter 8

8. Conclusions and future directions

Nanoparticles derived from proteins have shown significant potential in the development of clinically beneficial drug delivery systems and imaging agents. These systems can overcome the clinical issues related to the administration of conventional drugs, such as insolubility, toxicity, and unfavourable interactions with other biochemical materials during delivery [299,300].

This study focused on engineering protein nanoparticles for use as novel drug delivery and imaging agents with which to deliver bioactive materials to the targeted tumour cells. Table 8.1 summarises the nanoparticles derived from proteins constructed in this study and their potential biomedical applications.

Construct	Function and potential applications	Characterisation	*In vitro* study
Afb2C-PbS QDs	Drug delivery/Imaging agent/PDT	√	√
ZnPP-Afb2C-PbS QDs	Drug delivery/Imaging agent/PDT	√	√
***G*Luc-*Li*Dps-ZnPP**	PDT/Imaging agent	√	√
***G*Luc-miniSOG-LTVSPWY**	PDT/Imaging agent	√	**X**
Afb-HuAft:miniSOG-HuAft	PDT/Imaging agent	On going	**X**
***G*Luc-*Li*Dps:miniSOG-*Li*Dps**	PDT/Imaging agent	On going	**X**

Table 8.1: The progress of nanoparticles derived from proteins within this study.

8.1 Cage-like proteins as PDT and imaging agents

In this study, we presented *Li*Dps and ferritin proteins as promising scaffolds for the design of PDT and imaging agents. *Li*Dps proteins were modified to generate *G*Luc-*Li*Dps-ZnPP and *G*Luc-*Li*Dps:miniSOG-*Li*Dps systems that function as PDTs utilising a BRET mechanism.

The *G*Luc-*Li*Dps:miniSOG-*Li*Dps construct was synthesised by dissociating and reassembling *Li*Dps subunits to produce hybrid cages (composed of different types of chimeric *Li*Dps subunits). Characterisation of hybrid cage formation was challenging because of the dissimilarity and the large size of the miniSOG and *G*Luc proteins fused to the *Li*Dps subunits. This was also observed in the characterisation of Afb-HuAft:miniSOG-HuAft constructs in which the hybrid cages appeared to be smaller than Afb-HuAft and miniSOG-HuAft. However, because these constructs offer several advantages in clinical settings (Chapter Four), we need to conduct more studies to confirm their final structure as well as their biological activity in the treatment of tumours.

Furthermore our results indicate that the *G*Luc-*Li*Dps-ZnPP in the presence of coelenterazine exhibits anti-proliferative activity against SKBR3 breast cancer cells. The anticancer activity was mainly attributable to the production of singlet oxygen by ZnPP through irradiation from the *G*Luc's blue light. The main mechanism of cellular death induced by *G*Luc-*Li*Dps-ZnPP plus coelenterazine was apoptosis.

This was evidenced by the absence of Bcl-2 and Mcl-1 anti-apoptotic proteins, which were not detectable in the Western blots after treatment with *G*Luc-*Li*Dps-ZnPP plus coelenterazine. *G*Luc-*Li*Dps-ZnPP-mediated PDT also inhibited cancer cell migration. *G*Luc-*Li*Dps-ZnPP showed high selectivity for breast cancer cells over healthy cells, as observed from its uptake by SKBR3 and MDA-MB-231 cells but not MRC5 cells. Furthermore, previous studies demonstrated that the proteins and polymers with molecular weight larger than 40 kDa exhibit EPR effect [301–303]. Therefore we surmise that the EPR effect may enhance *G*Luc-*Li*Dps-ZnPP (515.2 kDa) accumulation at tumour tissues relative to healthy tissues. However, this need to be confirmed as the EPR effect can only be achieved in an *in vivo* environment [242]. Confocal microscopy provided high-resolution images of tumour cells after treatment with *G*Luc-*Li*Dps-ZnPP. Excitation of these cells at λ_{ex}= 425 nm showed that the *G*Luc-*Li*Dps-ZnPP nanoparticles were specifically localised in the cytoplasm of SKBR3 and MDA-MB-231 breast cancer cells, while no fluorescent signal was detected in MRC5 non-tumourigenic cells. Furthermore, the design of this construct to work based on BRET makes it attractive for use in *in vivo* applications than other PDTs which are poorer internal light sources that could reduce their efficiency for treatment of deep tissues. These results indicated that *G*Luc-*Li*Dps-ZnPP is a promising tool for cancer cell treatment and tumour tissue imaging.

Further *in vitro* and *in vivo* studies are needed before initiating human clinical trials to assess possible immune responses, which could be addressed by conjugating *G*Luc-*Li*Dps-ZnPP to PEG [294,295]. Such studies would assess the potential of the developed nanoconstruct as a PDT agent.

8.2 HER2-targeting systems for breast cancer therapy

As outlined previously, HER2 transmembrane receptors are overexpressed and present at the cell surface in several types of cancers, such as breast, ovarian, and gastric cancer. Further, *HER2* gene amplification and protein overexpression mostly correlate with a high rate of cellular proliferation and the absence of receptors for ER and PR, features related to metastatic breast cancer occurrence [304–306].

In this study, LTVSPWY and Afb2C, peptides with high affinity for HER2, were conjugated to different anticancer therapy molecules to target HER2-overexpressing breast cancer cells.

*G*Luc-miniSOG-LTVSPWY was successfully constructed with full recovery of protein activity. The activity of each component was studied, and the results indicated improvement in *G*Luc activity (i.e. *G*Luc bioluminescence). The yellow colour of miniSOG was clearly observed after *G*Luc-miniSOG-LTVSPWY expression. Mironova *et al.*

synthesised a comparable construct in which they fused the single-chain variable fragment of a humanised antibody (4D5scFv) as a HER2-targeting peptide with miniSOG (4D5scFv-miniSOG). They found that this construct exerted highly specific anticancer activity against SKBR3 cells [130]. However, their construct was not capable of self-illumination unlike our construct meaning that the activity of 4D5scFv-miniSOG may be reduced when it is used in *in vivo* studies. This is because the tissue absorption and scattering diminish the visible light required for PDT initiation. Further studies that monitor *in vitro* and *in vivo* ROS generation are needed to confirm the PDT activity of *G*Luc-miniSOG-LTVSPWY. In addition, the ability of *G*Luc-miniSOG-LTVSPWY to target and localise to HER2-overexpressing cancer cells and its usefulness for imaging tumour sites must be investigated to characterise *G*Luc-miniSOG-LTVSPWY behaviour inside targeted cells.

Another HER2-targeting peptide, Mutated Afb2C, was used to coat PbS QDs. From our results, we conclude that Afb2C successfully delivered PbS QDs to HER2-overexpressing SKBR3 cells without targeting MDA-MB-231 cells, which lack HER2. This study provides evidence for the ability of Afb2C-PbS QDs to induce cancer cell apoptosis. These include cell cycle arrest at pre-G1, associated with a reduction in the number of cells in G1, S, and G2/M and indicative of apoptosis-induced DNA fragmentation. Moreover, flow cytometry analysis indicated that the SKBR3 cell population in the late apoptosis quadrant increased

significantly after treatment with Afb2C-PbS QDs. The suppression of Bcl-2 expression by Afb2C-PbS QDs is consistent with other *in vitro* studies, and it strongly suggested a cellular apoptotic fate through DNA degradation. Previous research has shown that apoferritin-encapsulated PbS QDs can significantly inhibit the growth of colorectal carcinoma cells by inducing cancer cell apoptosis, consistent with the present study [209]. Several researchers have synthesised PbS QDs coated with different ligands. However, most were designed for tumour site imaging that exploit their unique optical properties [222,223,297]. The novel feature of Afb2C-PbS QDs is the direct conjugation of Afb2C to the PbS QDs. This made it highly selective for HER2 overexpressing cells and consequently reduced their cytotoxic side effects, ultimately improving their anticancer activity.

These results indicate that Afb2C-PbS QDs are a promising tool for cancer treatment. They encourage further *in vivo* studies of Afb2C-PbS QDs to confirm its anticancer activity in clinical applications and its usefulness as an imaging agent in the second NIR window. The anti-proliferative effect of Afb2C-PbS QDs need also to assess using healthy cell line.

Afb2C-PbS QDs was further modified by conjugation with ZnPP to provide it with additional anticancer and imaging functions. Our results demonstrated that improvement of ZnPP-Afb2C-PbS QDs anti-proliferative activity was accompanied by reducing its selectivity for

HER2-overexpressing SKBR3 cells. This was evident from its inhibitory effect on MDA-MB-231 cell growth which was not observed with Afb2C-PbS QDs. However, the growth inhibitory effect of ZnPP-Afb2C-PbS QDs on SKBR3 cells was significantly higher than on MDA-MB-231 cells. ZnPP-Afb2C-PbS QDs are similar to Afb2C-PbS QDs in that they promoted pre-G1 cell cycle arrest and DNA fragmentation. However, ZnPP-Afb2C-PbS QDs, unlike Afb2C-PbS QDs, mainly induced SKBR3 cell necrosis. This might be due to the more potent anticancer activity of ZnPP-Afb2C-PbS QDs that is caused by ZnPP, relative to that of Afb2C-PbS QDs. High-resolution images of intracellular ZnPP-Afb2C-PbS QDs localisation obtained using confocal microscopy indicated that ZnPP-Afb2C-PbS QDs are an attractive candidate for use as a tumour tissue and cancer cell imaging agent. In the future, the activity of ZnPP-Afb2C-PbS QDs needs to be investigated in greater detail through *in vivo* and clinical studies. Also, healthy cell line needs to use as a control for clear observation of ZnPP-Afb2C-PbS QDs activity.

9 References

[1] M. Jahanshahi, Z. Babaei, Protein nanoparticle: a unique system as drug delivery vehicles, *African J. Biotechnol*. **7** (2008) 4926–4934.

[2] W. Lohcharoenkal, L. Wang, Y.C. Chen, Y. Rojanasakul, Protein nanoparticles as drug delivery carriers for cancer therapy, *Biomed Res. Int*. **2014** (2014) 1–12.

[3] K. Wadu-Mesthrige, S. Xu, N.A. Amro, G. Liu, Fabrication and imaging of nanometer-sized protein patterns, *Langmuir*. **15** (1999) 8580–8583.

[4] S. Rana, Y.-C. Yeh, V.M. Rotello, Engineering the nanoparticle–protein interface: applications and possibilities, *Curr. Opin. Chem. Biol*. **14** (2010) 828–834.

[5] S. Srivastava, A. Verma, B.L. Frankamp, V.M. Rotello, Controlled assembly of protein–nanoparticle composites through protein surface recognition, *Adv. Mater*. **17** (2005) 617–621.

[6] M. Liang, K. Fan, M. Zhou, D. Duan, J. Zheng, D. Yang, J. Feng, X. Yan, H-ferritin–nanocaged doxorubicin nanoparticles specifically target and kill tumors with a single-dose injection, *Proc. Natl. Acad. Sci. U. S. A*. **111** (2014) 14900–14905.

[7] W. Kim, C. Brady, E.L. Chaikof, Amphiphilic protein micelles for targeted *in vivo* imaging, *Acta Biomater*. **8** (2012) 2476–2482.

[8] A. MaHam, Z. Tang, H. Wu, J. Wang, Y. Lin, Protein-Based Nanomedicine Platforms for Drug Delivery, *Small*. **5** (2009) 1706–1721.

[9] C.S. Kim, R. Mout, Y. Zhao, Y.-C. Yeh, R. Tang, Y. Jeong, B. Duncan, J.A. Hardy, V.M. Rotello, Co-Delivery of Protein and Small Molecule Therapeutics Using Nanoparticle-Stabilized Nanocapsules, *Bioconjug. Chem*. **26** (2015) 950–954.

[10] B.S. Sylla, C.P. Wild, A million africans a year dying from cancer by 2030: what can cancer research and control offer to the continent?, *Int. J. Cancer*. **130** (2012) 245–250.

[11] B.B. Orang-Ojong, J.E. Munyangaju, M.S. Wei, M. Lin, F.G. Wei, C. Foukunang, Y. Zhu, Impact of natural resources and research on cancer treatment and prevention: A perspective from Cameroon (Review), *Mol. Clin. Oncol.* **1** (2013) 610–620.

[12] J.N. Latosińska, M. Latosińska, Anticancer Drug Discovery-From

Serendipity to Rational Design, in: El-Shemy HA (Ed.), Drug Discov., INTECH Open Access Publisher, Poland, 2013: pp. 35–74.

[13] L. Han, S. Shi, T. Gong, Z. Zhang, X. Sun, Cancer stem cells: therapeutic implications and perspectives in cancer therapy, *Acta Pharm. Sin. B.* **3** (2013) 65–75.

[14] S. Jaracz, J. Chen, L. V Kuznetsova, I. Ojima, Recent advances in tumor-targeting anticancer drug conjugates, *Bioorg. Med. Chem*. **13** (2005) 5043–5054.

[15] S.D. Steichen, M. Caldorera-Moore, N.A. Peppas, A review of current nanoparticle and targeting moieties for the delivery of cancer therapeutics, *Eur. J. Pharm. Sci*. **48** (2013) 416–427.

[16] S. Sripriyalakshmi, P. Jose, A. Ravindran, C.H. Anjali, Recent trends in drug delivery system using protein nanoparticles, *Cell Biochem. Biophys*. **70** (2014) 17–26.

[17] A. Mahor, S. Alok, S. Prajapati, A. Verma, P. Yadav, M. Shringrishi, Protein nanoparticles: Future of drug delivery systems, *Int. J. Pharm. Sci. Res.* **5** (2014) 790.

[18] J. Ferlay, I. Soerjomataram, R. Dikshit, S. Eser, C. Mathers, M. Rebelo, D.M. Parkin, D. Forman, F. Bray, Cancer incidence and mortality worldwide: sources, methods and major patterns in GLOBOCAN 2012, *Int. J. Cancer*. **136** (2015) E359–E386.

[19] I.A. for R. on Cancer, W.H. Organization, GLOBOCAN 2012: Estimated cancer incidence, mortality and prevalence worldwide in 2012. h ttp, Globocan. Iarc. fr/Pages/fact_sheets_population. Aspx. Accessed. 14 (2015).

[20] D. He, J. Marles-Wright, Ferritin family proteins and their use in bionanotechnology, *N. Biotechnol*. **32** (2015) 651–657.

[21] M. Uchida, S. Kang, C. Reichhardt, K. Harlen, T. Douglas, The ferritin superfamily: Supramolecular templates for materials synthesis, *Biochim. Biophys. Acta*. **1800** (2010) 834–845.

[22] G. Jutz, P. van Rijn, B. Santos Miranda, A. Böker, Ferritin: a versatile building block for bionanotechnology, *Chem. Rev*. **115** (2015) 1653–1701.

[23] Z. Tang, H. Wu, Y. Zhang, Z. Li, Y. Lin, Enzyme-mimic activity of ferric nano-core residing in ferritin and its biosensing applications, *Anal. Chem*. **83** (2011) 8611–8616.

[24] M.L. Flenniken, M. Uchida, L.O. Liepold, S. Kang, M.J. Young, T. Douglas, A library of protein cage architectures as nanomaterials, Springer Berlin Heidelberg, Berlin, 2009.

[25] K. Cabán-Hernández, J.F. Gaudier, A.M. Espino, Characterization and differential expression of a ferritin protein from *Fasciola hepatica*, *Mol. Biochem. Parasitol*. **182** (2012) 54–61.

[26] G. Dai, R. Li, H. Chen, C. Jiang, X. You, Y. Wu, A ferritin-like protein with antioxidant activity in *Ureaplasma urealyticum*, *BMC Microbiol*. **15** (2015) 145.

[27] F.M. Michel, H.-A. Hosein, D.B. Hausner, S. Debnath, J.B. Parise, D.R. Strongin, Reactivity of ferritin and the structure of ferritin-derived ferrihydrite, *Biochim. Biophys. Acta.* **1800** (2010) 871–885.

[28] F. Carmona, Ò. Palacios, N. Gálvez, R. Cuesta, S. Atrian, M. Capdevila, J.M. Domínguez-Vera, Ferritin iron uptake and release in the presence of metals and metalloproteins: chemical implications in the brain, *Coord. Chem. Rev*. **257** (2013) 2752–2764.

[29] J.M. Slocik, C.A. Crouse, J.E. Spowart, R.R. Naik, Biologically tunable reactivity of energetic nanomaterials using protein cages, *Nano Lett*. **13** (2013) 2535–2540.

[30] Z. Wang, P. Huang, O. Jacobson, Z. Wang, Y. Liu, L. Lin, J. Lin, N. Lu, H. Zhang, R. Tian, Biomineralization-Inspired Synthesis of Copper Sulfide-Ferritin Nanocages as Cancer Theranostics, *ACS Nano*. **10** (2016) 3453–3460.

[31] M. Truffi, L. Fiandra, L. Sorrentino, M. Monieri, F. Corsi, S. Mazzucchelli, Ferritin nanocages: a biological platform for drug delivery, imaging and theranostics in cancer, *Pharmacol. Res*. **107** (2016) 57–65.

[32] B. Sana, E. Johnson, P. Le Magueres, A. Criswell, D. Cascio, S. Lim, The role of nonconserved residues of *Archaeoglobus fulgidus* ferritin on its unique structure and biophysical properties, *J. Biol. Chem*. **288** (2013) 32663–32672.

[33] A.A. Alkhateeb, J.R. Connor, Nuclear ferritin: a new role for ferritin in cell biology, *Biochim. Biophys. Acta*. **1800** (2010) 793–797.

[34] P. Arosio, F. Carmona, R. Gozzelino, F. Maccarinelli, M. Poli, The importance of eukaryotic ferritins in iron handling and cytoprotection, *Biochem. J*. **472** (2015) 1–15.

[35] T. Takahashi, S. Kuyucak, Functional properties of threefold and fourfold channels in ferritin deduced from electrostatic calculations, *Biophys. J.* **84** (2003) 2256–2263.

[36] E.C. Theil, Ferritin: the protein nanocage and iron biomineral in health and in disease, *Inorg. Chem.* **52** (2013) 12223–12233.

[37] S. Levi, E. Rovida, Neuroferritinopathy: From ferritin structure modification to pathogenetic mechanism, *Neurobiol. Dis*. **81** (2015) 134–143.

[38] Z. Wang, C. Li, M. Ellenburg, E. Soistman, J. Ruble, B. Wright, J.X. Ho, D.C. Carter, Structure of human ferritin L chain, *Acta Crystallogr. Sect. D Biol. Crystallogr*. **62** (2006) 800–806.

[39] M.C. Linder, Mobilization of stored iron in mammals: A review, *Nutrients*. **5** (2013) 4022–4050.

[40] N.D. Chasteen, P.M. Harrison, Mineralization in ferritin: an efficient means of iron storage, *J. Struct. Biol.* **126** (1999) 182–194.

[41] R. Yang, Z. Zhou, G. Sun, Y. Gao, J. Xu, Ferritin, a novel vehicle for iron supplementation and food nutritional factors encapsulation, *Trends Food Sci. Technol.* **44** (2015) 189–200.

[42] E.C. Theil, R.K. Behera, T. Tosha, Ferritins for chemistry and for life, *Coord. Chem. Rev*. **257** (2013) 579–586.

[43] Y. Cai, C. Cao, X. He, C. Yang, L. Tian, R. Zhu, Y. Pan, Enhanced magnetic resonance imaging and staining of cancer cells using ferrimagnetic h-ferritin nanoparticles with increasing core size, *Int. J. Nanomedicine*. **10** (2015) 2619–2634.

[44] X. He, J. Cai, B. Liu, Y. Zhong, Y. Qin, Cellular magnetic resonance imaging contrast generated by the ferritin heavy chain genetic reporter under the control of a Tet-On switch, *Stem Cell Res. Ther*. **6** (2015) 207.

[45] S. Kim, G.S. Kim, J. Seo, G. Gowri Rangaswamy, I.-S. So, R.-W. Park, B.-H. Lee, I.-S. Kim, Double-chambered ferritin platform: dual-function payloads of cytotoxic peptides and fluorescent protein, *Biomacromolecules*. **17** (2016) 12–19.

[46] T. Kitagawa, H. Kosuge, M. Uchida, M.M. Dua, Y. Iida, R.L. Dalman, T. Douglas, M. V McConnell, RGD-conjugated human ferritin nanoparticles for imaging vascular inflammation and angiogenesis in experimental carotid and aortic disease, *Mol. Imaging Biol*. **14** (2012) 315–324.

[47] K. Fan, L. Gao, X. Yan, Human ferritin for tumor detection and therapy, Wiley

Interdiscip. Rev. *Nanomedicine Nanobiotechnology*. **5** (2013) 287–298.

[48] S.G. Crich, M. Cadenazzi, S. Lanzardo, L. Conti, R. Ruiu, D. Alberti, F. Cavallo, J.C. Cutrin, S. Aime, Targeting ferritin receptors for the selective delivery of imaging and therapeutic agents to breast cancer cells, *Nanoscale*. **7** (2015) 6527–6533.

[49] L.F. Huergo, H. Rahman, A. Ibrahimovic, C.J. Day, V. Korolik, *Campylobacter jejuni* Dps protein binds DNA in the presence of iron or hydrogen peroxide, *J. Bacteriol*. **195** (2013) 1970–1978.

[50] O.P. Narayan, N. Kumari, P. Bhargava, H. Rajaram, L.C. Rai, A single gene all3940 (Dps) overexpression in *Anabaena sp*. PCC 7120 confers multiple abiotic stress tolerance via proteomic alterations, *Funct. Integr. Genomics*. **16** (2016) 67–78.

[51] Z. Du, R. Nandakumar, K.W. Nickerson, X. Li, Proteomic adaptations to starvation prepare *Escherichia coli* for disinfection tolerance, *Water Res*. **69** (2015) 110–119.

[52] V.O. Karas, I. Westerlaken, A.S. Meyer, The DNA-binding protein from starved cells (Dps) utilizes dual functions to defend cells against multiple stresses, *J. Bacteriol*. **197** (2015) 3206–3215.

[53] A.R. Arnold, J.K. Barton, DNA protection by the bacterial ferritin Dps via DNA charge transport, *J. Am. Chem. Soc*. **135** (2013) 15726–15729.

[54] J.-C. Shu, P.-C. Soo, J.-C. Chen, S.-H. Hsu, L.-C. Chen, C.-C.C.-Y. Chen, S.-H. Liang, L.-M. Buu, C.-C.C.-Y. Chen, Differential regulation and activity against oxidative stress of Dps proteins in *Bacillus cereus*, *Int. J. Med. Microbiol*. **303** (2013) 662–673.

[55] V. V Melekhov, U.S. Shvyreva, A.A. Timchenko, M.N. Tutukina, E. V Preobrazhenskaya, D. V Burkova, V.G. Artiukhov, O.N. Ozoline, S.S. Antipov, Modes of *Escherichia coli* Dps Interaction with DNA as Revealed by Atomic Force Microscopy, *PLoS One*. **10** (2015) e0126504.

[56] P. Ceci, S. Cellai, E. Falvo, C. Rivetti, G.L. Rossi, E. Chiancone, DNA condensation and self-aggregation of *Escherichia coli* Dps are coupled phenomena related to the properties of the N-terminus, *Nucleic Acids Res*. **32** (2004) 5935–5944.

[57] A. Ilari, S. Stefanini, E. Chiancone, D. Tsernoglou, The dodecameric ferritin from *Listeria innocua* contains a novel intersubunit iron-binding site., *Nat. Struct. Biol*. **7** (2000) 38–43.

[58] K. Zeth, Dps biomineralizing proteins: multifunctional architects of nature, *Biochem. J*. **445** (2012) 297–311.

[59] L.N. Calhoun, Y.M. Kwon, Structure, function and regulation of the DNA-binding protein Dps and its role in acid and oxidative stress resistance in *Escherichia coli*: A review, *J. Appl. Microbiol.* **110** (2011) 375–386.

[60] E. Chiancone, P. Ceci, The multifaceted capacity of Dps proteins to combat bacterial stress conditions: detoxification of iron and hydrogen peroxide and DNA binding, *Biochim. Biophys. Acta*. **1800** (2010) 798–805.

[61] R.M. Kramer, C. Li, D.C. Carter, M.O. Stone, R.R. Naik, Engineered protein cages for nanomaterial synthesis, *J. Am. Chem. Soc*. **126** (2004) 13282–13286.

[62] T.J. Stillman, M. Upadhyay, V.A. Norte, S.E. Sedelnikova, M. Carradus, S. Tzokov, P.A. Bullough, C.A. Shearman, M.J. Gasson, C.H. Williams, P.J. Artymiuk, J. Green, The crystal structures of *Lactococcus lactis* MG1363 Dps proteins reveal the presence of an N-terminal helix that is required for DNA binding, *Mol. Microbiol.* **57** (2005) 1101–1112.

[63] S. Roy, S. Gupta, S. Das, K. Sekar, D. Chatterji, M. Vijayan, X-ray analysis of *Mycobacterium smegmatis* Dps and a comparative study involving other Dps and Dps-like molecules, *J. Mol. Biol.* **339** (2004) 1103–1113.

[64] M. Okuda, Y. Suzumoto, K. Iwahori, S. Kang, M. Uchida, T. Douglas, I. Yamashita, Bio-templated CdSe nanoparticle synthesis in a cage shaped protein, *Listeria*-Dps, and their two dimensional ordered array self-assembly, *Chem. Commun*. **46** (2009) 8797–8799.

[65] J. Pesek, R. Büchler, R. Albrecht, W. Boland, K. Zeth, Structure and mechanism of iron translocation by a Dps protein from *Microbacterium arborescens*, *J. Biol. Chem.* **286** (2011) 34872–34882.

[66] K. Zeth, E. Hoiczyk, M. Okuda, Ferroxidase-Mediated Iron Oxide Biomineralization: Novel Pathways to Multifunctional Nanoparticles, *Trends Biochem. Sci*. **41** (2016) 190–203.

[67] G. Bellapadrona, M. Ardini, P. Ceci, S. Stefanini, E. Chiancone, Dps proteins prevent Fenton-mediated oxidative damage by trapping hydroxyl radicals within the protein shell, *Free Radic. Biol. Med*. **48** (2010) 292–297.

[68] B. Zhang, J.N. Harb, R.C. Davis, S. Choi, J. Kim, T. Miller, S. Chu, G.D. Watt, Electron Exchange between Fe (II) -Horse Spleen Ferritin and Co (III)/ Mn (III) Reconstituted Horse Spleen and *Azotobacter V*

inelandii Ferritins, *Biochemistry*. **45** (2006) 5766–5774.

[69] S. Kang, L.M. Oltrogge, C.C. Broomell, L.O. Liepold, P.E. Prevelige, M. Young, T. Douglas, Controlled assembly of bifunctional chimeric protein cages and composition analysis using noncovalent mass spectrometry, *J. Am. Chem. Soc*. **130** (2008) 16527–16529.

[70] M.M. Rahman, M. Lee, Y. Tsai, A. Higo, H. Sekhar, M. Igarashi, M.E. Syazwan, Y. Hoshi, K. Sawano, N. Usami, Impact of silicon quantum dot super lattice and quantum well structure as intermediate layer on p-i-n silicon solar cells, *Prog. Photovoltaics Res. Appl*. **24** (2016) 774–780.

[71] L. Ma, F. Li, T. Fang, J. Zhang, Q. Wang, Controlled Self-Assembly of Proteins into Discrete Nanoarchitectures Templated by Gold Nanoparticles via Monovalent Interfacial Engineering, *ACS Appl. Mater. Interfaces*. **7** (2015) 11024–11031.

[72] P.A. Suci, S. Kang, M. Young, T. Douglas, A streptavidin−protein cage janus particle for polarized targeting and modular functionalization, *J. Am. Chem. Soc*. **131** (2009) 9164–9165.

[73] R. Ackroyd, C. Kelty, N. Brown, M. Reed, The history of photodetection and photodynamic therapy, *Photochem. Photobiol*. **74** (2001) 656–669.

[74] S. Shahzidi, M. Sioud, A. Brech, S. Patzke, J.M. Nesland, Q. Peng, Intermediate Filament Proteins of Lamin A/C and Cytokeratin 18 are involved in Apoptotic Induction by Photodynamic Therapy with Hexaminolevulinate in Human Colon Carcinoma Cells, *J. Carcinog. Mutagen*. **6** (2014) 212.

[75] W. Park, S. Park, K. Na, The controlled photoactivity of nanoparticles derived from ionic interactions between a water soluble polymeric photosensitizer and polysaccharide quencher, *Biomaterials*. **32** (2011) 8261–8270.

[76] J. Wang, L. Zhang, M. Chen, S. Gao, L. Zhu, Activatable Ferritin Nanocomplex for Real-Time Monitoring of Caspase-3 Activation during Photodynamic Therapy, *ACS Appl. Mater. Interfaces*. **7** (2015) 23248–23256.

[77] M. Bio, P. Rajaputra, Y. You, Photodynamic therapy via FRET following bioorthogonal click reaction in cancer cells, *Bioorganic Med. Chem. Lett.* **26** (2016) 145–148.

[78] K. Davia, D. King, Y. Hong, S. Swavey, A porphyrin–ruthenium photosensitizer as a potential photodynamic therapy agent, *Inorg. Chem. Commun*. **11** (2008) 584–586.

[79] Z. Huang, A review of progress in clinical photodynamic therapy., *Technol. Cancer Res. Treat*. **4** (2005) 283–293.

[80] R. Saini, C.F. Poh, Photodynamic therapy: A review and its prospective role in the management of oral potentially malignant disorders, *Oral Dis*. (2012).

[81] H. Yuan, H. Chong, B. Wang, C. Zhu, L. Liu, Q. Yang, F. Lv, S. Wang, Chemical molecule-induced light-activated system for anticancer and antifungal activities, *J. Am. Chem. Soc*. **134** (2012) 13184–13187.

[82] P. Mroz, A. Yaroslavsky, G.B. Kharkwal, M.R. Hamblin, Cell death pathways in photodynamic therapy of cancer, *Cancers (Basel)*. **3** (2011) 2516–2539.

[83] T.G. St Denis, D. Vecchio, A. Zadlo, A. Rineh, M. Sadasivam, P. Avci, L. Huang, A. Kozinska, R. Chandran, T. Sarna, M.R. Hamblin, Thiocyanate potentiates antimicrobial photodynamic therapy: In situ generation of the sulfur trioxide radical anion by singlet oxygen, *Free Radic. Biol. Med*. **65** (2013) 800–810.

[84] S. Wang, R. Gao, F. Zhou, M. Selke, Nanomaterials and singlet oxygen photosensitizers: potential applications in photodynamic therapy, *J. Mater. Chem*. **14** (2004) 487–493.

[85] L. Huang, Y. Xuan, Y. Koide, T. Zhiyentayev, M. Tanaka, M.R. Hamblin, Type I and Type II mechanisms of antimicrobial photodynamic therapy: An *in vitro* study on gram-negative and gram-positive bacteria, *Lasers Surg. Med*. **44** (2012) 490–499.

[86] S.S. Lucky, K.C. Soo, Y. Zhang, Nanoparticles in photodynamic therapy, *Chem. Rev*. **115** (2015) 1990–2042.

[87] C.S. Foote, Definition of type I and type II photosensitized oxidation, *Photochem. Photobiol*. **54** (1991) 659.

[88] D.E. Dolmans, D. Fukumura, R.K. Jain, Photodynamic therapy for cancer, *Nat. Rev. Cancer*. **3** (2003) 380–387.

[89] S.-R. Tsai, R. Yin, Y.-Y. Huang, B.-C. Sheu, S.-C. Lee, M.R. Hamblin, Low-level light therapy potentiates NPe6-mediated photodynamic therapy in a human osteosarcoma cell line via increased ATP, *Photodiagnosis Photodyn. Ther*. **12** (2015) 123–130.

[90] T.A. Debele, S. Peng, H.-C. Tsai, Drug Carrier for Photodynamic Cancer Therapy, *Int. J. Mol. Sci*. **16** (2015) 22094–22136.

[91] J.O. Lee, B. Lim, Y.P. Kim, Bioluminescence resonance energy transfer

nanoprobes for imaging, *IEEE J. Sel. Top. Quantum Electron*. **20** (2014).

[92] M. Kumar, D. Zhang, D. Broyles, S.K. Deo, A rapid, sensitive, and selective bioluminescence resonance energy transfer (BRET)-based nucleic acid sensing system, *Biosens. Bioelectron*. **30** (2011) 133–139.

[93] Y.R. Kim, S. Kim, J.W. Choi, S.Y. Choi, S.-H.H. Lee, H. Kim, S.K. Hahn, G.Y. Koh, S.H. Yun, Bioluminescence-activated deep-tissue photodynamic therapy of cancer, *Theranostics*. **5** (2015) 805–817.

[94] Z. Xia, J. Rao, Biosensing and imaging based on bioluminescence resonance energy transfer, *Curr. Opin. Biotechnol*. **20** (2009) 37–44.

[95] D. Ramsay, E. Kellett, M. McVEY, R. Stephen, G. Milligan, Homo-and hetero-oligomeric interactions between G-protein-coupled receptors in living cells monitored by two variants of bioluminescence resonance energy transfer (BRET): hetero-oligomers between receptor subtypes form more efficiently than between less c, *Biochem. J*. **365** (2002) 429–440.

[96] K.D.G. Pfleger, K.A. Eidne, Monitoring the formation of dynamic G-protein-coupled receptor–protein complexes in living cells, *Biochem. J*. **385** (2005) 625–637.

[97] H. Baubet, Valérie Le Mouellic, P. Brulet, Chimeric green fluorescent protein-aequorin as bioluminescent Ca^{2+} reporters at the single cell level, *Proc. Natl. Acad. Sci. U. S. A*. **97** (2000) 7260–7265.

[98] A.B. Fajardo, T. Sudhaharan, A.R. Trimby, J. Jeffery, A. Jones, A.K. Campbell, Measurement of proteases using chemiluminescence-resonance-energy-transfer chimaeras between green fluorescent protein and aequorin, *Biochem. J*. **357** (2001) 687–697.

[99] R. Arai, H. Nakagawa, A. Kitayama, H. Ueda, T. Nagamune, Detection of protein-protein interaction by bioluminescence resonance energy transfer from firefly luciferase to red fluorescent protein, *J. Biosci. Bioeng*. **94** (2002) 362–364.

[100] L. Wang, W.C. Jackson, P.A. Steinbach, R.Y. Tsien, Evolution of new nonantibody proteins via iterative somatic hypermutation, *Proc. Natl. Acad. Sci. U. S. A.* **101** (2004) 16745–16749.

[101] R.E. Campbell, O. Tour, A.E. Palmer, P.A. Steinbach, G.S. Baird, D.A. Zacharias, R.Y. Tsien, A monomeric red fluorescent protein, *Proc. Natl. Acad. Sci. U. S. A.* **99** (2002) 7877–7882.

[102] N.C. Shaner, M.Z. Lin, M.R. McKeown, P.A. Steinbach, K.L. Hazelwood,

M.W. Davidson, R.Y. Tsien, Improving the photostability of bright monomeric orange and red fluorescent proteins, *Nat. Methods*. **5** (2008) 545–551.

[103] Y. Yamakawa, H. Veda, A. Kitayama, T. Nagamune, Rapid homogeneous immunoassay of peptides based on bioluminescence resonance energy transfer from firefly luciferase, *J. Biosci. Bioeng*. **93** (2002) 537–542.

[104] S.K. Deo, M. Mirasoli, S. Daunert, Bioluminescence resonance energy transfer from aequorin to a fluorophore: an artificial *jellyfish* for applications in multianalyte detection, *Anal. Bioanal. Chem*. **381** (2005) 1387–1394.

[105] M. So, C. Xu, A.M. Loening, S.S. Gambhir, J. Rao, Self-illuminating quantum dot conjugates for *in vivo* imaging, *Nat. Biotechnol*. **24** (2006) 339–343.

[106] K. Berg, P.K. Selbo, A. Weyergang, A. Dietze, L. Prasmickaite, A. Bonsted, B.Ø. Engesaeter, E. Angell-Petersen, T. Warloe, N. Frandsen, Porphyrin-related photosensitizers for cancer imaging and therapeutic applications, *J. Microsc*. **218** (2005) 133–147.

[107] A.E. O'Connor, W.M. Gallagher, A.T. Byrne, Porphyrin and nonporphyrin photosensitizers in oncology: preclinical and clinical advances in photodynamic therapy, *Photochem. Photobiol*. **85** (2009) 1053–1074.

[108] R.R. Allison, C.H. Sibata, Oncologic photodynamic therapy photosensitizers: a clinical review, *Photodiagnosis Photodyn. Ther*. **7** (2010) 61–75.

[109] M.N. Mwangi, S. Maskey, P.E.A. Andang'o, N.K. Shinali, J.M. Roth, L. Trijsburg, A.M. Mwangi, H. Zuilhof, B. van Lagen, H.F.J. Savelkoul, A.Y. Demir, H. Verhoef, Diagnostic utility of zinc protoporphyrin to detect iron deficiency in Kenyan pregnant women, *BMC Med*. **12** (2014) 229.

[110] A.A. Lamola and, T. Yamane, Zinc protoporphyrin in the erythrocytes of patients with lead intoxication and iron deficiency anemia, *Science*. **186** (1974) 936–938.

[111] R.F. Labbé, H.J. Vreman, D.K. Stevenson, Zinc protoporphyrin: a metabolite with a mission, *Clin. Chem*. **45** (1999) 2060–2072.

[112] O.P. Soldin, J.C. Pezzullo, B. Hanak, M. Miller, S.J. Soldin, Changing trends in the epidemiology of pediatric lead exposure: interrelationship of blood lead and ZPP concentrations and a comparison to the US population, *Ther. Drug Monit*. **25** (2003) 415.

[113] R. Crowell, A.M. Ferris, R.J. Wood, P. Joyce, H. Slivka, Comparative effectiveness of zinc protoporphyrin and hemoglobin concentrations in

identifying iron deficiency in a group of low-income, preschool-aged children: practical implications of recent illness, *Pediatrics*. **118** (2006) 224–232.

[114] J. Fang, K. Tsukigawa, L. Liao, H. Yin, K. Eguchi, H. Maeda, Styrene-maleic acid-copolymer conjugated zinc protoporphyrin as a candidate drug for tumor-targeted therapy and imaging, *J. Drug Target*. **24** (2016) 399–407.

[115] K. Huvaere, L.H. Skibsted, Flavonoids protecting food and beverages against light, *J. Sci. Food Agric*. **95** (2015) 20–35.

[116] J. Fang, L. Liao, H. Yin, H. Nakamura, V. Subr, K. Ulbrich, H. Maeda, Photodynamic therapy and imaging based on tumor-targeted nanoprobe, polymer-conjugated zinc protoporphyrin, *Futur. Sci. OA.* **1** (2015).

[117] E.M. Becker, D.R. Cardoso, L.H. Skibsted, Quenching of excited states of red-pigment zinc protoporphyrin IX by hemin and natural reductors in dry-cured hams, *Eur. Food Res. Technol.* **232** (2011) 343–349.

[118] C.-C. Cheng, S.-S. Guan, H.-J. Yang, C.-C. Chang, T.-Y. Luo, J. Chang, A.-S. Ho, Blocking heme oxygenase-1 by zinc protoporphyrin reduces tumor hypoxia-mediated VEGF release and inhibits tumor angiogenesis as a potential therapeutic agent against colorectal cancer, *J. Biomed. Sci*. **23** (2016) 18.

[119] J.S. Kang, I.-W. Choi, M.H. Han, D.-S. Lee, G.-Y. Kim, H.J. Hwang, B.W. Kim, C.M. Kim, Y.H. Yoo, Y.H. Choi, The cytoprotective effect of petalonia binghamiae methanol extract against oxidative stress in C2C12 myoblasts: mediation by upregulation of heme oxygenase-1 and nuclear factor-erythroid 2 related factor 2, *Mar. Drugs*. **13** (2015) 2666–2679.

[120] L. Bao, J. Ma, G. Chen, J. Hou, T.K. Hei, K.N. Yu, W. Han, Role of heme Oxygenase-1 in low dose Radioadaptive response, *Redox Biol*. **8** (2016) 333–340.

[121] K. Tsukigawa, H. Nakamura, J. Fang, M. Otagiri, H. Maeda, Effect of different chemical bonds in pegylation of zinc protoporphyrin that affects drug release, intracellular uptake, and therapeutic effect in the tumor, *Eur. J. Pharm. Biopharm*. **89** (2015) 259–270.

[122] A.K. Iyer, K. Greish, T. Seki, S. Okazaki, J. Fang, K. Takeshita, H. Maeda, Polymeric micelles of zinc protoporphyrin for tumor targeted delivery based on EPR effect and singlet oxygen generation, *J. Drug Target*. **15** (2007) 496–506.

[123] S. Dragojevic, J.S. Ryu, D. Raucher, Polymer-Based Prodrugs: Improving Tumor Targeting and the Solubility of Small Molecule Drugs

in Cancer Therapy, *Molecules*. **20** (2015) 21750–21769.

[124] K. Noma, Y. Jin, Optogenetic mutagenesis in *Caenorhabditis elegans*, *Nat. Commun*. **6** (2015).

[125] D.M. Shcherbakova, A.A. Shemetov, A.A. Kaberniuk, V. V Verkhusha, Natural photoreceptors as a source of fluorescent proteins, biosensors, and optogenetic tools, *Annu. Rev. Biochem*. **84** (2015) 519–550.

[126] R. Ruiz-Gonzáleza, A. Rodríguez-Pulidob, J. Torraa, S. Nonell, C. Flors, Genetically Encoded Singlet Oxygen Photosensitizers, in: N. Santi, F. Christina (Eds.), Singlet Oxyg. Appl. Biosci. Nanosci. Vol. 1, Royal Society of Chemistry, 2016: pp. 271–282.

[127] X. Shu, V. Lev-Ram, T.J. Deerinck, Y. Qi, E.B. Ramko, M.W. Davidson, Y. Jin, M.H. Ellisman, R.Y. Tsien, A genetically encoded tag for correlated light and electron microscopy of intact cells, tissues, and organisms, *PLoS Biol.* **9** (2011) e1001041.

[128] S. Xu, A.D. Chisholm, Highly efficient optogenetic cell ablation in *C. elegans* using membrane-targeted miniSOG, *Sci. Rep*. **6** (2016).

[129] M. Westberg, L. Holmegaard, F.M. Pimenta, M. Etzerodt, P.R. Ogilby, Rational design of an efficient, genetically encodable, protein-encased singlet oxygen photosensitizer, *J. Am. Chem. Soc*. **137** (2015) 1632–1642.

[130] K.E. Mironova, G.M. Proshkina, A. V Ryabova, O.A. Stremovskiy, S.A. Lukyanov, R. V Petrov, S.M. Deyev, Genetically encoded immunophotosensitizer 4D5scFv-miniSOG is a highly selective agent for targeted photokilling of tumor cells *in vitro*., *Theranostics*. **3** (2013) 831–840.

[131] F.M. Pimenta, R.L. Jensen, T. Breitenbach, M. Etzerodt, P.R. Ogilby, Oxygen-Dependent Photochemistry and Photophysics of "MiniSOG," a Protein-Encased Flavin, *Photochem. Photobiol*. **89** (2013) 1116–1126.

[132] M.B.E. Turbay, V. Rey, N.M. Argañaraz, F.E.M. Vieyra, A. Aspée, E.A. Lissi, C.D. Borsarelli, Effect of dye localization and self-interactions on the photosensitized generation of singlet oxygen by rose bengal bound to bovine serum albumin, *J. Photochem. Photobiol. B Biol*. **141** (2014) 275–282.

[133] R. Ruiz-González, A.L. Cortajarena, S.H. Mejias, M. Agut, S. Nonell, C. Flors, Singlet oxygen generation by the genetically encoded tag miniSOG, *J. Am. Chem. Soc*. **135** (2013) 9564–9567.

[134] Y.B. Qi, E.J. Garren, X. Shu, R.Y. Tsien, Y. Jin, Photo-inducible cell ablation in *Caenorhabditis elegans* using the genetically encoded singlet oxygen

generating protein miniSOG, *Proc. Natl. Acad. Sci*. **109** (2012) 7499–7504.

[135] A.S. Mishin, V. V Belousov, K.M. Solntsev, K.A. Lukyanov, Novel uses of fluorescent proteins, *Curr. Opin. Chem. Biol*. **27** (2015) 1–9.

[136] G.M. Proshkina, O.N. Shilova, A. V Ryabova, O.A. Stremovskiy, S.M. Deyev, A new anticancer toxin based on HER2/neu-specific DARPin and photoactive flavoprotein miniSOG, *Biochimie*. **118** (2015) 116–122.

[137] X.X. Zhou, M. Pan, M.Z. Lin, Investigating neuronal function with optically controllable proteins, *Front. Mol. Neurosci*. **8** (2015).

[138] H.J. Powers, Riboflavin (vitamin B-2) and health, *Am. J. Clin. Nutr*. **77** (2003) 1352–1360.

[139] E. Huskisson, S. Maggini, M. Ruf, The role of vitamins and minerals in energy metabolism and well-being, *J. Int. Med. Res*. **35** (2007) 277–289.

[140] J.M. Christie, K. Hitomi, A.S. Arvai, K.A. Hartfield, M. Mettlen, A.J. Pratt, J.A. Tainer, E.D. Getzoff, Structural tuning of the fluorescent protein iLOV for improved photostability, *J. Biol. Chem*. **287** (2012) 22295–22304.

[141] R. Cheraghi, S. Hosseinkhani, J. Davoodi, M. Nazari, Z. Amini-Bayat, H. Karimi, M. Shamseddin, F. Gheidari, Structural and functional effects of circular permutation on firefly luciferase: *in vitro* assay of caspase 3/7, *Int. J. Biol. Macromol*. **58** (2013) 336–342.

[142] B.R. Branchini, T.L. Southworth, D.M. Fontaine, D. Kohrt, M. Talukder, E. Michelini, L. Cevenini, A. Roda, M.J. Grossel, An enhanced chimeric firefly luciferase-inspired enzyme for ATP detection and bioluminescence reporter and imaging applications, *Anal. Biochem*. **484** (2015) 148–153.

[143] W. Wang, Q. Zhao, M. Luo, M. Li, D. Wang, Y. Wang, Q. Liu, Immobilization of firefly luciferase on PVA-co-PE nanofibers membrane as biosensor for bioluminescent detection of ATP, *ACS Appl. Mater. Interfaces*. **7** (2015) 20046–20052.

[144] M. Moradi, S. Hosseinkhani, R. Emamzadeh, Implication of an unfavorable residue (Thr346) in intrinsic flexibility of firefly luciferase, *Enzyme Microb. Technol*. **51** (2012) 186–192.

[145] S. Karimzadeh, M. Moradi, S. Hosseinkhani, Delicate balance of electrostatic interactions and disulfide bridges in thermostability of firefly luciferase, *Int. J. Biol. Macromol*. **51** (2012) 837–844.

[146] J.-B. Kim, K. Urban, E. Cochran, S. Lee, A. Ang, B. Rice, A. Bata, K. Campbell, R. Coffee, A. Gorodinsky, Non-invasive detection of a small

number of bioluminescent cancer cells *in vivo*, PLoS One. 5 (2010) e9364.

[147] L. Xue, I.A. Karpenko, J. Hiblot, K. Johnsson, Imaging and manipulating proteins in live cells through covalent labeling, *Nat. Chem. Biol*. **11** (2015) 917–923.

[148] K.E. Luker, L.A. Mihalko, B.T. Schmidt, S.A. Lewin, P. Ray, D. Shcherbo, D.M. Chudakov, G.D. Luker, *In vivo* imaging of ligand receptor binding with *Gaussia* luciferase complementation, *Nat. Med*. **18** (2012) 172–177.

[149] J. Lux, A.G. White, M. Chan, C.J. Anderson, A. Almutairi, Nanogels from metal-chelating crosslinkers as versatile platforms applied to copper-64 PET imaging of tumors and metastases, *Theranostics*. **5** (2015) 277–288.

[150] N. Wu, T. Kamioka, Y. Kuroda, A novel screening system based on VanX mediated autolysis-application to *Gaussia* luciferase, *Biotechnol. Bioeng*. **113** (2016) 1413–1420.

[151] T. Xu, D. Close, W. Handagama, E. Marr, G. Sayler, S. Ripp, The expanding toolbox of *in vivo* bioluminescent imaging, *Front. Oncol*. **6** (2016).

[152] M.H. Degeling, M.S.S. Bovenberg, G.K. Lewandrowski, M.C. de Gooijer, C.L.A. Vleggeert-Lankamp, M. Tannous, C.A. Maguire, B.A. Tannous, Directed molecular evolution reveals *Gaussia* luciferase variants with enhanced light output stability, *Anal. Chem*. **85** (2013) 3006–3012.

[153] S. Inouye, Y. Sahara-Miura, J. Sato, R. Iimori, S. Yoshida, T. Hosoya, Expression, purification and luminescence properties of coelenterazine-utilizing luciferases from *Renilla*, *Oplophorus* and *Gaussia*: Comparison of substrate specificity for C2-modified coelenterazines, *Protein Expr. Purif*. **88** (2013) 150–156.

[154] N. Wu, T. Rathnayaka, Y. Kuroda, Bacterial expression and re-engineering of *Gaussia princeps* luciferase and its use as a reporter protein, *Biochim. Biophys. Acta (BBA)-Proteins Proteomics*. 1854 (2015) 1392–1399.

[155] H. Oyama, I. Morita, Y. Kiguchi, S. Miyake, A. Moriuchi, T. Akisada, T. Niwa, N. Kobayashi, *Gaussia* Luciferase as a Genetic Fusion Partner with Antibody Fragments for Sensitive Immunoassay Monitoring of Clinical Biomarkers, *Anal. Chem*. **87** (2015) 12387–12395.

[156] E.L. von Der Heyde, B. Klein, L. Abram, A. Hallmann, The inducible nitA promoter provides a powerful molecular switch for transgene expression in *Volvox carteri*, *BMC Biotechnol*. **15** (2015) 5.

[157] S. V Markova, M.D. Larionova, L.P. Burakova, E.S. Vysotski, The smallest natural high-active luciferase: Cloning and characterization of novel 16.5-kDa luciferase from *copepod Metridia longa*, *Biochem. Biophys. Res. Commun*. **457** (2015) 77–82.

[158] B.A. Tannous, D.-E. Kim, J.L. Fernandez, R. Weissleder, X.O. Breakefield, Codon-optimized *Gaussia* luciferase cDNA for mammalian gene expression in culture and *in vivo*, *Mol. Ther*. **11** (2005) 435–443.

[159] J.E. Kim, S. Kalimuthu, B.-C. Ahn, *In vivo* cell tracking with bioluminescence imaging, *Nucl. Med. Mol. Imaging.* **49** (2015) 3–10.

[160] M.A. Kalwat, C. Wichaidit, A.Y. Nava Garcia, M.K. McCoy, K. McGlynn, I.H. Hwang, J.B. MacMillan, B.A. Posner, M.H. Cobb, Insulin promoter-driven *Gaussia* luciferase-based insulin secretion biosensor assay for discovery of β-cell glucose-sensing pathways. *ACS Sensors*. **1** (2016) 1208–1212.

[161] J.D. Hulleman, S.J. Brown, H. Rosen, J.W. Kelly, A high-throughput cell-based *Gaussia* luciferase reporter assay for identifying modulators of fibulin-3 secretion, *J. Biomol. Screen*. **18** (2013) 647–658.

[162] M. Srinivasarao, C. V. Galliford, P.S. Low, Principles in the design of ligand-targeted cancer therapeutics and imaging agents, *Nat. Rev. Drug Discov*. **14** (2015) 203–219.

[163] I. Mellman, Y. Yarden, Endocytosis and cancer, Cold Spring Harb. Perspect. Biol. (2013) a016949.

[164] S. Trousil, S. Hoppmann, Q.-D. Nguyen, M. Kaliszczak, G. Tomasi, P. Iveson, D. Hiscock, E.O. Aboagye, Positron emission tomography imaging with 18F-labeled ZHER2: 2891 affibody for detection of HER2 expression and pharmacodynamic response to HER2-modulating therapies, *Clin. Cancer Res*. **20** (2014) 1632–1643.

[165] A. Ravalli, C.G. da Rocha, H. Yamanaka, G. Marrazza, A label-free electrochemical affisensor for cancer marker detection: The case of HER2, *Bioelectrochemistry*. **106** (2015) 268–275.

[166] C. Eigenbrot, M. Ultsch, A. Dubnovitsky, L. Abrahmsén, T. Härd, Structural basis for high-affinity HER2 receptor binding by an engineered protein, *Proc. Natl. Acad. Sci. U. S. A*. **107** (2010) 15039–15044.

[167] J. Feldwisch, V. Tolmachev, C. Lendel, N. Herne, A. Sjöberg, B. Larsson, D. Rosik, E. Lindqvist, G. Fant, I. Höidén-Guthenberg, Design of an optimized scaffold for affibody molecules, *J. Mol. Biol*. **398** (2010) 232–247.

[168] J. Sörensen, D. Sandberg, M. Sandström, A. Wennborg, J. Feldwisch, V. Tolmachev, G. Åström, M. Lubberink, U. Garske-Román, J. Carlsson, First-in-human molecular imaging of HER2 expression in breast cancer metastases using the 111In-ABY-025 affibody molecule, *J. Nucl. Med*. **55** (2014) 730–735.

[169] H. Liu, J. Seijsing, F.Y. Frejd, V. Tolmachev, T. Gräslund, Target-specific cytotoxic effects on HER2-expressing cells by the tripartite fusion toxin ZHER2: 2891-ABD-PE38X8, including a targeting affibody molecule and a half-life extension domain, *Int. J. Oncol*. **47** (2015) 601–609.

[170] V. Tolmachev, F.Y. Nilsson, C. Widström, K. Andersson, D. Rosik, L. Gedda, A. Wennborg, A. Orlova, 111In-benzyl-DTPA–ZHER2: 342, an affibody-based conjugate for *in vivo* imaging of HER2 expression in malignant tumors, *J. Nucl. Med*. **47** (2006) 846–853.

[171] C. Xavier, A. Blykers, I. Vaneycken, M. D'Huyvetter, J. Heemskerk, T. Lahoutte, N. Devoogdt, V. Caveliers, 18 F-Nanobody for PET imaging of HER2 overexpressing tumors, *Nucl. Med. Biol*. **43** (2016) 247–252.

[172] A. Chopra, LTVSPWY peptide–modified PEGylated chitosan magnetic nanoparticles, MICAD. (2004).

[173] A.L. Bole, P. Manesiotis, Advanced Materials for the Recognition and Capture of Whole Cells and Microorganisms, *Adv. Mater*. **28** (2016) 5349–5366.

[174] B. Ndeboko, G.J. Lemamy, P.E. Nielsen, L. Cova, Therapeutic Potential of Cell Penetrating Peptides (CPPs) and Cationic Polymers for Chronic Hepatitis B, *Int. J. Mol. Sci*. **16** (2015) 28230–28241.

[175] M. Shadidi, M. Sioud, Selective targeting of cancer cells using synthetic peptides, *Drug Resist. Updat*. **6** (2003) 363–371.

[176] G. Palui, F. Aldeek, W. Wang, H. Mattoussi, Strategies for interfacing inorganic nanocrystals with biological systems based on polymer-coating, *Chem. Soc. Rev*. **44** (2015) 193–227.

[177] S. Jin, Y. Hu, Z. Gu, L. Liu, H.-C. Wu, Application of quantum dots in biological imaging, *J. Nanomater*. **2011** (2011) 13.

[178] M.M. Barroso, Quantum dots in cell biology, *J. Histochem. Cytochem*. **59** (2011) 237–251.

[179] I.L. Medintz, H.T. Uyeda, E.R. Goldman, H. Mattoussi, Quantum dot bioconjugates for imaging, labelling and sensing, *Nat. Mater*. **4** (2005) 435.

[180] T. Frecker, D. Bailey, X. Arzeta-Ferrer, J. McBride, S.J. Rosenthal,

Review—Quantum Dots and Their Application in Lighting, Displays, and Biology, *ECS J. Solid State Sci. Technol*. **5** (2016) R3019–R3031.

[181] R. Bilan, F. Fleury, I. Nabiev, A. Sukhanova, Quantum dot surface chemistry and functionalization for cell targeting and imaging, *Bioconjug. Chem*. **26** (2015) 609–624.

[182] N.C. Anheier, Nanotechnology: Colourful particles for spectrometry, *Nature*. **523** (2015) 39–40.

[183] J. Sambrook, D.W. Russell, Preparation of cDNA libraries and gene identification., in: Mol. Cloning. A Lab. Manual. Vol. **2**, New York: Cold Spring Harbor Laboratory Press, 2001.

[184] S. Roy, V. Kumar, A Practical Approach on SDS PAGE for Separation of Protein, *Int. J. Sci. Res*. **3** (2014) 955–960.

[185] L.G. Rodriguez, X. Wu, J.-L. Guan, Wound-healing assay, *Cell Migr. Dev. Methods Protoc*. (2005) 23–29.

[186] I. Nicoletti, G. Migliorati, M.C. Pagliacci, F. Grignani, C. Riccardi, A rapid and simple method for measuring thymocyte apoptosis by propidium iodide staining and flow cytometry, *J. Immunol. Methods*. **139** (1991) 271–279.

[187] T. Mahmood, P.-C. Yang, Western blot: technique, theory, and trouble shooting, *N. Am. J. Med. Sci*. **4** (2012) 429–434.

[188] M.M. Bradford, A rapid and sensitive method for the quantitation of microgram quantities of protein utilizing the principle of protein-dye binding, *Anal. Biochem*. **72** (1976) 248–254.

[189] E.A. Souslova, K.E. Mironova, S.M. Deyev, Applications of genetically encoded photosensitizer miniSOG: from correlative light electron microscopy to immunophotosensitizing, *J. Biophotonics.* **10** (2017) 338–352.

[190] L. Jullien, A. Gautier, Fluorogen-based reporters for fluorescence imaging: a review, *Methods Appl. Fluoresc*. **3** (2015) 42007.

[191] M. V Shirmanova, E.O. Serebrovskaya, L.B. Snopova, M.M. Kuznetsova, A.P. Ryumina, I. V Turchin, E.A. Sergeeva, N.I. Ignatova, N. V Klementieva, K.A. Lukyanov, KillerRed and miniSOG as genetically encoded photosensitizers for photodynamic therapy of cancer, in: Eur. Conf. Biomed. Opt., International Society for Optics and Photonics, 2013: p. 88030L–88030L.

[192] M. Shadidi, M. Sioud, Identification of novel carrier peptides for the specific delivery of therapeutics into cancer cells, *FASEB J*. **17** (2003) 256–258.

[193] M. Michalska, A. Florczak, H. Dams-Kozlowska, J. Gapinski, S. Jurga, R.

Schneider, Peptide-functionalized ZCIS QDs as fluorescent nanoprobe for targeted HER2-positive breast cancer cells imaging, *Acta Biomater*. **35** (2016) 293–304.

[194] M. Sioud, What are the key targeted delivery technologies of siRNA now?, *RNA Ther. Funct. Des. Deliv*. (2010) 91–105.

[195] S.L. Deutscher, Phage display in molecular imaging and diagnosis of cancer, *Chem. Rev.* **110** (2010) 3196–3211.

[196] J.-P. Nam, K.-J. Lee, J.-W. Choi, C.-O. Yun, J.-W. Nah, Targeting delivery of tocopherol and doxorubicin grafted-chitosan polymeric micelles for cancer therapy: *In vitro* and *in vivo* evaluation, *Colloids Surfaces B Biointerfaces*. **133** (2015) 254–262.

[197] Y. Zhang, S. Jiang, D. Zhang, X. Bai, S.M. Hecht, S. Chen, DNA–affibody nanoparticles for inhibiting breast cancer cells overexpressing HER2, *Chem. Commun*. **53** (2017) 573–576.

[198] J. Lobstein, C.A. Emrich, C. Jeans, M. Faulkner, P. Riggs, M. Berkmen, SHuffle, a novel *Escherichia coli* protein expression strain capable of correctly folding disulfide bonded proteins in its cytoplasm, *Microb. Cell Fact*. **11** (2012) 753.

[199] S. Bonissone, N. Gupta, M. Romine, R.A. Bradshaw, P.A. Pevzner, N-terminal protein processing: a comparative proteogenomic analysis, *Mol. Cell. Proteomics*. **12** (2013) 14–28.

[200] T. Ouidir, F. Jarnier, P. Cosette, T. Jouenne, J. Hardouin, Characterization of N-terminal protein modifications in *Pseudomonas aeruginosa* PA14, *J. Proteomics*. **114** (2015) 214–225.

[201] J. Ge, M. Lan, B. Zhou, W. Liu, L. Guo, H. Wang, Q. Jia, G. Niu, X. Huang, H. Zhou, A graphene quantum dot photodynamic therapy agent with high singlet oxygen generation, *Nat. Commun*. **5** (2014).

[202] T.B. Shrestha, G.M. Seo, M.T. Basel, M. Kalita, H. Wang, D. Villanueva, M. Pyle, S. Balivada, R.S. Rachakatla, H. Shinogle, Stem cell-based photodynamic therapy, *Photochem. Photobiol. Sci*. **11** (2012) 1251–1258.

[203] R. Lincoln, A.M. Durantini, L.E. Greene, S.R. Martínez, R. Knox, M.C. Becerra, G. Cosa, meso-Acetoxymethyl BODIPY dyes for photodynamic therapy: improved photostability of singlet oxygen photosensitizers, *Photochem. Photobiol. Sci*. **16** (2017) 178–184.

[204] Y. Zhang, B.P. Orner, Self-assembly in the ferritin nano-cage protein

superfamily, *Int. J. Mol. Sci*. **12** (2011) 5406–5421.

[205] R. Chiaraluce, V. Consalvi, S. Cavallo, A. Ilari, S. Stefanini, E. Chiancone, The unusual dodecameric ferritin from *Listeria innocua* dissociates below pH 2.0, *Eur. J. Biochem*. **267** (2000) 5733–5741.

[206] M. Kim, Y. Rho, K.S. Jin, B. Ahn, S. Jung, H. Kim, M. Ree, pH-dependent structures of ferritin and apoferritin in solution: disassembly and reassembly, *Biomacromolecules*. **12** (2011) 1629–1640.

[207] R.M. Neve, H.A. Lane, N.E. Hynes, The role of overexpressed HER2 in transformation, *Ann. Oncol*. **12** (2001) S9–S13.

[208] J. Zhang, X. Zhao, S. Wang, N. Wang, J. Han, L. Jia, X. Ren, Monitoring therapeutic response of human ovarian cancer to trastuzumab by SPECT imaging with 99m Tc-peptide-Z HER2: 342, *Nucl. Med. Biol*. **42** (2015) 541–546.

[209] T.D. Bradshaw, M. Junor, A. Patanè, P. Clarke, N.R. Thomas, M. Li, S. Mann, L. Turyanska, Apoferritin-encapsulated PbS quantum dots significantly inhibit growth of colorectal carcinoma cells, *J. Mater. Chem. B*. **1** (2013) 6254–6260.

[210] A.I. Kuruppu, L. Zhang, H. Collins, L. Turyanska, N.R. Thomas, T.D. Bradshaw, An Apoferritin-Based Drug Delivery System for the Tyrosine Kinase Inhibitor Gefitinib, *Adv. Healthc. Mater*. **4** (2015) 2816–2821.

[211] E. Falvo, E. Tremante, A. Arcovito, M. Papi, N. Elad, A. Boffi, V. Morea, G. Conti, G. Toffoli, G. Fracasso, Improved Doxorubicin Encapsulation and Pharmacokinetics of Ferritin–Fusion Protein Nanocarriers Bearing Proline, Serine, and Alanine Elements, *Biomacromolecules*. **17** (2015) 514–522.

[212] K.A. Majorek, M.L. Kuhn, M. Chruszcz, W.F. Anderson, W. Minor, Double trouble—Buffer selection and His-tag presence may be responsible for nonreproducibility of biomedical experiments, *Protein Sci*. **23** (2014) 1359–1368.

[213] W. Yang, L. Zhang, Z. Lu, W. Tao, Z. Zhai, A new method for protein coexpression in *Escherichia coli* using two incompatible plasmids, *Protein Expr. Purif*. **22** (2001) 472–478.

[214] V.A. Mikhailov, T.H. Mize, J.L.P. Benesch, C. V Robinson, Mass-selective soft-landing of protein assemblies with controlled landing energies, *Anal. Chem*. **86** (2014) 8321–8328.

[215] P. Ceci, E. Chiancone, O. Kasyutich, G. Bellapadrona, L. Castelli, M.

Fittipaldi, D. Gatteschi, C. Innocenti, C. Sangregorio, Synthesis of Iron Oxide Nanoparticles in *Listeria innocua* Dps (DNA-Binding Protein from Starved Cells): A Study with the Wild-Type Protein and a Catalytic Centre Mutant, *Chem. Eur. J*. **16** (2010) 709–717.

[216] T. Haikarainen, A.C. Papageorgiou, Dps-like proteins: structural and functional insights into a versatile protein family, *Cell. Mol. Life Sci*. **67** (2010) 341–351.

[217] E.A. Hunt, A. Moutsiopoulou, S. Ioannou, K. Ahern, K. Woodward, E. Dikici, S. Daunert, S.K. Deo, Truncated Variants of *Gaussia* Luciferase with Tyrosine Linker for Site-Specific Bioconjugate Applications, *Sci. Rep*. **6** (2016) 26814.

[218] K. Fujioka, F. Kalish, R.J. Wong, D.K. Stevenson, Inhibition of heme oxygenase activity using a microparticle formulation of zinc protoporphyrin in an acute hemolytic newborn mouse model, *Pediatr. Res*. **79** (2015) 251–257.

[219] D. Nowis, M. Bugajski, M. Winiarska, J. Bil, A. Szokalska, P. Salwa, T. Issat, H. Was, A. Jozkowicz, J. Dulak, Zinc protoporphyrin IX, a heme oxygenase-1 inhibitor, demonstrates potent antitumor effects but is unable to potentiate antitumor effects of chemotherapeutics in mice, *BMC Cancer*. **8** (2008) 197.

[220] K. Hirai, T. Sasahira, H. Ohmori, K. Fujii, H. Kuniyasu, Inhibition of heme oxygenase-1 by zinc protoporphyrin IX reduces tumor growth of LL/2 lung cancer in C57BL mice, *Int. J. Cancer*. **120** (2007) 500–505.

[221] S. Inouye, Y. Sahara, Identification of two catalytic domains in a luciferase secreted by the *copepod Gaussia* princeps, *Biochem. Biophys. Res. Commun*. **365** (2008) 96–101.

[222] A. Sasaki, Y. Tsukasaki, A. Komatsuzaki, T. Sakata, H. Yasuda, T. Jin, Recombinant protein (EGFP-Protein G)-coated PbS quantum dots for *in vitro* and *in vivo* dual fluorescence (visible and second-NIR) imaging of breast tumors, *Nanoscale*. **7** (2015) 5115–5119.

[223] Y. Nakane, Y. Tsukasaki, T. Sakata, H. Yasuda, T. Jin, Aqueous synthesis of glutathione-coated PbS quantum dots with tunable emission for non-invasive fluorescence imaging in the second near-infrared biological window (1000–1400 nm), *Chem. Commun*. **49** (2013) 7584–7586.

[224] X. Zhao, I. Gorelikov, S. Musikhin, S. Cauchi, V. Sukhovatkin, E.H. Sargent, E. Kumacheva, Synthesis and optical properties of thiol-stabilized PbS nanocrystals, *Langmuir*. **21** (2005) 1086–1090.

[225] D. Wang, J. Qian, F. Cai, S. He, S. Han, Y. Mu, "Green"-synthesized near-infrared PbS quantum dots with silica–PEG dual-layer coating: ultrastable and biocompatible optical probes for *in vivo* animal imaging, *Nanotechnology*. **23** (2012) 245701.

[226] D. Deng, W. Zhang, X. Chen, F. Liu, J. Zhang, Y. Gu, J. Hong, Facile Synthesis of High-Quality, Water-Soluble, Near-Infrared-Emitting PbS Quantum Dots, *Eur. J. Inorg. Chem*. **2009** (2009) 3440–3446.

[227] Y. Yu, K. Zhang, S. Sun, One-pot aqueous synthesis of near infrared emitting PbS quantum dots, *Appl. Surf. Sci*. **258** (2012) 7181–7187.

[228] N. Ma, A.F. Marshall, J. Rao, Near-infrared light emitting luciferase via biomineralization, *J. Am. Chem. Soc*. **132** (2010) 6884–6885.

[229] A. Orlova, M. Magnusson, T.L.J. Eriksson, M. Nilsson, B. Larsson, I. Höidén-Guthenberg, C. Widström, J. Carlsson, V. Tolmachev, S. Ståhl, Tumor imaging using a picomolar affinity HER2 binding affibody molecule, *Cancer Res*. **66** (2006) 4339–4348.

[230] V. Tolmachev, A. Orlova, R. Pehrson, J. Galli, B. Baastrup, K. Andersson, M. Sandström, D. Rosik, J. Carlsson, H. Lundqvist, Radionuclide therapy of HER2-positive microxenografts using a 177Lu-labeled HER2-specific Affibody molecule, *Cancer Res*. **67** (2007) 2773–2782.

[231] S.B. Lee, M. Hassan, R. Fisher, O. Chertov, V. Chernomordik, G. Kramer-Marek, A. Gandjbakhche, J. Capala, Affibody molecules for *in vivo* characterization of HER2-positive tumors by near-infrared imaging, *Clin. Cancer Res*. **14** (2008) 3840–3849.

[232] S.K. Sahoo, T. Sawa, J. Fang, S. Tanaka, Y. Miyamoto, T. Akaike, H. Maeda, Pegylated zinc protoporphyrin: a water-soluble heme oxygenase inhibitor with tumor-targeting capacity, *Bioconjug. Chem*. **13** (2002) 1031–1038.

[233] H. Nakamura, L. Liao, Y. Hitaka, K. Tsukigawa, V. Subr, J. Fang, K. Ulbrich, H. Maeda, Micelles of zinc protoporphyrin conjugated to N-(2-hydroxypropyl) methacrylamide (HPMA) copolymer for imaging and light-induced antitumor effects *in vivo*, *J. Control. Release*. **165** (2013) 191–198.

[234] I. Moreels, K. Lambert, D. Smeets, D. De Muynck, T. Nollet, J.C.

Martins, F. Vanhaecke, A. Vantomme, C. Delerue, G. Allan, Size-dependent optical properties of colloidal PbS quantum dots, *ACS Nano*. **3** (2009) 3023–3030.

[235] S. Sahdev, S.K. Khattar, K.S. Saini, Production of active eukaryotic proteins through bacterial expression systems: a review of the existing biotechnology strategies, *Mol. Cell. Biochem*. **307** (2008) 249–264.

[236] F. Baneyx, Recombinant protein expression in *Escherichia coli*, *Curr Opin Biotechnol*. **10** (1999) 411–421.

[237] A. Sivashanmugam, V. Murray, C. Cui, Y. Zhang, J. Wang, Q. Li, Practical protocols for production of very high yields of recombinant proteins using *Escherichia coli*, *Protein Sci*. **18** (2009) 936–948.

[238] R.W. L. Mielanczyk, N. Matysiak, O. Klymenko, The Transmission Electron Microscope–Theory and Applications, 2015. http://www.intechopen.com/books/the-transmission-electronmicroscope-%0Atheory-and-applications.

[239] K.M. Kern, J.R. Schroeder, Comparison of cantharidin toxicity in breast cancer cells to two common chemotherapeutics, *Int. J. Breast Cancer*. **2014** (2014).

[240] L. Hartsuiker, N.J.L. Zeijen, L.W.M.M. Terstappen, C. Otto, A comparison of breast cancer tumor cells with varying expression of the Her2/neu receptor by Raman microspectroscopic imaging, *Analyst*. **135** (2010) 3220–3226.

[241] J.M. Dixon, ABC of breast diseases, John Wiley & Sons, London, 2009.

[242] A. Kuruppu, The role of HER family signalling in breast cancer, University of Nottingham, 2016. PhD thesis.

[243] S. Jeelani, R.C.J. Reddy, T. Maheswaran, G.S. Asokan, A. Dany, B. Anand, Theranostics: A treasured tailor for tomorrow, *J. Pharm. Bioallied Sci*. **6** (2014) 6–8.

[244] G. Mosoyan, C. Nagi, S. Marukian, A. Teixeira, A. Simonian, L. Resnick-Silverman, A. DiFeo, D. Johnston, S.R. Reynolds, D.F. Roses, Multiple breast cancer cell-lines derived from a single tumor differ in their molecular characteristics and tumorigenic potential, *PLoS One*. **8** (2013) e55145.

[245] K. Subik, J.-F. Lee, L. Baxter, T. Strzepek, D. Costello, P. Crowley, L. Xing, M.-C. Hung, T. Bonfiglio, D.G. Hicks, The expression patterns of ER, PR, HER2, CK5/6, EGFR, Ki-67 and AR by immunohistochemical analysis in breast cancer cell lines, *Breast Cancer Basic Clin. Res*. **4** (2010) 35–41.

[246] D.L. Holliday, V. Speirs, Choosing the right cell line for breast cancer research, *Breast Cancer Res*. **13** (2011) 215.

[247] X. Dai, L. Xiang, T. Li, Z. Bai, Cancer Hallmarks, Biomarkers and Breast Cancer Molecular Subtypes, *J. Cancer*. **7** (2016) 1281.

[248] X. Dai, T. Li, Z. Bai, Y. Yang, X. Liu, J. Zhan, B. Shi, Breast cancer intrinsic subtype classification, clinical use and future trends, *Am. J. Cancer Res*. **5** (2015) 2929.

[249] R.M. Neve, K. Chin, J. Fridlyand, J. Yeh, F.L. Baehner, T. Fevr, L. Clark, N. Bayani, J.-P. Coppe, F. Tong, A collection of breast cancer cell lines for the study of functionally distinct cancer subtypes, *Cancer Cell*. **10** (2006) 515–527.

[250] D.J. Wong, S.A. Hurvitz, Recent advances in the development of anti-HER2 antibodies and antibody-drug conjugates., *Ann. Transl. Med*. **2** (2014).

[251] A. Prat, J.S. Parker, O. Karginova, C. Fan, C. Livasy, J.I. Herschkowitz, X. He, C.M. Perou, Phenotypic and molecular characterization of the claudin-low intrinsic subtype of breast cancer, *Breast Cancer Res*. **12** (2010) R68.

[252] J.P. Jacobs, C.M. Jones, J.P. Baille, Characteristics of a Human Diploid Cell Designated MRC-5, *Nat. Publ. Gr*. **227** (1970) 168–170.

[253] S. Schrader, S.J. Tuft, M. Beaconsfield, M. Borrelli, G. Geerling, J.T. Daniels, Evaluation of human MRC-5 cells as a feeder layer in a xenobiotic-free culture system for conjunctival epithelial progenitor cells, *Curr. Eye Res*. **37** (2012) 1067–1074.

[254] N. Iqbal, N. Iqbal, Human epidermal growth factor receptor 2 (HER2) in cancers: overexpression and therapeutic implications, *Mol. Biol. Int*. **2014** (2014).

[255] M.J. Wieduwilt, M.M. Moasser, The epidermal growth factor receptor family: biology driving targeted therapeutics, *Cell. Mol. Life Sci*. **65** (2008) 1566–1584.

[256] L.A. Bazley, W.J. Gullick, The epidermal growth factor receptor family, *Endocr. Relat. Cancer*. **12** (2005) S17–S27.

[257] R. Nahta, G.N. Hortobagyi, F.J. Esteva, Growth factor receptors in breast cancer: potential for therapeutic intervention, *Oncologist*. **8** (2003) 5–17.

[258] S. Damodaran, E.M. Olson, Targeting the human epidermal growth factor receptor 2 pathway in breast cancer, *Hosp. Pract*. **40** (2012) 7–15.

[259] A. Beck, J.M. Reichert, Antibody-drug conjugates: present and future, *MAbs*. **6** (2014) 15–17.

[260] M. Guerin, R. Sabatier, A. Goncalves, Trastuzumab emtansine (Kadcyla (®)) approval in HER2-positive metastatic breast cancers, *Bull. Cancer*. **102** (2015) 390–397.

[261] L. Ekerljung, M. Lindborg, L. Gedda, F.Y. Frejd, J. Carlsson, J. Lennartsson, Dimeric HER2-specific affibody molecules inhibit proliferation of the SKBR-3 breast cancer cell line, *Biochem. Biophys. Res. Commun*. **377** (2008) 489–494.

[262] G.M. Cooper, Chapter 14: the eukaryotic cell cycle, in: Cell a Mol. Approach, 2 nd, Washington, DC: ASM Press., 2000.

[263] K.A. Schafer, The cell cycle: a review, *Vet. Pathol. Online*. **35** (1998) 461–478.

[264] K. Vermeulen, D.R. Van Bockstaele, Z.N. Berneman, The cell cycle: a review of regulation, deregulation and therapeutic targets in cancer, *Cell Prolif*. **36** (2003) 131–149.

[265] D. Hanahan, R.A. Weinberg, The hallmarks of cancer, *Cell*. **100** (2000) 57–70.

[266] D.O. Morgan, The cell cycle: principles of control, New Science Press Ltd: London, UK., London, 2007.

[267] W. Chaabane, S.D. User, M. El-Gazzah, R. Jaksik, E. Sajjadi, J. Rzeszowska-Wolny, M.J. Łos, Autophagy, apoptosis, mitoptosis and necrosis: interdependence between those pathways and effects on cancer, *Arch. Immunol. Ther. Exp*. *(Warsz)*. **61** (2013) 43–58.

[268] L. Ouyang, Z. Shi, S. Zhao, F. Wang, T. Zhou, B. Liu, J. Bao, Programmed cell death pathways in cancer: a review of apoptosis, autophagy and programmed necrosis, *Cell Prolif*. **45** (2012) 487–498.

[269] Y. Soini, V. Kinnula, R. Kaarteenaho-Wiik, E. Kurttila, K. Linnainmaa, P. Pääkkö, Apoptosis and expression of apoptosis regulating proteins bcl-2, mcl-1, bcl-X, and bax in malignant mesothelioma, *Clin. Cancer Res*. **5** (1999) 3508–3515.

[270] Y. Xiao, P. Nimmer, G.S. Sheppard, M. Bruncko, P. Hessler, X. Lu, L. Roberts-Rapp, W.N. Pappano, S.W. Elmore, A.J. Souers, MCL-1 is a key determinant of breast cancer cell survival: Validation of MCL-1 dependency utilizing a highly selective small molecule inhibitor, *Mol. Cancer Ther*. **14** (2015) 1837–1847.

[271] S.Y. Proskuryakov, A.G. Konoplyannikov, V.L. Gabai, Necrosis: a specific form of programmed cell death?, *Exp. Cell Res*. **283** (2003) 1–16.

[272] NECROSIS APOPTOSIS 2, (2016) http://symposcium.com/necrosis-

apoptosis-2/.

[273] G.-Y. Liou, P. Storz, Reactive oxygen species in cancer, *Free Radic. Res*. **44** (2010) 479–496.

[274] G. Waris, H. Ahsan, Reactive oxygen species: role in the development of cancer and various chronic conditions, *J. Carcinog*. **5** (2006) 14.

[275] L.B. Sullivan, N.S. Chandel, Mitochondrial reactive oxygen species and cancer, *Cancer Metab*. **2** (2014) 17.

[276] J.M. Matés, F.M. Sánchez-Jiménez, Role of reactive oxygen species in apoptosis: implications for cancer therapy, *Int. J. Biochem. Cell Biol*. **32** (2000) 157–170.

[277] H. Yin, L. Liao, J. Fang, Enhanced permeability and retention (EPR) effect based tumor targeting: the concept, application and prospect, *JSM Clin Oncol Res*. **2** (2014) 1010.

[278] Y. Nakamura, A. Mochida, P.L. Choyke, H. Kobayashi, Nanodrug Delivery: Is the Enhanced Permeability and Retention Effect Sufficient for Curing Cancer?, *Bioconjug. Chem*. **27** (2016) 2225–2238.

[279] M.E. Qazzaz, V.J. Raja, K.-H. Lim, T.-S. Kam, J.B. Lee, P. Gershkovich, T.D. Bradshaw, *In vitro* anticancer properties and biological evaluation of novel natural alkaloid jerantinine b, *Cancer Lett*. **370** (2016) 185–197.

[280] S.K. Niture, A.K. Jaiswal, Antioxidant inhibition of GSK-3β stabilizes anti-apoptotic factor Mcl-1 leading to decreased apoptosis and increased cell survival., *Cancer Res*. **73** (2013) 601.

[281] L. Xue, S. Chiu, N.L. Oleinick, Photochemical destruction of the Bcl-2 oncoprotein during photodynamic therapy with the phthalocyanine photosensitizer Pc 4, *Oncogene*. **20** (2001) 3420–3427.

[282] E.J. Lim, C.-H. Oak, J. Heo, Y.-H. Kim, Methylene blue-mediated photodynamic therapy enhances apoptosis in lung cancer cells, *Oncol. Rep.* **30** (2013) 856–862.

[283] J. Cai, J. Yang, D. Jones, Mitochondrial control of apoptosis: the role of cytochrome c, *Biochim. Biophys. Acta (BBA)-Bioenergetics*. **1366** (1998) 139–149.

[284] G. Sollberger, G.E. Strittmatter, M. Garstkiewicz, J. Sand, H.-D. Beer, Caspase-1: the inflammasome and beyond, *Innate Immun*. **20** (2014) 115–125.

[285] E.M. Creagh, Caspase crosstalk: integration of apoptotic and innate

immune signalling pathways, *Trends Immunol*. **35** (2014) 631–640.

[286] R. Riahi, Y. Yang, D.D. Zhang, P.K. Wong, Advances in wound-healing assays for probing collective cell migration, *J. Lab. Autom*. **17** (2012) 59–65.

[287] B.C. Koehler, A.-L. Scherr, S. Lorenz, T. Urbanik, N. Kautz, C. Elssner, S. Welte, J.L. Bermejo, D. Jäger, H. Schulze-Bergkamen, Beyond cell death–antiapoptotic Bcl-2 proteins regulate migration and invasion of colorectal cancer cells *in vitro*, *PLoS One*. **8** (2013) e76446.

[288] K.M. Detjen, K. Farwig, M. Welzel, B. Wiedenmann, S. Rosewicz, Interferon γ inhibits growth of human pancreatic carcinoma cells via caspase-1 dependent induction of apoptosis, *Gut*. **49** (2001) 251–262.

[289] A.M. Rieger, K.L. Nelson, J.D. Konowalchuk, D.R. Barreda, Modified annexin V/propidium iodide apoptosis assay for accurate assessment of cell death, *J. Vis. Exp*. **50** (2011) e2597.

[290] D.M. Hockenbery, Z.N. Oltvai, X.-M. Yin, C.L. Milliman, S.J. Korsmeyer, Bcl-2 functions in an antioxidant pathway to prevent apoptosis, *Cell*. **75** (1993) 241–251.

[291] A. Chalkidou, K. Simeonidis, M. Angelakeris, T. Samaras, C. Martinez-Boubeta, L. Balcells, K. Papazisis, C. Dendrinou-Samara, O. Kalogirou, *In vitro* application of Fe/MgO nanoparticles as magnetically mediated hyperthermia agents for cancer treatment, *J. Magn. Magn. Mater*. **323** (2011) 775–780.

[292] S.E. Cross, Y.-S. Jin, J. Tondre, R. Wong, J. Rao, J.K. Gimzewski, AFM-based analysis of human metastatic cancer cells, *Nanotechnology*. **19** (2008) 384003.

[293] L. Xue, S. Chiu, N.L. Oleinick, Differential responses of Mcl-1 in photosensitized epithelial vs lymphoid-derived human cancer cells, *Oncogene*. **24** (2005) 6987–6992.

[294] D. Bhadra, S. Bhadra, P. Jain, N.K. Jain, Pegnology: a review of PEG-ylated systems., *Pharmazie*. **57** (2002) 5–29.

[295] S. Hermeling, D.J.A. Crommelin, H. Schellekens, W. Jiskoot, Structure-immunogenicity relationships of therapeutic proteins, *Pharm. Res*. **21** (2004) 897–903.

[296] M. Altai, H. Wållberg, H. Honarvar, J. Strand, A. Orlova, Z. Varasteh, M. Sandström, J. Löfblom, E. Larsson, S.-E. Strand, 188Re-ZHER2: V2, a promising affibody-based targeting agent against HER2-expressing

tumors: preclinical assessment, *J. Nucl. Med*. **55** (2014) 1842–1848.

[297] J. Sun, M. Zhu, K. Fu, N. Lewinski, R.A. Drezek, Lead sulfide near-infrared quantum dot bioconjugates for targeted molecular imaging, *Int. J. Nanomedicine*. **2** (2007) 235–240.

[298] S. Katari, M. Wallack, M. Huebschman, P. Pantano, H. Garner, Fabrication and evaluation of a near-infrared hyperspectral imaging system, *J. Microsc*. **236** (2009) 11–17.

[299] U. Shimanovich, G.J.L. Bernardes, T.P.J. Knowles, A. Cavaco-Paulo, Protein micro-and nano-capsules for biomedical applications, *Chem. Soc. Rev*. **43** (2014) 1361–1371.

[300] C.P. Reis, R.J. Neufeld, A.J. Ribeiro, F. Veiga, Nanoencapsulation II. Biomedical applications and current status of peptide and protein nanoparticulate delivery systems, *Nanomedicine Nanotechnology, Biol. Med*. **2** (2006) 53–65.

[301] Y. Noguchi, J. Wu, R. Duncan, J. Strohalm, K. Ulbrich, T. Akaike, H. Maeda, Early phase tumor accumulation of macromolecules: a great difference in clearance rate between tumor and normal tissues, *Cancer Sci*. **89** (1998) 307–314.

[302] M.H. Matsumura Y, A New Concept for Macromolecular Therapeutics in Cancer Chemotherapy: Mechanism of Tumoritropic Accumulation of Proteins and the Antitumor Agent Smancs, *Cancer Res*. **46** (1986) 6387–6392.

[303] J. Fang, H. Nakamura, H. Maeda, The EPR effect: unique features of tumor blood vessels for drug delivery, factors involved, and limitations and augmentation of the effect, *Adv. Drug Deliv. Rev*. **63** (2011) 136–151.

[304] F.F.T. Barros, D.G. Powe, I.O. Ellis, A.R. Green, Understanding the HER family in breast cancer: interaction with ligands, dimerization and treatments, *Histopathology*. **56** (2010) 560–572.

[305] A.K. Koutras, T.R. Evans, The epidermal growth factor receptor family in breast cancer, *OncoTargets Ther*. **1** (2008) 5–19.

[306] I. Überall, Z. Kolář, R. Trojanec, J. Berkovcova, M. Hajduch, The status and role of ErbB receptors in human cancer, *Exp. Mol. Pathol*. **84** (2008) 79–89.

10 Appendix

10.1 Bacterial strains

Cell lines	Description	Applications	Origin/Source
BL21 (DE3)	F-, ompT, hsdS_{β} (r_{β}-m_{β}-), dcm, gal, (DE3) *ton*A.	Used for protein expression.	*E.coli* (Ca^{2+} competent cell)/ Invitrogen
Shuffle (DE3)	*F'* lac, pro, lacIQ/ Δ(ara-leu)7697 araD139 fhuA2 lacZ::T7 gene1 Δ(phoA)PvuIIphoRahpC* galE (or U) galKλatt::pNEB3-r1-cDsbC *(SpecR, lacIq)*ΔtrxB rpsL150(StrR) Δgor Δ(malF)3	Used for expression of proteins requiring assistance forming disulfide bonds.	*E.coli* (Ca^{2+} competent cell)/ Invitrogen
DH5ɑ	F-, Ø80dlacZΔM15, Δ(lacZYA-argF)U169, deoR, recA1, endA1, hsdR17(rK-, mK+), phoA, supE44, λ-, thi-1, gyrA96, relA1	Used for DNA manipulation.	*E.coli* (Ca^{2+} competent cell)/ Invitrogen
XL1-Blue	*recA1 endA1 gyrA96 thi-1 hsdR17 supE44 relA1 lac [F' proAB lacIqZΔM15 Tn10 (Tetr)]*	Used for mutagenesis transformation	*E.coli* (electro-competent cell)/ Invitrogen

10.2 PCR primers

	Primer sequence (5'—3')
pJ411fwd (T7 promoter)	TAATACGACTCACTATAGGGG
pJ411rev (T7 terminator)	GCTAGTTATTGCTCAGCGG
pJ401fwd (T5 promoter)	CGCTCACAATTCCACAACG
rHuLK108C rev	CAGCAGCGCCTGGTTCAAGCACTTTTCCAGCGCCATCGC
miniSOG fwd	AACGCCCCATATGGCGGAAAAGAGC
miniSOG rev	CACCTTCTCGAGTTAGTGATGGTGATG
*Li*Dps rev	CGGGCCTCGAGCTACTCTAATGGAGCTTTTCC
Q5SDM Afb2C fwd	TTGTGGCGGATCCCTCGAGTAACC
Q5SDM Afb2C rev	CCACAACCGCCGTCGACCTTCGG
BamHI-miniSOG fwd	GCATAAGGATCCGCGGAAAAGAGCTTTGTGATT
XhoI-miniSOG rev	TTATGCCTCGAGATCCAGCTGCACACCAAT

10.3 Plasmids

Vector	Gene	Promoter	Antibiotic resistance	Source
pJexpress411:39732	*G*Luc-HuAft	T7	Kanamycin	DNA2.0
pJexpress414:39732–*G*Luc	*G*Luc	T7	Ampicillin	DNA2.0
pJexpress414:LTVSPWY	LTVSPWY	T7	Ampicillin	DNA2.0
pJexpress401:Afb	Afb	T5	Kanamycin	DNA2.0
pMA-T:miniSOG	miniSOG	Non-inducible	Ampicillin	DNA2.0
pMA-T:His-Tag	His-Tag	Non-inducible	Ampicillin	DNA2.0
pJexpress414:*Li*Dps	*Li*Dps	T7	Ampicillin	Dr. Phil Hill University of Nottingham
pJexpress411:*G*Luc-*Li*Dps	*G*Luc-*Li*Dps	T7	Kanamycin	This work
pJexpress411:miniSOG-*Li*Dps	miniSOG-*Li*Dps	T7	Kanamycin	This work
pJexpress411:His Tag-miniSOG-*Li*Dps	His Tag-miniSOG-*Li*Dps	T7	Kanamycin	This work
pJexpress414:miniSOG-*Li*Dps	miniSOG-*Li*Dps	T7	Ampicillin	This work
pJexpress401:AfbC mutant	Afb (1 Cys mutant)	T5	Kanamycin	This work
pJexpress401:Afb2C mutants	Afb (2 Cys mutant)	T5	Kanamycin	This work
pJexpress414:*G*Luc-miniSOG-LTVSPWY	*G*Luc-miniSOG-LTVSPWY	T7	Ampicillin	This work

10.4 Media

10.4.1 Bacteria culture media

Media	Components	Quantity
Luria Bertani (LB) medium	10 g Tryptone 5 g Bacto-yeast extract 10 g NaCl	25 g LB in 1 L deionised water
LB Agar	10 g Bactotryptone 5 g Bacto-yeast extract 10 g Micro Agar 10 g NaCl	25 g LB in 1 L deionised water
SOC outgrowth medium	2% Vegetable Peptone 0.5% Yeast Extract 20 mM Glucose 10 mM $MgSO_4$ 10 mM $MgCl_2$ 2.5 mM KCl 10 mM NaCl	1 x SOC outgrowth medium
M9 medium	M9 salt solution (5 x) Na_2HPO_4 (33.7 mM) KH_2PO_4 (22.0 mM) NH_4Cl (9.35 mM) NaCl (8.55 mM)	200 mL
	20% (w/v) Glucose	20 mL
	1 M $MgSO_4.7H_2O$	1.0 mL
	1 M $CaCl_2.2H_2O$	0.3 mL
	Biotin (10 mg/mL) Thiamin.HCl (10 mg/mL)	1.0 mL
	Trace elements solution (100 x) EDTA (13.4 mM) $FeCl_3.6H_2O$ (3.1 mM) $ZnCl_2$ (0.62 mM) $CuCl_2.2H_2O$ (76 µM) $CoCl_2.6H_2O$ (42 µM) H_3BO_3 (162 µM) $MnCl_2.4H_2O$ (8.1 µM)	10 mL
	Sterile water	767 mL

***** LB, LB-agar, M9 salt, glucose, $MgSO_4$, $CaCl_2$, biotin and thiamine were purchased from Sigma. SOC outgrowth medium supplied with Q5® Site-Directed Mutagenesis Kit (New England Biolabs™).

10.4.2 Mammalian culture media

Media	Components	Final concentration
RPMI 1640	RPMI 1640 (500 mL) Fetal bovine serum Penicillin-streptomycin (10,000 U/mL)	N/A 10% (v/v) 1% (v/v)
Minimum Essential Medium (MEM)	MEM (500 mL) Fetal bovine serum penicillin-streptomycin non-essential amino acid sodium bicarbonate L-glutamine HEPES	N/A 10% (v/v) 1% (v/v) 1% (v/v) 1% (v/v) 1% (v/v) 1% (v/v)

***** RPMI 1640 and Minimum Essential Media, FBS, L-glutamine, non-essential amino acid, HEPES, sodium bicarbonate and penicillin-streptomycin solutions were purchased from Sigma-Aldrich.